Karlsruhe Institute of Technology

Rheological Characterization of Glass-Forming Colloidal Suspensions: Experimental Investigations and Comparison to Mode Coupling Theory

Zur Erlangung des akademischen Grades eines

DOKTORS DER NATURWISSENSCHAFTEN

(Dr. rer. nat.)

von der KIT-Fakultät für Chemie und Biowissenschaften
des Karlsruher Instituts für Technologie (KIT)

genehmigte

DISSERTATION

von

M.Sc. Lea Fischer

aus Karlsruhe

1. Referent:	Prof. Dr. Manfred Wilhelm
2. Referent:	Prof. Dr. Patrick Théato
Tag der mündlichen Prüfung:	15. Juli 2024

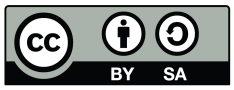

Die vorliegende Arbeit wurde von April 2020 bis Juni 2024 unter der Betreuung von Herrn Prof. Dr. Manfred Wilhelm am Institut für Technische Chemie und Polymerchemie (ITCP) des Karlsruher Institut für Technologie (KIT) - Universitätsbereich angefertigt.

Ich versichere hiermit wahrheitsgemäß, die Arbeit selbstständig verfasst, alle benutzten Hilfsmittel vollständig und genau angegeben, und alles kenntlich gemacht zu haben, was aus Arbeiten anderer unverändert oder mit Abänderungen entnommen wurde, sowie die Satzung des KIT zur Sicherung guter wissenschaftlicher Praxis in der jeweils gültigen Fassung beachtet zu haben.

Lea Fischer

Karlsruhe, den 18.10.2024

Zusammenfassung

Glassartige Materialien finden aufgrund ihrer einzigartigen Eigenschaften und Vielseitigkeit breite Anwendungen in unterschiedlichen Industriezweigen. Von optischen Geräten bis hin zu Verpackungsmaterialien spielen sie eine entscheidende Rolle in der modernen Technologie und Fertigung.
Unter den unterschiedlichen Arten von glasartigen Materialien finden sich molekulare, atomare, polymere und kolloidale Gläser. Trotz ihrer Unterschiede in der Größe der Bausteine folgen sie alle denselben grundlegenden Dynamiken, die zu ihrem glasartigen Verhalten beitragen. Kolloidale Gläser dienen als leicht zugängliche Modellsysteme zur Charakterisierung des glasartigen Zustands. Diese Modellsysteme weisen die größten Bausteine der glasbildenden Materialien auf, was den experimentellen Zugang zu ihren glasartigen Dynamiken erleichtert.
Diese Arbeit beschäftigt sich mit rheologischen Untersuchungen von glasbildenden kolloidalen Suspensionen im glasartigen und unterkühlten Zustand, um Einblicke in die Dynamik und die mechanischen Eigenschaften glasbildender Systeme zu gewinnen. Darüber hinaus werden die Ergebnisse mit Vorhersagen der Modenkopplungstheorie (MCT) verglichen.
Im ersten Teil wird ein kolloidales Modellsystem synthetisiert und charakterisiert. Das Modellsystem besteht aus sterisch stabilisierten Kolloiden mit einem Polystyrol (PS) Kern und einer vernetzten Poly-*N*-isopropylacrylamid (PNIPAm) Schale. PNIPAm zeigt in Wasser eine untere kritische Lösungstemperatur (T_{LCST}), was zu einem temperaturabhängigen hydrodynamischen Radius (R_{H}) führt. Dies ermöglicht eine präzise Einstellung des effektiven Volumenbruchs (ϕ_{eff}) durch kontrollierte Temperaturveränderungen. Der effektive Volumenbruch beeinflusst direkt das Phasenverhalten kolloidaler Suspensionen. Um einen rein glasartigen Zustand zu untersuchen, muss die Kristallisation der Partikel verhindert werden. Im Gegensatz zu früheren Studien wird in dieser Arbeit eine bimodale Mischung von Partikeln mit engen Größenverteilungen verwendet, um die Kristallisation zu unterdrücken. Die geringe Dispersität der einzelnen Partikelgrößenverteilungen verbessert die Vergleichbarkeit mit MCT Vorhersagen, die normalerweise auf monodispersen harten Kugeln basieren.
Im zweiten Teil werden das rheologische Verhalten und die Dynamik der glasbildenden kolloidalen Suspension charakterisiert. Das Material wird sowohl im ruhenden als auch im stetig verscherten Zustand, der zum Fließen des Materials führt, untersucht und die Ergebnisse mit den Vorhersagen der MCT verglichen. Oszillatorische rheologische Untersuchungen werden durchgeführt, um zu bestätigen, dass das ausgewählte Modellsystem

die typischen rheologischen Eigenschaften im glasartigen sowie im unterkühlten Zustand aufweist. Darüber hinaus zeigen diese Messungen eine starke Abhängigkeit der Relaxationszeitskala der normierten α-Relaxation der kolloidalen Partikel vom Volumenbruch $\frac{\tau_\alpha}{\tau_0} \propto \phi_{\text{eff}}^m$ mit $m \approx 124$.

Parallele Superpositionsrheologie und MCT Berechnungen zeigen, dass die gleichmäßige Scherbewegung einen verflüssigenden Effekt auf die kolloidale Suspension hat, wobei eine direkte antiproportionale Beziehung zwischen der normierten α-Relaxationszeit und der normierten Scherrate besteht, $\frac{\tau_\alpha}{\tau_0} \propto Pe_0^{-1}$. Weiterhin wird die normierte α-Relaxationszeit im verscherten Zustand unabhängig von ϕ_{eff}.

Im dritten Teil der Arbeit wird das glasbildende kolloidale Modellsystem unter nichtlinearer oszillatorischen Verscherung (engl. medium and large amplitude oscillatory shear (MAOS) und (LAOS)) unter Verwendung von Fourier-Transformations-Rheologie untersucht. Die Anharmonizität der Spannungsantwort unter MAOS und LAOS wird durch die Intensität der dritten Harmonischen, normiert auf die Intensität bei der Grundfrequenz ($I_{3/1} = \frac{I_3}{I_1}$), sowie im Rahmen des intrinsischen Nichtlinearitätsparameter quantifiziert ($Q_0 = \lim_{\gamma_0 \to 0} \frac{I_{3/1}}{\gamma_0^2}$).

Im glasartigen Zustand zeigt $I_{3/1}$ einen Übergang von der erwarteten Skalierung von $I_{3/1} \propto \gamma_0^2$ zu einer ungewöhnlichen Skalierung von $I_{3/1} \propto \gamma_0^4$. Bei niedrigen Frequenzen ($\omega_1 = 4 \times 10^{-2}\,\text{rad}\,\text{s}^{-1}$) zeigt $I_{3/1}$ nur die ungewöhnliche Skalierung von $I_{3/1} \propto \gamma_0^4$. In amorphen polymeren Materialien wurde in einer früheren Arbeit ebenfalls ein Übergang von einer Skalierung von $I_{3/1} \propto \gamma_0^2$ zu $I_{3/1} \propto \gamma_0^4$ beobachtet, wenn diese plastische Verformung erfahren.

In dieser Arbeit wird die Frequenzsweep MAOS Methode angewendet, um die Frequenzabhängigkeit der Anharmonizität der Spannungsantwort zu untersuchen und auf kritische Verhaltensweisen im unterkühlten Zustand nahe dem Glasübergang zu testen, die von der MCT vorhergesagt wurden. Darüber hinaus werden die experimentellen Untersuchungen und die MCT Vorhersagen auf den glasartigen Zustand ausgeweitet. Durch Anwendung dieser zeiteffizienten Methodik wird die Frequenzabhängigkeit der Anharmonizität der Spannungsantwort über ein breites Spektrum von Volumenanteilen und Frequenzen untersucht. Im unterkühlten Zustand weist Q_0 ein Maximum im Bereich der α-Relaxation auf, das mit zunehmenden ϕ_{eff} zu niedrigen Péclet Zahlen und höheren Q_0 Werten verschiebt. Im unterkühlten Zustand liegt das Maximum in Q_0 bei 2 bis 6, was ca. dem 100 fachen der Maximalwerte in Polymerschmelzen entspricht. Im Gegensatz zum unterkühlten Zustand, weist die Suspension im glasartigen Zustand kein Maximum in Q_0 auf. Stattdessen nimmt Q_0 mit abnehmender Frequenz zu, da die α-Relaxation in kolloidalen Gläsern signifikant verlangsamt ist. Diese und weitere rheologische Befunde stimmen mit den Vorhersagen der MCT überein, wie der prinzipielle Verlauf von Q_0, die ermittelten Skalierungsgesetze von Q_0, die Überlagerung von Q_0 für unterschiedliche ϕ_{eff} im unterkühlten Zustand im Hochfrequenzbereich sowie der intrinsischen dritten Harmonischen $[I_3] = \lim_{\gamma_0 \to 0} \frac{I_3}{\gamma_0^2}$ für unterschiedliche ϕ_{eff} im glasartigen Zustand. Diese Ergebnisse unterstreichen die Leistungsfähigkeit der MCT bei der Vorhersage des rheologischen Verhaltens glasbildender kolloidaler Suspensionen.

Abstract

Glassy materials find wide-ranging applications across various industries due to their unique properties and versatility. From optical devices to packaging materials, they play crucial roles in modern technology and manufacturing processes. Among the diverse range of glass-forming materials are molecular, atomic, polymeric, and colloidal glasses. Despite their differences in building block sizes, they all operate under the same fundamental dynamics, contributing to their glassy behavior. Colloidal glasses serve as easily accessible model systems for the characterization of the glassy state. These model systems have the largest building blocks of the glass-forming materials which facilitates the experimental access to their glassy dynamics.

This thesis deals with rheological investigations of glass-forming colloidal suspensions in the glassy and the supercooled states to gain insight into the dynamics and the mechanical properties of glass-forming systems. Moreover, the results are compared to mode coupling theory (MCT) predicitions.

In the first part, a colloidal model system is synthesized and characterized. The model system consists of sterically stabilized colloids with a polystyrene (PS)-core and a crosslinked poly(*N*-isopropylacrylamide) (PNIPAm)-shell. PNIPAm exhibits a lower critical solution temperature (T_{LCST}) in water resulting in a temperature dependent hydrodynamic radius (R_{H}). This allows a precise adjustment of the effective volume fraction by changing the temperature. The effective volume fraction directly controls the phase behavior of colloidal suspensions. To study a pure glassy state, particle crystallization must be prevented. In contrast to previous studies, a binary mixture of particles with narrow size distributions is used in this thesis, to suppress particle crystallization. The low dispersity of the individual particle size distributions improves comparability to MCT studies which are usually based on monodisperse hard spheres.

In the second part, the rheological behavior and dynamics of the glass-forming colloidal suspension are characterized. The quiescent as well as the steady sheared state leading to yielding are investigated and compared to MCT predictions. Oscillatory rheological investigations were used to confirm that the chosen model system exhibits the typical rheological characteristcs in the glassy as well as in the supercooled state. Moreover, these measurements revealed a strong dependence of the relaxation time scale of the normalized out-of-cage relaxation (α-relaxation) of the colloidal particles on the volume fraction $\frac{\tau_\alpha}{\tau_0} \propto \phi_{\mathrm{eff}}^m$ with $m \approx 124$.

Parallel superposition rheology and MCT predictions revealed the steady shear motion to have a liquidifiying effect on the colloidal suspension with a direct antiproportionality of

the normalized α-relaxation time to the normalized shear rate $\frac{\tau_\alpha}{\tau_0} \propto Pe_0^{-1}$. The normalized α-relaxation time in the sheared state becomes independent of ϕ_{eff}.

In the third part of the thesis, the glass-forming colloidal model system is investigated under medium and large amplitude oscillatory shear (MAOS and LAOS) using Fourier transform (FT) rheology. The anharmonicity of the stress response under MAOS and LAOS is quantified by the intensity of the third harmonic normalized to the fundamental ($I_{3/1} = \frac{I_3}{I_1}$) and within the intrinsic nonlinearity framework of the Q-parameter ($Q_0 = \lim_{\gamma_0 \to 0} \frac{I_{3/1}}{\gamma_0^2}$). In the glassy state, $I_{3/1}$ shows a transition from the expected scaling of $I_{3/1} \propto \gamma_0^2$ to an unusual scaling of $I_{3/1} \propto \gamma_0^4$. At low frequencies ($\omega_1 = 4 \times 10^{-2}\,\text{rad}\,\text{s}^{-1}$), $I_{3/1}$ only exhibits the unusual scaling of $I_{3/1} \propto \gamma_0^4$. In amorphous polymeric materials, a previous study also observed a transition from a scaling of $I_{3/1} \propto \gamma_0^2$ to $I_{3/1} \propto \gamma_0^4$ when they undergo plastic deformation.

In this thesis, the frequency sweep MAOS methology is applied to investigate the frequency dependence of the anharmonicity of the stress response to test for critical behavior in the supercooled state near the glass transition as predicted by MCT. Furthermore, the experimental investigations and MCT predictions are extended to the glassy state. Applying the time-efficient frequency sweep MAOS methodology, the frequency dependence of the anharmonicity of the stress response is investigated over a wide range of volume fractions and frequencies. In the supercooled state, Q_0 exhibits a maximum in the range of the α-relaxation, which shifts to lower Péclet numbers and higher Q_0 values with increasing ϕ_{eff}. In the supercooled state, the maximum in Q_0 ranges from 2 to 6, which is approximately 2 decades higher than the maximum values observed in polymer melts. The colloidal glasses do not exhibit a maximum in Q_0, but an increase in Q_0 with decreasing frequency, since the α-relaxation slows down significantly in colloidal glasses. Several rheological findings are consistent with the predictions of MCT, such as the principle course of Q_0, the determined scaling laws, the collapse of Q_0 for different ϕ_{eff} in the supercooled state, and the collapse of the intrinsic third harmonic $[I_3] = \lim_{\gamma_0 \to 0} \frac{I_3}{\gamma_0}$ for different ϕ_{eff} in the glassy state in the high frequency regime. These findings support the capability of MCT to predict the rheological behavior of glass-forming colloidal suspensions.

Contents

1 Introduction

The term suspension refers to a heterogeneous mixture of solid particles dispersed in a homogeneous liquid[1]. The term colloidal suspension specifies the diameter of the solid particles to be in the range of 1 nm to 1 µm according to the IUPAC definition[2,3]. These colloidal suspensions have numerous technological applications, ranging from cosmetics and food science to building materials. In most of these colloidal suspensions water is used as dispersion medium.

Under certain conditions, colloidal suspensions form glasses. The glassy state is a solid state characterized by a short-range order without having the long-range order present in a crystal. Glass-forming materials are of great interest for industry as glassy materials are used for a wide variety of different industrial applications ranging from optical devices to packaging materials[4,5]. Among the diverse range of glassy materials are molecular, atomic, polymeric, and colloidal glasses[6]. Despite their differences in building block sizes, they all operate under the same fundamental physics and respective dynamics, contributing to their glassy behavior. The simplest model system for a glassy material is a colloidal glass consisting of monodisperse hard sphere particles. The nanometer size of the particles results in slower dynamics compared to atomic or molecular glasses, which makes the dynamics easier accessible experimentally, while preserving their principle behavior. Therefore, glass-forming colloidal suspensions are an appropriate model system for investigating the fundamental physics, such as the phase behavior and dynamics of glass-forming materials. In colloidal suspensions, when a critical volume fraction is exceeded, monodisperse particles can enter either a glassy or a crystalline state. If the critical volume fraction is reached quickly, the crystallization process is kinetically suppressed, leading to the formation of the metastable glassy state. The glassy state is only stable for a limited time scale which is usually in the range of minutes to hours[6] for suspensions and depends on the volume fraction of the system. For times exceeding this time scale, the system will rearrange to enter the thermodynamically stable crystalline state. Furthermore, while investigating the mechanical properties through rheological measurements, shear induced crystallization can occur[7]. Therefore, kinetic suppression of the particle crystallization is not sufficient to study a pure glassy state on time scales of several hours. To study a pure glassy state on these time scales, the crystallization has to be sterically prevented for example by introducing a dispersity of the radius distributions. Crystallization is fully suppressed for relative standard deviations of the radius distribution of $\sigma_{\mathrm{rel}} = \left(\langle R^2\rangle - \langle R\rangle^2\right)^{-\frac{1}{2}} / \langle R\rangle > 12\,\%$[8,9].

The glassy state of colloids is marked by trapping the particles in a cage formed by the surrounding particles, which restricts their movement[10]. This constraint of particle movement causes the colloidal suspension to exhibit viscoelastic behavior in the glassy state as well as a yield stress[11–19] often needed for processing and real life application. In addition, colloidal suspensions exhibit significant nonlinear mechanical behavior when exposed to large deformation, as documented in several publications[18,20–25]. Understanding this nonlinear mechanical behavior is crucial since materials frequently undergo large deformations during industrial processing and application.

Summarizing, the mechanical properties of colloidal suspensions and especially colloidal glasses are of great interest due to their industrial application. Additionally, they are interesting for fundamental physics as they represent a simple and easy-to-study model system for glass-forming materials in general.

Therefore, the objective of this work is to characterize the rheological properties of a glass-forming colloidal suspension in the supercooled state, where the constraints of particle motion cause the suspension to undergo viscoelastic behavior, and in the glassy state, where the material additionally exhibits a yield stress. The rheological properties are compared to mode coupling theory (MCT), which is a fully microscopic theory describing the structure and the dynamics of glass-forming suspensions using first principle mechanics[26,27].

Previous rheological studies[17,22,28,29] on glass-forming colloidal suspensions were based on systems with high relative standard deviations (e.g., $\sigma_{\mathrm{rel}} \approx 17\,\%$[17,22,28,29]) of the radius distribution to suppress particle crystallization. These studies were compared in detail to MCT predictions, although MCT calculations usually assume an ideal monodisperse distribution of the radius. Therefore, in this work a binary system consisting of two rather monodisperse ($\sigma_{\mathrm{rel}} < 6\,\%$) particle suspensions with a weight ratio of 90:10 is developed to improve comparability to MCT and other theoretical approaches like Brownian dynamics simulation. In addition, the chosen model system consists of thermoresponsive core-shell particles, which allows precise adjustment of the effective volume fraction. This enables changing the state of the model system from supercooled to glassy, depending on the focus of the investigation.

The first part of the thesis deals with the synthesis, purification and characterization of these polymer based thermoresponsive core-shell systems used as a model system for glass-forming colloidal suspensions. The core particles are synthesized via emulsion polymerization and purified using dialysis. Their size and size distribution are analyzed with dynamic light scattering (DLS) and scanning electron microscopy (SEM). The shell is synthesized on those core particles using seeded emulsion polymerization and purified with ultrafiltration. The shape, structure, size, size distribution, swelling behavior and colloidal stability in the shrunken and the swollen state of the core-shell particles are investigated with several methods.

The second part of the thesis deals with the mechanical characterization of the colloidal suspension in the supercooled and the glassy state under simple shear motions, namely oscillatory shear in the linear regime of the samples and under steady shear. Using linear oscillatory shear, the relaxation times of the particles in the suspension depending on

the volume fraction are analyzed, and estimations about the hardness of the interaction potential between the particles are made. The response of the material to a linear oscillatory shear motion is compared to MCT predictions, which are fitted to the experimental data. These predictions were kindly provided by Manuel Maier from the group of Prof. Fuchs in Konstanz. Moreover, the yielding behavior of the colloidal suspensions is investigated under steady shear motion with focus on the start-up of shear and the steady state reached after a certain strain deformation. This allows to distinguish between the static and dynamic yield stress. Finally, the influence of a steady shear motion on the relaxation times is investigated and compared to MCT predictions.
The third and final part deals with the yielding behavior, nonlinearity and anharmonicity of the colloidal suspension under nonlinear oscillatory shear deformations. The moduli and the yield strain are analyzed giving insights into the microstructural changes caused by the oscillatory shear deformation. Nonlinear oscillatory shear provides a quantification of the nonlinear behavior with the ability of investigating the influence of the timescale and the extent of deformation. The dependence of the anharmonicity of the stress response of the material on the applied frequency is analyzed in the supercooled and the glassy state. The response is compared to MCT predictions in the supercooled state by Seyboldt *et al.*[29] and to MCT predictions in the supercooled and glassy state kindly provided by Leonhard Lang from the group of Prof. Fuchs in Konstanz.

2 Synthesis, Characterization and Stability of Colloidal Suspensions

This chapter provides an overview of the polymerization techniques and characterization methods used in this thesis. First, the polymerization techniques free radical polymerization, emulsion polymerization and seeded emulsion polymerization are introduced and the mechanisms are discussed. Then, the characterization methods dynamic light scattering, scanning electron microscopy, environmental scanning electron microscopy and differential centrifugal sedimentation are introduced and the advantages and disadvantages of the methods are addressed. Finally, the different intermolecular forces acting on colloidal particles and the appropriate interplay of them resulting in stability of colloidal suspensions are discussed.

2.1 Synthesis of Colloidal Suspensions

2.1.1 Free Radical Polymerization

Worldwide, nearly 50 % of commercial synthetic polymers are produced by radical polymerization[30]. This process is preferred for its accessibility to numerous monomers and ease of practical implementation, as the polymers can be prepared under mild reaction conditions and the reaction tolerates water, and a wide range of temperatures[31]. Free radical polymerization is a chain-growth polymerization. The reaction mechanism is divided into three reaction steps: chain initiation, propagation, and termination, schematically shown in Figure 2.1 using $K_2S_2O_8$ as the initiator and styrene as the monomer. Due to statistical termination in the non-living free radical polymerization the dispersities are typically comparativeliy high ($Đ \geq 1.8$). Additionally, chain transfer reactions occur as side reactions influencing the molecular weight, dispersity and topology of the polymer.

Initiation

The first step of the polymerization reaction is the initiation. The free radicals that initiate the reaction are formed *in-situ* by thermal or light induced cleavage of atomic bonds of an initiator. The free radicals then react with the first monomer unit. Azo or peroxide compounds are most commonly used as initiators. Other commonly used initiators are redox sytems or organometallics.

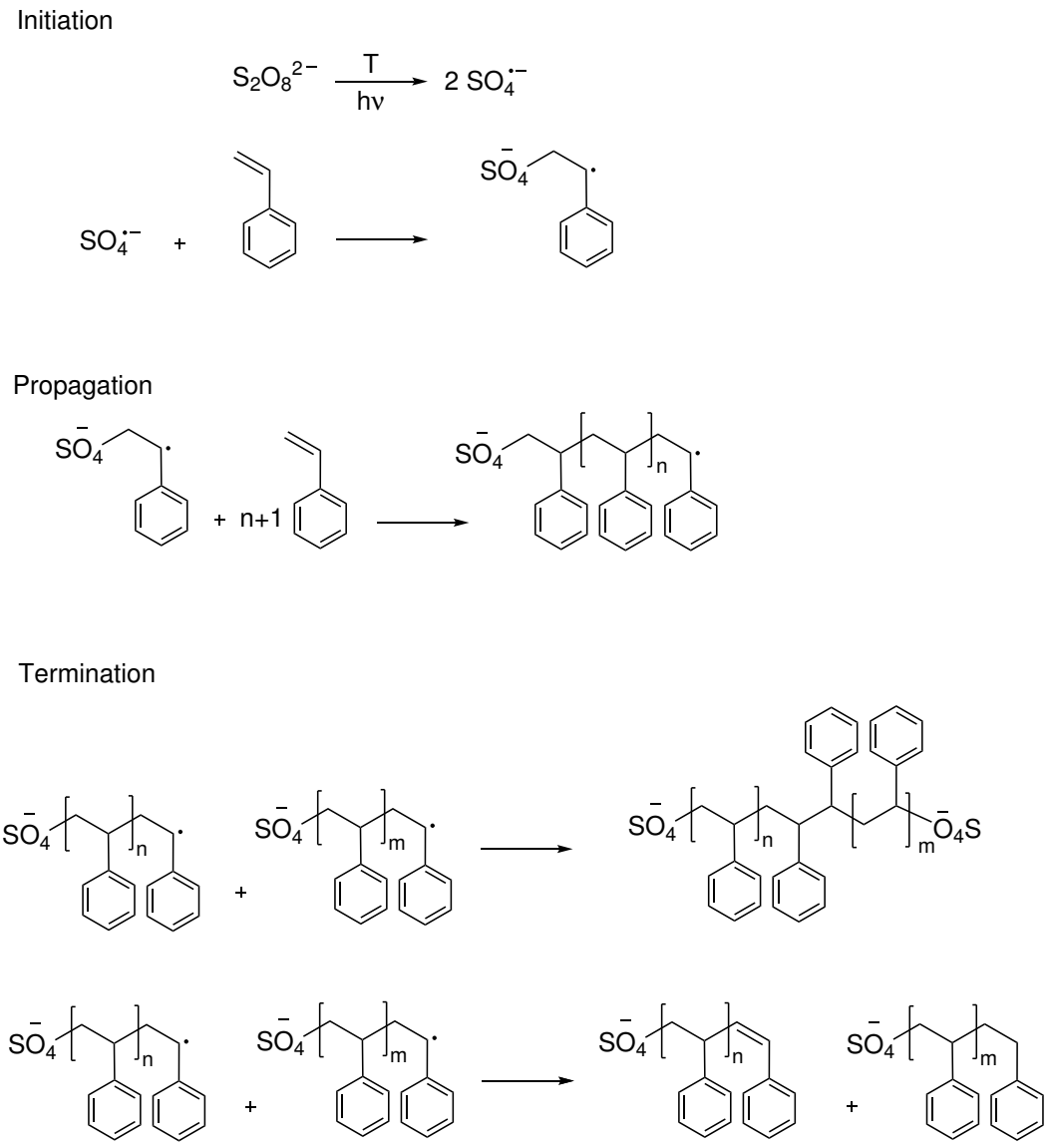

Figure 2.1: Reaction mechanism of a free radical polymerization using $K_2S_2O_8$ as an initiator and styrene as a monomer. In the initiation step, the initiator is decomposed building radicals, which react with the first monomer unit. In the second step, the propagation, further monomers are added to the growing chain. In all initiation and propagation steps, the most probable position for the attack by the radical is assumed, leading to the dominating head-to-tail sequence in polymeric chains. In the third step, the termination, two radicals are consumed by either recombination or disproportionation. Recombination results in a doubling of the molecular weight, whereas disproportionation creates two molecules. One of them is a macromonomer that can be consumed by another growing chain in a propagation step, leading to chain branching.

Propagation

In the second step, the propagation, the radical attacks monomer molecules that are added to the growing chain. During the propagation, the most probable position for the attack by the radical is assumed, leading to the dominating head-to-tail sequence in the polymeric chains. The chains propagate until termination occurs.

Termination

The third and final step, the termination, can either occur by recombination or dispropotionation of two radicals ending the reaction of those two chains. In the recombination reaction, two radical electrons combine forming a single bond between two polymer chains resulting in a doubling of the molecular weight. In the disproportionation reaction, one radical abstracts a hydrogen atom from another radical, which creates a polymer with a double bond at the end and a second polymer with a saturated end group. The polymer with the double bond acts like a macromonomer that can be consumed by another growing chain in a propagation step, leading to chain branching.

Both termination reactions occur simultaneously, with recombination occurring preferentially at lower temperatures because disproportionation has a higher activation energy. At higher temperatures the activation energy of both termination reactions is small compared to the thermal energy, resulting in equal occurance of recombination and disproportionation. The temperature until which recombination is dominating depends on the polymer.

Termination may also be triggered by the addition of an inhibitor, whereby a transfer reaction forms an inert radical. As inhibitors, aromatic compounds are commonly used[32] due to their ability to stabilize the unpaired electron through resonance with the π electrons.

Chain Transfer Reaction

Chain transfer reactions are a common side reaction in which the radical center is transferred to another molecule by the abstraction of a hydrogen or a halogen. These reactions can take place on monomers, polymers, solvents or initiators. Depending on the reactivity of the resulting radical, either further propagation or chain termination occurs due to chain transfer reaction.

2.1.2 Emulsion Polymerization

Emulsion polymerization is a specific type of radical polymerization. It is used to synthesize suspensions consisting of solid polymer particles dispersed in a dispersion medium, frequently water, which are used in various commercial products. Either the resulting suspension itself is the final product, as in paints, adhesives or coatings, or the solid polymer materials are used as the final product. In this case, the suspension medium must be removed after the polymerization process. For example, styrene-butadiene rubber, which is used in tires, shoe heels and soles, and gaskets, is often synthesized by emulsion polymerization.[33]

In an emulsion polymerization the free radical polymerization takes place in particles, which are isolated by the reaction medium. This leads to a high polymerization rate that is possible due to the heat dissipitation in the low-viscous reaction medium. In addition, the isolation also leads to reduced termination and thus high molecular weights of the polymers. Emulsion polymerization is most commonly carried out in water and is therefore less harmful to the environment than chemical reactions using volatile organic liquids as the reaction medium.

In the simplest case, the reaction mixture of an emulsion polymerization consists of water, a surfactant, a monomer and a water-soluble initiator (see Figure 2.2 on page 9). De-

pending on the water solubility of the monomer and the concentration of the surfactant, different nucleation processes take place. If the solubility of the monomer is very low (e.g., styrene $0.03\,\mathrm{g\,g^{-1}}$ in water at $25\,^{\circ}\mathrm{C}$[34]) and the concentration of the surfactant exceeds the concentration above which micelles form referred to as critical micelle concentration, the micellar particle nucleation proposed by Smith and Ewart[35] is preferred.
If the solubility of the monomer in water is higher (e.g., methyl methacrylate $1.6\,\mathrm{g\,g^{-1}}$ in water at $20\,^{\circ}\mathrm{C}$[36]) or the concentration of the surfactant lower than the critical micelle concentration, the homogeneous nucleation proposed by Fitch *et al.*[37] is preferred.
When the surfactant concentration exceeds the critical micelle concentration, the surfactant molecules form micelles. In the case of the micellar nucleation, the polymerization process begins and continues in the aqueous phase until a critical degree of polymerization is reached, where the oligomer becomes a surface active substance. This critical degree of polymerization depends on the monomer and is $n = 3$ for styrene. Then, the growing chain radical enters a micelle and the polymerization process continues in the micelle until a second radical enters, which terminates the reaction. As soon as a new radical enters the micelle, the polymerization in the micelle restarts.
When the homogeneous nucleation occurs, the reaction still begins in the water phase. In the absence of micelles or at high monomer concentration in the solution, the radicals begin to coagulate when the chain length is reached where the polymer becomes surface active. The radicals form precursor particles that are stabilized by the charged end groups of the oligomer chains and by adsorption of surfactant molecules. The radical chains grow by propagation and further absorption of oligomer chains.

2.1.2.1 Micellar Particle Nucleation: Smith Ewarts Theory

The micellar particle nucleation was first proposed by Smith and Ewarts[35]. This mechanism is favored when the solubility of the monomer in water is very low (e.g., styrene $0.03\,\mathrm{g\,g^{-1}}$ at $25\,^{\circ}\mathrm{C}$[34]), and the surfactant concentration exceeds the critical micelle concentration. The initial emulsion contains water, the initiator, which is dissolved in the water, monomer droplets, and micelles, which are swollen with monomer. In addition, a small part of the monomer is dissolved in the water. The monomer droplets have diameters of approximately $1\,\mu\mathrm{m}$ to $5\,\mu\mathrm{m}$ and are stabilized against coagulation by a monomolecular layer of the surfactant molecules. In contrast, the micelles have a diameter of around $10\,\mathrm{nm}$[38].
The emulsion polymerization mechanism is divided in three different intervals, the nucleation (interval 1), the growth (interval 2) and the monomer finishing (interval 3).

Interval I: Nucleation

A schematic illustration of the first interval, the nucleation, of the emulsion polymerization is shown in Figure 2.2. It starts with the decomposition of the initiator, which leads to initiator radicals. They start the polymerization reaction by attacking the monomer molecules, which are dissolved in the water, building oligomeric chain radicals. Once the critical degree of polymerization is reached where the chains become surface active, the oligomers either enter an existing micelle or form a new one by aggregating with free surfactant molecules. The probability that a radical chain enters a monomer droplet

instead of entering a micelle is low as the total surface of the monomer droplets is way lower than the total surface of the micelles. If the surfactant is present at concentrations of a few weight percent of monomer, the number concentration of monomer swollen micelles (later latex particles) is high compared to the number concentration of monomer droplets. These micelles have a diameter of approximately 10 nm with a number concentration of around $10^{18}\,L^{-1}$ to $10^{21}\,L^{-1}$. In contrast, the monomer droplets are present at a lower concentration of around $10^{10}\,L^{-1}$ to $10^{12}\,L^{-1}$ and are significantly larger[38] resulting in a lower total surface area of monomer droplets compared to the total surface area of the micelles.

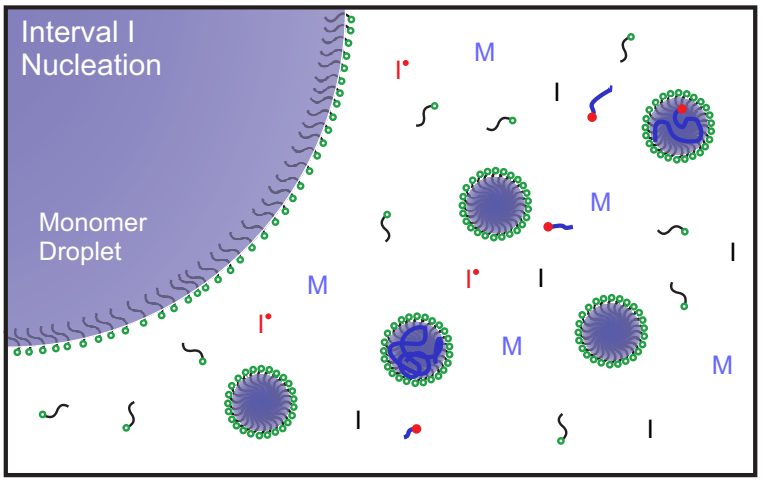

Figure 2.2: Interval I of the Smith-Ewarts mechanism: the nucleation[35]. The **I** represents the initiator molecules, the $\mathbf{R}^{\bullet}$ the decomposed initiator, the surfactant molecules are depicted as o- with an open circle, while the oligomer/polymer chains are depicted similar, but with an closed circle. The **M** represents the part of the monomer, which is dissolved in water. The monomer in the monomer droplets and in the monomer swollen micelles is depicted in the same color. The polymerization process begins in the water phase. As soon as the oligomer radicals exceed the critical chain length at which they become surface active, they enter a micelle or form new primary particles. The polymerization then proceeds inside the particles.

When a radical chain enters a micelle, a fast polymerization reaction starts as the monomer concentration within the micelle is high. The micelle turns into a polymer particle, a so called latex particle. The size of the particles increases rapidly, thus the interface between the particles and the water is increasing, resulting in a decrease of free surfactant molecules. The nucleation interval ends when the interface becomes so large that all the surfactant molecules are needed to stabilize the interface. From then on, the number of particles remains constant as no surfactant molecules are present for building new micelles. Particles, which are build at the beginning of the nucleation phase contain more polymer molecules, than particles, which are build at the end of the nucleation phase. In interval II, the growth phase, larger particles grow with a slightly higher propability than smaller particles due to the higher total surface. Therefore, the shorter the nucleation phase compared to interval II, the growth phase, the lower the dispersity of the particle diameter distribution. Thus, the higher the monomer to surfactant ratio, the lower the dispersity of the diameter of the resulting latex.

Interval II: Growth

During the growth phase the number of particles is constant and they are swollen with monomer and polymer. As soon as a radical chain enters a particle, the polymerization reaction of this chain is accelerated as the concentration of the monomer in the particles is high compared to the concentration in the water phase. Additionally, monomer diffuses from the monomer droplets through the water phase to the particles. This diffusion is faster than the consumption of the monomer molecules leading to a constant monomer to polymer ratio inside the particles, which depends on the solubility of the monomer in water and in the particle. Therefore, the reaction rate is staying constant during this phase. The reaction in a specific particle stops as soon as a second radical is entering the particle as the particles have a low volume leading to a termination reaction of the radicals rather than the start of a second growing chain. The reaction in the particle stops until another radical enters the particle. Thus, for each single latex particle in the suspension, the period of growth is always followed by a period of stagnation. On average, these phases are of equal length due to statistics. The rate of polymerization is constant during this phase. Interval II is considered complete when the monomer droplets are fully consumed. The remaining monomer is dissolved in the water phase and in the latex particles.

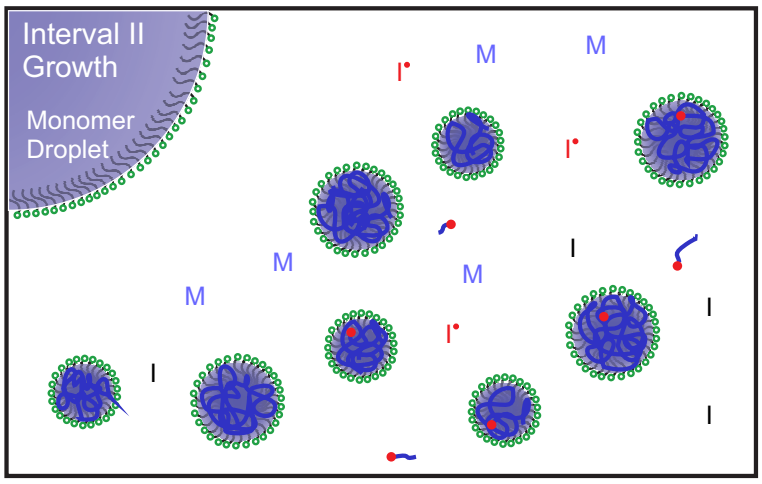

Figure 2.3: Interval II of the Smith-Ewarts mechanism: the growth. All the surfactant molecules o- are needed to stabilize the interface between the monomer droplets and the latex particles. The number of particles is remaining constant througout the rest of the polymerization process and the particles are growing.

Interval III: Monomer Finishing

The phase of monomer finishing commences once the reaction yield reaches the level where the residual monomer can dissolve entirely in the water phase and the latex particles. Subsequently, the monomer droplets disappear, and the remaining monomer in the particles and in the water phase is consumed. At this point, two different effects are reducing the likelihood of the termination of the reaction compared to the second interval. First, the polymer concentration within the particles is considerably high, resulting in a high viscosity and respectively slower diffusion of monomer in the particles. Second, the volume of a particle is larger compared to the second interval. Therefore, the presence of multiple

radicals within a single particle is possible.
After the monomer is completely consumed, the reaction ends. The latex particles consist typically of a few hundred polymer molecules and have an average diameter between 30 nm to 1000 nm[39]. The average diameter and the dispersity of the diameter distribution of the latex particles highly depend on the ratio of surfactant to monomer and initiator to monomer concentration. The concentrations of monomer, intiator and surfactant determine the length of the nucleation phase and the number of particles present at the end of this phase. The number of particles and the amount of monomer determine the particle size at the end of the emulsion polymerization process. The dispersity is affected by these ratios as it depends on the ratio of the duration of the nucleation phase compared to the duration of the growth phase. A higher monomer to surfactant ratio results directly in a higher average diameter of the latex particles and additionally directly in a lower dispersity of the diameter distribution. Thus, the higher the average diameter of the particles, the narrower the diameter distribution.

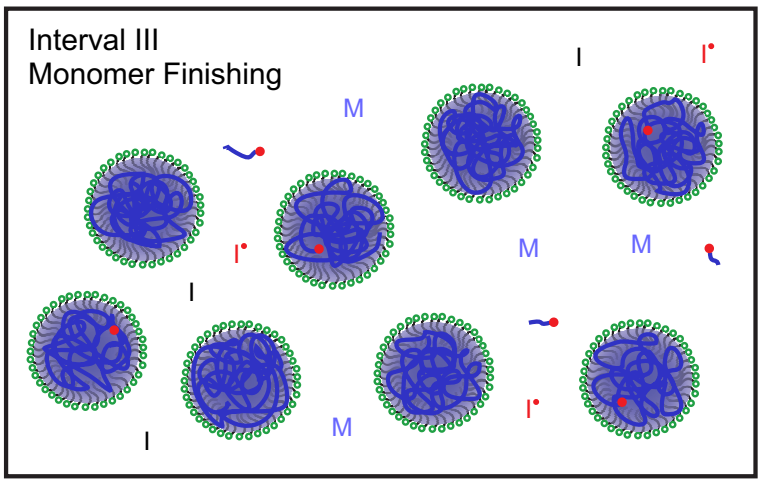

Figure 2.4: Interval III of the Smith-Ewarts mechanism: the monomer finishing. The polymerization process has progressed to the point where the remaining monomer is completely soluble in the polymer particles and the water. The reaction continues within the polymer particles until all remaining monomer is converted to polymer.

2.1.2.2 Homogeneous Particle Nucleation

The mechanism of the homogeneous particle nucleation first proposed by Fitch *et al.*[37] is preferred, when the surfactant concentration is below the critical micelle concentration[40]. The polymerization reaction is still starting in the water phase. As soon as the oligomer radicals become unsoluble in water, they are precipitating onto themselves or onto other oligomer radicals in the dispersion medium[37,41]. The so formed primary particles are stabilized by the charged end groups of the oligomers and by adsorbing surfactant molecules. The reaction continues by absorbing monomer and further oligomer chains from the water phase.

2.1.3 Seeded Emulsion Polymerization

For the synthesis of core-shell particles a two-stage seeded emulsion polymerization is commonly utilized. For this process, a second, independent emulsion polymerization reaction follows the previously described one. The latex particles formed during the first reaction serve as seeds. For synthesizing the shell material onto the core particles, a water-soluble initiator and the second monomer are added to the seed latex. The newly formed oligomer radicals in the aqueous phase coagulate on the seed particles as soon as they become surface active and further polymerize on the surface. From the polymerization process, spherical core-shell particles are obtained[42].
One of the main challenges in seeded emulsion poylmerization is to avoid the creation of new particles in the second step of the polymerization process. Adding the second monomer already as comonomer in the first polymerization step increases the probability of coagulation of the oligomer radicals onto the core seeds in the second polymerization step reducing the formation of new particles by optimizing the van der Waals interactions. The monomer introduced in the second step, can either have a low or high water solubility. When adding a monomer with low water solubility, the core particles will swell with the monomer, necessitating additional surfactant to ensure the stability of the growing seed particles. It is important to ensure that the concentration of surfactant does not exceed the critical micelle concentration at any point to avoid the possibility of micellar nucleation. More water-soluble monomers can eliminate the need for additional surfactant molecules in the second step, but it requires lower rates of radical generation to avoid creating new particles instead of adsorption onto the cores.[38] Hence, in the case of more water soluble monomers, it is required to keep the concentration of the surfactant and the initiator concentration low in the second step of the seeded emulsion polymerization.

2.2 Characterization of the Size and the Size Distribution of Colloids

There are several methods for determining the size and the size distribution of nanoparticles or colloids. The most commonly used methods are high resolution microscopy techniques such as scanning electron microscopy and diffusion-based methods such as dynamic light scattering (DLS). High-resolution microscopy techniques provide images of the particles, from which number-weighted diameter and respective radius distributions can be obtained, when the particles have a spherical shape. These techniques have a limited throughput, which raises the question of whether the data obtained are statistically representative. In addition, they are performed under high vacuum conditions, measuring the size distribution in the dry state neglecting phenomena that occur in suspension[43]. In contrast, DLS is an ensemble technique that measures the entire sample in suspension, providing information about the radius of the colloid in the suspended state rather than in the dry state, while assuming a spherical shape of the particles. Using DLS, an intensity weighted radius distribution with high precision in the mean value of R_{H}, but a high uncertainty in the shape and width of the distribution is obtained. In contrast, differential centrifugal

sedimentation (DCS) gives resolution for the whole distribution. Environmental scanning electron microscopy (ESEM) is a high-resolution microscopy technique allowing for taking images of samples with a low content of water at water pressures in the sample chamber of 10 Pa to 2500 Pa[44]. In the following, an overview about those methods used for the characterization of the size and size distribution is provided. First, DLS is introduced and discussed in detail. Then, a brief introduction into SEM, ESEM and DCS is given.

2.2.1 Dynamic Light Scattering

DLS is a common technique for the characterization of the size and size distribution of colloids and polymers in solution. It is based on the scattering of laser light by the suspended or diluted particles. In Figure 2.5 the basic principle of DLS is illustrated. When light hits small particles, it is scattered in all directions. In DLS, the intensity of this scattered light is measured at a fixed angle, typically 90°, with high time resolution of several µs[45]. The movement of the particles in the suspension causes fluctuations of the number of particles inside the light beam and therefore fluctuations in the intensity of the scattered light, which can be used to determine the translational diffusion coefficient of the particles. From this, the hydrodynamic radius (R_H) of the particles can be calculated using the Stokes-Einstein relation assuming a spherical shape of the particles.

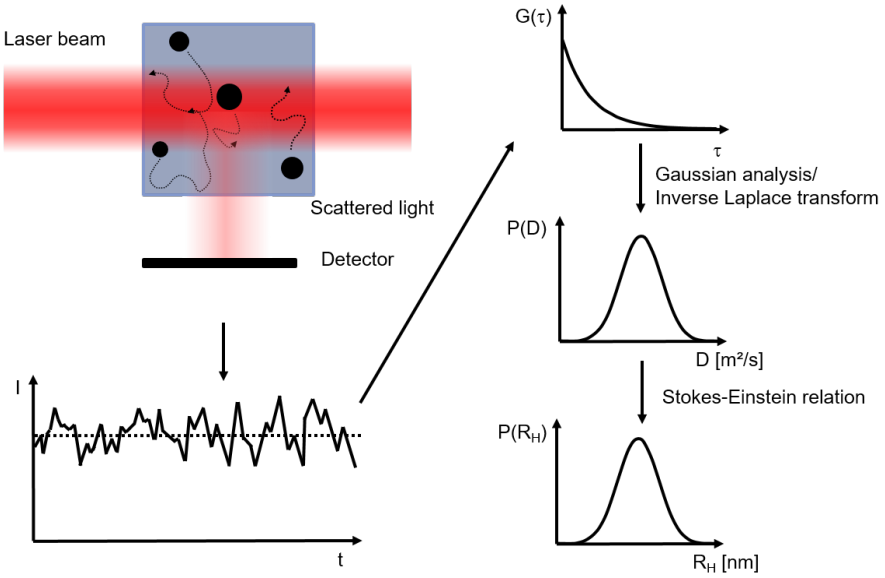

Figure 2.5: Schematic illustration of the basic principles of dynamic light scattering. The fluctuations in the intensity of the light that is scattered by polymers or colloidal particles are detected. These fluctuations are caused by fluctuations in the number of particles in the light beam due to the movement of the particles in the suspension. From this, the autocorrelation function of the intensity is calculated and converted to a diffusion coefficient distribution by either Gaussian analysis or inverse Laplace transformation. The Stokes-Einstein relation is used to convert this diffusion coefficient distribution to the hydrodynamic radius distribution of the particles. For better visibility only the scattering of one particle at an angle of 90° is illustrated, although every particle present in the laser beam scatters the light in all directions.

From the intensity fluctuations of the scattered light, the autocorrelation function $g^{(2)}(q,\tau)$, often referred to as the second order autocorrelation function[46], is determined

$$g^{(2)}(q,\tau) = \frac{\langle I(t)\, I(t+\tau)\rangle}{\langle I(t)\rangle^2} \tag{2.1}$$

at a particular wave vector (q) with τ being the delay time and $I(t)$ being the intensity at a specific time t. For short time intervals, i.e. low τ values, the autocorrelation is high because the particles do not move far from their initial state within short times. The two intensity signals remain almost identical when compared after this short time. As time intervals become longer, the autocorrelation function gradually decreases as the correlation between the initial state and the state at $t+\tau$ is becoming lower for increasing τ. Note that the normalized intensity autocorrelation function decays to 1 for $\tau \to \infty$ as the nominater of Equation 2.1 simplifies to $\langle I(t)\rangle^2$ for $\tau \to \infty$[45]. For the simplest case of monodisperse, spherical particles at high dilution, the autocorrelation function is a single exponential decay[46].

$$g^{(2)}(q,\tau) = C_0 e^{-2D_0 q^2 \tau} + 1 \tag{2.2}$$

$$C_0 = \frac{\langle I^2(t)\rangle - \langle I(t)\rangle^2}{\langle I(t)\rangle^2} \tag{2.3}$$

C_0 denotes the prefactor and D_0 the translational diffusion coefficient of the particles under high dilution. The prefactor is needed as in DLS experiments the measured scattering intensity is influenced by fluctuations in the intensity of the laser beam. For a Gaussian distribution of the fluctuations caused by the particles, the relation between the autocorrelation function of the intensity $g^{(2)}(q,\tau)$ and the autocorrelation function of the electrical field $g^{(1)}(q,\tau)$, is given by the Siegert relation.

$$\text{Siegert relation:}\quad g^{(2)}(q,\tau) = 1 + \left[g^{(1)}(q,\tau)\right]^2 \tag{2.4}$$

$$\text{with}\quad g^{(1)}(q,\tau) = \frac{\langle E(t)\, E(t+\tau)\rangle}{\langle E(t)\rangle^2} \tag{2.5}$$

From Equation 2.3 and the Siegert relation in Equation 2.5 it results

$$g^{(1)}(q,\tau) = \sqrt{C_0}\, e^{-D_0 q^2 \tau} \tag{2.6}$$

valid for monodisperse, spherical particles at high dilution. Thus, diffusion coefficient under high dilution (D_0) can be determined by measuring the intensity autocorrelation function. Using the Stokes-Einstein relation for monodisperse and spherical particles, R_H can be calculated from D_0.

$$R_\mathrm{H} = \frac{k_\mathrm{B} T}{6\pi\eta_s D_0} \tag{2.7}$$

with the Boltzmann constant (k_B), the absolute temperature (T) and the solvent viscosity (η_s).

Real colloidal systems are typically not monodisperse, but have a certain size distribution which is accounted for by generalizing the autocorrelation functions. The autocorrelation functions then consist of a weighted sum of exponential decays with different D_0 or an integral in continous notation.

$$g^{(2)}(q,\tau) = \sum_i C_{0,i} f_i^2 e^{-2D_{0,i}q^2\tau} + 1 \tag{2.8}$$

$$g^{(1)}(q,\tau) = \sum_i \sqrt{C_{0,i}} f_i e^{-D_{0,i}q^2\tau} \tag{2.9}$$

$$g^{(1)}(q,\tau) = \int_0^\infty W\left(D_0 q^2\right) e^{-D_0 q^2 \tau} dD_0 \tag{2.10}$$

The weighting coefficient (f_i) describes the relative scattering intensities of the different particle sizes. $W\left(D_0 q^2\right)$ is the distribution function. The scattering intensity is caused by Rayleigh scattering, therefore it depends quadratically on the volume (V) of the particles and hence it depends on R_H as follows.

$$I \propto V^2 \propto R_\mathrm{H}^6 \tag{2.11}$$

The inversion of Equation 2.8 to obtain the D_0 distribution is an ill-posed problem. It can be solved by an inverse Laplace transform, which is not mathematically unique. For solving the inversion by the inverse Laplace transform, an algorithm is needed. The obtained solution highly depends on the input parameters for the transform. In addition, the number of parameters that need to be determined increases significantly compared to the monodisperse case. Therefore, the cumulant method is often used instead for simple distributions. It is based on the concept that a distribution function can be fully characterized by its moments or cumulants which are closely linked to each other. The cumulant function of $W\left(D_0 q^2\right)$ corresponds to the natural logarithm of $g^{(1)}(q,\tau)$.

$$\ln\left(g^{(1)}(q,\tau)\right) = A_0 + \sum_{m=1}^{\infty} A_m \frac{(-\tau)^2}{m!} = A_0 - A_1\tau + A_2\frac{\tau}{2!} - A_3\frac{\tau^3}{3!} \pm ... \tag{2.12}$$

A_1 represents the z-mean, A_2 the width of the distribution, and A_3 represents a measure of the asymmetry. This simplified approach can be used to determine multiple distribution types, but is primarily utilized assuming a Gaussian distribution of the radius of the particles as the quadratic regression gives the full information about the Gaussian distribution.

$$g^{(1)}(q,\tau) = \frac{c}{\sqrt{2\pi}\sigma_G} \int_0^\infty e^{\frac{-(D_0-\langle D_0\rangle)^2}{2\sigma_G^2}} e^{-D_0 q^2\tau} dD_0 \tag{2.13}$$

$$\ln\left(g^{(1)}(q,\tau)\right) = a_0 + a_1\tau + a_2\tau^2 = a_0 - D_0 q^2\tau + \sigma_G^2 q^4 \tau^2 \tag{2.14}$$

For monodisperse samples, a straight line is obtained, when plotting $\ln\left(g^{(1)}(q,\tau)\right)$ versus τ. Thus, for a Gaussian distribution, the width of the distribution has to be obtained from the curvature of the curve $\ln\left(g^{(1)}(q,\tau)\right)$ versus τ. These deviations from the straight line

are quite small for the typical relative standard deviation (σ_{rel}) of the radius (and therefore of the D_0) of a colloidal system ($\sigma_{\mathrm{rel}} \leq 10\,\%$). Therefore, the uncertainty of the width of the distribution is high (up to dispersities of about $\sigma_{\mathrm{rel}} \leq 20\,\%$), while the intensity-weighted average of the D_0 and thus R_{H} can be determined with high precision.
As mentioned before, from DLS always the intensity-weighted average and distribution is obtained as the scattering intensity depends on the R_{H} to the power of six (see Equation 2.11). The number- and weight-weighted distribution functions can be obtained, either if the exact distribution is known or by assuming a Gaussian distribution. The uncertainty in the number- and weight-weighted distributions and mean values is higher than the uncertainty in the intensity-weighted quantities because the uncertainty in the width, which is needed to calculate the other weightings of the distribution, is large.

2.2.2 Scanning Electron Microscopy

SEM is a common technique for the characterization of the radius and radius distribution of colloids in the dry state. It produces an optical image of the surface of a sample by scanning it with a focused beam of electrons and detecting the secondary electrons emitted from the sample as they interact with the incident electron beam[47]. The method must be performed under high vacuum, otherwise the electron beam would be scattered by the molecules in the surrounding gas attenuating the electron beam. Therefore, SEM cannot be performed on a colloidal suspension, but only on the dried colloids. SEM images have a resolution of about 2 nm to 3 nm due to the moderate electron energies used for the SEM analysis[43]. In addition, it requires conductive substrates, so non-conductive samples are coated with a metallic film with a thickness of 5 nm to 10 nm[43] to make them visible.

2.2.2.1 Environmental Scanning Electron Microscopy

In ESEM, the samples can be observed in an evacuated chamber at relative humidities of 0 % to 100 %. This allows for the analysis of non-conductive substances without requiring coating and of samples containing a small amount of water. The majority of the path of the electron beam is still under high vacuum while the sample chamber contains water vapor. Differential pumping is used to achieve this by creating a series of pressure zones with decreasing levels of pressure. Each zone has its own designated pumping pathway and is separated from neighboring regions by narrow openings. The size of the openings regulates the movement of gas molecules from one zone to the other.[47]
Depending on the water pressure in the sample chamber, which is typically in the range of 10 Pa to 2500 Pa[44], water either condenses onto or evaporates from the cooled sample (approx. 5 °C). So, the water content of the sample can be adjusted by the water vapor pressure and the temperature. The accuracy of the settings is critical because even a layer of water with a thickness of a few micrometers above the sample would result in the inability to resolve the sample since the penetration depth of the electron beam is only a few micrometers. In general, the water vapor above the sample causes a scattering of some electrons from the electron beam, resulting in a reduced resolution of ESEM compared to SEM. In summary, ESEM allows to analyze a sample with low water content, making swelling behavior visible, but has a lower spatial resolution than SEM.

2.2.3 Differential Centrifugal Sedimentation

Differential centrifugal sedimentation (DCS) is a method to determine the radius and radius distribution of colloids in suspension. It is based on the separation of colloids in a centrifugal field schematically shown in Figure 2.6. The sample is injected into the center of a rapidly rotating disk containing liquids with a density gradient (e.g., sugar solutions in water with a concentration gradient) whose densities increase toward the outer wall. The centrifugal force leads to a particle flow towards the outer wall of the rotating disc. The light extinction caused by the light scattering of the particles is measured at a fixed position. From the light extinction at different times, the relative intensity of particles with a distinct sedimentation coefficient is determined. Assuming a spherical shape of the particles, the sedimentation coefficient distribution can be converted to a particle size distribution.

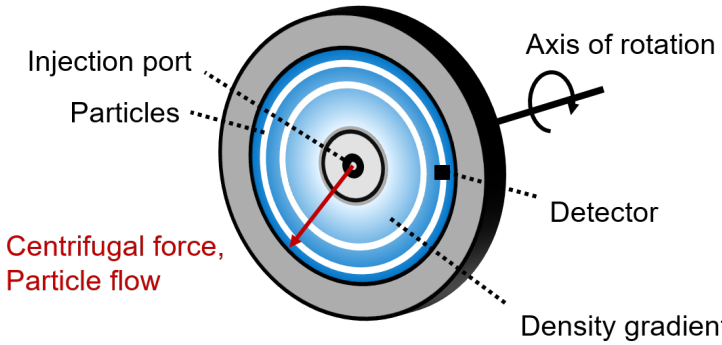

Figure 2.6: Schematic illustration of the basic principles of differential centrifugal sedimentation. The suspended sample is injected in the middle of a fast rotating disc filled with liquids with a density gradient. The centrifugal force causes a particle flow towards the outer wall. The light extinction caused by the light scattering of the particles is measured at a fixed position. From the light extinction at different times, the sedimentation coefficient distribution is determined. Assuming a spherical shape of the particles, the sedimentation coefficient distribution can be converted to a particle size distribution.

2.3 Stability of Colloidal Suspensions

The stability of colloidal suspensions is governed by a complex interplay of forces between the suspended particles[1,48]. Colloidal particles are small enough to undergo Brownian motion, a random movement resulting from collisions between the particles. This motion prevents particles from settling due to gravity by constantly redistributing them throughout the suspension. Additionally, this motions requires a high rate of particle-particle interactions, so they come close to each other, where they experience an attraction to one another caused by van der Waals forces. The intermolecular van der Waals forces result from fluctuations in the electron distribution within the molecules and can cause aggregation and settling of the colloids if no sufficient repulsive forces are present. Thus, colloidal stability depends on a balance between the van der Waals attraction and repulsive forces. One of the primary mechanisms for stabilizing colloids is electrostatic repulsion. When colloidal particles acquire similar surface charges (either naturally or by adding charged stabilizing agents), they repel each other. This electrostatic barrier prevents particle aggregation.

The interaction potential between the particles of colloidal suspensions is often described using the DLVO theory[49,50], named after Derjaguin, Landau, Verwey, and Overbeek. This theory combines the electrostatic double layer repulsion (V_{DL}) and van der Waals attraction (V_{vdW}) resulting in a total interaction potential referred to as DLVO potential (V_{DLVO}) which depends on the distance (d) between the particles and can be extended by steric and depletion interactions (V_{steric}, $V_{\mathrm{depletion}}$).

$$V_{\mathrm{DLVO}}(d) = V_{\mathrm{DL}}(d) + V_{\mathrm{vdW}}(d) \tag{2.15}$$

$$V_{\mathrm{DLVO,extended}}(d) = V_{\mathrm{DL}}(d) + V_{\mathrm{vdW}}(d) + V_{\mathrm{steric}}(d) + V_{\mathrm{depletion}}(d) \tag{2.16}$$

The repulsive potential between two spheres depends on the thickness of the diffuse double layer[51], which is known as the Debye screening length (κ^{-1}).

$$V_{\mathrm{DL}}(d) \propto \frac{\exp(-\kappa d)}{d} \tag{2.17}$$

The van der Waals attraction potential between two spheres with the radius R is inverse proportional to the distance d of the two spheres following Equation 2.18.

$$V_{\mathrm{vdW}}(d) = -\frac{AR}{6d} \tag{2.18}$$

Where A is the Hamaker constant, which depends on the van der Waals interactions between two particles and between a particle and the dispersion medium. The greater the refractive index difference between a particle and the dispersion medium, the greater the van der Waals attraction between the particles[52]. For example, the Hamaker constant is around 1×10^{-20} J for negatively charged polysterene latices[53]. The resulting net potential strongly depends on the material properties, surface charges and radii of the colloids. An exemplary course of the net potential of a colloidal system is shown schematically in Figure 2.7.

It consists of a secondary ($V_{\mathrm{min,2}}$), a primary minimum ($V_{\mathrm{min,1}}$) and a maximum in between (V_{max}) between them. When the particles approach the distance d corresponding to $V_{\mathrm{min,2}}$, they flocculate (reversible). When particles approach the distance d corresponding to $V_{\mathrm{min,1}}$, they coagulate (irreversible). The colloidal suspension is stable, when the potential barrier is large compared to the thermal energy $V_{\mathrm{max}} - V_{\mathrm{min,2}} \gg k_{\mathrm{B}}T$.

In addition to electrostatic stabilization, colloids can also be stabilized through steric stabilization. This is accomplished by adding polymers or molecules with long chains to the system. These chains can be either covalently bonded to or adsorbed onto the surface of the colloidal particles, creating a steric barrier. This barrier physically hinders the particles from coming close to each other and prevents them from overcoming the potential barrier.

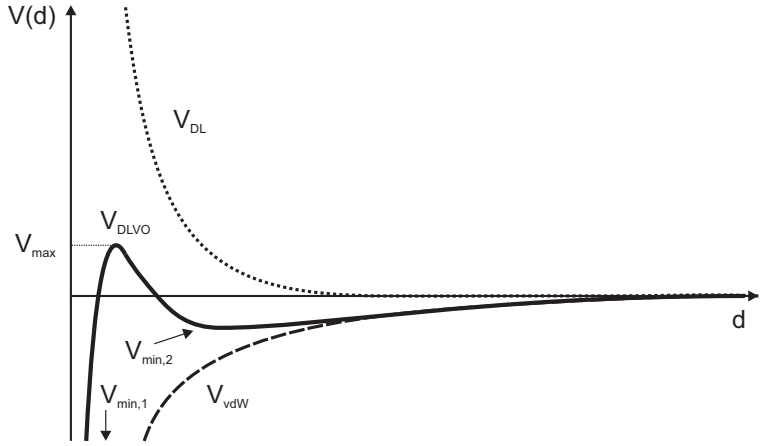

Figure 2.7: DLVO interaction potential between colloidal particles depending on the distance d between the particles. The sum of the electrostatic double layer interaction potential V_{DL} and the van der Waals interaction potential V_{vdW} gives the total interaction potential V_{DLVO} exhibiting a primary ($V_{\mathrm{min},1}$) and a secondary minimum ($V_{\mathrm{min},2}$). Colloidal stability is achieved when the potential barrier is large compared to the thermal energy $V_{\mathrm{max}} - V_{\mathrm{min},2} \gg k_{\mathrm{B}}T$. The DLVO-potential only contains van-der-Waals and double layer interactions, but can be extended by depletion and steric interactions.

3 Linear and Nonlinear Shear Rheology

This chapter first describes the fundamentals of rheology. Starting from the basic principles, viscoelastic models and steady shear viscosities going to the response to oscillatory shear deformation in the linear region, i.e. small amplitude oscillatory shear (SAOS). Furthermore, the response of the material to nonlinear oscillatory shear is discussed and the concept of Fourier-transform rheology is explained. Finally, the use of frequency sweep medium amplitude oscillatory shear (MAOS) instead of strain sweep MAOS is introduced. In the fundamental descriptions of rheology colloidal suspensions are used as examples.

Rheology is defined as the study of the flow and deformation of matter[54,55]. From the response of a material to a deformation or stress applied to it, conclusions about its microstructure can be drawn. Rheology includes phenomena such as creep, stress relaxation, viscoelasticity, nonlinear stress deformation, and viscosity[56].

3.1 Shear Experiment

The simplest rheological experiment is the shear experiment. Shear is denoted as a deformation of a body that occurs when the applied force is parallel to the area on which it acts and can be described using the two plate model, depicted in Figure 3.1. In the two plate model, a material is placed in between two parallel plates with the distance between the plates (h) and the area (A) of each of the two plates. A force (F), respectively a shear stress (σ), is applied to the upper plate acting parallel to the plate, while the lower plate is fixed in its position. This results in a displacement (Δx) of the upper plate and a shear deformation of the material between the plates. The stress is defined as the ratio between F and A of the plates.

$$\sigma = \frac{F}{A} \tag{3.1}$$

For a given σ the Δx of the upper plate depends on the height of the material, therefore Δx is normalized to h giving the unitless quantity of the deformation, called strain (γ).

$$\gamma = \frac{\Delta x}{h} \tag{3.2}$$

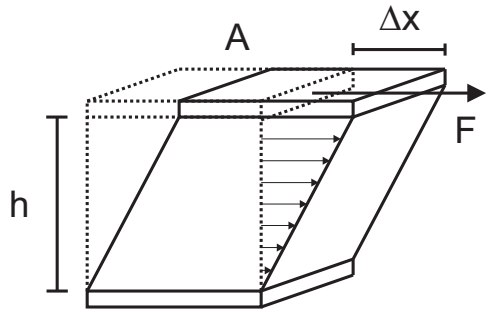

Figure 3.1: The simplest rheological experiment: the shear experiment on the example of the two plate model. A material is placed between two parallel plates with the distance between the plates (h) to each other and an area (A) of each plate. The upper plate is moved by a force (F) by a certain displacement (Δx) while the lower plate is fixed resulting in a shear deformation of the material.

In analog, the velocity (v) of the shear motion is not uniform along the height of the material. Therefore, the shear rate ($\dot{\gamma}$) is used instead of v. The shear rate is defined as the first derivative of the γ with time (t), which can also be written as the velocity normalized to h of each layer between the parallel plates.

$$\dot{\gamma} = \frac{d\gamma}{dt} = \frac{v}{h} = \frac{1}{h}\left(\frac{d\Delta x}{dt}\right) \tag{3.3}$$

3.2 Viscoelasticity and Phenomenological Models

Two idealized types of material behavior on a deformation or stress exist. Ideal elastic solids like pure metals, alloys and amorphous solids and ideal viscous fluids like water, organic solvents and oils[57]. An ideal elastic solid, which can be described by an ideal spring (see Figure 3.2), obeys Hooke's law, i.e. σ is direct proportional to the γ with the proportionality constant G, called the shear modulus.

$$\sigma = G\gamma \tag{3.4}$$

When a stress σ is applied, the deformation of the material occurs immediately and after the applied stress is removed, the material restores its initial state immediately. The shear modulus is a characteristic material constant that provides information about the rigidity of a material and depends on the temperature. Typical orders of the moduli of different materials are listed in Table 3.1.

Table 3.1: Typical shear moduli of different materials.[55,57–59]

Material	G [Pa]
Molecular glasses, metals	$> 10^{10}$
Ice, $-4\,^{\circ}\mathrm{C}$	10^{9}
Paints	$10^{1} - 5 \times 10^{1}$
Colloidal glasses	$10^{1} - 10^{3}$
Polymer melts and glasses	$10^{-1} - 10^{9}$
Hydrogels	$10^{2} - 10^{4}$

In contrast, for an ideal viscous liquid, so called Newtonian liquid, σ is not a function of γ, but of $\dot{\gamma}$. The proportionality factor is the viscosity (η).

$$\sigma = \eta\dot{\gamma} \tag{3.5}$$

Typical orders of magnitudes of the viscosities of different materials are shown in Table 3.2.

Table 3.2: Typical viscosities of different materials.[56,57,60,61]

Material	η [Pa s]
Water	10^{-3}
Blood	$2 \times 10^{-3} - 9 \times 10^{-3}$
Honey	$2 - 10$
Polymer melts ($\dot{\gamma} = 10\,\mathrm{s}^{-1}$ to $1000\,\mathrm{s}^{-1}$)	$10^{1} - 10^{4}$
Polymer melts ($\dot{\gamma} < 1\,\mathrm{s}^{-1}$)	$10^{3} - 10^{6}$
Colloidal glasses ($\dot{\gamma} = 10\,\mathrm{s}^{-1}$ to $1000\,\mathrm{s}^{-1}$)	$10^{-1} - 10^{1}$
Colloidal glasses ($\dot{\gamma} \ll 1\,\mathrm{s}^{-1}$)	$10^{3} - 10^{5}$

An ideal viscous liquid can be modeled by a Newtonian dashpot (see Figure 3.2(b)). Unlike an ideal solid material, the deformation of an ideal viscous material occurs not immediately when a stress is applied and the ideal viscous material does not return in its initial state after the removal of the applied stress.

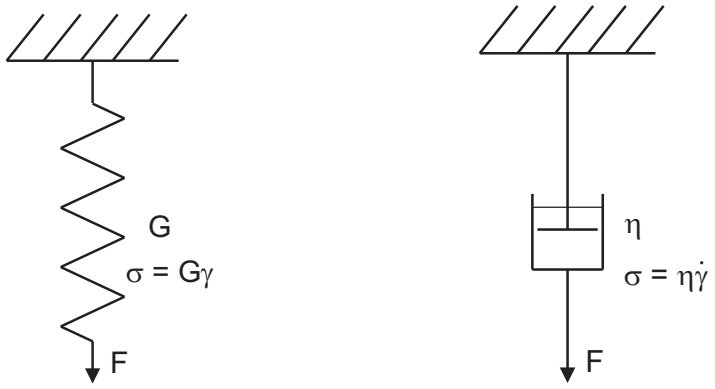

(a) Hooke model (b) Newton model

Figure 3.2: The simple linear 1-dimensional rheological models, **(a)** the Hooke model (spring) for modeling ideal solids and **(b)** the Newton model (dashpot) for modeling ideal liquids. Applying a stress, the spring deforms immediately and returns immediately to its initial state, when the stress is removed. In contrast, the deformation of the dashpot is not immediate. It does not return to its initial state after removing the stress, respective force.

Most materials do not show one of these idealized behaviors but a mixture of both of them. Depending on the time scale, they show either more viscous or more elastic behavior. Therefore, these materials are referred to as viscoelastic materials. The simplest models for describing viscoelastic behavior are the Maxwell and the Kelvin-Voigt model. In the Maxwell model a spring and a dashpot are combined in series (see Figure 3.3(a)), whereas in the Kelvin-Voigt model they are combined in parallel (see Figure 3.3(b)).

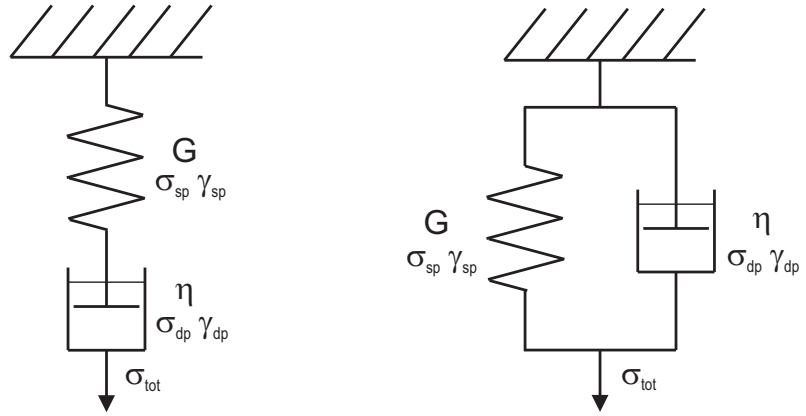

(a) Maxwell model (b) Kelvin-Voigt model

Figure 3.3: The simplest combination of the linear 1-dimensional rheological models to describe viscoelasticity. **(a)** The Maxwell model to decribe viscous materials with a small elastic component and **(b)** the Kelvin-Voigt model for modeling elastic materials with a small viscous component.

The Maxwell model is used to describe viscoelastic liquids, which exhibit liquid-like behavior with a small elastic component. When an applied external stress is removed, the system does not return completely to its initial state due to the viscous part, the dashpot. The total stress is equal to the individual stresses (see Equation 3.6), whereas the total strain (indexed with 'tot') is the sum of the strain of the dashpot (indexed with 'dp') and the strain of the spring (indexed with 'sp'). The total strain rate is the sum of the strain rate of the dashpot and the strain rate of the spring (see Equation 3.8).

$$\sigma_{\text{tot}} = \sigma_{\text{sp}} = \sigma_{\text{dp}} \tag{3.6}$$

$$\gamma_{\text{tot}} = \gamma_{\text{sp}} + \gamma_{\text{dp}} \tag{3.7}$$

$$\dot{\gamma}_{\text{tot}} = \dot{\gamma}_{\text{sp}} + \dot{\gamma}_{\text{dp}} \tag{3.8}$$

The differential equation for the total strain rate of the Maxwell model (Equation 3.9) is obtained by substituting Newtons law (Equation 3.5) and the time derivative of Hooke's law (the time derivative of Equation 3.4) into Equation 3.8. By transforming Equation 3.9 and introducing the relaxation time $\tau = \frac{\eta}{G}$ the differential equation of the stress of the Maxwell model is obtained (Equation 3.10).

$$\dot{\gamma}_{\text{tot}} = \frac{\dot{\sigma}}{G} + \frac{\sigma}{\eta} \tag{3.9}$$

$$\dot{\sigma} = G\dot{\gamma}_{\text{tot}} - \frac{\sigma}{\tau} \tag{3.10}$$

The Maxwell model can be used to predict the response of the material to an external stimulus. When a constant shear rate ($\dot{\gamma} = \text{const.}$) is applied, the time-evolution of the stress referred to as start-up shear behavior can be predicted, which evolves due to the elastic contribution of the spring. After a certain time, which depends on the relaxation

time, a steady state is reached. The plateau value of the stress of this steady state is given by the viscosity according to Newton's law $\sigma = \eta\dot{\gamma}$.

$$\sigma(t) = G\tau\left(1 - \exp\left(\frac{-t}{\tau}\right)\right) \tag{3.11}$$

Most real materials do not show simple Maxwell behavior, neither for the start-up shear nor for the steady state stress. For instance, colloidal glasses exhibit an overshoot in their start-up shear behavior[28]. Exemplary start-up shear behavior for a Maxwell model and a stressovershoot material are shown in Figure 3.4. Additionally, the steady state viscosity in depends on the shear rate due to microstructural rearrangements, orientation effects or, for polymeric systems, chain stretching. The viscosity either increases or decreases with the shear rate. A material is referred as shear thickening, when the viscosity increases with the shear rate and as shear thinning, when the viscosity decreases with the shear rate. The majority of investigated materials show shear thinning behavior. Exemplary dependence of σ and η on the shear rate for a shear thinning fluid, a Newtonian fluid and a yield stress fluid are depicted in Figure 3.5.

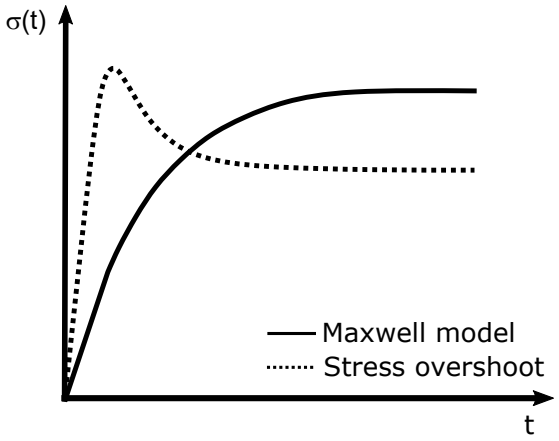

Figure 3.4: Exemplary start up shear behavior of a material following the Maxwell model (solid line) and a material with a stress overshoot (dashed line), both sheared at a constant shear rate. The material following the Maxwell model shows a linear increase for short times and approaches a plateau value for long times. The stress overshoot material shows a linear increase followed by an overshoot in the stress. This overshoot stress is attributed to the stress needed to build a certain microstructure enabling better flowability of the material.

Shear thinning fluids without a yield stress show typically three different regions in the flow curve. This shear thinning behavior is valid for a certain shear rate range for each of these materials. Most of the shear thinning materials show a first Newtonian plateau at low shear rates followed by the shear thinning region, where the viscosity shows a power law dependence on the shear rate, and a second Newtonian plateau at high shear rates. The viscosity at the first Newtonian plateau is referred to as zero shear viscosity (η_0), whereas the viscostiy at the second Newtonian plateau is referred to as high shear viscosity (η_∞). For moderately concentrated colloidal suspensions, i.e. colloidal suspensions in the supercooled state, the first and the second Newtonian plateaus are accessible by the use of common rheometers (oscillatory shear rheometer and capillary rheometers), whereas for polymer melts the second Newtonian plateau is not accessible due to the restricted shear rates

of the rheometers. Depending on which parts of the flow curves are accessible, different empirical models can be used to describe the shear rate dependence of the viscosity or the stress. A simple empirical function to describe shear thinning and shear thickening is the Ostwald-de-Waele model (see Equation 3.12)[62].

$$\text{Ostwald-de-Waele:} \quad \sigma = K\dot{\gamma}^c \tag{3.12}$$

Here K and c are empirical parameter. When $c > 1$ the material is shear thickening, whereas when $c < 1$, the material is shear thinning. Note that the unit of K is [Pa s^c] and c does not have to be an integer. The simplest models, which capture the first Newtonian plateau, i.e. a zero shear viscosity η_0, and the second Newtonian plateau, i.e. a high shear viscosity η_∞, are the Cross model (Equation 3.13)[63] and the Carreau-Yasuda model (Equation 3.14)[64]. Those models describe pseudoplastic flow of materials with asymptotic viscosities at zero and infinite shear rates and without a yield stress.

$$\text{Cross:} \quad \eta\left(\dot{\gamma}\right) = \eta_\infty + \frac{\eta_0 - \eta_\infty}{1 + \left(k\dot{\gamma}\right)^n} \tag{3.13}$$

$$\text{Carreau-Yasuda:} \quad \eta\left(\dot{\gamma}\right) = \left(1 + \left(\lambda\dot{\gamma}\right)^a\right)^{\frac{n-1}{a}} \left(\eta_0 - \eta_\infty\right) + \eta_\infty \tag{3.14}$$

The parameters of the Cross model are k a characteristic time of the material and n a parameter, which adjusts the width of the transition region between zero shear region and the shear thinning region. In the Carreau-Yasuda model, λ is a characteristic time for the material, n the negative of the power law slope and a a parameter, which adjusts the width of the transition region between the zero shear region and the power law region[64].

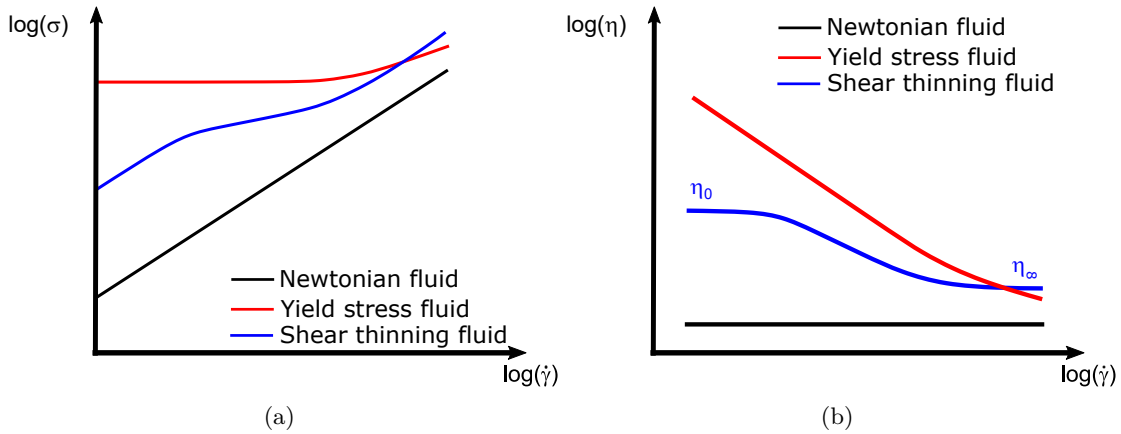

Figure 3.5: Exemplary shear rate dependence of the **(a)** stress and **(b)** viscosity of a Newtonian (black line), a yield stress fluid (red line) and a shear thinning fluid without a yield stress (blue line).

For some materials like high concentrated dispersions no zero-shear viscosity plateau is observable. Below a certain stress the materials do not flow, but behave like a solid. Above this stress, the materials start to flow, i.e. they show a solid to liquid transition, which is

termed yielding. The critical stress at which this solid to liquid transition occurs is referred to as yield stress σ_y. This yield stress is related to the stress, which is needed to break down a structure in the material, which hinders flow. The simplest models to describe the shear-rate dependent stress of a yield stress fluid are the Bingham model[65] and the Herschel-Bulkley[66] model shown in Equation 3.15 and in Equation 3.16. The Bingham model describes a material, which shows a Newtonian flow above the yield stress, whereas the Herschel-Bulkley model describes a material, which shows a power law dependence (Ostwald-de Walde model) above the yield stress.

$$\text{Bingham:} \quad \sigma(\dot{\gamma}) = \sigma_y + \eta\dot{\gamma} \tag{3.15}$$

$$\text{Herschel-Bulkley:} \quad \sigma(\dot{\gamma}) = \sigma_y + K\dot{\gamma}^c \tag{3.16}$$

3.3 Small Amplitude Oscillatory Shear

Small amplitude oscillatory shear (SAOS) measurements are used to quantify the elastic and the viscous parts of a viscoelastic material and to determine its relaxation times. The material is subjected to an oscillatory sinusoidal shear deformation $\gamma(t)$ with a small strain amplitude γ_0 at the excitation angular frequency ω_1 over a time t and the stress signal $\sigma(t)$ is recorded. Exemplary time dependencies of the resulting stress and strain amplitude (γ_0) are depicted in Figure 3.6.

$$\gamma(t) = \gamma_0 \sin(\omega_1 t) \tag{3.17}$$

The strain amplitude γ_0 is chosen in a way that the response of the material does not depend on the strain amplitude, yielding a pure sinusoidal stress response. This region is called the linear viscoelastic regime. For ideal Hookean solids, the stress signal is in phase with the oscillatory shear deformation as obtained by combining Equation 3.4 and Equation 3.17.

$$\sigma(t) = G\gamma_0 \sin(\omega_1 t) \tag{3.18}$$

In contrast, for ideal Newtonian liquids, the stress signal has a phase shift of $\delta = 90°$ as obtained by combining Equation 3.5 and Equation 3.17.

$$\sigma(t) = \eta\gamma_0\omega_1 \cos(\omega_1 t) = \eta\gamma_0\omega_1 \sin\left(\omega_1 t + \frac{\pi}{2}\right) \tag{3.19}$$

In Figure 3.6 the oscillatory deformation γ and response σ is illustrated schematically for the two ideal materials.
Viscoelastic materials, which have both elastic and viscous parts, show a phase shift between $\delta = 0°$ to $90°$. The response of the system can be divided into the in-phase ($\delta = 0°$) and the out-of-phase part ($\delta = 90°$), which allows a quantitative determination of the elastic and viscous fractions of the material.

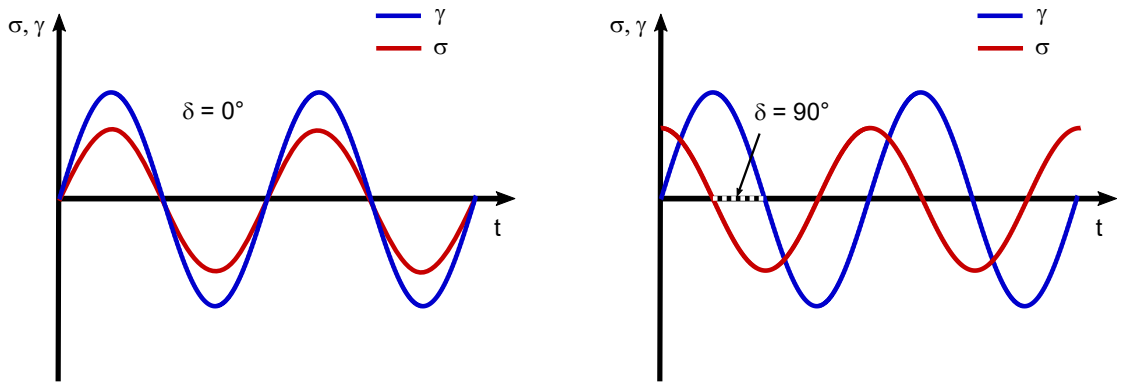

(a) (b)

Figure 3.6: Response of a material to a sinusoidal strain excitation in the linear regime for **(a)** an ideal solid and **(b)** an ideal liquid. The ideal solid exhibits a stress that is in-phase with the applied deformation ($\delta = 0°$), whereas the stress exhibited by an ideal liquid has a phase shift of $\delta = 90°$ relative to the strain deformation.

$$\sigma(t) = G'\gamma_0 \sin(\omega_1 t) + G''\gamma_0 \cos(\omega_1 t) \tag{3.20}$$

The storage modulus G' describes the energy stored by the elastic part, while the loss modulus G'' describes the energy dissipated by the viscous part of the system. The loss tangent is given by the quotient of G'' and G'.

$$\tan(\delta) = \frac{G''}{G'} \tag{3.21}$$

For ideal elastic behavior $\tan(\delta) \to 0$ applies, while for ideal viscous behavior $\tan(\delta) \to \infty$ applies.

The response of a viscoelastic liquid, which exhibits similar behavior as a Newtonian liquid with a small elastic component, on an oscillatory shear motion can be estimated using the Maxwell model. Combining the differential equation for a Maxwell model obtained in Section 3.2 with Equation 3.17 and defining a relaxation time $\tau = \frac{\eta}{G}$ yields[58,67]

$$\sigma(t) = \gamma_0 \left(G \frac{(\omega_1\tau)^2}{1+(\omega_1\tau)^2} \sin(\omega_1 t) + G \frac{\omega_1\tau}{1+(\omega_1\tau)^2} \cos(\omega_1 t) \right) \tag{3.22}$$

$$= \gamma_0 \left(G' \sin(\omega_1 t) + G'' \cos(\omega_1 t) \right) \tag{3.23}$$

giving explicit expressions of the storage modulus (G') and the loss modulus (G'') as a function of the angular frequency (ω_1) and relaxation time (τ)[68].

$$G'(\omega_1) = G \frac{(\omega_1\tau)^2}{1+(\omega_1\tau)^2} \tag{3.24}$$

$$G''(\omega_1) = G \frac{\omega_1\tau}{1+(\omega_1\tau)^2} \tag{3.25}$$

In Figure 3.7 the ω_1 dependence of G' and G'' resulting from the Maxwell model are plotted. For low ω_1, $G'' > G'$ is evident, i.e. the viscous behavior of the material dominates. The limiting power law exponents are $G' \propto \omega^2$ and $G'' \propto \omega^1$ by approaching $\lim_{\omega_1 \to 0}$. For $\omega_1 \tau = 1$, G' and G'' are equal. Therefore, τ of a material can be calculated from the crossover point of the moduli. For higher frequencies, the elastic behavior of the sample dominates. G' saturates whereas G'' declines with an antiproportional relationship to the angular frequency $G'' \propto \omega^{-1}$ resulting in dominant elastic behavior at high frequencies.

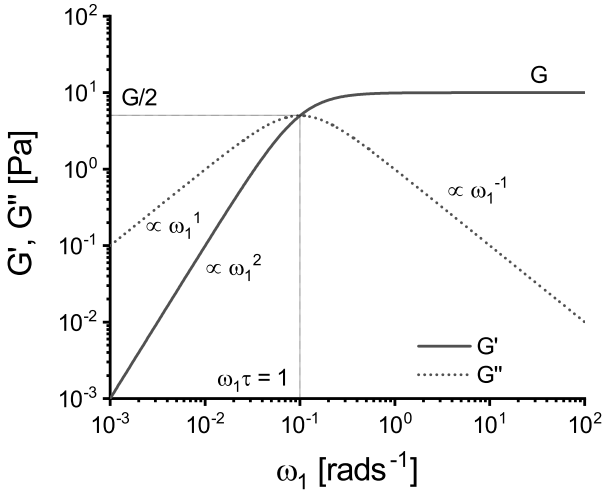

Figure 3.7: Frequency dependence of the storage (G') and the loss modulus (G'') resulting from the Maxwell model (see Figure 3.3(a)) with $G = 10\,\text{Pa}$ and $\tau = \frac{\eta}{G} = 10\,\text{s}$. In the low frequency regime referred to as terminal regime, G' and G'' show a power law dependence on ω_1 with $G' \propto \omega_1^2$ and $G'' \propto \omega_1^1$. The moduli cross at $\omega_1 \tau = 1$ at $G' = G'' = \frac{G}{2}$. At higher angular frequencies, G' approaches the plateau value G and G'' decreases with a power law dependence of $\propto \omega_1^{-1}$ resulting in dominant elastic behavior at high frequencies.

3.4 Large Amplitude Oscillatory Shear

If γ_0 exceeds a certain material and frequency dependent limit, the stress signal is not a pure sine anymore. The corresponding experiment is called medium or large amplitude oscillatory shear (MAOS, LAOS) experiment. The anharmonicity of the stress response of the material can be quantified using Fourier transform rheology (FT-rheology) established by Wilhelm *et al.*[69–71] and Hyun *et al.*[72,73].

Fourier Transform Rheology

Exemplary courses of the material parameters G' and G'' depending on γ_0 and the time dependent σ signal in the nonlinear regime are shown in Figure 3.8. The σ signal can be described as a superposition of the angular frequency of the excitation ω_1 and its higher harmonics $n\omega_1$ with $n \in \mathbb{N}$, when $\sigma(t) = \sigma(t + T)$ with the period length T. The FT is a transform that converts a given dimension into its reciprocal dimension. In rheology, the FT is used to transform the stress time signal $\sigma(t)$ into its frequency spectrum $S^*(\omega_1)$ obtaining the intensities of the higher harmonics I_n.

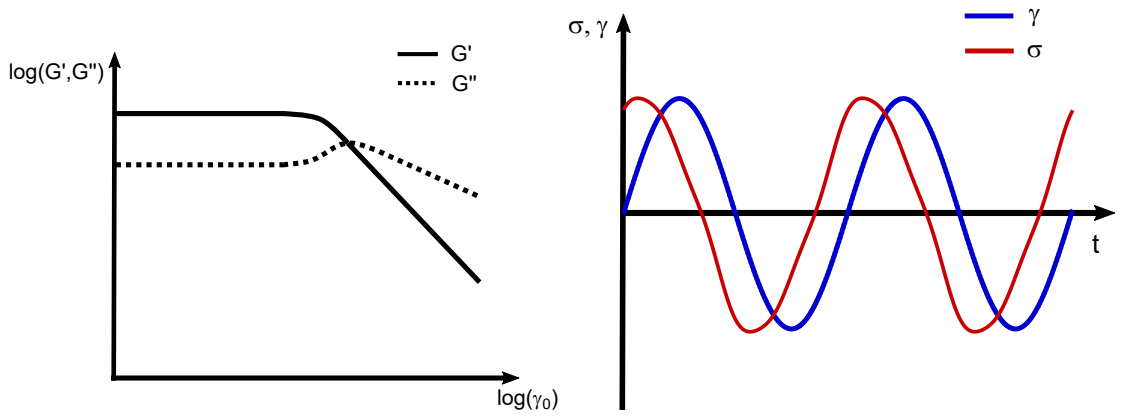

(a) (b)

Figure 3.8: Exemplary course of **(a)** the strain amplitude dependent moduli and **(b)** the stress response of a material to a sinusoidal strain excitation in the nonlinear regime. The course of the moduli of a material with an overshoot in G'' without showing an overshoot in G' is shown as this is the typical behavior of colloidal glasses[21,74–76]. The stress response consists of the sum of sines with the arguments $(n\omega_1 + \delta_n)$ with $n \in \mathbb{N}$.

$$S^*(\omega_1) = \int_{-\infty}^{\infty} \sigma(t)\, e^{-i\omega_1 t} \mathrm{d}t \tag{3.26}$$

Since the FT is inherently complex, the transform of the $\sigma(t)$ signal results in a complex spectrum, which can either be described by its real (Re) and imaginary part (Im) or by the magnitude/intensity (I) and the phase (δ) of the signal.

$$S^*(\omega_1) = Re(\omega_1) + iIm(\omega_1) = I(\omega_1)\, e^{i\delta(\omega_1)} \tag{3.27}$$

$$I(\omega_1) = \sqrt{Re(\omega_1)^2 + Im(\omega_1)^2} \tag{3.28}$$

$$\delta(\omega_1) = \arctan\left(\frac{Im(\omega_1)}{Re(\omega_1)}\right) \tag{3.29}$$

In Figure 3.9 the connection of the different representations is visualized in a Gauss plane.

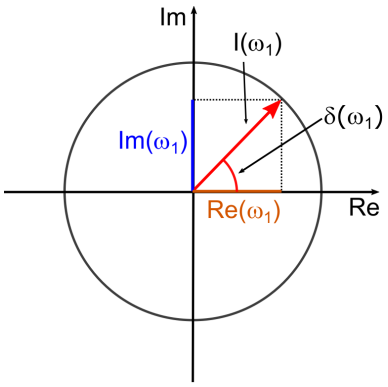

Figure 3.9: Schematic representation of a complex number in the Gauss plane visualizing the connection between the two different representations either by its real (Re) and imaginary (Im) part, or by the magnitude/intensity (I) and the phase (δ) of the signal.

The intensities of the higher harmonics I_n and the corresponding phase angles δ_n can be obtained from the intensity $I_n(n\omega_1)$ and phase spectra $\delta_n(n\omega_1)$ at n with $n \in \mathbb{N}$. The anharmonic shear stress can be reconstructed using the intensities and phase angles[72,77].

$$\sigma(t) = \sum_{n\in\mathbb{N}} I_n \sin(n\omega_1 t + \delta_n) \tag{3.30}$$

The γ_0 dependence of the intensities of the higher harmonics I_n can be estimated using an approximation for the flow of non-Newtonian fluids. Newtonian fluids are described using Newton's law with a viscosity, which is independent of the applied shear rate.

$$\sigma = \eta\dot{\gamma} \tag{3.31}$$

For non-Newtonian fluids, η becomes a function of $\dot{\gamma}$, but is still independent of the direction of shear, i.e. $\eta(\dot{\gamma}) = \eta(-\dot{\gamma})$. For small $\dot{\gamma}$, the viscosity can be approximated by a Taylor series with only even terms with respect to the shear rate.

$$\eta = \eta_0 + c_1\dot{\gamma}^2 + c_2\dot{\gamma}^4 + ... \tag{3.32}$$

For a simple oscillatory shear motion the strain is given by Equation 3.17. In a simplified complex notation this yields

$$\gamma(t) = \gamma_0 e^{i\omega_1 t} \tag{3.33}$$

The shear rate is given by the time derivative of the strain.

$$\dot{\gamma}(t) = i\omega_1\gamma_0 e^{i\omega_1 t} \tag{3.34}$$

Using the approximation of the viscosity (Equation 3.32) and Equation 3.31, the shear rate dependence of the stress can be described by the following equation.

$$\sigma(\dot{\gamma}) = \left(\eta_0 + c_1\dot{\gamma}^2 + c_2\dot{\gamma}^4 + ...\right)\dot{\gamma} = \eta_0\dot{\gamma} + c_1\dot{\gamma}^3 + c_1\dot{\gamma}^5 + ... \tag{3.35}$$

Inserting the shear rate of the sinusoidal strain deformation (Equation 3.34) in Equation 3.35 yields

$$\sigma(\dot{\gamma}) = \underbrace{\eta_0 i\omega_1\gamma_0}_{I_1\propto\gamma_0} e^{i\omega_1 t} + \underbrace{c_1 i^3\omega^3\gamma_0^3}_{I_3\propto\gamma_0^3} e^{i3\omega_1 t} + \underbrace{c_2 i^5\omega^5\gamma_0^5}_{I_5\propto\gamma_0^5} e^{i5\omega_1 t} + ... \tag{3.36}$$

Consequently, for a symmetrical flow response the frequency spectrum consists only of the odd higher harmonics of the excitation frequency. Even harmonics only appear, if the symmetry is broken, which can be due to an anisotropy of the structure of the sample[78] or measurement artifacts like stick-slip[25].

Measurement Procedure of Fourier Transform Rheology

The measurement and analysis procedure of FT-rheology is shown schematically in Figure 3.10(a). In (1) the time dependent stress signal is shown. By a FT of this stress signal, a magnitude frequency spectrum (2) is obtained. The ratio of the magnitude of the third harmonic to the fundamental $I_{3/1} = \frac{I_3}{I_1}$ can be used as a measure for the anharmonicity of the material. Three different regions can be defined depending on the course of relative intensity of the third harmonic ($I_{3/1}$). In the SAOS region, the anharmonicities are zero. A proportionality of $I_{3/1} \propto \gamma_0^{-1}$ is obtained as $I_1 \propto \gamma_0$, and I_3 only records the noise level that is assumed to be constant. For higher strain amplitudes, i.e. in the MAOS region, a proportionality of $I_{3/1} \propto \gamma_0^2$ is generally expected (see Equation 3.36 and Figure 3.10(a)(3)). For even higher strain amplitudes, i.e. in the large amplitude oscillatory shear (LAOS) region, $I_{3/1}$ levels off to a plateau value. To quantify the intrinsic anharmonicity of complex fluids as a function of the frequency, a pure frequency dependent parameter $Q_0(\omega_1)$ introduced by Hyun *et al.*[72] can be obtained from the asymptotic regime at low strain amplitudes.

From the anharmonicity parameter $Q(\omega_1, \gamma_0) = \frac{I_{3/1}}{\gamma_0^2}$ (see Figure 3.10(a)(4)), the intrinsic anharmonicity parameter (Q_0) can be determined, which is defined as $Q_0(\omega_1) = \lim_{\gamma_0 \to 0} Q(\omega_1, \gamma_0) = \lim_{\gamma_0 \to 0} \frac{I_{3/1}}{\gamma_0^2}$ as described in Cziep *et al.*[79]. This procedure is repeated for different frequencies to obtain the frequency dependence of the intrinsic anharmonicity $Q_0(\omega_1)$, illustrated in Figure 3.10(a)(5). To obtain the frequency dependence, a strain amplitude sweep at all relevant ω_1 is necessary. Depending on the applied frequency, the investigated amplitude region, and the data point density of the strain sweep, a single experimental strain sweeps can take up to several days. Therefore, this method is time and sample consuming, particularly when exploring a wide frequency range or focusing on the material's low frequency behavior. For polymer melts, the time temperature superposition principle is used to reduce the measurement time to obtain the Q_0 value over a broad frequency range[72,79]. However, for colloidal suspensions, the time temperature superposition principle is not applicable[80]. For water-based systems, the measurement time per sample loading is limited due to evaporation. Often, evaporation is so pronounced that it is necessary to seal the sample from the environment. If the sample cannot be separated from the sealing material, the sample can only be used within one rheometer loading. To overcome these limitations, the frequency sweep MAOS method was introduced by Singh *et al.*[81]. In the asymptotic MAOS regime, the intrinsic anharmonicity parameter $Q(\omega_1, \gamma_0)$ is a plateau value, as shown in Figure 3.10(a)(4). Therefore, rather than extrapolating the amplitude dependence of $I_{3/1}$, the intrinsic anharmonicity can be calculated from one value of $I_{3/1}$ by the following equation.

$$Q_0(\omega_1) = \frac{I_{3/1}(\omega_1)}{\gamma_0^2} \tag{3.37}$$

Consequently, one frequency sweep is sufficient to obtain the frequency dependence of the intrinsic anharmonicity Q_0 if the boundaries of the MAOS region of the sample are known.

The boundaries of the MAOS regime can be tested with two strain sweeps at the highest and lowest angular frequency ω_1 of interest, as schematically shown in Figure 3.10(b).

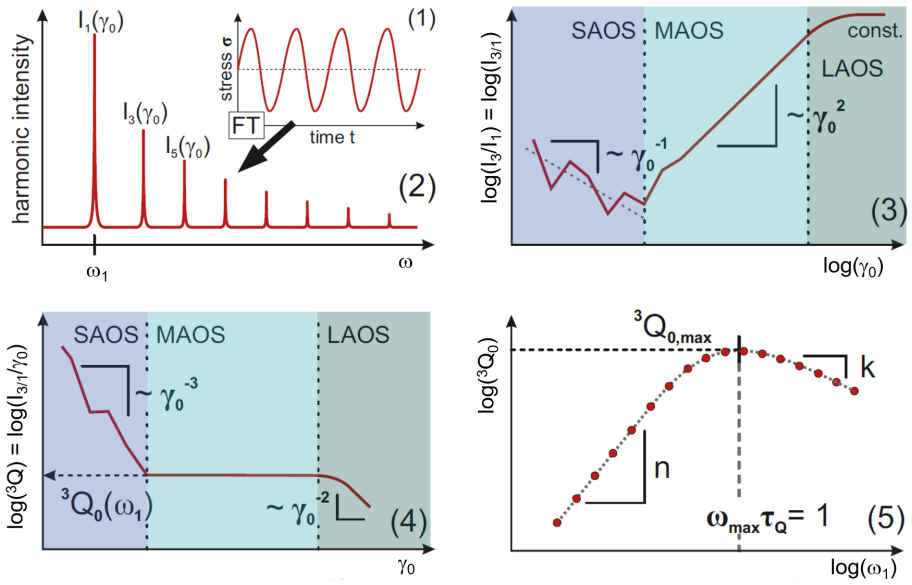

(a) Schematic illustration of the amplitude sweep MAOS

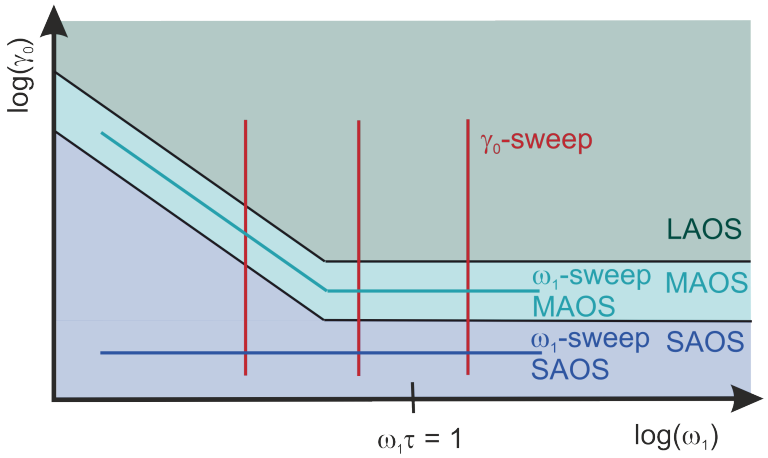

(b) Schematic illustration of the frequency sweep MAOS including the nontrivial ω_1 trajectory, where the strain amplitude is changed during the frequency sweep

Figure 3.10: **(a)** Schematic illustration of the analysis procedure of the frequency dependence of a material using strain amplitude sweep LAOS measurements adapted with permission from Cziep *et al.*[79] Copyright 2016 American Chemical Society. In the nonlinear regime, the stress response of a material becomes distorted **(1)**. Fourier transform of this stress signal leads to the intensity spectrum of the harmonics **(2)**. $I_{3/1} = \frac{I_3}{I_1}$ can be used as a measure for the anharmonicity of the sample. In the asymptotic region, $I_{3/1}$ shows a dependence on γ_0 with $I_{3/1}(\gamma_0,\omega_1) \propto \gamma_0^2$ **(3)**. The normalization to γ_0^2 yields the Q-parameter **(4)**. To obtain a pure frequency dependent parameter, the intrinsic anharmonicity $Q_0(\omega_1) = \lim_{\gamma_0 \to 0} \frac{I_{3/1}}{\gamma_0^2}$ is determined by extrapolation to zero strain **(5)**. **(b)** Schematic illustration of the SAOS, MAOS, and LAOS regime in the $\log(\omega_1) - \log(\gamma_0)$-space to illustrate, that this process can be shortened to a frequency sweep MAOS procedure introduced by Singh *et al.*[81], if the boundaries of the MAOS region are known. For the frequency sweep MAOS, a nontrivial ω_1 trajectory must be used, where the strain amplitude is adjusted during the frequency sweep. Three trajectories of strain sweeps are shown in red.

Furthermore, estimations about the boundaries of the MAOS regime can be made. For Deborah numbers $De = \omega_1 \tau_\alpha$ equal to or greater than 1, the departure from linearity is a γ_0-controlled process, whereas for $De \ll 1$ the departure from linearity is a $\dot{\gamma}_0$-controlled process[82]. Therefore, for $De \approx 1$ and $De > 1$, the strain amplitude of the asymptotic anharmonic behavior is expected to be independent of the frequency $\gamma_0 \neq \gamma_0(\omega_1)$, whereas for lower Deborah numbers $De \ll 1$ the strain amplitude is expected to be inversely proportional to the frequency $\gamma_0 \propto \omega_1^{-1}$, as $\dot{\gamma}_0 = \gamma_0 \omega_1$.

4 Structure, Dynamics and Rheology of Colloidal Suspensions

This chapter focuses on the fundamentals of colloidal suspensions. Starting from the definition and the simplest model system of colloidal particles followed by the influence of the effective volume fraction on the zero-shear viscosity and the characteristic time and energy scales of colloidal particles. The second part of the chapter discusses the basics of the phase behavior and dynamics of colloidal suspensions and the relation to their rheological behavior. The third and final part of the chapter addresses the mode coupling theory (MCT) used for predicting the dynamics and rheological behavior of colloidal suspensions.

The term suspension refers to a heterogeneous mixture of solid particles dispersed in a homogeneous liquid[1]. The term colloidal suspension specifies the diameter of the solid particles to be in the range of 1 nm to 1 µm according to the IUPAC definition[2,3]. Below a particle size of 1 nm, the system is referred to as a solution. Above the size of 1 µm the used term is suspension. Note that the size limits in which the different terms are used in the literature are not strict. The upper limit of the size range is required to ensure that thermal forces are significant for the motion of the colloids. Because of the randomization of particle motion due to the Brownian motion, gravitational settling, i.e. sedimentation, is hindered. The lower limit of the range is required that the mass of the solid particles is significantly larger than the mass of the molecules of the surrounding medium. Thus, the surrounding medium can be considered as a continuum on the time and length scale of colloidal motion.[83]
Important characteristics of a colloidal suspension influencing the stability of the colloids and the colloidal motion are the volume fraction of the colloids in the surrounding medium, the particle size, size distribution and shape, and particle surface properties like charge density or the thickness and softness of a stabilizing layer.

Hard Sphere Systems
The simplest model system is a hard sphere system consisting of spherical particles of equal radius (R) dispersed in a Newtonian fluid. In a hard sphere system, the particles have no interaction until they are in direct contact, at which point they experience pure repulsion, as illustrated in Figure 4.1 in blue. Real systems do not exhibit this simple hard sphere potential, as colloids experience attractive van-der-Waals interactions as described in

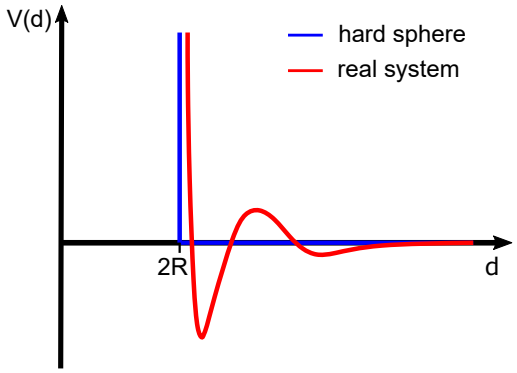

Figure 4.1: Potential $V(d)$ of a hard sphere system (blue) defined by $V = d^{\infty}$ and an exemplary potential of a real system (red) depending on the distance d between the centers of spherical particles with the radius R. A more detailed description of an exemplary interaction potential of colloidal particles is given in Section 2.3.

Section 2.3. In addition, electrostatic double layer interactions as well as steric or depletion interactions can be present. These interactions have different dependencies on the distance (d) between the centers of the particles resulting in a complex dependency of the overall interaction potential on d. An exemplary interaction potential of a real system is shown in Figure 4.1 in red. A more detailed description of the typical interaction potential of colloidal particles is given in Section 2.3.
For the simple model system of monodisperse hard sphere systems, the structure and dynamics and therefore the mechanical properties highly depend on the volume fraction (ϕ) of the particles in the surrounding medium. The ϕ is given by the volume of the colloids V_{colloid} divided by the total volume of the colloidal suspension. The volume fraction can be calculated by the radius and the number density (ρ_{n}) of the particles.

$$\phi = \frac{V_{\text{colloid}}}{V_{\text{fluid}} + V_{\text{colloid}}} = \frac{4\pi R^3}{3}\rho_{\text{n}} \tag{4.1}$$

4.1 Zero Shear Viscosity

The relative zero shear viscosity ($\eta_{0,\text{rel}}$) of colloidal suspensions in dilution ($\phi < 0.05$) was first estimated by Einstein[84,85]. Einstein's law is based on the assumption that the particles do not interact with each other, as the likelihood of contact is too low to have an impact on the zero-shear viscosity. Therefore, the zero-shear viscosity can be estimated by considering only the flow of the suspension medium around a particle.

$$\text{Einstein:}\quad \eta_{0,\text{rel}} = 1 + 2.5\phi \tag{4.2}$$

For $\phi > 0.05$ particle interaction cannot be neglected anymore. Consequently, Einstein's law can be extended by a quadratic term taking the collision of two particles and hydrodynamic effects into account.

$$\text{Batchelor:}\quad \eta_{0,\text{rel}} = 1 + 2.5\phi + c_2\phi^2 \tag{4.3}$$

Depending on the initial microstructure, the second order coefficient (c_2) was found to be between five and six[83]. In literature, for $c_2 = 6.2$ and $c_2 = 5.9$ the extension of Einstein's law is often referred to as the Batchelor equation, citing a publication, in which Batchelor[86] published, that measurements of suspensions in dilution did not yield an empirical value for the second order coefficient.

For volume fractions above $\phi > 0.15$, the increase in ϕ results in a stronger increase of $\eta_{0,\mathrm{rel}}$. Higher order term approximations are inadequate as it extends the range of validity by only a minor amount[83]. Effective medium approximations are utilized instead of further extending Einstein's law. Widely recognized methods include the equations of Krieger-Dougherty[87,88] (Equation 4.4) and Quemada/Maron-Pierce[89–91] (Equation 4.5) both taking into account the divergence of $\eta_{0,\mathrm{rel}}$ at the maximum volume fraction (ϕ_{max}). For a glassy monodisperse system, ϕ_{max} corresponds to the packing fraction of random close packing, which is $\phi_{\mathrm{max}} = \phi_{\mathrm{rcp}} = 0.638$. For a crystalline monodisperse system, ϕ_{max} corresponds to the maximal packing fraction of the face-centered cubic packing, which is $\phi_{\mathrm{max}} = \phi_{\mathrm{fcc}} = 0.74$. Section 4.3 provides a detailed description of the different phases of colloidal suspension.

$$\text{Krieger-Dougherty:}\quad \eta_{0,\mathrm{rel}} = \left(1 - \frac{\phi}{\phi_{\mathrm{max}}}\right)^{-2.5\phi_{\mathrm{max}}} \tag{4.4}$$

$$\text{Quemada/Maron-Pierce:}\quad \eta_{0,\mathrm{rel}} = \left(1 - \frac{\phi}{\phi_{\mathrm{max}}}\right)^{-2} \tag{4.5}$$

Figure 4.2 illustrates the relationship between the relative viscosity, $\eta_{0,\mathrm{rel}}$, and volume fraction, ϕ, for the mentioned viscosity models. The Einstein and Batchelor equations do not accurately describe the behavior of highly concentrated suspensions, whereas the Krieger-Dougherty[87,88] and the Quemada/Maron-Pierce[89–91] equation depicts the divergence of $\eta_{0,\mathrm{rel}}$ approaching ϕ_{max}.

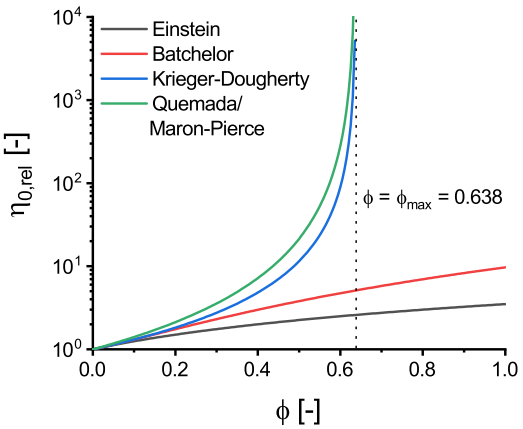

Figure 4.2: Course of different models describing the dependence of $\eta_{0,\mathrm{rel}}$ on ϕ. The Einstein model describes $\eta_{0,\mathrm{rel}}$ sufficiently for $\phi < 0.1$, while the Batchelor model describes it sufficiently for $\phi < 0.15$. The Krieger-Dougherty and Quemada/Maron-Pierce models describe $\eta_{0,\mathrm{rel}}$ for concentrated systems depicting both the low ϕ behavior and the divergence at ϕ_{max}. In this representation, the packing fraction of random close packing $\phi_{\mathrm{max}} = \phi_{\mathrm{rcp}} = 0.638$ was used as the maximum packing fraction applying to glassy systems.

4.2 Characteristic Time and Energy Scales

As shown above, $\eta_{0,\mathrm{rel}}$ solely depends on ϕ of the suspension. For different sizes of the colloids the principle dynamics remain the same, but the timescales of the dynamics are shifted. For colloidal particles, the thermal motion of the solvent molecules generates a force that affects the movement of the suspended particles. This so called Brownian motion leads to characteristic time and energy scales of the colloidal suspension. The characteristic timescale depends on R and the diffusion coefficient under high dilution (D_0) of the particles. The relaxation time τ_0 is the time it takes for a particle to diffuse by its own radius. The calculation of the diffusion coefficient under high dilution (D_0) can be performed by applying the Stokes-Einstein equation[92]. This calculation takes into consideration the characteristic energy scale of $k_\mathrm{B}T$ and the solvent viscosity (η_s).

$$D_0 = \frac{k_\mathrm{B}T}{6\pi\eta_\mathrm{s}R} \tag{4.6}$$

The diffusion of the particles leads to an equilibrated state in the suspension, randomizing the structure of the suspension. Applying an external force, for example a shear motion, modifies the structure of the suspension. Concerning the characteristic timescale of the colloids, a dimensionless number of the applied shear rate ($\dot{\gamma}$) or angular frequency (ω_1) can be defined, known as the Péclet number (Pe). To distinguish between the Péclet number in steady shear (Pe_0) and the Péclet number in oscillatory shear (Pe_ω) different indices are used.

$$Pe_0 = \tau_0\dot{\gamma} = \frac{R^2}{D_0}\dot{\gamma} = \frac{6\pi\eta_\mathrm{s}R^3}{k_\mathrm{B}T}\dot{\gamma} \tag{4.7}$$

$$Pe_\omega = \tau_0\omega_1 = \frac{R^2}{D_0}\omega = \frac{6\pi\eta_\mathrm{s}R^3}{k_\mathrm{B}T}\omega_1 \tag{4.8}$$

It can be ascertained whether the applied motion is fast or slow in relation to the colloids' characteristic timescale. From this, it can be determined if the equilibration of the structure or the structuring due to the shear field prevails. If the structuring due to the shear field dominates, this results in nonlinear effects such as shear thinning[67].
Concerning the energy scale per characteristic volume of a particle $\frac{k_\mathrm{B}T}{R^3}$, a natural scaling factor for the stress can be defined resulting in a reduced stress (σ_red).

$$\sigma_\mathrm{red} = \frac{R^3}{k_\mathrm{B}T}\sigma \tag{4.9}$$

With the reduced stress it can be depicted if the applied stress is large or small relative to the characteristic stress arising from Brownian motion of the colloids. These dimensionless numbers of the stress and the shear motion can be used to compare suspensions of differently sized particles and to compare experimental results to theoretical predictions.

4.3 Phase Behavior and Dynamics

The macroscopic mechanical properties of a material depend on its microscopic dynamics. The dynamics of a colloidal suspension depend solely on its phase behavior, which only depends on the volume fraction of the colloids in the surrounding medium. Note that for different sizes of the colloids, the particle size causes a shift in timescales, but the principle dynamics remain the same.

Figure 4.3(a) illustrates the phase diagram of a monodisperse hard sphere suspension. At low volume fractions of $\phi < \phi_\mathrm{f} = 0.494$, the particles form a disordered fluid structure, which is followed by a coexistence region $\phi_\mathrm{f} < \phi < \phi_\mathrm{c}$ between a fluid and a crystalline phase. As the volume fractions approaches greater values than $\phi > \phi_\mathrm{c} = 0.54$, the sample can form a crystalline structure. In practice, slow crystallization kinetics often impede the ordering of the structure. Then, a metastable disordered solid state, known as the glassy state, is observed when the volume fraction surpasses the glass transition volume fraction $\phi > \phi_\mathrm{g} = 0.58$. This glassy state can exist up to the volume fraction of random close packing $\phi_\mathrm{rcp} = 0.638$. In contrast, the ordered solid state, the crystalline state, can persist up to a volume fraction of a face-centered cubic (fcc) lattice of spheres in direct contact with $\phi_\mathrm{fcc} = 0.74$. This is the highest possible packing density for spheres of equal radius. The crystalline state is the thermodynamic stable one. Therefore, the glassy state, which can be formed in a volume fraction range of $0.58 < \phi < 0.638$, is only stable for a certain timescale in monodisperse systems. For times above this timescale (which can be up to several hours), the system crystallizes[6]. While investigating the mechanical properties of the glassy state, shear induced crystallization can intervene the investigations of a glassy state already on shorter timescales of several minutes[7].

In disperse samples, the crystallization process can be completely suppressed if the relative standard deviation of $\sigma_\mathrm{rel} = \left(\langle R^2\rangle - \langle R\rangle^2\right)^{-\frac{1}{2}} / \langle R\rangle$ of the radius distribution exceeds $12\,\%$[8,9]. Then, the phase diagram simplifies to a transition from a disordered fluid to a supercooled state to the glassy state. A complete suppression of the crystallization can also be achieved by utilizing a bimodal mixture of particles with different sizes.

Figure 4.3(b) illustrates the time dependence of the density autocorrelation function $\Phi_q(t)$ (defined in Equation 4.10) for the particles in the suspension in the fluid state, the supercooled state and the glassy state. This correlation function provides insights into the diffusivity of the particles.

In the fluid region, the particles undergo unrestricted diffusion throughout the suspension medium, resulting in the decay of the autocorrelation function as a single exponential. The spatial correlation of the particles dissipates completely.

In the supercooled state, particles are densely packed, causing the surrounding particles to trap a particle within a cage for extended times. This effect is called cage effect. The particles can diffuse freely within this cage, known as β-relaxation process, while out-of-cage motion is repressed at low and medium timescales, resulting in a plateau in the autocorrelation function. As timescales lengthen, the cages are opened due to the diffusion of the surrounding particles, allowing for out-of-cage relaxation known as α-relaxation.

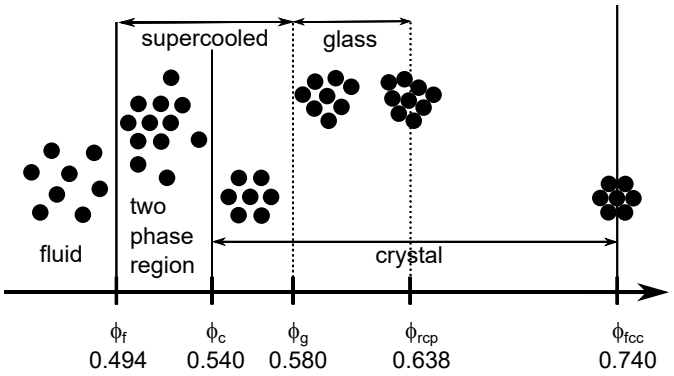

(a)

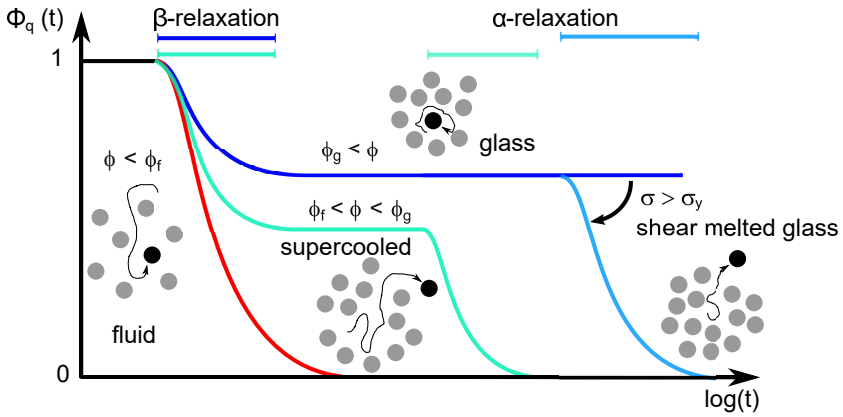

(b)

Figure 4.3: **(a)** Phase diagram of a monodisperse hard sphere colloidal system, which is only dependent on ϕ of the system. Inspired by Hunter *et al.*[93]. For more information see the main text. Below **(b)** Its pair autocorrelation function $\Phi_q(t)$ providing insights into the dynamics of the particles. Inspired by Merger[94].

The plateau value height and relaxation mechanisms' timescale are greatly dependent on the system's volume fraction.

For volume fractions above the glass transition volume fraction, the particles are so densely packed that the α-relaxation slows down considerably, rendering it outside the timescale of typical investigations. The cages cannot be opened within the timescales of investigation except a certain stress is applied exceeding the yield stress (σ_y). Then, the external stress favors the relaxation of the particles causing the material to flow and resulting in faster τ_α- and τ_β-relaxation compared to the undisturbed state.

4.4 Mode Coupling Theory

In the following section the fundamentals of the mode coupling theory (MCT) will be explained. The theory was developed in the 1980s by Götze *et al.*[95,96] to describe the dynamics of hard sphere glass-forming colloidal suspensions in the quiescent state. The theory was expanded by Fuchs, Cates and Brader[13,97] to the sheared steady states, the linear and nonlinear[98] viscoelastic regime and transients during the start-up of a steady shear[28]. The starting point of the theory is the coupling of the Brownian motion of

the particles present in the suspension resulting in an equation of motion, which cannot be solved analytically. Therefore, various projection formalisms and approximations are utilized to make it solvable. Response theory is used to obtain the system's response to a shear input, making the predictions comparable to rheology.

4.4.1 Dynamics in the Quiescent State

While solidifying from a liquid like to a glassy state, a material undergoes only minor structural changes, but exhibits a tremendous slowdown of several decades of the dynamics. The MCT is a fully microscopic theory describing the structure and the dynamics of glass-forming suspensions by calculating the density auto correlation functions $\Phi(t)$ using first principle mechanics[26,27]. The wave vector (q) dependent correlator $\Phi_q(t)$ represents all two-body interactions over many decades in time and is connected to the intermediate scattering function $f(q,t) = \Phi_q(t) S_q$ with the static structure factor (S_q).

$$\Phi_q(t) = \frac{\langle \rho_q(t=0)^* \rho_q(t) \rangle}{S_q} \tag{4.10}$$

The intermediate scattering function is directly measurable with light scattering experiments[99,100] and represents the static structure factor S_q for $t = 0$. The structure factor S_q contains the interactions between the particles and introduces experimental parameters like temperature and density[101]. The theory assumes hard spheres and utilizes the Percus-Yevick approximation for the static structure factor. Thus, the static structure depends solely on the packing fraction.
Applying the Zwanzig-Mori projection formalism[102,103] to the exact equation of motion of a supercooled colloidal suspension close to the glass transition leads to the Langevin equation (Equation 4.11)[97] describing the coupling of the random Brownian motion of the particles.

$$\dot{\Phi}_q(t) + \Gamma_q(t) \left[\Phi_q(t) + \int_0^t dt' m_q(t-t') \dot{\Phi}_q(t) \right] = 0 \tag{4.11}$$

The initial decay rate $\Gamma_q = q^2 D_0 / S_q$ depends on statics and hydrodynamics. The memory function $m_q(t-t')$ contains the mobility of the particles and therefore the complexity of the system. The shear induced migration of the particles can be included via the memory function. But, even for the quiescent state, the exact expression of the memory function cannot be solved analytically. Therefore, assumptions and simplifications are made to be able to gain macroscopic predictions from theory, which can be compared to rheological results.
In the following, first the assumptions and simplifications made for gaining the response of a material in a system with small perturbations (linear response) are described. Followed by the introduction of two different models, which can be used to simplify the MCT calculations of systems with shear induced migration. First, the isotropically sheared hard sphere model (ISHSM) model, where the q dependence is not excluded, is introduced,

which is used to calculate the rheological behavior under nonlinear steady shear excitation. Secondly, the schematic model, where the wave vector dependence is neglected, is introduced to make the equations solvable for more complex shear motions used for comparison with nonlinear oscillatory shear experiments.

4.4.2 Linear Response

The flow-induced linear stress response for a small externally applied simple shear flow is given by

$$\langle \sigma_{xy}(\vec{q},t)\rangle^{\text{lin.resp.}} = -\int_{-\infty}^{t} \mathrm{d}t' C^{(\sigma)}_{xyxy}(\vec{q},t-t')\, iq_x v_y(\vec{q},t') \tag{4.12}$$

$v_y(\vec{q},t')$ is the Fourier mode of the perturbation and the averages on the right-hand side are performed in the unperturbed equilibrium system. The shear stress autocorrelation function for linear deformations is

$$C_\sigma(\vec{q},t-t') = \frac{n}{k_B T}\langle \sigma_{xy}(\vec{q},t-t')^*\, \sigma_{xy}(\vec{q})\rangle. \tag{4.13}$$

It contains the correlations between all stresses and provides the response of the off-diagonal element of the stress $\sigma_{xy}(\vec{q})$ at time t to the gradient of the velocity field at time t'. Note that Equation 4.12 is only valid for perturbations in the linear regime, i.e., with small amplitudes, where the material parameters do not depend on the amplitude. For calculations of the response to a nonlinear deformation, a more complex expression is needed. In the macroscopic limit $q \to 0$, relevant for rheology, C_σ simplifies to[104]

$$C_\sigma(\vec{q},t) = G_0^\perp(t) + (P(\vec{q})-1)\frac{q^2\left(G_0^\perp(t)\right)^2}{nk_\mathrm{B}T} K_q^\perp(t), \tag{4.14}$$

where $P(\vec{q}) = 4\frac{q_x^2 q_y^2}{q^4} + \frac{q_z^2}{q^2}$ contains the angular dependence. $G_0^\perp(t)$ is the $G_q^\perp(t)$ for $q \to 0$ and denotes a generalized viscosity or shear modulus. In MCT approximation

$$G_q^\perp(t) = \frac{1}{2} n^2 k_B T \int \frac{d\vec{k}}{(2\pi)^3}\frac{1}{q^2}\left[(k^2-k_z^2)(c_k+c_p)^2\right] S_k S_p \phi_k(t)\phi_p(t) \tag{4.15}$$

where $\vec{p} = \vec{q} - \vec{k}$ denotes the momentum transfer. The term $K^\perp q$ is related to the force correlations and can be determined from $G^\perp q$. Due to the structure of C_σ, two main contributions can be distinguished: one along the axis where $q_x = q_z = 0$ and another along the diagonal where $q_x = q_y = q/\sqrt{2}$.
For small amplitude oscillatory shear deformation $-iq_x v_y(\vec{q},t') = \omega_1\gamma_0\cos(\omega_1 t)$, the linear response is determined by C'_σ and C''_σ, which are closely related to the reduced storage modulus (G'_red) and the reduced loss modulus (G''_red). Adjustments to C'_σ and C''_σ must

be made to match G'_{red} and G''_{red} from rheological measurements. These adjustments are explained in more detail in Section 6.2.2.

$$C'_\sigma(\omega_1) = \frac{\omega_1}{\gamma_0}\int_0^\infty dt' \sin(\omega_1 t)\, C_\sigma(q,\omega_1) \tag{4.16}$$

$$C''_\sigma(\omega_1) = \frac{\omega_1}{\gamma_0}\int_0^\infty dt' \cos(\omega_1 t)\, C_\sigma(q,\omega_1)\,. \tag{4.17}$$

For small wave vectors, which represent the macroscopic rheological behavior, the spectra are dependent on the magnitude q and the direction of the wave vector.

4.4.3 Isotropically Sheared Hard Sphere Model

The next step after describing the dynamics of concentrated suspensions in the case of a linear perturbation is the prediction of the dynamics under stronger shear fields. For $Pe_0 \ll 1$, the Brownian motion of the particles outweighs the shear motion resulting in a randomized structure of the material.
The density fluctuations present in an unperturbed system are illustrated in Figure 4.4 as light gray rectangles along the y-axis with their initial distance or wavelength λ_{x}. Applying a steady shear along the x-direction leads to a shift and a tilt in x-direction called advection. At a certain time after starting the shear, the advected wave fluctuations shown as dark gray rectangles have a finite distance or wavelength in the y-direction λ_{y}, which decreases with the shear rate as follows:

$$\frac{\lambda_{\mathrm{x}}}{\lambda_{\mathrm{y}}} = \frac{\Delta\mathrm{x}}{\Delta\mathrm{y}} = \dot{\gamma}t \tag{4.18}$$

while the distance in x-direction is independent of the shear rate. The shortening of the distance in y-direction due to shear leads to a faster decay of the density fluctuation compared to the unperturbed state and causes the shear melting of a glass[97].

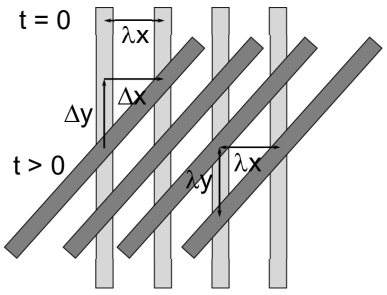

Figure 4.4: Illustration of the density fluctuations at the time $t = 0$ (light gray rectangles) and a time $t > 0$ (dark gray rectangles) after starting the application of a steady shear motion[97]. The density fluctuations are changing their direction due to the shear motion. Initially, they only exhibit a distance or wavelength λ_{x} in x-direction. After a certain time t, they exhibit additionally a wavelength λ_{y} in y-direction, which is decreasing for increasing shear rates. Additionally, λ_{y} decreases for increasing times.

In the ISHSM model, it is assumed that the motion stays locally isotropic. Therefore, the equation of motion for the density fluctuations at time t after starting the shear motion is approximated by the one of the quiescent system (see Equation 4.11). The shear motion is introduced via the advective wave vector, which enters the memory function. Additionally, the equation is projected onto the pairs of density fluctuations.

$$m_q(t) \approx \frac{1}{2N} \sum_k V_{q,t}^{(\dot{\gamma})}(t) \Phi_k(t) \Phi_{|q-k|}(t) \tag{4.19}$$

with

$$V_{q,t}^{(\dot{\gamma})} = \frac{n^2 S_q S_k S_p}{q^4} \left[\vec{q} \cdot \vec{k} c_{k(t)} + \vec{q} \cdot \vec{p} c_{p(t)}\right] [\vec{q} \cdot \vec{k} c_k + \vec{q} \cdot \vec{p} c_p] \tag{4.20}$$

$$k(t) = k \left(1 + \frac{(t\dot{\gamma}/\gamma_y)^2}{3}\right)^{\frac{1}{2}} \tag{4.21}$$

describing the coupling of the wave vectors, with $\vec{p} = \vec{q} - \vec{k}$. $k(t)$ is the approximation of the time dependent length of the advected wave vector. The γ_y is the deformation needed to break the cages. The vertex $V_{q,t}^{(\dot{\gamma})}$ describes two competing effects: the increase with increasing particle-particle interactions induced by an increase in effective volume fraction (ϕ_{eff}) leading to a non-ergodicity transition in the absence of shear, and decorrelation due to shear motion resulting in a vanishing $V_{q,t}^{(\dot{\gamma})}$ with time.
Using response theory yields an expression, which connects the stress with the density auto correlation function. Expanding this equation for $q \to 0$, a simplified expression for the stress is obtained[97].

$$\sigma = \frac{k_B T \dot{\gamma}}{60\pi^2} \int_0^\infty dt \int_0^\infty dk k^5 \frac{S_k' S_{k(t)}'}{k(t) S_k^2} \left(\Phi_{k(t)}(t)\right)^2 \tag{4.22}$$

The stress for $q \to 0$ is of particular interest as it corresponds to the macroscopic stress measurable with rheology.
The approach of the ISHSM model is used for the prediction of the response to nonlinear steady shear motion capturing the transient stress during start-up of shear and the stress after reaching the steady state. It has the advantage over the schematic MCT that the q-dependence is not excluded giving rise to new results on the dependence on the direction of investigation. However, it is more complex than the schematic model and therefore cannot be solved analytically for nonlinear oscillatory shear motion. Thus, the schematic MCT is used to predict the response to a nonlinear oscillatory shear motion.

4.4.4 Schematic Mode Coupling Theory

In the schematic MCT model the two competing effects of the increase of the correlation by increasing the effective volume fraction due to increased particle interactions and the

decorrelation due to shear motion resulting in a vanishing memory function with time are still included, while the wave vector dependence is removed gaining a simplified equation of motion according to Equation 4.23.
Additionally, the memory function is approximated with a second order polynomial of the density correlator according to Equation 4.24 resulting in a closed theory. The terms including $\Phi(t,s)$ describe the slowing down of the dynamics caused by increasing particle interactions with increasing ϕ_{eff}, while the $h(t,t')$ includes the acceleration of the correlator decay due to shear forces. In the quiescent state, i.e. without shear ($\dot{\gamma}=0$), $h(t,t')$ becomes one, while for a nonlinear oscillatory shear motion it is depicted in Equation 4.26.

$$0 = \dot{\Phi}(t,t') + \Gamma\left(\Phi(t,t') + \int_t^{t'} ds\, m(t,s,t')\dot{\Phi}(s,t')\right) \tag{4.23}$$

$$m(t,s,t') = h(t,t')h(t,s)\left(\nu_1\Phi(t,s) + \nu_2\Phi^2(t,s)\right) \tag{4.24}$$

$$h(t,t') = \left[1 + \frac{1}{\gamma_{\text{y}}^2}\left(\int_t^{t'} ds\,\dot{\gamma}(s)\right)^2\right]^{-1} \tag{4.25}$$

$$h(t,t') = \left[1 + \frac{\gamma_0^2}{\gamma_{\text{y}}^2}\left(\sin(\omega_1 t) - \sin(\omega_1 t')\right)^2\right]^{-1} \tag{4.26}$$

The coupling parameters ν_1 and ν_2 between particles are chosen to be $\nu_1 = 2\left(\sqrt{2}-1\right) + \epsilon\left(\sqrt{2}-1\right)^{-1}$ and $\nu_2 = 2$ according to literature[98]. The separation parameter (ϵ) is defined as $\epsilon = \frac{\phi_{\text{eff}}-\phi_{\text{g}}}{\phi_{\text{g}}}$ with glass transition volume fraction (ϕ_{g}) the glass transition volume fraction. The separation parameter describes the distance from the glass transition volume fraction and specifies the thermodynamic state of the system. For $\epsilon < 0$, the system is in the liquid or supercooled state, while for $\epsilon > 0$ it is in the glassy state. The parameter ν_1 increase for increasing ϕ_{eff} or ϵ due to increased particle caging. The γ_{y} is the deformation needed to break the cages and known in rheology as the yield strain.
The theory can be related to the rheological response of a glass-forming colloidal system to a shear excitation using response theory. Assuming that stress fluctuation relaxation is caused by structural relaxation, the response function $G(t,t')$ is represented by a single-mode transient density correlator $\Phi(t,t')$ shown in Equation 4.27. The correlator function specifies the correlation of a system at time t with the system at an earlier time t' and can be obtained from the equation of motion (Equation 4.23).

$$G(t,t') = \nu_\sigma\Phi^2(t,t') + \eta_{\omega,\infty}\delta(t-t') \tag{4.27}$$

The parameter ν_σ is a measure of the strength of the stress fluctuations. Hydrodynamic interactions can be included via the viscosity $\eta_{\omega,\infty}$. They are included for the calculations of G_1' and G_1'', but are neglected for $n > 1$ leading to distortions of the results at large ω_1. The shear stress caused by an oscillatory shear deformation $\gamma(t) = \gamma_0\sin(\omega_1 t)$ is given by a generalized Green-Kubo relation[18].

$$\sigma(t) = \int_{-\infty}^{t} dt' \dot{\gamma}(t') G(t, t') \tag{4.28}$$

The stress signal can be written as a Fourier series.

$$\sigma(t) = \frac{\omega_1}{2\pi} \int_{-\frac{\pi}{\omega_1}}^{\frac{\pi}{\omega_1}} dt\sigma(t) + \gamma_0 \sum_{n=1}^{\infty} G'_n(\omega_1, \gamma_0) \sin(n\omega_1 t) + \gamma_0 \sum_{n=1}^{\infty} G''_n(\omega_1, \gamma_0) \cos(n\omega_1 t) \tag{4.29}$$

where the Fourier coefficients G'_n and G''_n are given by

$$G'_n(\omega_1) = \frac{\omega_1}{\pi\gamma_0} \int_{-\frac{\pi}{\omega_1}}^{\frac{\pi}{\omega_1}} dt\sigma(t) \sin(n\omega_1 t) \tag{4.30}$$

$$G''_n(\omega_1) = \frac{\omega_1}{\pi\gamma_0} \int_{-\frac{\pi}{\omega_1}}^{\frac{\pi}{\omega_1}} dt\sigma(t) \cos(n\omega_1 t) \tag{4.31}$$

with $n \in \mathbb{N}$. The first term in Equation 4.29 is neglected for the calculations as it would only account for a stress offset.
The approach of the schematic MCT is used for the prediction of the response to a nonlinear oscillatory shear motion (see Chapter 7).

5 Colloidal Model System

In this chapter, the colloidal core-shell model system used for the rheological characterization is introduced. First, the synthesis and purification of the core particles are described, which serve as a seed in the shell synthesis. Second, their properties such as shape, size and size distribution are investigated. The shell synthesis on these core seed latices and the purification of the obtained core-shell particles are described. Moreover, the properties of the core-shell system such as shape, structure, size, size distribution, swelling behavior and the colloidal stability in the swollen and the shrunken state are investigated. Subsequently, a bimodal mixture of two core-shell systems is employed to suppress the crystallization process to obtain a glass-forming colloidal model system. Finally, the bimodal mixture is characterized.

The colloidal model system used in this work has to fulfill different requirements which arise from the scope of this work. The scope of this work is to investigate the rheological behavior of glass-forming colloidal suspensions covering the range from the supercooled state to the glassy state. Moreover, the obtained findings are compared to MCT predicitions. Therefore, the requirements are as follows:

1. The particles must have a spherical shape.
2. The particle must not undergo crystallization.
3. The effective volume fraction (ϕ_{eff}) must be precisely adjustable ($\Delta\phi_{\text{eff}} < 0.01$).
4. The particles should have an interaction potential, which is as hard as possible.
5. The particles should have a defined, narrow radius distribution.

The particle must have a spherical shape as anisotropies in the shape influence the rheological behavior. To obtain a stable glassy state, the particle crystallization has to be suppressed by introducing a relative standard deviation of $\sigma_{\text{rel}} > 12\,\%$[8,9] of the radius distribution as otherwise shear induced crystallization can intervene the rheological investigations[7]. An easy adjustable ϕ_{eff} allows for directly controlling the phase behavior of the colloidal suspension. The requierement of the hard interaction potential arises from the fact that MCT is based on hard sphere interactions. This includes that neither electrostatic interactions nor a softness of the particles are present in the predictions. Furthermore, MCT calculations are based on monodisperse particles. However, monodisperse particles undergo particle crystallization. Therefore, the particles should have a defined, narrow radius distribution, which is sufficient to suppress this particle crystallization.

The following section introduces commonly used model systems for glass-forming colloidal suspensions. Subsequently, the chosen model system for this thesis is discussed, along with an overview of how the model system meets the required criteria, elaborated further in subsequent sections.

5.1 Model Systems for Glass-Forming Colloidal Suspensions

Different model systems with varying interaction potentials, ranging from hard to ultra-soft, are frequently used for the rheological investigation of glass-forming colloidal suspensions[105] (as illustrated in Figure 5.1).
Ideal hard sphere systems are defined by the interaction potential between the particles. The particles have no interaction until they are in direct contact, at which point they experience pure repulsion. However, this is not achievable in real systems due to inherent attraction caused by van der Waals interactions. Therefore, colloids must be stabilized by repulsive interactions such as electrostatic or steric interactions. Polymer chains are often used to introduce steric interactions resulting in a softness of the system. In direct contact, the polymer chains deform instead of causing pure repulsion of the particles.
Sterically stabilized poly(methyl methacrylate) (PMMA) particles are often used as model systems for hard spheres[15,20,105–109]. The particles are usually in a hydrodynamic radius range of $R_{\mathrm{H}} = 130\,\mathrm{nm}$ to $360\,\mathrm{nm}$ with a stabilizing layer of chemically grafted poly-hydro-stearic acid (PHSA) chains with a thickness of about $10\,\mathrm{nm}$. They are dispersed in *cis*-decalin or octadecane/bromonaphthalene mixtures. The PMMA particles show almost hard sphere interaction potentials[110] as the thickness of the stabilizing layer is comparably small. However, the synthesis of the system is complex and the used dispersion mediums are toxic. Additionally, ϕ_{eff} is not adjustable precisely as it has to be adjusted by centrifugation followed by a dilution series.

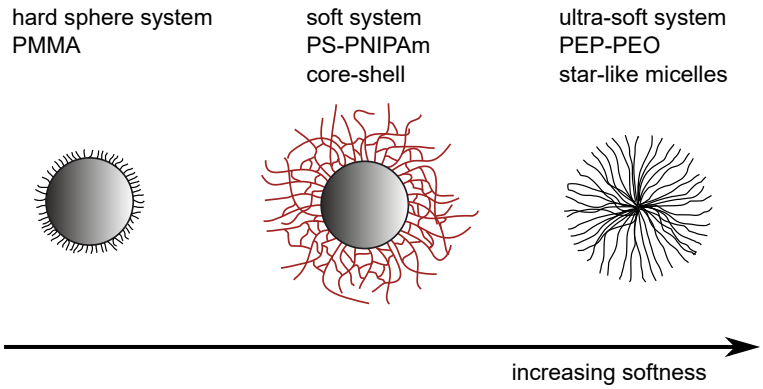

Figure 5.1: Frequently used model systems for glass-forming colloidal suspensions with different softnesses of the interaction potential. In this thesis, the PS-PNIPAm core-shell model system is used. It combines the advantage of an easy adjustable effective volume fraction by changing the temperature, while having a comparably hard interaction potential.

The second model systems frequently used for the investigation of glass-forming colloidal suspensions are microgels or core-shell microgels. The most commonly used system is a thermoresponsive core-shell microgel with a polystyrene (PS) core and a poly(*N*-isopropylacrylamide) (PNIPAm) shell dispersed in water[17,29,105,108,111–113]. By heating, the

hydrogen bonds between the water and the amide molecules weaken, causing the crosslinked shell to shrink[114]. This leads to a decrease in hydrodynamic radius (R_H) and thus a decrease in ϕ_{eff}. Therefore, ϕ_{eff} can be precisely adjusted by changing the temperature. The system has a certain softness, which depends on the thickness and crosslinking density of the polymeric shell.

Star-like micelles are used as ultra-soft model systems. Copolymers consisting of poly(ethylene-*co*-propylene) (PEP) and polyethylene oxide (PEO)[105] or of polypropylene oxide (PPO) and PEO[115] are often used. The copolymers form stable micelles without kinetic exchange in water. These micelles are thermoresponsive[105]. Due to their thermoresponsiveness, ϕ_{eff} can be precisely adjusted. However, they have a much softer interaction potential than the core-shell microgels because the polymer chains are not crosslinked and the micelles do not contain a solid core.

In this work, the thermoresponsive PS-PNIPAm core-shell particles were chosen as model system because they meet the criterion of a precisely adjustable ϕ_{eff}, while preserving a certain hardness of the system compared to star-like micelles. The subsequent sections elaborate on how well the model system satisfies the specified requirements.

The spherical core-shell structure of the particles is confirmed in Section 5.3.3.1. The swelling behavior leading to the adjustable ϕ_{eff} is investigated in Section 5.3.3.2. A bimodal mixture of two core-shell particles with a narrow radius distribution is developed in Section 5.4.1 to suppress particle crystallization. This mixture is used in all subsequent rheological measurements to allow for the investigation of a stable glassy state. The synthesis path of the core-shell particles leads to charges on the particle surface resulting from the use of a charged initiator. Therefore, KCl is added to the bimodal mixture to screen the electrostatic interactions. The concentration $c_{KCl} = 0.05\,\mathrm{mol\,L^{-1}}$, resulting in a Debye length of $\lambda_D = 1.3\,\mathrm{nm}$, is chosen according to literature[112]. The stability of the model system is confirmed in Section 5.3.3.3 and the interaction potential is evaluated in Section 6.2.3.

5.2 Synthesis and Characterization of the Core Particles

5.2.1 Synthesis - Emulsion Polymerization

The synthesis of the core particles is conducted as an emulsion polymerization as a free radical polymerization using potassium persulfate ($K_2S_2O_8$) as initiator, sodium dodecyl sulfate (SDS) as surfactant and styrene as monomer. Additionally, about 5 mol % of *N*-isopropyl acrylamide (NIPAm) are added as comonomer to enhance the deposition of oligo-NIPAm onto the cores during the shell synthesis. The quantities of the educts are given in the Appendix in A.1.2 in Table A1. The synthesis scheme is given in Figure 5.2. The used initiator $K_2S_2O_8$ decomposes under heat forming two radical anions $2SO_4^{\bullet -}$ which start the growing chains. Therefore, the polymer chains in the colloidal particles have at least one charged end group resulting in a negative surface charge of the core particles, which stabilizes the particles by preventing coagulation. As a product of the systhesis, a stable dispersion of PS-core particles in water is obtained. After the synthesis, the core

particles are purified by dialysis against deionized water to remove the surfactant, SDS. The details about the purification process are given in the Appendix in A.3.1.1.

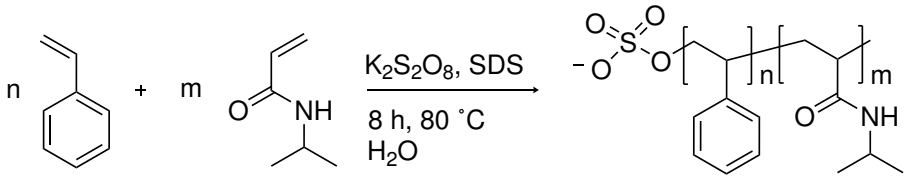

Figure 5.2: Synthesis scheme of the emulsion polymerization performed to obtain the core particles. The weighted in quantities result in a ratio of $\frac{\mathrm{n}}{\mathrm{m}} = 20$ of styrene to *N*-isopropylacrylamide. Potassium persulfate ($K_2S_2O_8$) is the initiator and sodium dodecyl sulfate (SDS) the surfactant. The initiator decomposes forming two radical anions, resulting in negatively charged engroups of the polymer chains.

Six different core particles with different core sizes and relative standard deviations of the radius distribution were synthesized by varying the ratio of surfactant to monomer in the synthesis (see Table 5.1). Different analytical methods can be applied to characterize the size of the synthesized core particles. The nomenclature of the core systems was adapted to the R_H obtained from DLS. A more detailed discussion of the core radii, disperisties and the possible analytical methods is given in Section 5.2.2.2.

Table 5.1: Characteristics of the synthesized core systems. The surfactant to monomer ratios $\frac{n_\mathrm{SDS}}{n_\mathrm{Mono}}$, the R_H values measured with DLS at $T = 25\,^\circ\mathrm{C}$, the relative standard deviation of the radius distribution $\sigma_\mathrm{rel,SEM}$ determined with SEM, the volume V and the mass fraction w of the core suspension. The samples are referred to as PScore-$R_\mathrm{H,DLS}$. Higher surfactant to monomer ratios lead to lower radii as expected from the reaction mechanism of emulsion polymerization. A more detailed discussion of the correlation between the synthesis parameters, R_H and σ_rel is given in Section 5.2.2.2.

Core Particle	$\frac{n_\mathrm{SDS}}{n_\mathrm{Mono}}$ [−]	$R_\mathrm{H,DLS}$ [nm]	$\sigma_\mathrm{rel,SEM}$ [%]	V [mL]	w [wt%]
PScore-33	1.36×10^{-2}	33.3	–	1200	34.3
PScore-37	1.35×10^{-2}	36.7	16.3	1200	34.3
PScore-40	6.83×10^{-3}	40.0	–	1200	33.7
PScore-42	6.79×10^{-3}	41.5	–	1200	33.8
PScore-47	6.84×10^{-3}	47.2	–	1200	33.7
PScore-51	6.76×10^{-3}	50.8	10.2	1200	34.0

5.2.2 Characterization of the Core Particles

With DLS, the hydrodynamic radius of the particles can be obtained with an accuracy of 2 %[116]. In contrast, the relative standard deviation of the radius distribution has high uncertainties up to $\sigma_\mathrm{rel} \leq 20\,\%$ as described in Section 2.2.1. Furthermore, the shape and structure of the particles cannot be obtained. Therefore, scanning electron microscopy (SEM) was utilized as an additional analysis method to obtain the shape, structure and the size distribution to fully characterize the core particles.

5.2.2.1 Shape and Structure of the Core Particles

To obtain the shape and structure of the core particles, SEM images were taken for the different cores. Exemplary images of PScore-37 and PScore-51 are shown in Figure 5.3. These core particles are used as seeds for the core-shell particles PS-37-PNIPAm-75 and PS-51-PNIPAm-131, which are used in the bimodal mixture (see Section 5.4.1). The SEM images of all synthesized core particles are depicted in the Appendix in A.3.1.2 in Figure A.3.3 on page 144.

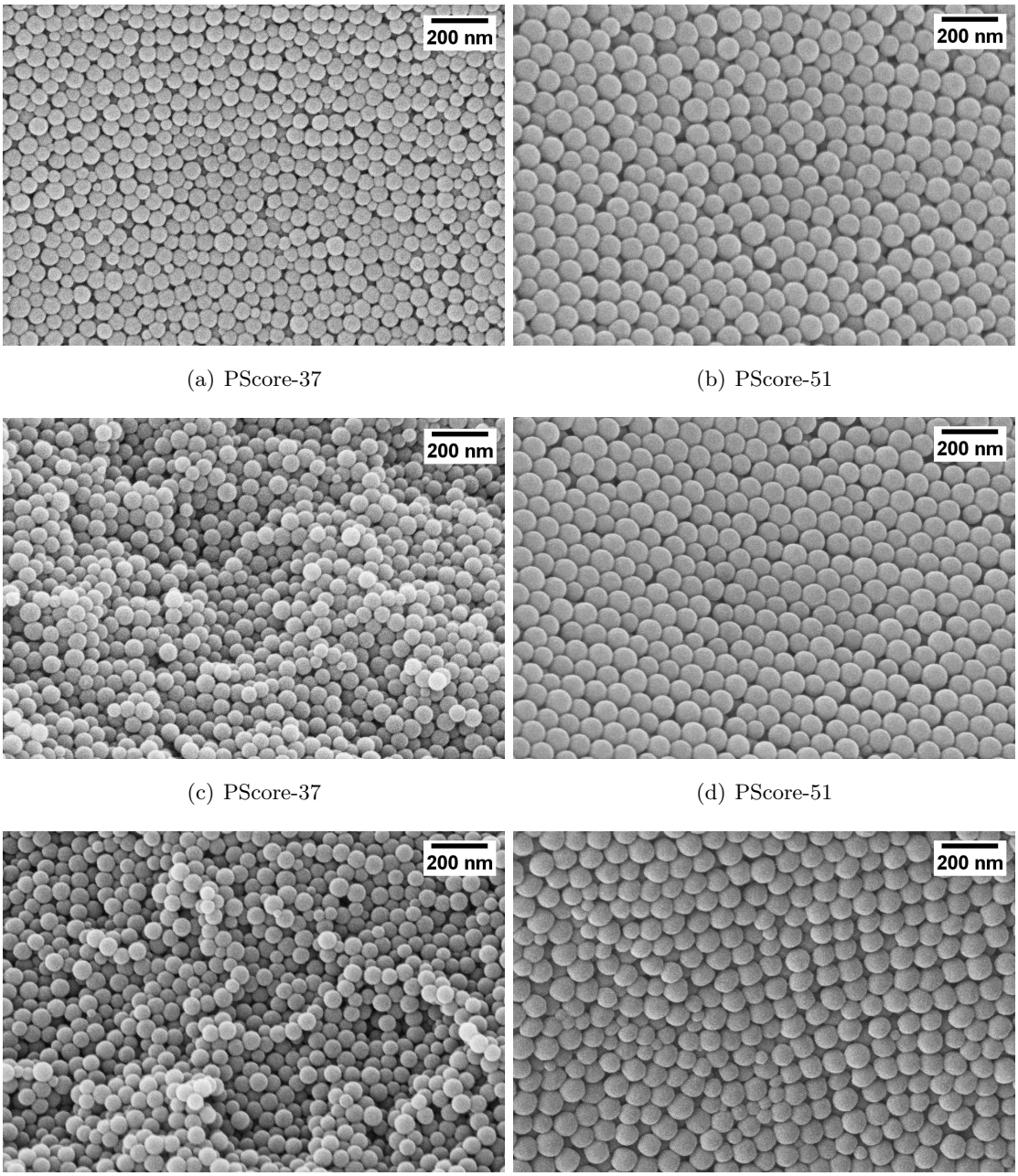

(a) PScore-37 (b) PScore-51

(c) PScore-37 (d) PScore-51

(e) PScore-37 (f) PScore-51

Figure 5.3: SEM images of the dried core particles **(left)** PScore-37 and **(right)** PScore-51. The particles are spherical. In the images of PScore-51 an ordering of the particles is visible, while in the images of PScore-37 no ordering of the particles is visible.

The SEM images in Figure 5.3 show that the particles are spherical. Sample PScore-51 displays a particle arrangement resembling the crystal plane of a face-centered cubic crystal, while for PScore-37 no ordering of the particles is observed. These findings indicate that PScore-51 crystallizes, while PScore-37 builds a glassy structure. This can be attributed to the higher dispersity of PScore-37 of $\sigma_{\mathrm{rel}} = 16.3\,\%$ compared to the dispersity of PScore-51 of $\sigma_{\mathrm{rel}} = 10.2\,\%$ (obtained from the analysis of the transmission electron microscopy (TEM) images described in Section 5.2.2.2) supporting the findings, that $\sigma_{\mathrm{rel}} > 12\,\%$ leads to a complete suppression of particle crystallization[8,9]. However, the evidence for a crystalline structure in PScore-51 and a glassy structure in PScore-37 is not conclusive as the images only depict parts of the sample. It is possible that the samples undergo phase separation, leading to the formation of various structures. To address this, numerous images were captured, presenting only exemplary ones here. Evidence for phase separation was not observed.

5.2.2.2 Size and Size Distribution of the Core Particles

Scanning Electron Microscopy

The diameter distributions of the particles PScore-37 and PScore-51 were analyzed by the determination of the diameter of the core particles of five SEM images including the ones shown in Figure 5.3 using the software ImageJ. The diameter distributions obtained from this analysis are shown in Figure 5.4, including a normal distribution and a Weibull distribution fitted to the obtained diameter distributions. The size distributions exhibit asymmetry with a lower diameter tail. The Weibull distribution is more accurate in representing the actual distribution of the core particle sizes due to its ability to account for the asymmetry in the distribution.

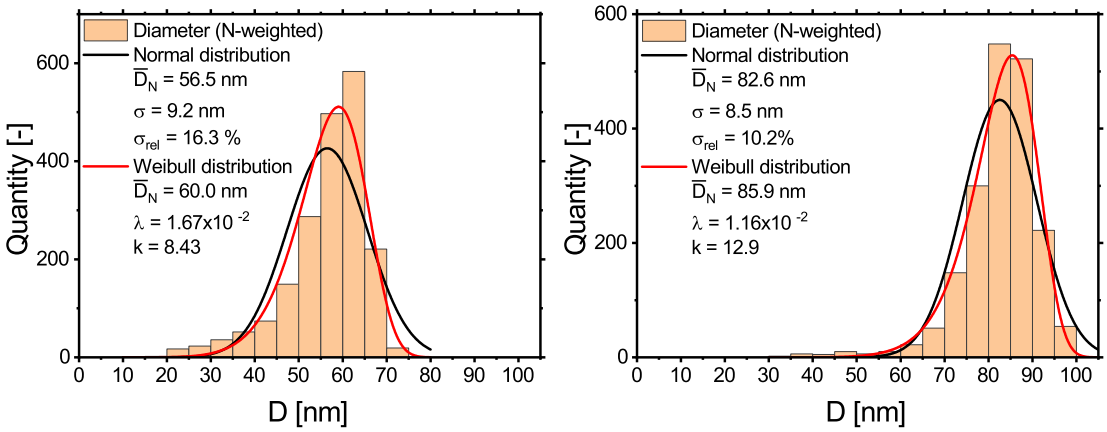

(a) PScore-37 (b) PScore-51

Figure 5.4: Diameter distributions of the dried core particles obtained from the SEM images. The orange bars demonstrate the quantity of particles within a specific size range, whereas the black and red lines exhibit the optimal fit of the distributions as a normal and Weibull distribution. The distribution of the diameter is asymmetric with a lower diameter tail.

$$\text{Normal:}\quad f(D) = \frac{1}{\sqrt{2\pi\sigma^2}} \exp\left(-\frac{1}{2}\left(\frac{D-\overline{D}_N}{\sigma}\right)^2\right) \tag{5.1}$$

$$\text{Weibull:}\quad f(D) = \lambda k\,(\lambda D)^{k-1}\, e^{-(\lambda D)^k} \tag{5.2}$$

The normal distribution is determined by calculating the average diameter and standard deviation of the measured diameters, i.e. these parameters represent the ones of the actual distribution. It is evident that PScore-37, with an average diameter of $\overline{D}_\mathrm{N} = 56.5\,\mathrm{nm}$, has a smaller diameter than PScore-51, which has an average diameter of $\overline{D}_\mathrm{N} = 82.6\,\mathrm{nm}$. Furthermore, the core with the smaller diameter exhibits a higher relative standard deviation of $\sigma_\mathrm{rel} = 16.3\,\%$, compared to the larger core with $\sigma_\mathrm{rel} = 10.2\,\%$.

Comparison to Dynamic Light Scattering

In Table 5.2 the average core radii determined by DLS and SEM and the dispersities of the core size distributions determined by SEM are depicted. Note that the diameter and not the radius was shown in the analysis of the SEM images, as this is the direct measured variable. In the following, the radius will be used instead of the diameter.

The different methods obtain differently weighted average radiii. In DLS, the radii of the particles are obtained from the autocorrelation function of the intensity of the scattered light. This intensity depends on R_H with $I_\mathrm{S} \propto R_\mathrm{H}^6$ leading to an intensity-weighted average radius R_I, where larger particles have a higher impact on the mean value compared to smaller ones. In contrast, in SEM every particle present in the image is counted once, resulting in a number-weighted average radius R_N that is smaller than the intensity-weighted radius for every distribution.

$$\text{Number-weighted average radius:}\quad R_\mathrm{N} = \frac{\sum N_i R_i}{\sum N_i} \tag{5.3}$$

$$\text{Weight-weighted average radius:}\quad R_\mathrm{W} = \frac{\sum W_i R_i}{\sum W_i} \tag{5.4}$$

$$\text{Intensity-weighted average radius:}\quad R_\mathrm{I} = \frac{\sum I_i R_i}{\sum I_i} \tag{5.5}$$

The intensity-weighted average radius is calculated from the number-weighted distribution determined by SEM. This allows for a comparison with the values obtained from DLS. The intensity-weighted average value obtained from this calculation, represented as $R_\mathrm{Dry,I,SEM}$ in Table 5.2, is 12.0 % to 14.0 % lower than the average radius obtained with DLS $R_\mathrm{H,I,DLS}$. This results from the differences in the methods. DLS determines the radius distribution by the diffusion of the particles in suspension. Therefore, the hydrodynamic radius of the particle, including the diffusing ion cloud is determined, resulting in an overestimation of the radius. In contrast, SEM determines the radius in the dry state. The method is based on the scattering of electrons on atoms. Since the boundaries of the particles contain less material, the scattering on the boundaries is not as pronounced, resulting in

underestimation of the radius by SEM. The differences in the diameters obtained from SEM and DLS are demonstrated in Figure 5.5.

Table 5.2: Comparison of the average radii of the synthesized core systems determined with SEM and DLS. The average radii obtained with DLS are intensity-weighted, while the average radii obtained with SEM are number-weighted. The average radii obtained with SEM are converted into the intensity-weighted average radii to allow comparability with the average radii obtained with DLS by changing the weighting according to Equation 5.5. Additionally, the dispersities of the size distribution obtained from the SEM images are listed.

Core Particle	$R_{\mathrm{H,I,DLS}}$ [nm]	$R_{\mathrm{Dry,N,SEM}}$ [nm]	$R_{\mathrm{Dry,I,SEM}}$ [nm]	$\sigma_{\mathrm{rel,SEM}}$ [%]
PScore-37	36.7	28.3	32.3	16.3
PScore-51	50.8	41.3	43.7	10.2

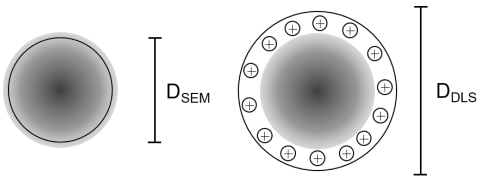

Figure 5.5: Scheme of the difference in diameter obtained from SEM images of the dried core particles and determined with DLS measuring the hydrodynamic radius of the particles.

Differences between the Different Cores

In Table 5.3 the average radius of the different synthesized cores determined with DLS and SEM and the ratio of surfactant to monomer $\frac{n_{\mathrm{SDS}}}{n_{\mathrm{Mono}}}$ are shown. PScore-37 and PScore-33 are synthesized with a comparable surfactant to monomer ratio of $1.356 \times 10^{-2} \pm 5 \times 10^{-5}$ (deviation $< 1\,\%$), while the other core systems were synthesized with a surfactant to monomer ratio of $6.81 \times 10^{-3} \pm 5 \times 10^{-5}$ (highest deviation $< 1\,\%$). The other synthesis parameters were kept the same for all the core syntheses (see Table A1 in the synthesis Section in the Appendix in A.1.2).

Table 5.3: Comparison of the radii and the dispersities of the synthesized core systems depending on the surfactant to monomer ratio. The hydrodynamic radius of the core particles obtained with DLS is higher than the average radius obtained with SEM. Higher surfactant to monomer ratios $\frac{n_{\mathrm{SDS}}}{n_{\mathrm{Mono}}}$ lead to lower radii and higher dispersities as expected from the reaction mechanism of emulsion polymerization.

Core Particle	$\frac{n_{\mathrm{SDS}}}{n_{\mathrm{Mono}}}$ [−]	$R_{\mathrm{H,DLS}}$ [nm]	$R_{\mathrm{Dry,I,SEM}}$ [nm]	$\sigma_{\mathrm{rel,SEM}}$ [%]
PScore-33	1.36×10^{-2}	33.3	–	–
PScore-37	1.35×10^{-2}	36.7	32.3	16.3
PScore-40	6.83×10^{-3}	40.0	–	–
PScore-42	6.79×10^{-3}	41.5	–	–
PScore-47	6.84×10^{-3}	47.2	–	–
PScore-51	6.76×10^{-3}	50.8	43.7	10.2

The hydrodynamic radius of 35.0 ± 1.7 nm of the cores synthesized with the higher surfactant to monomer ratio is smaller than the hydrodynamic radius of 44.9 ± 5.9 nm of the cores synthesized with lower surfactant to monomer ratio. The smaller core PScore-37 has a

higher dispersity of the radius distributions of 16.3 % compared to the dispersity of the radius of PScore-51 of 10.2 %.
A higher surfactant to monomer ratio results in smaller particles since the monomer must be distributed to a greater number of particles in the suspension (N). The variation in dispersities can be explained according to the reaction mechanism, which is explained in detail in Section 2.1.2. A higher ratio of surfactant to monomer increases the ratio of the duration of interval I to interval II (nucleation/growth) during emulsion polymerization. Particles, which are build at the beginning of the nucleation phase contain more polymer molecules, i.e. are larger, than particles, which are build at the end of the nucleation phase[38]. Therefore, the longer the duration of nucleation in comparison to the growth phase, the higher the dispersity in particle size distribution. This implies that a surfactant to monomer ratio increase results in a higher dispersity of the radius distribution. Additionally, a higher surfactant to monomer ratio results in smaller particles. Therefore, smaller particles generally have distribution with higher dispersities than larger particles, when all other synthesis parameters are kept the same (as evident here). The synthesis details can be found in the Appendix in Section A.1.2, in Table A1.
However, the average radii of the core particles synthesized with the same synthesis parameters (PScore-40, -42, -47, -51) and (PScore-33, -37) exhibit a standard deviation of the radius of up to 13 %. The R_{H} of the particles synthesized via emulsion polymerization highly depend on the synthesis parameters like the concentration of monomer, initiator, surfactant, the mass fraction and the temperature at which the synthesis is carried out, the stirring speed of the KPG stirrer and the effective stirring speed. The first five named parameters are adjusted precisely (deviations $< 1\,\%$) resulting in only minor deviations in R_{H} of the synthesized cores. The most critical and influencing part is the stirring speed and the effective stirring speed. For emulsion polymerization, KPG stirrer are used, which have an estimated uncertainty of ± 50 RPM. The effective stirring speed depends additionally on the exact localization of the stirring blade within the flask.

5.3 Synthesis, Purification and Characterization of the Core-Shell Systems

5.3.1 Synthesis - Seeded Emulsion Polymerization

The crosslinked poly-*N*-isopropyl acrylamide shell is synthesized onto the core particles in a seeded emulsion polymerization process as a free radical polymerization. In Figure 5.6, the synthesis scheme is depicted. The previously synthesized core particles are used as seeds in the seeded emulsion polymerization. As a crosslinker 2.5 mol % of *N,N'*-methylenebisacrylamide (MBA) are used. The same radical initiator potassium persulfate ($K_2S_2O_8$) as in the core synthesis is used. It decomposes in two radical anions, which start the growing chains, resulting in polymer chains with a charged end group and thus in surface charges of the core-shell particles.
The parameter characterizing the synthesized model systems are summarized in Table 5.4.

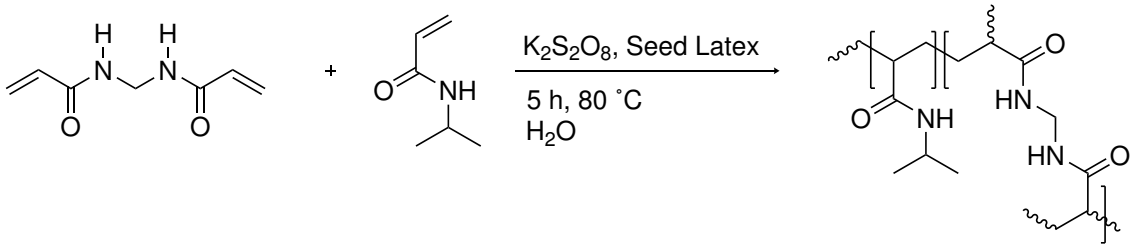

Figure 5.6: Synthesis scheme of the seeded emulsion polymerization of the PNIPAm shell onto the core particles. *N,N'*-methylenebisacrylamide (MBA) is used as a crosslinker with a molar ratio of 2.5 mol % resulting in a crosslinked shell with an average crosslinking density of 2.5 mol %. As initiator potassium persulfate ($K_2S_2O_8$) is used as in the core synthesis resulting in negatively charged end groups of the PNIPAm chains.

The nomenclature of the core-shell systems was adapted to the R_H of the core and the core-shell particles measured with DLS at 25 °C. The synthesis parameter are listed more in detail in Table A2 in the Appendix in A.1.2.

Table 5.4: Characteristics of the synthesized core-shell systems. The seed latex used, the total volume V and the mass fraction (w) at which the synthesis was conducted, and the R_H of the core-shell particles at 25 °C measured with DLS. The nomenclature of the core-shell systems was adapted to the R_H of the core and the core-shell particles measured with DLS at 25 °C.

Core-Shell Particle	Seed Latex	V [mL]	w [wt%]	$R_{H,DLS}$ [nm]
PS-37-PNIPAm-75	PScore-37	1700	7.9	75.2
PS-37-PNIPAm-83	PScore-37	240	5.6	82.7
PS-40-PNIPAm-86	PScore-40	1700	8.1	86.1
PS-40-PNIPAm-89	PScore-40	1500	9.4	89.4
PS-47-PNIPAm-106	PScore-47	1800	7.4	106.1
PS-51-PNIPAm-131	PScore-51	1600	8.3	131.1

5.3.2 Purification - Ultrafiltration

After the synthesis, the core-shell systems are purified by ultrafiltration against deionized water to remove remaining PNIPAm chains which are not attached to the shell. The free polymer must be removed before the rheological investigations as soluble polymer chains in colloidal suspensions cause depletion forces between the particles, which influence the interaction potential and thus the rheological behavior.

For the purification, an ultrafiltration set-up was build shown in Figure 5.7. The construction plans are shown in the Appendix in A.3.1.3 in Figure A.3.5 on page 147. The unpurified core-shell suspension is stirred in an ultrafiltration cell, which is attached to a reservoir filled with water. Pressurizing the system with 1.2 bar presses the water from the reservoir through the ultrafiltration cell and the membrane. The membrane has either a pore size of 50 nm or of 100 nm depending on the size of the swollen core-shell particles at room temperature. The pore size is selected to permit the unrestricted passage of free PNIPAm chains while retaining the core-shell particles. The electrical conductivity can be used for monitoring the progress as the removed polymer chains have charged end groups resulting from the use of the charged initiator.

The filtrate is collected and the conductivity is measured every 2 L. The flow rate highly depends on the concentration of the suspension and the impurities. It varies from 15 mL h^{-1} to 50 mL h^{-1} during the purification process, so the conductivity was checked every 2 to 5 days.

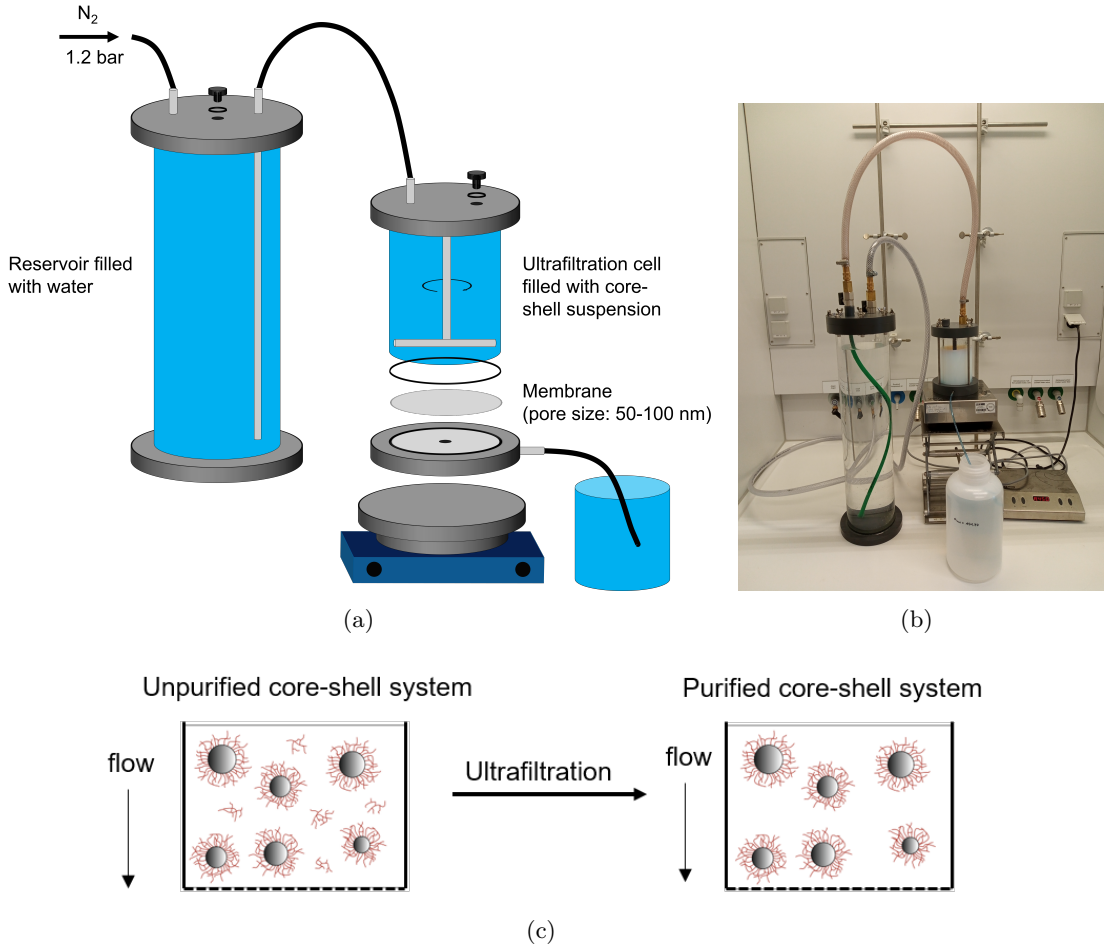

Figure 5.7: Purification of the core-shell particles via ultrafiltration: **(a)** Scheme of the purification set-up, **(b)** photo of the process and **(c)** schematic illustration of the purification procedure. The impurities are washed out through the membrane, while the core-shell particles are remaining in the ultrafiltration cell.

The conductivity of the filtrate in dependence of the total volume of the filtrate is shown in Figure 5.8 exemplary for the core-shell particle PS-37-PNIPAm-75. The electrical conductivity first follows an exponential decay and then levels off to a plateau value. The plateau value is reached after $V \approx 6\,\mathrm{L}$, which corresponds to $t \approx 200\,\mathrm{h}$. From this it is concluded, that most of the chains are washed out after a washing volume of $V = 6\,\mathrm{L}$.
The purification process is parallelized by using three ultrafiltration set-ups simultaneously as the maximal volume (V) at which the ultrafiltration can be conducted is about 450 mL and the mass fraction of the core-shell system during purification is restricted to about 3.5 wt%. Higher w lead to high viscosities that disrupt the redistribution of the particles by stirring. Due to these restrictions, a typical purification process (e.g., PS-37-PNIPAm-75) takes about 6 weeks.

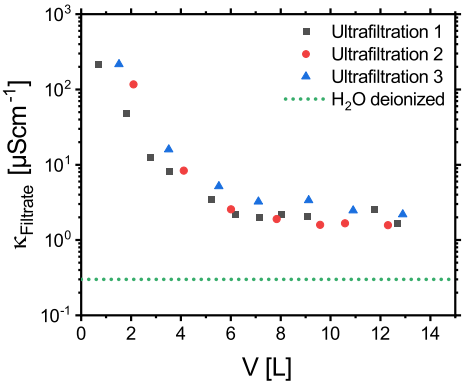

Figure 5.8: Progress of the ultrafiltration process of the core-shell particle PS-37-PNIPAm-75 tracked by the electrical conductivity of the filtrate $\kappa_{\mathrm{Filtrate}}$ in dependence on the total volume of the filtrate V for three different purification batches. The conductivity of the filtrate exhibits an exponential decay, which is followed by approaching a plateau value. The green dotted line represents the electrical conductivity of the used deionized water $\kappa_{\mathrm{H2O}} = 0.3\,\mu\mathrm{S\,cm}^{-1}$.

SEM images of an unpurified and a purified core-shell system are depicted in Figure 5.9. In the image of the purified system the particles appear more separated and have clearer boundaries compared to the particles in the image of the unpurified system. In the unpurified system, PNIPAm chains are present, which are not attached to the shell. They percipitate onto the surface of the particles while drying the suspension and leading to a bridging between the particles washing out clear boundaries, while the purified system contains almost no unbound PNIPAm chains anymore. In the purified system, only the shells of the particles are interpenetrating each other.

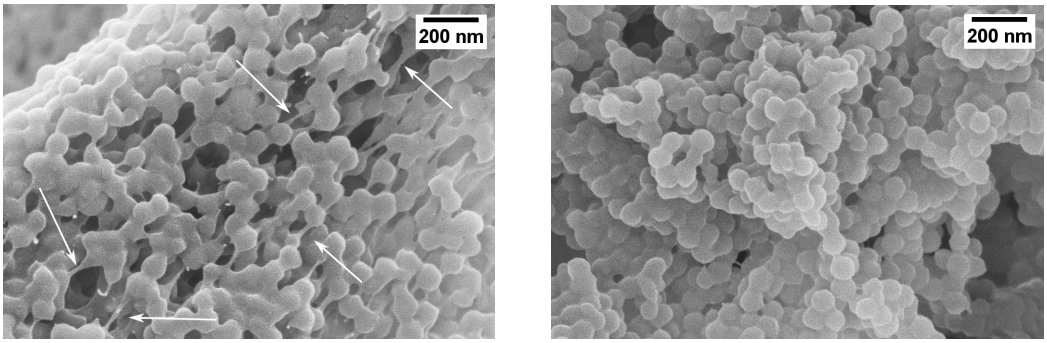

(a) unpurified (b) purified

Figure 5.9: SEM images of **(a)** a dried unpurified and **(b)** a dried purified core-shell suspension. In the unpurified system, a bridging between the particles is present due to the free PNIPAm chains, which percipitate onto the surfaces of the core-shell particles while drying the suspension. Some of these bridges are marked with white arrows. In the purified system, the particle boundaries are clearer because only the shells of the particles can interpenetrate in the dry state.

5.3.3 Characterization of the Core-Shell Particles

5.3.3.1 Core-Shell Structure of the Particles

The requirements on the model system (listed at the beginning of Chapter 5 on page 47) include a spherical shape of the particles. To reveal the spherical shape and the core-shell

structure of the synthesized particles transmission electron microscopy (TEM) and atomic force microscopy (AFM) images of the particles are taken.
TEM images of PS-37-PNIPAm-75, PS-51-PNIPAm-131 and PS-47-PNIPAm-106 are shown in Figure 5.10. The core-shell structure of the particles is revealed by the contrast difference between the inner and outer parts of the particles. Furthermore, the particles have a spherical shape. In the images of PS-51-PNIPAm-131, the core-shell structure appears clearer than in the images of the other two samples. The findings of TEM were confirmed with AFM measurements shown in the Appendix in A.3.1.4.

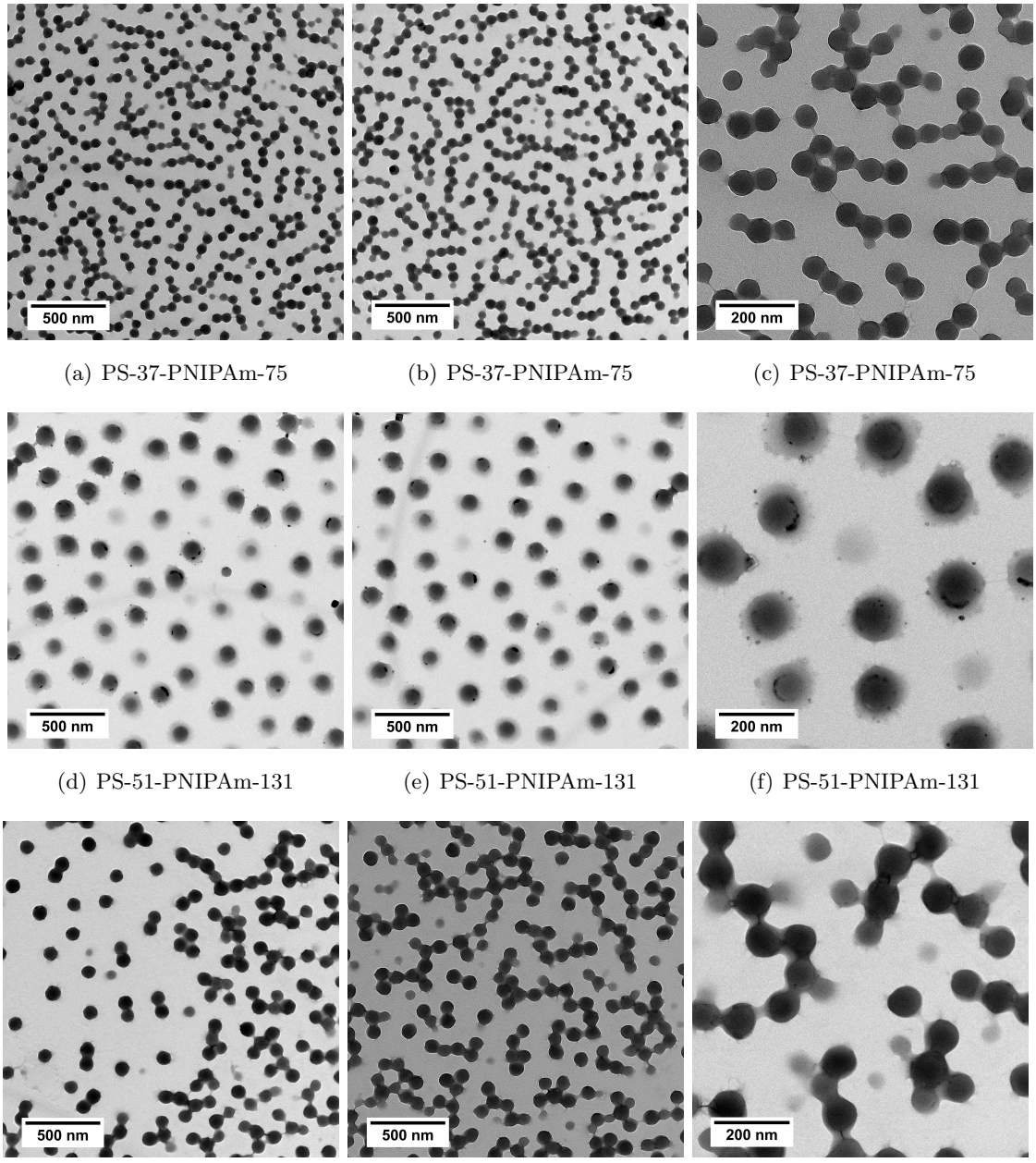

(a) PS-37-PNIPAm-75 (b) PS-37-PNIPAm-75 (c) PS-37-PNIPAm-75

(d) PS-51-PNIPAm-131 (e) PS-51-PNIPAm-131 (f) PS-51-PNIPAm-131

(g) PS-47-PNIPAm-106 (h) PS-47-PNIPAm-106 (i) PS-47-PNIPAm-106

Figure 5.10: Transmission electron microscopy images of the core-shell particles. The core-shell structure of the particles is confirmed by the contrast difference between their inner and outer parts. The clustering results from the PNIPAm chains, which interlink the shells. Due to the surface charge of the particles, the particles repel eachother, resulting in the characteristic linear chain-like structure.

The particles in the images of PS-37-PNIPAm-75 show chain-like clustering, while the particles in the images of the sample PS-51-PNIPAm-131 are separated from each other. The particles in the second and third image of PS-47-PNIPAm-106 also exhibit chain-like clustering, while in the first image there is a transition region from more separated particles to chain-like clusters. This phenomenon appears to be concentration-dependent and not specific to the sample. Clustering results from remaining impurities of PNIPAm chains which interlink the shells. Due to the surface charge of the particles, the particles in the cluster repel eachother, resulting in the characteristic linear chain-like structure.
It is evident that the particles in PS-51-PNIPAm-131 are larger than in PS-47-PNIPAm-106 and in PS-37-PNIPAm-75. Additionally, the particles within one sample vary in core and overall sizes. The analysis of the radii and the comparison with the radii obtained with DLS will be given in Section 5.3.3.2.

5.3.3.2 Swelling Behavior of the Core-Shell Particles

The PNIPAm used for the crosslinked shell has a lower critical solution temperature (T_{LCST}) with water. By heating, the hydrogen bonds between the water and the amide molecules weaken, causing the crosslinked shell to shrink[114]. This leads to a temperature dependence of R_{H} of the core-shell particles. At the T_{LCST}, this weakening results in a complete demixing of the PNIPAm and the water[114] resulting in a collapse of the crosslinked shell around the polystyrene core schematically shown in Figure 5.11(a).
The temperature dependence of R_{H} leads to a temperature dependence of the volume of the particles. Consequently, ϕ_{eff}, which is the only parameter changing the rheological behavior in monodisperse hard sphere colloidal systems as described in Section 4, can be adjusted precisely ($\Delta\phi_{eff} \approx 0.003$) by changing T ($\Delta T = 0.25\,^{\circ}\mathrm{C}$). This high precision in the adjustment of ϕ_{eff} is especially beneficial for the investigation of the transition region from the liquid to the glassy state and the detailed comparison to the MCT predictions.
The swelling behavior of the particles in dependence on the temperature is investigated using DLS. The temperature dependence of R_{H} of PS-37-PNIPAm-75, PS-51-PNIPAm-131 and PS-47-PNIPAm-106 is depicted in Figure 5.11(b). Between $T = 10\,^{\circ}\mathrm{C}$ to $25\,^{\circ}\mathrm{C}$ the hydrodynamic radius shows a linear dependence on the temperature with thermal expansion coefficients between $-0.5\,\mathrm{nm}\,^{\circ}\mathrm{C}^{-1}$ to $-1.0\,\mathrm{nm}\,^{\circ}\mathrm{C}^{-1}$ depending on the effective crosslinking density and the shell thickness of the particles.

$$\text{PS-51-PNIPAm-131: } R_{\mathrm{H}} = 154.7\,\mathrm{nm} - 0.99\,\mathrm{nm}\,^{\circ}\mathrm{C}^{-1} \cdot T \tag{5.6}$$

$$\text{PS-47-PNIPAm-106: } R_{\mathrm{H}} = 123.2\,\mathrm{nm} - 0.67\,\mathrm{nm}\,^{\circ}\mathrm{C}^{-1} \cdot T \tag{5.7}$$

$$\text{PS-37-PNIPAm-75: } R_{\mathrm{H}} = 88.4\,\mathrm{nm} - 0.47\,\mathrm{nm}\,^{\circ}\mathrm{C}^{-1} \cdot T \tag{5.8}$$

The linear dependence is followed by a drop with the highest first derivative at $T = T_{\mathrm{LCST}} = 32\,^{\circ}\mathrm{C}$. At temperatures above $T > 35\,^{\circ}\mathrm{C}$ R_{H} levels off to a plateau value.
Table 5.5 shows the radii of the core-shell particles in different states obtained using DLS and TEM. The core-shell radii determined with TEM are smaller than those obtained

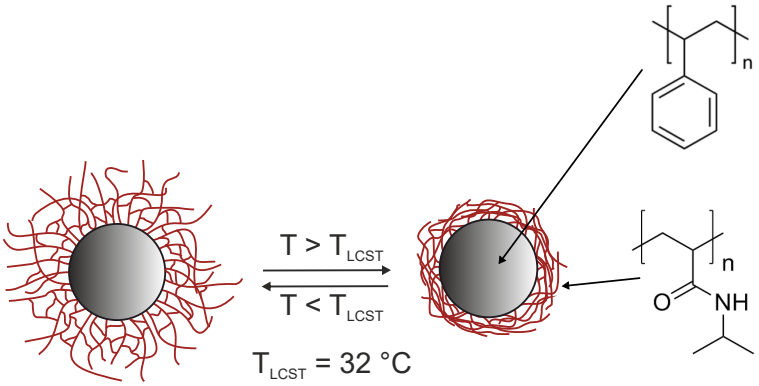

(a)

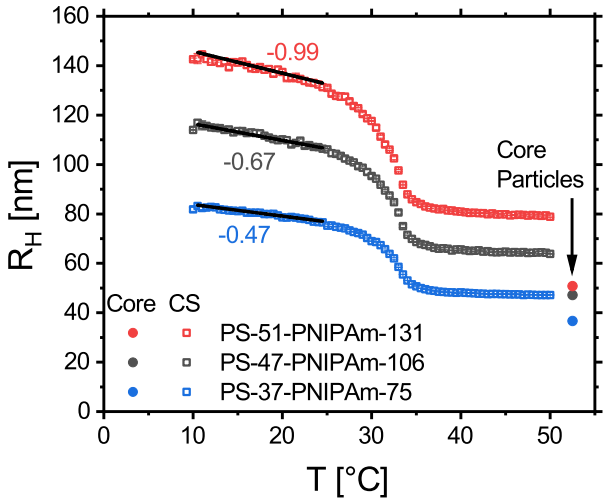

(b)

Figure 5.11: (a) Scheme of the volume transition of the thermoresponsive colloidal core-shell (CS) model system caused by swelling and deswelling of the shell. **(b)** Temperature dependence of R_H of three core-shell particles measured with DLS. The R_H of the core-shell particles follows a linear decrease with temperature in the region of $T = 10\,°C$ to $25\,°C$ followed by a sharp drop at $T_{LCST} = 32\,°C$. The R_H of the core particles is measured at $25\,°C$, despite that, it is indicated at a temperature of $52.5\,°C$ for better visibility of the ratio to the deswollen states of the shell.

with DLS because TEM measures the radius in the dry state, while DLS measures the hydrodynamic radius in the suspension. The radius obtained with DLS in a swollen state at $25\,°C$ is larger than the one obtained in the deswollen state at $50\,°C$.

From the size difference between the radius of the core-shell and the radius of the core particles shwon in Table 5.5, the shell thickness l_{shell} is calculated. The shell thickness in the swollen state at $25\,°C$ is about 2.8 to 3.5 times larger than in the deswollen state at $50\,°C$ for the different particles. For the samples PS-37-PNIPAm-75 and PS-47-PNIPAm-106 the shell thickness in the deswollen state is about 1.4 to 2.5 times larger than in the dry state measured with TEM. This trend is expected because the PNIPAm remains hydrolyzed in the shrunken state, but is expected to be completely dry when TEM measurements are conducted.

Assuming a volume concentration of 100 vol% of PNIPAm in the dried shell, the volume concentration of PNIPAm in the swollen and in the deswollen shell can be obtained. For

Table 5.5: Comparison of the hydrodynamic radii of the core-shell particles measured with DLS in the swollen state at 25 °C and the deswollen state at 50 °C, and the radius in the dry state measured with TEM. Additionally, the radius of the core particles is depicted as it is needed for the calculation of the thickness of the shell $l_{\mathrm{shell}} = R_{\mathrm{c}} - R_{\mathrm{cs}}$. The thickness of the shell is depicted for the swollen (DLS, 25 °C), deswollen (DLS, 50 °C) and the dry (TEM) state.

	$R_{\mathrm{H,DLS}}$ [nm]			R_{TEM} [nm]		l_{shell} [nm]		
Sample	25 °C	50 °C	Core	Dry	Core	DLS, 25 °C	DLS, 50 °C	TEM
PS-37-PNIPAm-75	75.2	47.2	36.7	30.6	26.3	38.5	10.9	4.3
PS-51-PNIPAm-131	131.1	78.8	50.8	74.3	45.3	80.3	28.9	29.0
PS-47-PNIPAm-106	106.1	64.9	47.2	49.9	37.6	58.9	17.7	12.3

PS-37-PNIPAm-75, the concentration of PNIPAm in the deswollen state is 40 vol% and in the deswollen state is 14 vol%, while for PS-47-PNIPAm-106 it is 70 vol% and 20 vol%, respectively.

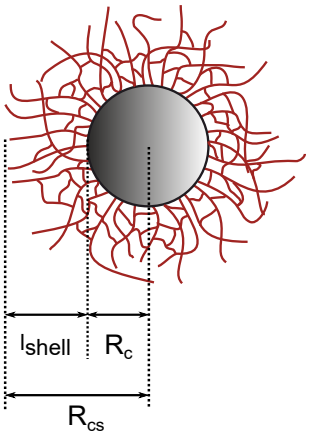

Figure 5.12: Schematic illustration of the radius of the core particles (R_{c}), of the core-shell particles (R_{cs}) and the thickness of the shell (l_{shell}).

In contrast to the other two core-shell particles, PS-51-PNIPAm-131 shows the same shell thickness measured with DLS in the deswollen state and measured with TEM. This leads to the assumption that the sample was not completely dry, while the TEM measurements were conducted. Hydrogels, and therefore microgels, are hygroscopic. If the sample was under atmosphere after the sample preparation including the drying process, the shell could already be partially swollen by adsorbing water from the atmosphere. The relatively low vacuum of 10^{-4} bar in TEM is not sufficient to completely dry the microgel within the short measuring time of a few minutes. This finding leads to the conclusion, that the obtained values for the volume concentration of the PNIPAm in the different states of the shell are an upper limit for this concentration, since the shell assumed to be dry may still contain some water.

5.3.3.3 Colloidal Stability of the Core-Shell Suspension

The colloidal stability of the core-shell suspension below and above $T_{\mathrm{LCST}} = 32\,^{\circ}\mathrm{C}$ is investigated in the purified and the unpurified state. Additionally, the stability of the purified suspension with added salt is investigated. The electrostatic interaction between

the particles affect their rheological behavior[117]. Therefore, a specific amount of potassium chloride ($c_{\mathrm{KCl}} = 0.05\,\mathrm{mol\,L^{-1}}$) is added to the suspension to screen these surface charges before investigation of the rheological behavior.

In Figure 5.13 an unpurified and a purified core-shell suspension are shown below and above T_{LCST} at $w = 8.5\,\mathrm{wt\%}$ and $0.5\,\mathrm{wt\%}$. Additionally, the purified suspension with added salt ($c_{\mathrm{KCl}} = 0.05\,\mathrm{mol\,L^{-1}}$ leading to a Debye length of $\lambda_{\mathrm{D}} \approx 1.3\,\mathrm{nm}$) is shown at the same mass fractions. The purified core-shell system shows colloidal stability at high and low concentration for all temperatures. The unpurified system and the system with added salt show colloidal stability below T_{LCST}, while at the high concentration, they precipitate as a solid above T_{LCST}. The low concentrated sample with added salt shows flocculation, while the unpurified system is colloidally stable above T_{LCST}. Cooling down to $T < T_{\mathrm{LCST}}$ leads to redispersion of the particles showing that the aggregation is reversible for all samples. Aggregation, precipitation and flocculation as well as the redispersion occur within minutes.

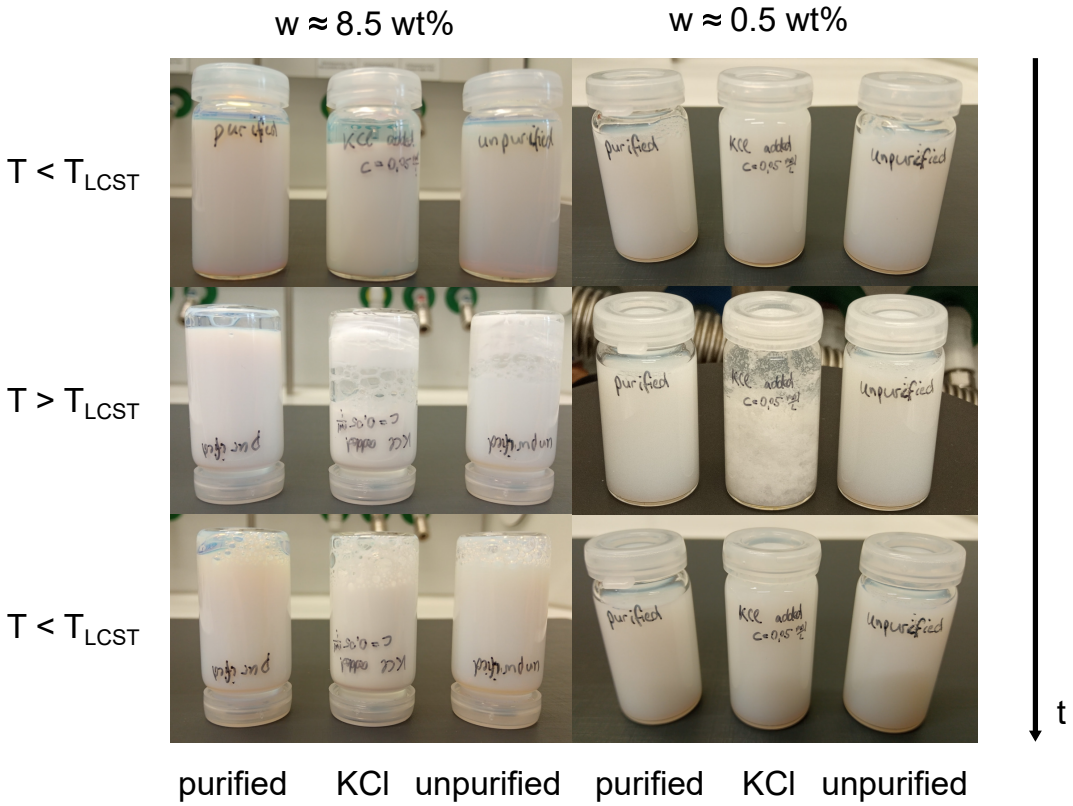

Figure 5.13: Images of the purified core-shell suspension, the purified suspension with added salt ($c_{\mathrm{KCl}} = 0.05\,\mathrm{mol\,L^{-1}}$) and the unpurified core-shell suspension at room temperature $T < T_{\mathrm{LCST}}$, heated up to $T > T_{\mathrm{LCST}}$ and cooled down again to $T < T_{\mathrm{LCST}}$ at two different mass fractions w to test colloidal stability. The purified system shows colloidal stability below and above T_{LCST}. In contrast, the purified suspension with added salt flocculates above T_{LCST} as the salt screens the stabilizing electrostatic interactions between the colloids. In the high concentrated unpurified system, the particles flocculate above T_{LCST}, while they are colloidally stable in at $w = 0.5\,\mathrm{wt\%}$. Cooling down to $T < T_{\mathrm{LCST}}$ leads to redispersion of the particles for all samples. The aggregation is reversible. Aggregation, precipitation and flocculation as well as the redispersion occur within minutes.

The crosslinked polymeric shell provides steric stabilization of the colloids, which is sufficient to stabilize them against aggregation in the swollen state below T_{LCST}. When heated above T_{LCST}, the shell shrinks around the core, as shown in Figure 5.11 on page 61. The thickness of the shell in the shrunken state is not sufficient to prevent the particles from aggregating by steric hindrance. Despite this, the purified system remains colloidally stable above T_{LCST} due to the surface charge resulting from the charged end groups of the polymer chains. The negatively charged end groups of the PNIPAm chains lead to electrostatic repulsion that hinder particle aggregation. Salt or other charged systems, such as the free PNIPAm chains not attached to the shells present in the unpurified system, screen those surface charges and cause loss of colloidal stability. In the system with the added salt, the concentration of the salt $c_{\mathrm{KCl}} = 0.05\,\mathrm{mol\,L^{-1}}$ leads to a Debye length of $\lambda_{\mathrm{D}} \approx 1.3\,\mathrm{nm}$, which is not sufficient to hinder aggregation. Thus, the particles aggregate, leading to a precipitation as a solid in a highly concentrated system and to flocculation in a low concentrated system. In the low concentrated system, the concentration of the free PNIPAm is insufficient to screen the surface charges to disrupt colloidal stability.
The reversibility of the aggregation shows that the swelling of the shell is sufficient to redisperse the particles. However, oligomers of the core-shell particles would not be visible by eye. DLS is very sensitive to aggregates as the scattering intensity depends on the hydrodynamic radius as follows $I_{\mathrm{S}} \propto R_{\mathrm{H}}^6$. Therefore, the intensity-weighted average hydrodynamic radius ($R_{\mathrm{H,I}}$) of the particles with added salt was measured with DLS for the system below T_{LCST}, followed by a heating above T_{LCST} leading to flocculation and cooling down again below T_{LCST} and measuring $R_{\mathrm{H,I}}$ again to proof the full redispersibility of the particles. The measurement before and after the heating up and cooling down cycle gained similar $R_{\mathrm{H,I}}$-values (deviation $< 10\,\%$) showing, that no aggregates are present after redispersion.

5.4 Suppression of the Crystallization Process

The scope of this work is to investigate the rheological properties of glass-forming colloidal suspensions and compare the results to MCT. MCT is based on monodisperse systems. However, monodisperse systems tend to crystallize. To study a pure glassy state, particle crystallization must be prevented. Previous studies used monomodal samples with a high dispersity of the radius to suppress particle crystallization (e.g., $\sigma_{\mathrm{rel}} > 17\,\%$ in Siebenbürger *et al.*[17,22,28]).
In contrast, within this thesis a binary mixture that closely resembles a monodisperse system is developed. To achieve this, a small particle is added to a large particle, both possessing low dispersities of the radius, until crystallization is sufficiently suppressed. This approach allows to closely approximate the systems underlying MCT while simultaneously suppressing particle crystallization.

5.4.1 Development of a Bimodal Mixture

To suppress the particle crystallization, a binary mixture of the core-shell suspensions PS-37-PNIPAm-75 and PS-51-PNIPAm-131 is utilized exhibiting a radius ratio of $\alpha = \frac{R_{\mathrm{H,small}}}{R_{\mathrm{H,large}}} \approx 0.58$ in the temperature range 10 °C to 20 °C, where the rheological measurements (compare Section 6 and 7) are conducted. The characteristics of the two samples are depicted in Table 5.6. Both samples have narrow radius distributions. To simplify the following discussion, the sample PS-37-PNIPAm-75 will be referred as small particle and, the sample PS-51-PNIPAm-131 as large particle in the following.

Table 5.6: Characteristics of the core-shell systems. The hydrodynamic radius of the core $R_{\mathrm{H,c}}$ and the core-shell $R_{\mathrm{H,cs}}$ system at 25 °C, the change of the R_{H} of the core-shell system with temperature $\frac{\Delta R_{\mathrm{H}}}{T}$ valid in the temperature range of 10 °C to 25 °C and the relative standard deviation σ_{rel} of the radius distribution obtained from differential centrifugal sedimentation (DCS).

Core-Shell Particle	$R_{\mathrm{H,c}}$ [nm]	$R_{\mathrm{H,cs}}$ [nm]	$\frac{\Delta R_{\mathrm{H}}}{T}$ $\left[\mathrm{nm\,°C^{-1}}\right]$	σ_{rel} [%]
PS-51-PNIPAm-131 Large Particle	50.8	131.1	0.99	3.9
PS-37-PNIPAm-75 Small Particle	36.7	75.2	0.47	5.8

Mixtures with different mass fraction of the large particle $w_{\mathrm{L}} = \frac{m_{\mathrm{L}}}{m_{\mathrm{S}}+m_{\mathrm{L}}}$, and hence different number fractions $x_{\mathrm{L}} = \frac{N_{\mathrm{L}}}{N_{\mathrm{L}}+N_{\mathrm{S}}}$, were prepared at a total mass fraction of $w_{\mathrm{tot}} = \frac{m_{\mathrm{L}}+m_{\mathrm{S}}}{m_{\mathrm{L}}+m_{\mathrm{S}}+m_{\mathrm{H2O}}+m_{\mathrm{KCl}}} = 8\,\%$ to $9\,\%$. The mixtures are designated as M-w_{S}S-w_{L}L. The mass fraction was chosen such as the colloids of the large particle crystallized at this mass fraction. The suspensions were set to rest for around two months and the samples were optically checked for crystals on a regular basis. In Table 5.7 w_{L} and x_{L} of the mixtures are depicted. x_{L} was calculated assuming the same density for the large and the small particle. For the pure large particle, the mixture M-1S-99L, M-3S-97L and M-5S-95L first crystals were observed within 1 h to 5 days. For MS-8S-92L first crystals were observed after 2 weeks, while for MS-10S-90L first crystals were observed after 8 weeks. The time for first observation of crystals increased with decreasing x_{L} consistent with the findings of Bartlett *et al.*[118]. Compared to a sample of pure large particles, the time until first crystals were observed for M-10S-90L increased significantly, from approximately 1 h to 8 weeks. This indicates that the crystallization has slowed enough to allow for investigating the rheological behavior of a pure glassy sample through overnight measurements. However, this evidence is not conclusive because the time of first observation of crystal exceeds the actual time of the onset of crystallization, since the crystals require a certain size before they become visible to the eye. Furthermore, only the crystals near the walls of the vial are visible due to the optical density of the sample. Therefore, rheological measurements are conducted to investigate the time scale of the crystallization process.

Table 5.7: Characteristics of the prepared mixtures. The weight fractions w_L and the number fractions x_L of the large particle. The mixtures are designated as M-w_SS-w_LL. The number fraction x_L of the large particle was calculated assuming the same density for the small and the large particle.

Samples	w_L [wt%]	x_L [%]
Large Particle	100	100
M-1S-99L	99.2	96.0
M-3S-97L	97.4	88.2
M-5S-95L	95.3	80.3
M-8S-92L	92.3	70.7
M-10S-90L	90.4	65.8
M-16S-84L	84.1	51.4
M-26S-74L	73.8	36.0
M-35S-65L	64.9	27.0
M-38S-62L	62.2	24.7
M-48S-52L	52.1	17.9
M-51S-49L	49.3	16.2
Small Particle	0	0

5.4.2 Rheological Investigation of the Crystallization Process

For conclusive evidence of the crystallization time for the pure large particle and the bimodal mixture M-10S-90L rheological measurements are conducted. Therefore, pure large particle and the mixture M-10S-90L with $w_L = 90.0\,\mathrm{wt\%}$ resulting in $x_L = 64.4\,\%$ were prepared at $w_{tot} = 8.2\,\mathrm{wt\%}$ and $9.3\,\mathrm{wt\%}$, respectively. Initially, the linear rheological behavior in the temperature range of 10 °C to 20 °C was investigated by conducting frequency sweeps at those temperatures. Before each frequency sweep, a preshear with $\dot{\gamma} = 100\,\mathrm{s^{-1}}$ was conducted for $t = 2\,\mathrm{min}$ to destroy the microstructure and shear history. The effective volume fraction ϕ_{eff} varies depending on the temperature due to the change of the radius of the particles.

For both samples, a temperature was selected, at which the sample exhibits the typicle behavior of a viscoelastic fluid, i.e. mainly elastic behavior at high freqeuncies and a terminal regime with mainly viscous behavior at low frequencies. This was carried out to ensure that the volume fractions of the samples are in the region in which the coexistence of fluid and crystalline phases of the sample is possible (see the phase diagram presented in Section 4 in Figure 4.3 on page 40). In this volume fraction region, the colloids are dense enough to undergo crystallization, but still loosely packed enough, that the crystallization is not hindered due to steric reasons.

Three subsequent frequency sweeps were performed at the chosen temperature of 20 °C and 19 °C for the large particle and the bimodal mixture, respectively. Before conducting the initial and final frequency sweeps, a preshear was performed at a shear rate of $\dot{\gamma} = 100\,\mathrm{s^{-1}}$ for a duration of 2 min to eliminate shear history and destroy any previously formed crystals. The frequency sweeps depicted in Figures 5.14(a) and 5.14(b) were performed from high to low frequencies and took $t = 67\,\mathrm{min}$ each. For the large particle, the typical course of viscoelastic fluids is seen from $\omega_1 = 628\,\mathrm{rad\,s^{-1}}$ to $0.169\,\mathrm{rad\,s^{-1}}$, then the storage

modulus (G') does not decrease anymore, but stays constant for a few angular frequencies, followed by an increase in G' and loss modulus (G''). In the second frequency sweep without preshear, G' is larger for the whole frequency region investigated than in the first frequency sweep. G'' shows a minimum around $\omega_1 \approx 1.69\,\mathrm{rad\,s^{-1}}$. No crossover of the moduli and no terminal regime are present. The final frequency sweep aligns almost completely with the initial one.

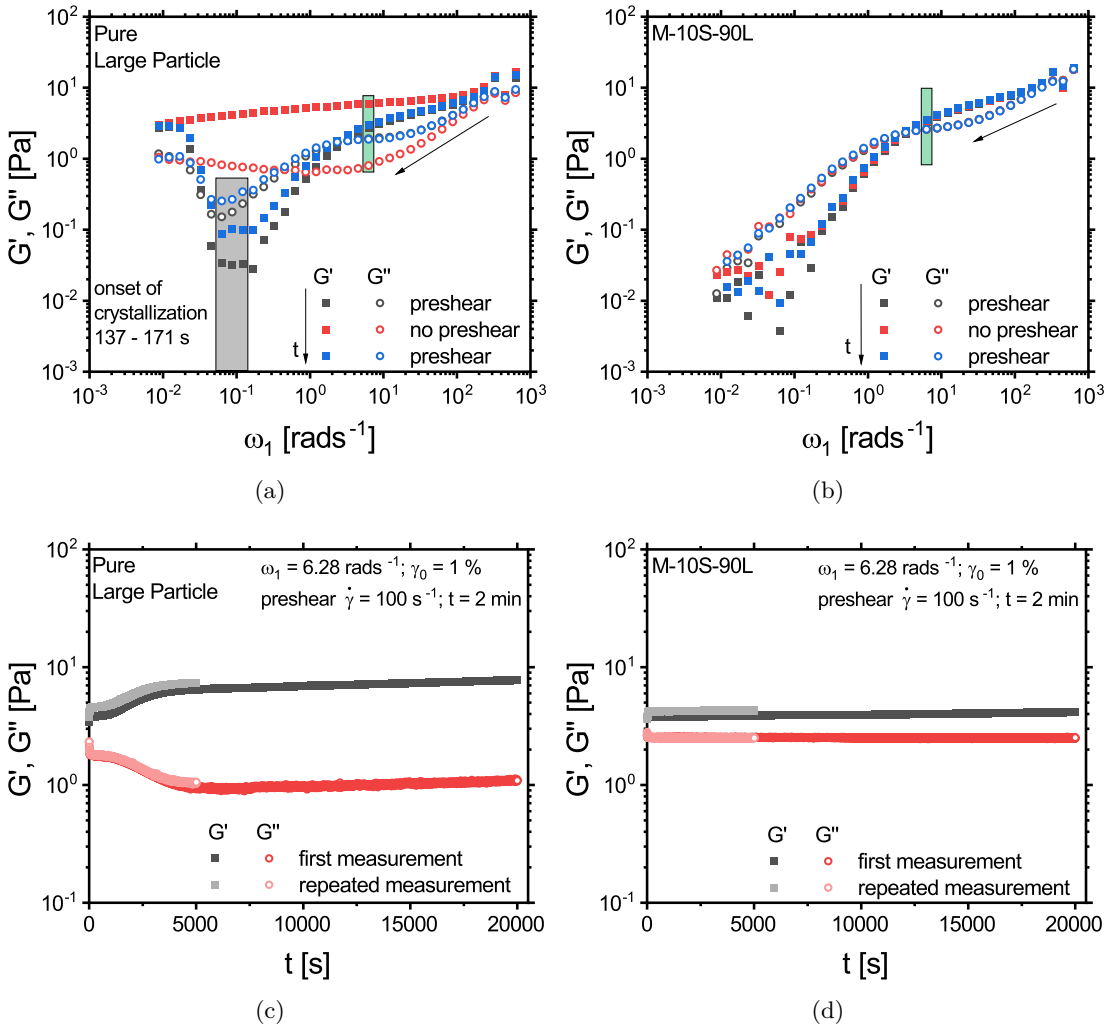

Figure 5.14: Rheological investigation of particle crystallization. **(a, b)** Frequency sweep (duration of each about 67 min) and **(c, d)** time sweep for the **(a, c)** large particle and **(b, d)** bimodal mixture. Before the initial and final frequency sweep, a preshear with $\dot{\gamma} = 100\,\mathrm{s^{-1}}$ for $t = 2\,\mathrm{min}$ is performed. In the frequency sweep of the large particle, G' and G'' increase after a certain time attributed to the onset of crystallization. The second frequency sweep performed without previous preshear shows larger G' values compared to the initial and final one. The frequency sweeps of M-10S-90L coincide, showing that no crystallization occurs. The angular frequencies at which the time sweeps are conducted are marked with a green box. In the time sweep of the large particle **(c)** G' and G'' first increase and then approach a plateau value. This increase is erasable with shear. In the time sweep of the bimodal mixture **(d)** only a non erasable increase of 8 % in G' and G'' is visible within 5.6 h arising from evaporation of the dispersion medium water confirming. This confirms that the bimodal mixture is not crystallizing within this time.

Based on these experimental findings, it can be inferred that particle crystallization occurs in the large particle, leading to a more solid-like response, characterized by higher values

of G'. The microstructure developed in the first frequency sweep is eliminated by the shear before the final frequency sweep, causing the first and initial frequency sweeps to coincide. The onset of crystallization takes place between $t = 137\,\mathrm{s}$ to $171\,\mathrm{s}$ after the preshear and completes in about $t \approx 1\,\mathrm{h}$, as observed in both initial and final frequency sweeps. Permanent effects on the sample due to evaporation of surrounding water, which would have led to increased volume fraction, can be excluded as the final frequency sweep coincides with the initial frequency sweep.

In contrast to the behavior of the large particle, all three frequency sweeps of the bimodal mixture show the behavior of a viscoelastic fluid and coincide completely. It can be concluded that no crystallization occurs for at least 2 h in M-10S-90L. In addition, there is no evaporation of the surrounding water, as this would result in higher G' values in the second and third frequency sweep compared to the first one.

Since rheological measurements were conducted for more than 2 h, additional time sweeps were performed to investigate if the employed bimodal mixture crystallizes over longer periods of time ($t = 5.6\,\mathrm{h}$). Before each time sweep, a preshear was performed at a shear rate of $100\,\mathrm{s}^{-1}$ for a duration of 2 min. In Figures 5.14(c) and 5.14(d) on page 67 these time sweeps are shown for the large particle and the bimodal mixture, respectively. They are performed at $\gamma_0 = 1\,\%$ and $\omega_1 = 6.28\,\mathrm{rad\,s}^{-1}$.

The time sweep of the large particle shows an increase in G' and a decrease in G'', while G' and G'' of the mixture remain almost constant (deviations about 8 %). Both are consistent with the frequency sweeps in the upper panel, where G' and G'' remained constant for the bimodal mixture, while G' increased and G'' decreased at $\omega_1 = 6.28\,\mathrm{rad\,s}^{-1}$ for the crystalline structure compared to the liquid one. The values of G' and G'' approach plateau values, after $t \approx 4300\,\mathrm{s} \approx 72\,\mathrm{min}$. This time is attributed to the time it takes for the particles to completely crystallize and is similar to the time determined from the frequency sweep. M-10S-90L shows no evidence of crystallization during the entire measurement time of $t = 20\,000\,\mathrm{s} \approx 5.6\,\mathrm{h}$.

The slight increase in G' of about 8 % in the time sweep of the bimodal mixture is attributed to the evaporation of water, which leads to a slight increase in volume fraction over time. For both samples, the second time sweep shows slightly higher initial values of G' compared to the first time sweep ($\approx 10\,\%$ increase) resulting from the same effect. For these measurements, a cone-plate geometry with a diameter of 50 mm and an angle of 0.02 rad was used with a silicone oil as a sealing on the outer radius to reduce water evaporation. However, water evaporation could not be neglected for times longer than 5.6 h with this geometry. Therefore, a 40 mm plate-plate geometry is used for long time measurements, as it allows for better control of evaporation over longer time scales of approximately 8 h (for more information, see the Appendix in A.2.7 and in A.3.2.2 in Figure A.3.9(a) on page 156), due to the higher volume-to-surface ratio and more accurate sample filling. The measurements shown in Figure A.3.9(a) furthermore confirm that particle crystallization is suppressed for at least 26 h.

Conclusively, the bimodal mixture shows no evidence of crystallization in either the frequency sweeps or in the time sweep measured for 5.6 h. The crystallization in M-10S-

90L is slowed down to such an extent that rheological measurements of the glassy state can be conducted for several hours. This mixture is used in all subsequent rheological measurements and will be referred to as the bimodal mixture in the following.

5.4.3 Swelling Behavior of the Bimodal Mixture

The temperature dependence of R_H of the bimodal mixture and its components measured with DLS is shown in Figure 5.15. The core-shell particles show a linear decrease of R_H in the range of $T = 10\,°C$ to $25\,°C$ followed by a drop with the highest first derivative at $T = T_{LCST} = 32\,°C$. At temperatures above $35\,°C$ R_H levels off to a plateau value. The general course of R_H and an explanation of the effects that are the cause of it have been discussed in Section 5.4.3.

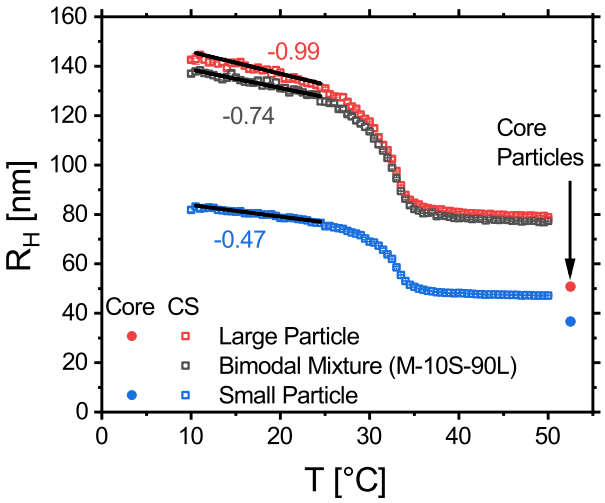

Figure 5.15: Temperature dependence of R_H of the small particle (PS-37-PNIPAm-75), the large particle (PS-51-PNIPAm-131) and the bimodal mixture measured with DLS. The R_H of the core-shell particles follows a linear decrease with temperature in the region of $T = 10\,°C$ to $25\,°C$ followed by a sharp drop at $T_{LCST} = 32\,°C$. R_H of the core particles is indicated at a temperature of $52.5\,°C$, despite it is measured at $25\,°C$, for a better visibility of the size difference to the deswollen state of the core-shell particles. The average radii of the bimodal mixture are closer to the radii of the large particle than to the radii of the small particle because the mixture contains a higher number fraction of the large particles. Additionally, with DLS the intensity-weighted average radius is obtained (as $I_s \propto R_H^6$, for more information see Section 2.2.1), which is more strongly influenced by larger particles than by smaller ones.

The bimodal mixture has a coefficient of thermal expansion of $-0.74\,nm\,°C^{-1}$, which is between that of the large particle and that of the small particle. Its hydrodynamic radius is much closer to the radius of the large particle than to that of the small particle. This is due to two effects. First, the bimodal mixture contains a higher number of large particles than small particles. Second, the scattering intensity in DLS depends strongly on the radius of the colloids $I_S \propto R_H^6$. Therefore, DLS measures the intensity-weighted average radius of the particles, resulting in a stronger influence of larger particles on the average radius compared to smaller ones.
The obtained linear dependencies valid in the region of $10\,°C$ to $25\,°C$ are as follows:

$$\text{Large Particle:} \quad R_\mathrm{H} = 154.7\,\mathrm{nm} - 0.99\,\mathrm{nm}\,^\circ\mathrm{C}^{-1} \cdot T \tag{5.9}$$

$$\text{Small Particle:} \quad R_\mathrm{H} = 88.4\,\mathrm{nm} - 0.47\,\mathrm{nm}\,^\circ\mathrm{C}^{-1} \cdot T \tag{5.10}$$

$$\text{Bimodal Mixture (M-10S-90L):} \quad R_\mathrm{H} = 146.0\,\mathrm{nm} - 0.74\,\mathrm{nm}\,^\circ\mathrm{C}^{-1} \cdot T \tag{5.11}$$

5.4.4 Characterization of the Bimodal Mixture

AFM images of the small particle, the large particle and the bimodal mixture are depicted in Figure 5.16. The image proves the bimodal sample to be a mixture of the small and the large particles.

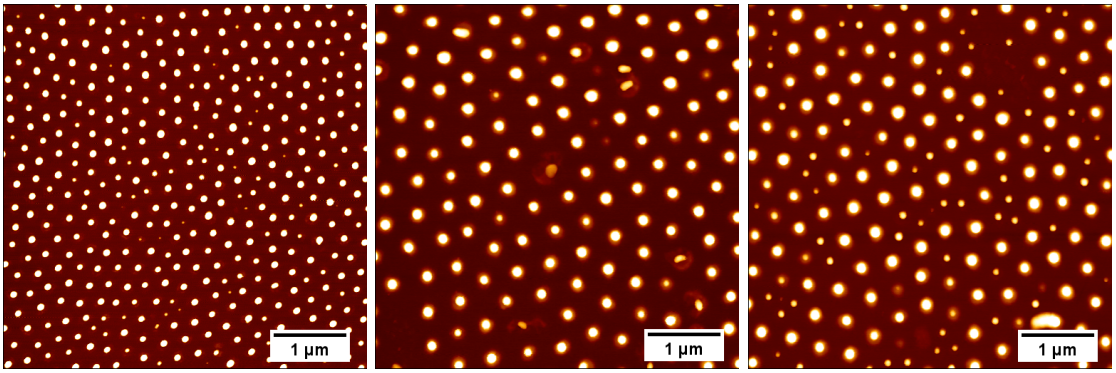

(a) Small particle (b) Large particle (c) Bimodal mixture

Figure 5.16: Atomic force microscopy images of the core-shell particles. The bimodal mixture consists of the large and the small particles. The image of the bimodal mixture contains a number fraction of the large particle of $x_\mathrm{L} = 61.6\,\%$ which is close to the number fraction $x_\mathrm{L} = 64.4\,\%$ determined from the weighted value.

By counting the large and the small particles present in the image of the bimodal mixture, a total number of $N_\mathrm{L} = 106$ and $N_\mathrm{S} = 66$ was found, resulting in a number fraction of the large particle of $x_\mathrm{L} = 61.6\,\%$. The number fraction found in the image is about $\Delta x_\mathrm{L} = 3.2\,\%$ smaller than the number fraction $x_\mathrm{L} = 64.4\,\%$ determined from the weighted value.

TEM images of the small particle, the large particle and the bimodal mixture are depicted in Figure 5.17. In the first image of the bimodal mixture, a total number of the large $N_\mathrm{L} = 133$ and the small $N_\mathrm{S} = 73$ particle was investigated, resulting in a number fraction of the large particle of $x_\mathrm{L} = 64.6\,\%$, which is $\Delta x_\mathrm{L} = 0.2\,\%$ higher than the calculated number fraction $x_\mathrm{L} = 64.4\,\%$ from the mass fraction of the particles.

In the TEM images of the small particle, chain-like clustering is visible, while the large particles are not in contact with each other like already discussed in Section 5.3.3.1. In the images of the bimodal mixture, black cubic crystals of KCl are visible, which has been added for rheological measurements (compare Section 5.1). The sample of the pure small and the pure large particle did not contain added salt. The core-shell structure of the particles is visible in all the images. In the TEM image of the mixture, the shells of the small particles are barely visible due to poor contrast. This lower contrast is caused by the salt deposits, which have a higher electron density than polymers and therefore reduce the contrast for the polymers.

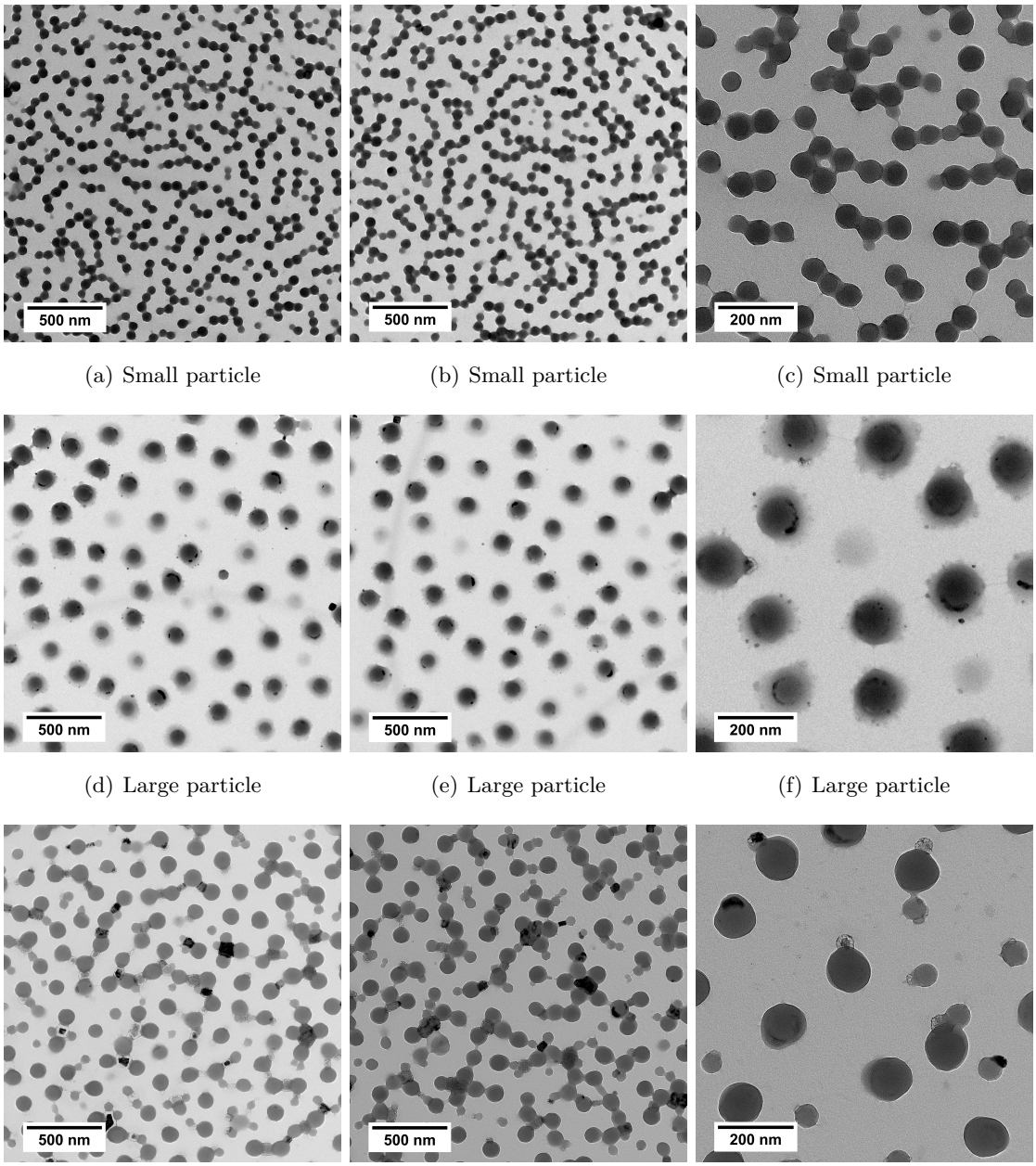

(a) Small particle (b) Small particle (c) Small particle

(d) Large particle (e) Large particle (f) Large particle

(g) Bimodal mixture (h) Bimodal mixture (i) Bimodal mixture

Figure 5.17: TEM images of the core-shell particles. The first two images in each row are taken at the same magnification but at different positions in the sample, while the third image is taken at a higher magnification. In all images, the core-shell structure of the particles is visible. The image confirms the bimodal sample to be a mixture of the small and the large particles. Additionally, the bimodal mixture contains black cubic crystals of KCl. KCl was only present in the sample of the bimodal mixture as here the same sample as used for rheological measurements was used. In this sample, KCl was added to screen the electrostatic interactions between the particles.

The core-shell particles of the large particle appear to be larger in the image of the pure particle compared to the image of the bimodal mixture. To investigate this quantitative, the core and core-shell average radii were determined by measuring the diameters of the core-shell particles in the images with ImageJ.

The radius of the small core-shell particle in the dry state measured with TEM appears to be about 4 % higher in the image of the bimodal mixture than in the image of the small

particles. This difference arises from the uncertainty of the determination of the radius from the image analysis.
In contrast, the large particle appears to be about 30 % larger in the image of the pure particle compared to the image of the bimodal mixture. This discrepancy cannot be attributed fully to the uncertainty of the imaging technique. This supports the assumption that the large particles was not completely dry while capturing the images of the pure large particle (see Section 5.3.3). From the size difference between the radius of the core-shell R_{cs} and the radius of the core particles R_c, the shell thickness l_{shell} is calculated and listed in Table 5.8. In the image of the bimodal mixture, the shell of the large particle is thinner as it contains less water.

Table 5.8: Comparison between the radii of the core and core-shell systems determined from DLS ($R_{H,DLS}$) and TEM (R_{TEM}). Unless otherwise specified, core-shell system radii are shown. At 25 °C, the shell is swollen, while it is shrunken around the core at 50 °C. The shell thickness is calculated from the difference of the core and the core-shell radii $l_{shell} = R_c - R_{cs}$.

	$R_{H,DLS}$ [nm]			R_{TEM} [nm]		l_{shell} [nm]		
Sample	25 °C	50 °C	Core	Dry	Core	DLS, 25 °C	DLS, 50 °C	TEM
Small particle	75.2	47.2	36.7	30.6	26.3	38.5	10.9	4.3
Large particle	131.1	78.8	50.8	74.3	45.3	80.3	28.9	29.0
Bimodal mixture	125.7	77.4	–	31.8 57.7	–	–	–	5.5 12.4

Assuming a volume concentration of PNIPAm of 100 vol% in the dried shell, the concentration of PNIPAm in the deswollen and the swollen state can be obtained. The analysis of the images of the bimodal mixture results in concentrations of 50 vol% PNIPAm in the deswollen state of the small particle and 43 vol% in the one of the large particle, while the shell contains about 15 vol% of PNIPAm in the swollen states for both particles. The obtained values are an upper limit of the concentrations as the shell in the measurements with TEM can still contain some water.

5.5 Summary

This chapter provided the details about the model system used for the rheological investigations on glass-forming colloids. This model system has to fulfill a set of requirements which arise from the scope of this work. The particles have to be of spherical shape and exhibit an easy adjustable volume fraction. Particle crystallization has to be prevented to obtain a stable glassy state. Additionally, the particles should exhibit an interaction potential close to hard spheres and have a defined, narrow radius distribution to improve comparability to MCT predictions.
To meet the criterion of a precisely adjustable ϕ_{eff}, thermoresponsive polymer based core-shell particles were chosen as a model system. Following the work of Dingenouts *et al.*[119], the colloidal particles PS-PNIPAm core-shell were synthesized in a two-step synthesis procedure via emulsion and seeded emulsion polymerization.

The core particles have a spherical shape with average radii in the range of 33 nm to 51 nm and serve as a seed in the second synthesis step. In the second synthesis step, the crosslinked PNIPAm shell with an average crosslinking density of 2.5 mol % is synthesized onto the core particles. Consequently, the particles exhibit a spherical core-shell structure as confirmed by TEM and AFM, see Figures 5.10 and A.3.7 on page 59 and 154. The radii of the synthesized core-shell systems are in the range of 75 nm to 131 nm at 25 °C. The expected temperature dependence of R_H of the chosen model system was confirmed using DLS, see Figure 5.11 on page 61. They show a linear dependence in the range of 10 °C to 25 °C. The temperature dependence of R_H leads to a temperature dependence of the volume of the particles. Consequently, ϕ_eff, which is the only parameter influencing the phase behavior in monodisperse hard sphere colloidal systems, can be adjusted precisely ($\Delta\phi_{eff} \approx 0.003$) by changing T ($\Delta T = 0.25\,°\mathrm{C}$). This high precision in the adjustment of ϕ_eff is especially beneficial for the investigation of the transition region from the liquid to the glassy state and the detailed comparison to MCT.

The synthesis path of the core-shell particles leads to charges on the particle surface resulting from the use of a charged initiator. To meet the criterion of a hard sphere interaction potential, these surface charges were screened by the addition of KCl with $c_\mathrm{KCl} = 0.05\,\mathrm{mol\,L^{-1}}$ in accordance with literature[112] resulting in a Debye length of 1.3 nm. It was shown, that the system is colloidally stable below T_LCST for this salt concentration, but loses colloidal stability above this temperature, see Figure 5.13 on page 63. Therefore, the rheological characterizations are limited to $T < T_\mathrm{LCST} = 32\,°\mathrm{C}$, which is sufficient to study both the supercooled as well as the glassy state.

To meet the criterion of the prevention of particle crystallization, a bimodal mixture of a large particle with $R_\mathrm{H}\,(15\,°\mathrm{C}) = 139.9\,\mathrm{nm}$ and a small particle with $R_\mathrm{H}\,(15\,°\mathrm{C}) = 81.4\,\mathrm{nm}$ was prepared. They exhibit a size ratio of about 0.58 in the temperature range of $T = 10\,°\mathrm{C}$ to $20\,°\mathrm{C}$ in which the rheological measurement were performed, see Chapters 6 and 7. The mass fraction of the large particle is $w_\mathrm{L} = 90\,\mathrm{wt\%}$. From this the number fraction of the large particle of $x_\mathrm{L} = 64.4\,\%$ was calculated. Imaging with AFM and TEM reveals this number fraction with deviations of $\Delta x_\mathrm{L} < 4\,\%$, see Figures 5.16 and 5.17 on page 70 and 71. Time-dependent rheological investigations confirmed that the suppression of crystallization is sufficient within the time scales of the rheological investigations of this thesis, see Figures 5.14 and A.3.9 on page 67 and 156.

In summary, it is concluded that the bimodal core-shell particle suspension fulfills all model system requirements outlined in this work. The synthesized particles exhibit a spherical core-shell structure as shown by AFM and TEM. They have a temperature dependence of R_H shown by DLS, which enables a precise adjustment of the volume fraction ($\Delta\phi_\mathrm{eff} = 0.003$) by changing the temperature ($\Delta T = 0.25\,°\mathrm{C}$). The electrostatic interactions due to charged end groups of the polymer chains are screened with KCl ($c_\mathrm{KCl} = 5 \times 10^{-2}\,\mathrm{mol\,L^{-1}}$), which leads to a Debye screening length of about $\lambda_\mathrm{D} = 1.3\,\mathrm{nm}$. This Debye screening length is smaller than the shell thickness leading to an interaction potential between the particles barely influenced by electrostatics. The shielding of the electrostatic repulsion leads to a sacrifice of colloidal stability at $T > T_\mathrm{LCST}$. Therefore,

rheological measurements are limited to $T < T_{\mathrm{LCST}}$. Particle crystallization is suppressed by using a bimodal mixture of a large particle ($R_{\mathrm{H}}(15\,^{\circ}\mathrm{C}) = 139.9\,\mathrm{nm}$) and a small particle ($R_{\mathrm{H}}(15\,^{\circ}\mathrm{C}) = 81.4\,\mathrm{nm}$) with a size ratio of $\alpha \approx 0.58$ in the temperature range of $10\,^{\circ}\mathrm{C}$ to $20\,^{\circ}\mathrm{C}$, in which the rheological measurements are conducted. The employed bimodal mixture is used as a model system for the investigations on a glass-forming colloidal suspension in all subsequent rheological measurements.

6 Linear and Nonlinear Rheological Characterization

In this Chapter, the dynamics and mechanical properties of the glass-forming colloidal model system introduced in Chapter 5 are investigated in the quiescent state and under steady shear. First the effective volume fraction, the glass transition volume fraction and the normalization constants are determined. Secondly, the mechanical properties and the relaxation times of the suspension in the quiescent state are studied applying small amplitude oscillatory shear (SAOS) measurements and the results are compared to mode coupling theory (MCT) calculations kindly provided by Manuel Maier from the university of Konstanz. Morevoer, the yielding behavior under steady shear is analyzed, focusing on the transient stress during the onset of flow. Finally, the influence of a steady shear motion on the relaxation times of the colloidal suspension is evaluated and compared to MCT predictions.
Some parts of the content of this Chapter and the corresponding sections in the Appendix have been published in the Journal of Rheology from the American Institute of Physics (AIP)[120] and have been adapted with permission. Lea Fischer is the first author of this article.

In the previous chapter, the model system used within this work was introduced. This model system consists of a binary mixture of thermoresponsive PS-PNIPAm core-shell particle suspensions. The bimodal model system is utilized to suppress particle crytallization. It consists of a small particle ($R_\mathrm{H} = 81.4\,\mathrm{nm}$ at $15\,^\circ\mathrm{C}$) and a large particle ($R_\mathrm{H} = 139.9\,\mathrm{nm}$ at $15\,^\circ\mathrm{C}$) with a radius ratio of 0.58 and a mass ratio of 10 : 90. Additionally, KCl is added with $c_\mathrm{KCl} = 5 \times 10^{-2}\,\mathrm{mol\,L^{-1}}$ to screen the electrostatic interactions. This bimodal model system dispersed in water is used in all following measurements. If not indicated otherwise, a mass fraction of $w = 8.30\,\mathrm{wt\%}$ of the bimodal mixture in water is used.

6.1 Determination of the Volume Fraction, the Glass Transition Volume Fraction and Normalization Constants

The rheological behavior of glass-forming colloidal suspensions depends on the phase behavior and the energy and time scales given by the radius of the colloids (described more in detail in Chapter 4). The phase behavior is determined by the distance of the effective volume fraction (ϕ_eff) of the particles in the suspension to the glass transition volume

fraction (ϕ_g). Therefore, the determination of ϕ_{eff} and ϕ_g is crucial. The ϕ_g depends on the radius dispersity and the interaction potential of the particles. Thus, ϕ_g has to be determined for each model system.
In order to be able to compare the rheological results of colloidal suspensions with different particle sizes and to compare the experimental results to theoretical predictions, it is necessary to normalize the data to the given energy and time scales.

6.1.1 Determination of the Effective Volume Fraction

The thermoresponsiveness of the particles of the model system used is advantageous because it enables precise adjustment of ϕ_{eff} by changing the temperature. However, it poses a challenge in the determination of ϕ_{eff}. Several methods used to obtain ϕ_{eff} of colloidal suspensions[15,106,107] cannot be used due to this thermoresponsiveness. Therefore, ϕ_{eff} is derived from the rheological behavior of the colloidal suspension.
The ϕ_{eff} of the bimodal PS-PNIPAm core-shell particle suspension used as model system in this work is determined by measuring the relative zero-shear viscosity $\eta_{rel} = \frac{\eta_0}{\eta_s}$ (with η_s the solvent viscosity) of a series of suspensions with different mass fractions (w) at 20 °C as proposed by Carrier *et al.*[75]. The results of these measurements are shown in Figure 6.1. A fit with the Krieger-Dougherty equation[87] (see Equation 6.1) yielded the factor $k\,(20\,°C) = 0.08462$ between the mass fraction w and ϕ_{eff} at 20 °C. The factor k varies for different temperatures due to the temperature dependence of the R_H of the core-shell particles. Therefore, it is only used to calculate ϕ_{eff} at $T = 20\,°C$.

$$\eta_{rel}\,(20\,°C) = \frac{\eta_0\,(20\,°C)}{\eta_s\,(20\,°C)} = \left(1 - \frac{\phi_{eff}\,(20\,°C)}{\phi_{max}}\right)^{(-2.5\phi_{max})} = \left(1 - \frac{k\,(20\,°C)\,w}{\phi_{max}}\right)^{(-2.5\phi_{max})} \tag{6.1}$$

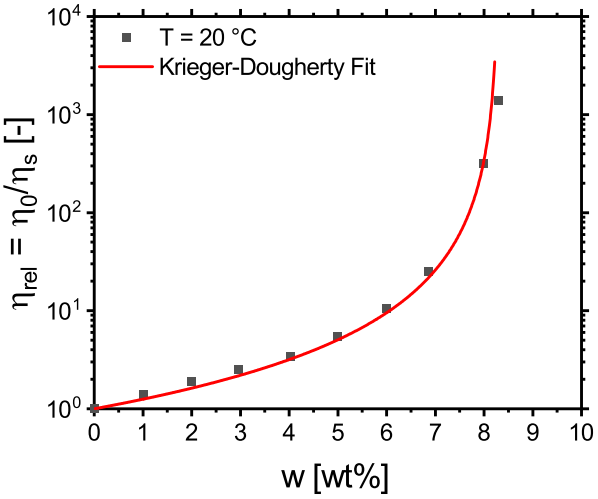

Figure 6.1: Relative zero-shear viscosity $\eta_{rel} = \frac{\eta_0}{\eta_s}$ of the colloidal suspension at different mass fractions w at $T = 20\,°C$. The red line is the fit with the Krieger-Dougherty Equation[87] (see Equation 6.1) obtaining the factor $k\,(20\,°C) = 0.08462$ between the mass fraction w and ϕ_{eff} at 20 °C.

The volume fractions at the other investigation temperatures T are calculated by normalizing ϕ_{eff} at 20 °C to the ratio of R_{H} at 20 °C to R_{H} at the investigation temperature. The required R_{H} values are obtained from the linear fit (see Equation 6.5) of the R_{H} values measured with dynamic light scattering (DLS). The resulting ϕ_{eff} values are presented in Table 6.1.

$$\phi_{\text{eff}}(T) = \phi_{\text{eff}}(20\,^{\circ}\text{C}) \left(\frac{R_{\text{H}}(T)}{R_{\text{H}}(20\,^{\circ}\text{C})} \right)^3 \tag{6.2}$$

6.1.2 Determination of the Normalization Constants

For a given ϕ_{eff}, for different sizes of colloids, the principle dynamics and thus the principle rheological behavior remain the same, but the energy and time scales shift. This is because the thermal motion of the particles depends on the particle size as described in Section 4.2. Therefore, the storage modulus (G'), the loss modulus (G'') and the stress (σ) are rescaled to this specific energy scale of a particle according to Equation 6.3. The angular frequency (ω_1) and the shear rate ($\dot{\gamma}$) are rescaled to the characteristic time scale of the diffusion of a single particle in dilution by its own radius (τ_0) according to Equation 6.4. With this the reduced storage modulus (G'_{red}), the reduced loss modulus (G''_{red}), the reduced stress (σ_{red}), the Péclet number in steady shear (Pe_0) and the Péclet number in oscillatory shear (Pe_ω) are obtained.

$$\frac{\sigma_{\text{red}}}{\sigma} = \frac{G'_{\text{red}}}{G'} = \frac{G''_{\text{red}}}{G''} = \frac{R_{\text{H}}^3}{k_{\text{B}}T} \tag{6.3}$$

$$\tau_0 = \frac{Pe_\omega}{\omega_1} = \frac{Pe_0}{\dot{\gamma}} = \frac{6\pi\eta_{\text{s}}R_{\text{H}}^3}{k_{\text{B}}T} \tag{6.4}$$

The rescaling enables the comparison of the rheological behavior of colloids of different sizes and its comparison with theoretical calculations. This is crucial for this work, as ϕ_{eff} is modified by adjusting R_{H} of the particles by changing the temperature. Additionally, the rheological results are compared to MCT calculations. The obtained rescaling factors are listed in Table 6.1.

In order to calculate the rescaling factors, it is crucial to precisely determine R_{H} at the respective measuring temperature. This was done by DLS measurements of the suspension at the relevant temperatures in a range between 10 °C and 25 °C.

This R_{H} was measured with DLS as described in Section 5.4.3. It follows a linear dependence on the temperature in the temperature range of 10 °C to 25 °C according to the following equation.

$$R_{\text{H}}(T) = 146.0\,\text{nm} - 0.74\,\text{nm}\,^{\circ}\text{C}^{-1} \cdot T \tag{6.5}$$

Table 6.1: Hydrodynamic radii R_H, and normalization constants for the angular frequency and shear rate, as well as the moduli and stress obtained from Equations (6.3) and (6.4) at the measurement temperatures T for the bimodal model system. Additionally, the volume fractions ϕ_eff for the bimodal mixture with a mass fraction of $w = 8.30\,\mathrm{wt\%}$ is depicted. The correlation between T and ϕ_eff depends on the mass fraction w of the sample, while R_H and the normalization factors are universal for a specific temperature.

T [°C]	ϕ_eff [-]	R_H [nm]	$\frac{Pe_\omega}{\omega_1} = \frac{Pe_0}{\dot{\gamma}}$ [s]	$\frac{\sigma_\mathrm{red}}{\sigma} = \frac{G'_\mathrm{red}}{G'} = \frac{G''_\mathrm{red}}{G''}$ $\left[\mathrm{m\,s^2\,kg^{-1}}\right]$
20	0.70	131.2	1.05×10^{-2}	5.58×10^{-1}
19	0.71	131.9	1.10×10^{-2}	5.69×10^{-1}
18	0.73	132.7	1.15×10^{-2}	5.81×10^{-1}
17	0.74	133.4	1.21×10^{-2}	5.93×10^{-1}
16	0.75	134.2	1.26×10^{-2}	6.05×10^{-1}
15	0.76	134.9	1.32×10^{-2}	6.17×10^{-1}
14	0.78	135.6	1.38×10^{-2}	6.29×10^{-1}
12	0.80	137.1	1.52×10^{-2}	6.55×10^{-1}
10	0.83	138.6	1.67×10^{-2}	6.81×10^{-1}

6.1.3 Determination of the Glass Transition Volume Fraction

The rheological behavior of a glass-forming colloidal system mainly depends on the phase behavior of the system as described in detail in Section 4.3. This phase behavior is determined by the distance of the volume fraction of the particles in the suspension to the glass transition volume fraction. Thus, a precise determination of the glass transition volume fraction is crucial.

In polymer science, the glass transition is defined as the point at which the system falls out of its thermodynamic equilibrium, which is between relaxation times of $\tau = 100\,\mathrm{s}$ to $1000\,\mathrm{s}$ of the system[121]. Consequently, the operational definition of the kinetic glass transition is the point where the longest relaxation time is slowed down to those values, corresponding to the crossover point in frequency sweeps being at a frequency of $f_1 = 0.01\,\mathrm{Hz}$ to $0.001\,\mathrm{Hz}$ or an angular frequency of $\omega_1 = 0.0628\,\mathrm{rad\,s^{-1}}$ to $0.006\,28\,\mathrm{rad\,s^{-1}}$.

In colloidal suspensions, the relaxation time of the particles, and therefore the kinetically defined glass transition volume fraction, highly depends on particle radius and the solvent viscosity.[122] For this reason, the beforementioned definition is not commonly used in colloid science. Instead, Pusey *et al.*[10] defined the glass transition in a monodisperse system as the volume fraction at which no crystallization occurs within weeks. This definition cannot be used for a system in which the crystallization is completely suppressed, which applies to the model system used in this work. In the absence of an unambiguous definition, in glass-forming systems, ϕ_g is often defined as the ϕ_eff, where G' shows a progressive increase and where a yield stress (σ_y) can be observed in shear flow measurements[21,105] and therefore depend on the measuring ranges and the sensitivity of the rheometer used. Since MCT predicts an ideal glass transition at which all movement of the particles is frozen, in this work, the glass transition volume fraction is defined as the volume fraction at which no decrease of G' can be found for the longest investigation time scales investigated within this work of $t = \frac{1}{\omega_1} \approx 3\,\mathrm{h}$.

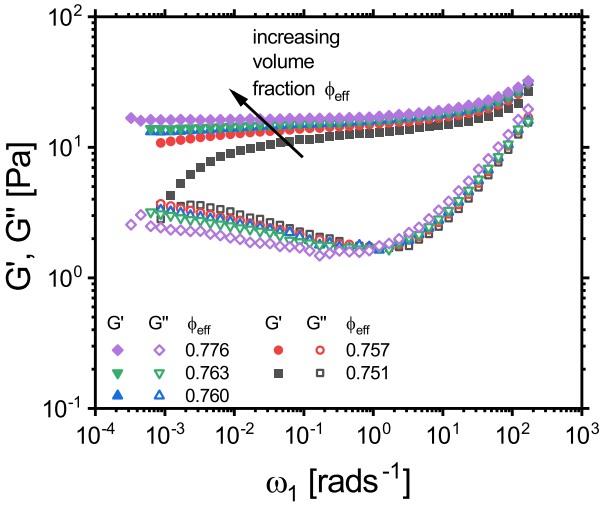

Figure 6.2: Dependence of G' and G'' on ω_1 for different ϕ_{eff} to determine ϕ_g. For $\phi_{\text{eff}} = 0.760$ no decrease of G' is found within $t = \frac{1}{\omega_1} \approx 3\,\text{h}$. Thus, the glass transition volume fraction is defined as $\phi_g = 0.76$.

Therefore, for the determination of ϕ_g, G' and G'' in dependence of ω_1 were measured for different ϕ_{eff}. From this, ϕ_g is found to be in the region between $\phi_{\text{eff}} = 0.75$ and $\phi_{\text{eff}} = 0.78$. To investigate ϕ_g more precisely, G' and G'' were measured in dependence of ω_1 for different ϕ_{eff} with small ϕ_{eff}-steps of $\Delta\phi_{\text{eff}} \approx 0.06$ in this region. The results are shown in Figure 6.2. For the volume fraction of $\phi_{\text{eff}} = 0.757$, the crossover of G' and G'' related to the α-relaxation vanished out of the investigated time scale of $t = \frac{1}{\omega_1} \approx 2\,\text{h}$, while for the volume fraction of $\phi_{\text{eff}} = 0.760$ not even a decrease of G' is found within $t = \frac{1}{\omega_1} \approx 3\,\text{h}$. Thus, the glass transition volume fraction is defined as $\phi_g = 0.76$. This glass transition volume fraction is higher than that observed for monodisperse hard sphere particles around $\phi_g = 0.58 \pm 0.02$ in computer simulations[123] and experimentally[10,124]. In contrast, MCT predicts ϕ_g of monodisperse hard sphere suspensions to be in the range of 0.52 to 0.54[95]. This discrepancy between the experimentally determined and the predicted ϕ_g of monodisperse hard sphere particles results from the approximations made in MCT for the determination of the structure factor S_q (see Section 4.4).
The higher ϕ_g found in the soft, bimodal system compared to ϕ_g in monodisperse hard sphere systems results from the softness and the dispersity of the radius of the particles[17,75,108]. Other investigations on similar thermoresponsive, but monomodal, systems found ϕ_g to be in the range of 0.64 to 0.80[17,75], consistent with the findings for the ϕ_g of the model system used in this thesis.

6.2 Linear Rheological Characterization

The principle rheological behavior and the relaxation times of the glass-forming colloidal suspension are studied using small amplitude oscillatory shear (SAOS). More information about SAOS can be found in Section 3.3.
The linear rheological behavior under oscillatory shear of the bimodal mixture is shown in Figure 6.3 for ϕ_{eff} above and below ϕ_g for a sample with $w = 8.30\,\text{wt}\%$. The measurements

were conducted in the linear regime at a strain amplitude of $\gamma_0 = 1\,\%$. The volume fraction was modified by varying the radius of the particles by changing the temperature. To allow comparison between the different volume fractions of the sample with different radii of the colloids and with theory, G', G'' and ω_1 are normalized, as described in Section 6.1.2. The normalization parameters for the distinct ϕ_{eff} are listed in Table 6.1 on page 78. The dependence of G' and G'' on ω_1 and additional frequency sweeps conducted with smaller ϕ_{eff}-steps are depicted in the Appendix in A.3.2.4 in Figure A.3.11 on page 158. Note, that the measurement covers 5 decades in Pe_ω, respective in w. For this, the evaporation of the dispersion medium, water, had to be slowed down considerably, which was enabled by sealing the gap with silicon oil. The selection of a suitable silicon oil is described in the Appendix in A.3.2.2.

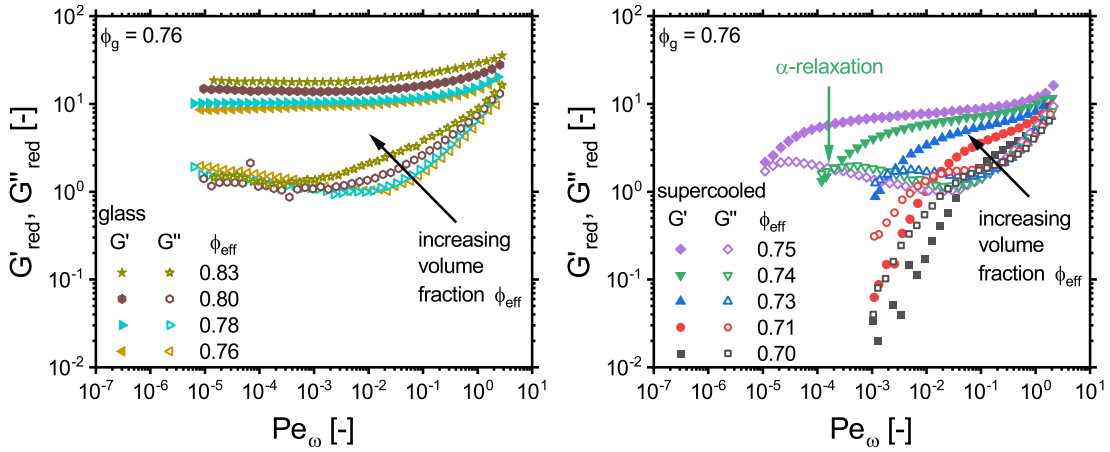

Figure 6.3: G'_{red} (filled symbols) and G''_{red} (open symbols) in dependence on Pe_ω **(a)** in the glassy regime ($\phi_{\mathrm{eff}} > \phi_{\mathrm{g}}$) and **(b)** in the supercooled regime ($\phi_{\mathrm{eff}} < \phi_{\mathrm{g}}$). The glassy samples exhibit a solid-like behavior ($G'_{\mathrm{red}} > G''_{\mathrm{red}}$) over the whole investigated frequency range, whereas the samples in the supercooled regime show a region with solid-like behavior followed by a crossover of G'_{red} and G''_{red} and a terminal regime for decreasing Pe_ω. The inverse of Pe_ω at the crossover points of G'_{red} and G''_{red} are related to the normalized α-relaxation times of the colloids, which increase for increasing volume fraction. The normalization constants to calculate Pe_ω, G'_{red} and G''_{red} are given in Table 6.1.

The samples with $\phi_{\mathrm{eff}} > \phi_{\mathrm{g}}$ exhibit a solid-like behavior over the whole studied angular frequency range with $G'_{\mathrm{red}} = \text{const.}$ referred to as the reduced plateau modulus ($G'_{\mathrm{red,P}}$). The $G'_{\mathrm{red,P}}$ value is increasing for increasing ϕ_{eff}. The reduced loss modulus G''_{red} is about one decade smaller than G'_{red} and exhibits a minimum.
The samples below the glass transition ($\phi_{\mathrm{eff}} < \phi_{\mathrm{g}}$) show the same behavior as the glassy samples for high rescaled frequencies Pe_ω with G'_{red} being lower than in the glassy samples. For lower frequencies (respectively Pe_ω) G'_{red} starts to decrease, while G''_{red} is first increasing and then decreasing resulting in a crossover point of G'_{red} and G''_{red} and a maximum in G''_{red} close to the crossover point. Below the crossover point, the samples show a flow regime. The behavior in the supercooled and the glassy state is typical for glass-forming colloids[7,17,74,75,113] and confirms the usability of the bimodal core-shell model system for investigating the rheological behavior of colloidal glasses.

The investigated rheological behavior is correlated to the microscopic dynamics of the system. In glass-forming colloidal suspensions in the supercooled state, the cage effect emerges. A particle is trapped in a cage by its surrounding particles hindering the long range diffusion of the particle. On short time scales, the particle can freely diffuse within the length scales of the cage called in-cage rattling (β-relaxation), but its long-range diffusion, i.e. the out-of-cage motion (α-relaxation), is suppressed.
Thus, the suspension exhibits a solid-like behavior with $G'_{\mathrm{red}} > G''_{\mathrm{red}}$ in the medium Pe_ω range, the limits of which depend strongly on the effective volume fraction of the system. For longer timescales, i.e. lower angular frequencies and respectively lower Pe_ω, the surrounding particles can open the cages enabling free diffusion of the particle resulting in a crossover of G'_{red} and G''_{red} followed by a dominance of the viscous contribution.
For volume fractions higher than the glass transition volume fraction $\phi_{\mathrm{eff}} > \phi_{\mathrm{g}}$, the α-relaxation time becomes slower than the investigation time ($t = \frac{1}{\omega_1} \approx 2\,\mathrm{h}$) as the particles are that densely packed, that they cannot escape their cages within this time. The increase in G''_{red} for decreasing Pe_ω indicates that the α-relaxation is not completely suppressed in the glass, but only slowed down considerably.
The Pe_ω at the crossover of G'_{red} and G''_{red} is correlated to the inverse of the normalized α-relaxation time of the particles, i.e. the time the particles need to escape their cages. The flow regime shows the possibility of free diffusion of the particles, which escaped their cages.
In the high frequency regime a second crossover point is expected for glass-formig colloids, which is not included in the experimental window. The high frequency response above this crossover probes the short time in-cage rattling[125,126] of the colloids[105] called the β-relaxation. For those time scales, the particles can freely diffuse within the cages causing $G''_{\mathrm{red}} > G'_{\mathrm{red}}$. The minimum of G''_{red} in between the two crossover points is related to the transition from the in-cage to the out-of-cage particle motion[105] with the characteristic time scale of $\frac{t_{\mathrm{min}}}{\tau_0} = \frac{1}{Pe_\omega\left(G''_{\mathrm{red,min}}\right)}$ with τ_0 the self-diffusion time in dilution. A minimum in G''_{red} is only observed, when the time scales of the α-relaxation and the β-relaxation are well separated (approx. 3 orders of magnitude). Consequently, in this work, the inverse of the Pe_ω at the minimum of the $\tan(\delta)$ is used instead as a measure for this time scale. In the following, the dependence of these time scales on ϕ_{eff} are investigated.

6.2.1 Relaxation Times of the Colloidal Suspension

The crossover in G'_{red} and G''_{red} and the minimum of the $\tan(\delta)$ observed in Figure 6.3 on page 80 are shifting to lower angular frequencies, i.e. the α-relaxation and the characteristic time scale of the transition from in-cage to out-of-cage particle motion increase for increasing effective volume fraction. Increasing the effective volume fraction leads to a more densely packed structure and therefore to stronger suppression of the relaxation processes.
To further investigate the volume fraction dependence of the time scales in the system, the inverse of Pe_ω at $G'_{\mathrm{red}} = G''_{\mathrm{red}}$ and at $\tan(\delta)_{\mathrm{min}}$ from the previously shown graphs and the graph shown in the appendix, are depicted in dependence on ϕ_{eff} in Figure 6.4.

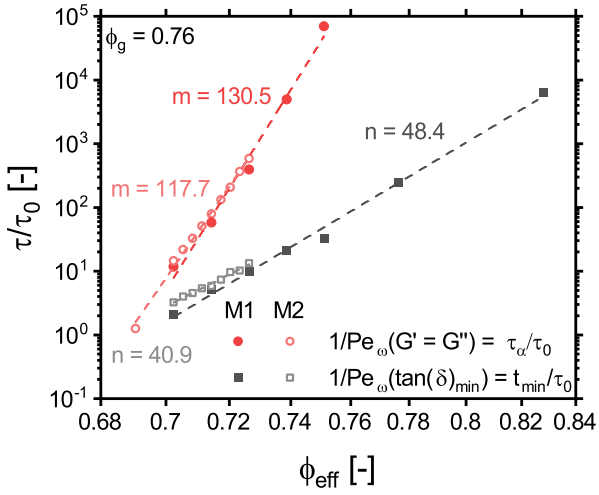

Figure 6.4: Volume fraction dependence of the inverse of the position in Pe_ω at the crossover point of G'_{red} and G''_{red} and the minimum in the loss factor $\tan(\delta)_{\mathrm{min}}$ giving the α-relaxation times and the characteristic times of the transition from α- to β-relaxation normalized to the self-diffusion time in dilution τ_0. The analysis was done for the frequency sweeps shown in Figure 6.3 on page 80 (M1) and shown in the appendix in Figure A.3.11 on page 158 (M2). The dotted lines display the linear fits in double logarithmic space resulting in $\frac{\tau_\alpha}{\tau_0} \propto \phi_{\mathrm{eff}}^m$ and $\frac{t_{\mathrm{min}}}{\tau_0} \propto \phi_{\mathrm{eff}}^n$.

The normalized α-relaxation time increases about 5 decades with increasing the volume fraction from 0.69 to 0.83. For the lowest investigated volume fraction in the supercooled regime of $\phi_{\mathrm{eff}} = 0.70$, the α-relaxation time is already about one decade longer than the self-diffusion time in dilution τ_0, since the diffusion of the particles is already significantly slowed down at volume fractions where the cage effect emerges. For $\phi_{\mathrm{eff}} = 0.69$, the sample is in the fluid regime.

The characteristic times show a power law dependence on the effective volume fraction with $\frac{\tau_\alpha}{\tau_0} \propto \phi_{\mathrm{eff}}^m$ with $m = 130.5$ for M1 and $m = 117.7$ for M2 resulting in $m \approx 124 \pm 7$ and $\frac{t_{\mathrm{min}}}{\tau_0} \propto \phi_{\mathrm{eff}}^n$ with $n = 48.4$ for M1 and $m = 40.9$ for M2 resulting in $n \approx 44.7 \pm 3.8$.

6.2.2 Comparison to Mode Coupling Theory Predictions

In the following, the linear rheological response of the glass-forming colloidal suspension is compared to mode coupling theory (MCT) predictions. MCT is a fully microscopic theory describing the structure and the dynamics of glass-forming suspensions by calculating the density auto correlation function $\Phi(t)$ using first principle mechanics[26,27]. The general approach of the theory is described more in detail in Section 4.4. In Section 4.4.2 the approach used here for the predictions of a response of a material to a small externally applied simple shear flow in the linear regime of the sample is described more in detail. In principle, the approach includes a wave vector (q) dependence. In this section, only the macroscopic limit of $q \to 0$ is calculated. A discussion of the q-dependence will follow in Section 6.2.4.

The expression obtained from theory for calculating G'_{red} and G''_{red} can be solved analytically and only depends on four different parameters. Namely the high frequency viscosity ($\eta_{\omega,\infty}$), the ratio of the collective short time diffusion coefficient (D_{s}) to the diffusion coefficient

under high dilution (D_0), the separation parameter (ϵ) giving the distance of the effective volume fraction to the glass transition volume fraction according to $\epsilon = \frac{\phi_{\mathrm{eff}} - \phi_{\mathrm{g}}}{\phi_{\mathrm{g}}}$ and the shift factor or fudge parameter (c_{y}).
To match the results derived from MCT predictions with G'_{red} and G''_{red} from the rheological experiments a fitting procedure is used. First, the ratio of the diffusion coefficients $\frac{D_{\mathrm{s}}}{D_0}$ is adjusted leading to a shift of the curves in the Pe_ω direction without changing the shape of the curves. This ratio is adjusted in a way that the moduli from theory match the high frequency behavior of the ones from the rheological measurements. For fitting the experimental data, the ratio of the diffusion coefficients is set to $\frac{D_s}{D_0} = 0.3$ according to literature[17].
Then, ϵ is adjusted to match the Pe_ω of the crossover of G'_{red} and G''_{red} from the experiments. Modifying ϵ does not change the high frequency course.
In the third step, the high frequency viscosity is adjusted to match the high frequency slope of G''_{red}. The high frequency viscosity has to be added as MCT does not include hydrodynamic interactions.

$$C''_\sigma = \bar{C}''_\sigma + Pe_\omega \eta_{\omega,\infty} \tag{6.6}$$

The $\bar{C}''_\sigma$ is the reduced loss modulus obtained from MCT, without the adjusted high frequency behavior and without the shift factor c_{y}. Finally, the c_{y} parameter is adjusted. The moduli derived from MCT are multiplied by this parameter to fit the amplitude of G'_{red} and G''_{red} of the experimental results. This fudge parameter is needed as MCT does not depict the increase in G'_{red} and G''_{red} with ϕ_{eff} in the supercooled regime.

$$G'_{\mathrm{red}} = c_{\mathrm{y}} C'_\sigma \tag{6.7}$$

$$G''_{\mathrm{red}} = c_{\mathrm{y}} \left(C''_\sigma + Pe_\omega \eta_{\omega,\infty} \right) \tag{6.8}$$

In Figure 6.5 the MCT predictions of G'_{red} and G''_{red} obtained from this fitting procedure kindly provided by Manuel Maier from the group of Prof. Fuchs in Konstanz are shown in comparison with the measurement data.
The MCT predictions of G'_{red} and G''_{red} depict the experimental results in the supercooled regime correctly. Approaching the glassy regime (see Figure 6.5(c)) G'_{red} can still be depicted without any deviations to the measured data. In contrast, the MCT predictions of the Pe_ω dependence of G''_{red} close to the maximum of G''_{red} show deviations from the experiments. The MCT predictions show a steeper transition from the maximum in G''_{red} to the minimum in G''_{red} compared to the experimental results. The flat transition from the maximum to the minimum in G''_{red} in the experiments for $\phi_{\mathrm{eff}} = 0.75$ arises from the α-relaxation time distribution resulting from the particle size distribution and heterogeneities in the structure arising close to ϕ_{g}. Furthermore, the softer interaction potential between the particles in the experiments lead to a flatter transition from the maximum to the minimum in G''_{red}. The distribution of the α-relaxation time due to the size distribution of

the particles and the softness of the particles cannot be covered by MCT as it is based on monomodal hard sphere particles, which all exhibit the same α-relaxation time.

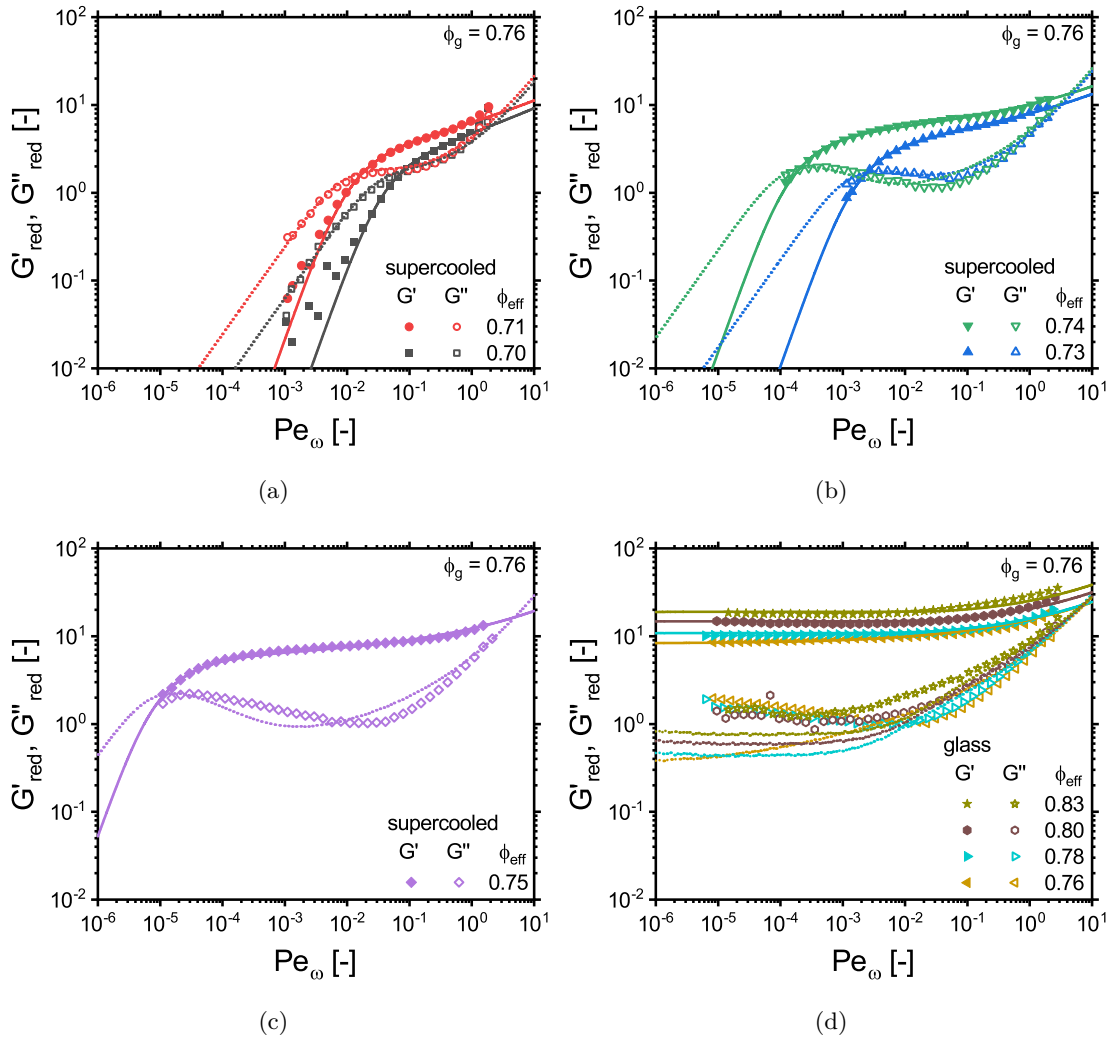

Figure 6.5: Experimental data of G'_{red} (filled symbols) and G''_{red} (open symbols) and the MCT predictions of G'_{red} (solid line) and G''_{red} (dotted line) in dependence on Pe_ω in **(a)**, **(b)** and **(c)** in the supercooled regime for different ϕ_{eff} and **(d)** in the glassy regime. The MCT predictions correctly reproduce the experimental results of G'_{red} in both, the supercooled and the glassy regime. In contrast, G''_{red} is only correctly predicted in the supercooled regime with a minimum distance of $\Delta\phi_{\mathrm{eff}} = 0.02$ to the glass transition volume fraction. For higher ϕ_{eff} in the supercooled regime, MCT predicts a sharper transition from the maximum to the minimum in G''_{red} than observed in the experiments (see **(c)**). In the glass, MCT predicts a plateau in G''_{red} at low Pe_ω, while in the experimental results G''_{red} increases for decreasingPe_ω in this region (see **(d)**).

The uncertainty of MCT in the region between the maximum and the minimum in G''_{red} was already observed in literature (see for example the fits in Fig. 5 of Siebenbürger *et al.*[17], Fig. 13 of Brader *et al.*[18] or Fig. 1 of Seyboldt *et al.*[29]). In the glassy regime (see Figure 6.5(d)) the deviations of MCT from the experimental data become even more pronounced, as MCT predicts G''_{red} to approach a plateau for $Pe_\omega \to 0$, while the experimentally determined G''_{red} values increase beyond the minimum for decreasing Pe_ω in agreement with literature[17,29,113]. The increase in G''_{red} indicates that the α-relaxation is not completely suppressed in the

glass, but only slowed down considerably. In contrast, MCT predicts a complete vanishing of the α-relaxation process in the glass and can therefore not cover this increase.
Crassous *et al.*[113] showed, that one additional relaxation time is not sufficient to match G''_{red}, by including an additional relaxation time of the order of 10^4 s in the calculations. This is due to the dispersity of the radius of the particles in the colloidal suspension. This dispersity of the radius results in a variation of the relaxation times of the particles. For higher effective volume fraction the relaxation time distribution broadens due to heterogeneities in the structure. These heterogeneities lead to different relaxation times of different domains in the suspension, resulting in a broadening of the relaxation time distributions.
In Table 6.2 the MCT parameters for the fitting of the experimental data are depicted. The separation parameter $\epsilon = \frac{\phi_{\mathrm{eff}} - \phi_{\mathrm{g}}}{\phi_{\mathrm{g}}}$ denotes the distance of the effective volume fraction to the glass transition volume fraction. Negative values describe the liquid and the supercooled state, while positive values describe the glassy state. The separation parameter ϵ decreases for increasing ϕ_{eff} and becomes negative for the fits to the experimental data of $\phi_{\mathrm{eff}} > \phi_{\mathrm{g}} = 0.76$. The ratio of D_{s} to D_0 was set to $\frac{D_{\mathrm{s}}}{D_0} = 0.3$ according to literature[17] as it depicts the behavior at all effective volume fractions properly. The obtained data from MCT have to be multiplied by the fudge parameter c_{y} since MCT does not depict the increase of the moduli for increasing effective volume fraction. Therefore, c_{y} increases for increasing ϕ_{eff}. This increase in the moduli results directly from the interaction potential of the particles and will be discussed more in detail in the following section. Furthermore, η_∞ decreases with increasing ϕ_{eff}, although it is expected to increase[17,29]. This discrepancy is primarly attributed to the limited experimental window, which insufficient to capture the asymptotic behavior of the high frequency process in the rheological measurements.

Table 6.2: The fit parameters of the MCT predictions for the frequency dependent moduli. The separation parameter $\epsilon = \frac{\phi_{\mathrm{eff}} - \phi_{\mathrm{g}}}{\phi_{\mathrm{g}}}$ defines the distance to the glass transition volume fraction, while $\frac{D_{\mathrm{s}}}{D_0}$ denotes the ratio of the collective short time diffusion coefficient to the diffusion coefficient under high dilution. The shift factor c_{y} of the moduli is needed as MCT does not depict the increase of the moduli with increasing ϕ_{eff}. The $\eta_{\omega,\infty}$ denotes the high frequency viscosity arising from hydrodynamic interactions, which are not included in the approach of the MCT.

T [°C]	ϕ_{eff} [−]	ϵ [−]	D_{s}/D_0 [−]	c_{y} [−]	$\eta_{\omega,\infty}$ [−]
20	0.70	-2.22×10^{-2}	0.3	1.71	0.80
19	0.71	-1.32×10^{-2}	0.3	1.99	0.80
18	0.73	-6.15×10^{-3}	0.3	2.26	0.80
17	0.74	-2.35×10^{-3}	0.3	2.71	0.70
16	0.75	-7.50×10^{-4}	0.3	3.19	0.65
15	0.76	1.00×10^{-5}	0.3	4.00	0.45
14	0.78	1.85×10^{-3}	0.3	4.00	0.50
12	0.80	2.85×10^{-3}	0.3	5.10	0.30
10	0.83	3.85×10^{-3}	0.3	6.20	0.20

6.2.3 Mastercurve and Interaction Potential

Assumptions of the interaction potential between the particles of the colloidal suspensions can be derived from the ϕ_{eff} dependence of $G'_{\text{red,P}}$[127–129]. In this section, the volume fraction dependence and the resulting interaction potentials are discussed. Furthermore, the reproducability of the data obtained with different rheometers and at different mass fractions of the particles in the suspension are briefly discussed. Additionally, the deviations between different rheometer loadings were tested and are depicted in the Appendix in A.3.2.3. The deviations are around 8 %.

The previously shown measurements were all conducted on the bimodal mixture with the same mass fraction $w = 8.30\,\text{wt\%}$ with the same geometry (PP40mm) at the same rheometer (ARES-G2, strain-controlled). In Figure 6.6, the $G'_{\text{red,P}}$ values ($G'_{\text{red,P}} = G'_{\text{red}}\,(\tan(\delta)_{\text{min}})$) obtained from the previously shown frequency sweeps and frequency sweeps conducted at the stress-controlled MCR 302 with a CP50mm and a PP43mm geometry at mass fractions of $w = 8.22\,\text{wt\%}$ and $w = 9.66\,\text{wt\%}$ are depicted.

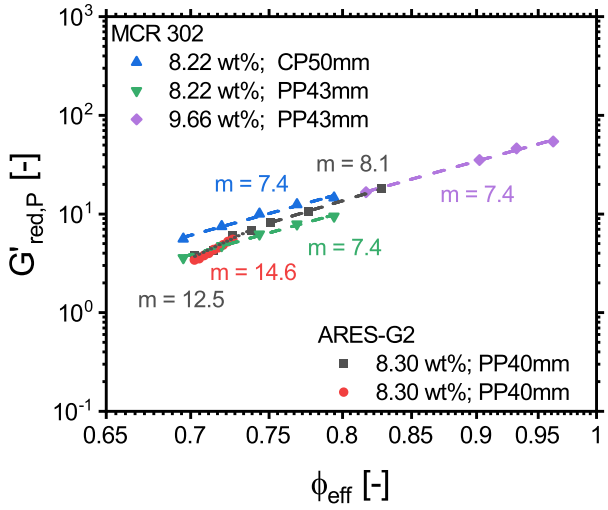

Figure 6.6: Dependence of $G'_{\text{red,P}}$ on ϕ_{eff} measured at different w with different geometries and rheometers. Below ϕ_{g} and above ϕ_{g} two different power law dependencies on ϕ_{eff} are found with $G'_{\text{red,P}} \propto {\phi_{\text{eff}}}^{m}$ with $m = 12.5$ to 14.6 and $m = 7.4$ to 8.1. From those dependencies, a simplified interaction potential between the particles of the suspension is assumed and illustrated in Figure 6.7 on page 88.

The $G'_{\text{red,P}}$ values in dependence on ϕ_{eff} obtained from the measurements conducted at $w = 8.30\,\text{wt\%}$ and $w = 9.66\,\text{wt\%}$ overlap completely, regardless of the rheometer and geometry used. In contrast, the derived values from measurements performed at $w = 8.22\,\text{wt\%}$ deviate up to 20 % from the values obtained from the other measurements. This can be attributed to sample filling and evaporation effects.

The deviation in the G'_{red} values measured at the same ϕ_{eff} resulting from different w and T are smaller than the deviations caused by other effects. Thus, it can be concluded, that different w and T combinations yielding the same ϕ_{eff} lead to similar rheological behavior. The G'_{red}-ϕ_{eff} curve can be used as a mastercurve for an alternative determination of ϕ_{eff}[109]. Assumptions of the interaction potential between the particles can be derived from the dependence of $G'_{\text{red,P}}$ on ϕ_{eff}[127–129]. The $G'_{\text{red,P}}$ is correlated to the distance between the

particles d and the interaction potential between them $G'_{\mathrm{red,P}} \propto \frac{1}{d}\left(\frac{\partial^2 U}{\partial d^2}\right)$. Furthermore, for an interaction potential of $U \propto d^{-n}$, a power law increase of $G'_{\mathrm{red,P}} \propto \phi_{\mathrm{eff}}^m$ with $m = 1 + \frac{n}{3}$ is predicted[130].

For volume fractions above ϕ_{g}, the core-shell model system exhibits a power law dependence of $G'_{\mathrm{red,P}} \propto \phi_{\mathrm{eff}}^m$ with $m \approx 7.6$. Below ϕ_{g} the exponent is $m \approx 13.6$. According to $n = 3(m-1)$ this results in interaction potentials of $U \propto d^{-n}$ with $n = 20$ and $n = 38$, respectively. This shows that above ϕ_{g}, the softness of the particles has a greater influence on the rheological behavior than below ϕ_{g}, resulting from higher compression of the outer shell of the particles at higher ϕ_{eff}.

Le Grand *et al.*[108] and Koumakis *et al.*[105] found similar power laws ($m = 4.9$ to 7.4 depending on the concentration of the system and $m = 7$, respectively) for a similar system of PS-PNIPAm core-shell particles. Additionally, they investigated a PMMA particle suspension typically used as model system for hard sphere systems and found a power law increase of G' and $G'_{\mathrm{red}} \propto \phi_{\mathrm{eff}}^m$ with $m \approx 50$ resulting in $n = 147$. Furthermore, for star-like micelles, which are used as a model system for ultra-soft particles, Koumakis *et al.*[105] found $m = 2$ resulting in $n = 3$. Note that Le Grand *et al.*[108] and Koumakis *et al.*[105] used G' and G'_{red} at a specific ω_1 and Pe_ω, respectively, and defined it as the plateau value instead of using $G'_{\mathrm{red}}(\tan(\delta)_{\mathrm{min}})$ leading to uncertainties especially for low ϕ_{eff}.

Potentials with the exponents experimentally found for the ultra-soft sphere ($n = 3$)[105], soft core-shell particles ($n = 20; 38$) and hard sphere systems ($n = 147$)[105,108] and with the exponent $n = \infty$, which defines the ideal hard sphere potential, are shown in Figure 6.7. The potential found for the soft core-shell system investigated in this work is closer to the potential of experimentally realizable and ideal hard sphere systems than to the potential of ultra-soft systems. Additionally, the potential of the core-shell particles has a higher exponent n, so a harder interaction potential, than the repulsive part of the empiric Lennard-Jones potential[131] $U_{\mathrm{rep}} \propto d^{-12}$. The Lennard-Jones potential is often used to model intermolecular interactions[132].

Soft core-shell particles exhibit a weaker increase in G'_{red} compared to hard sphere systems due to the softer interparticle interaction, but a stronger increase than ultra-soft systems. This is in agreement with measurements on other soft colloidal systems like multiarm star polymers[133] and microgels[134]. A stronger increase in $G'_{\mathrm{red,P}}$ results directly from harder interaction potentials.

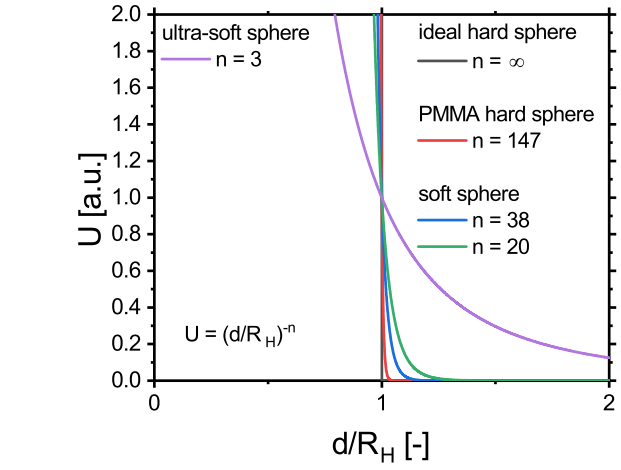

(a)

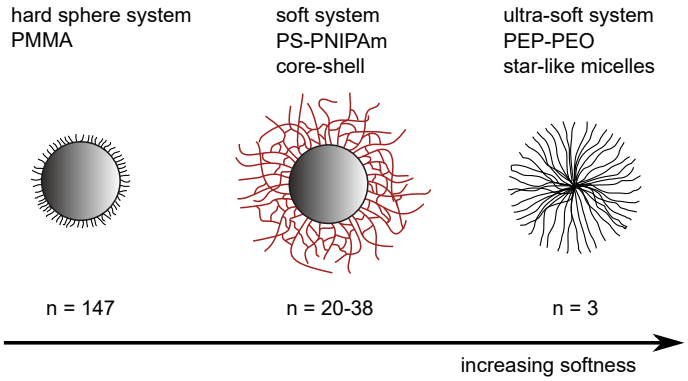

(b)

Figure 6.7: **(a)** Interaction potential of ideal hard sphere particles and simplified interaction potentials of experimentally realizable hard sphere, soft sphere and ultra-soft sphere particles estimated from the dependence of $G'_{\mathrm{red,P}}$ on ϕ_{eff}. An ideal hard sphere system is defined as having a potential of $U \propto \left(\frac{d}{R_{\mathrm{H}}}\right)^{-n}$ with $n = \infty$. For the model system used for hard spheres (PMMA particles) an interaction potential with $n = 147$ was found[105,108], while for the soft system used in this work, n varies from $n = 20$ to 38 depending on the volume fraction region and the swelling state of the shell. Furthermore, for ultra-soft systems $n = 3$ was found[105]. The interaction potential of a soft system aligns closer with hard sphere systems than with ultra-soft systems, as illustrated in **(a)**. **(b)** Schematic Illustration of the model systems with the different softnesses.

6.2.4 Dependence on the Boundaries

In linear rheology, it is expected that measuring the same sample with different geometries will give the same rheological results if the geometry is chosen from an appropriate range, i.e., a range, where the sample generates enough torque to give reliable results. Despite that, in the new approach of MCT used within this work, where the wave vector (q) dependence is not neglected, a dependence of the linear response on q is found. To obtain results, which are comparable to particles of different sizes, q is normalized to the inverse of the radius of the particles R.

The moduli obtained from MCT predictions for a qR-range of 7.81×10^{-4} to 3.20 for different separation parameters $\epsilon = \frac{\phi_{\mathrm{eff}} - \phi_{\mathrm{g}}}{\phi_{\mathrm{g}}}$ in the supercooled region are depicted in Figure 6.8. For the lowest separation parameter first deviations from the macroscopic limit of $qR \to 0$ are

visibile at $qR = 4.00 \times 10^{-1}$ while for the highest separation parameter, i.e. the results closest to the glass transition, first deviations are already visible for $qR = 1.25 \times 10^{-2}$. For increasing qR, the G'_{red} and G''_{red} values start to deviate from their values in the macroscopic limit of $qR \to 0$ for Pe_ω close to the crossover point. The deviations become stronger and start already at higher Pe_ω for increasing qR. In general, they are stronger in the terminal regime compared to the regime at higher Pe_ω. The deviations from the macroscopic limit become more pronounced for systems with higher α-relaxation times, i.e. for systems closer to the glass transition volume fraction. This is further illustrated as first deviations from the macroscopic limit arise at lower qR values for higher separation parameters, i.e. the results closer to the glass transition.

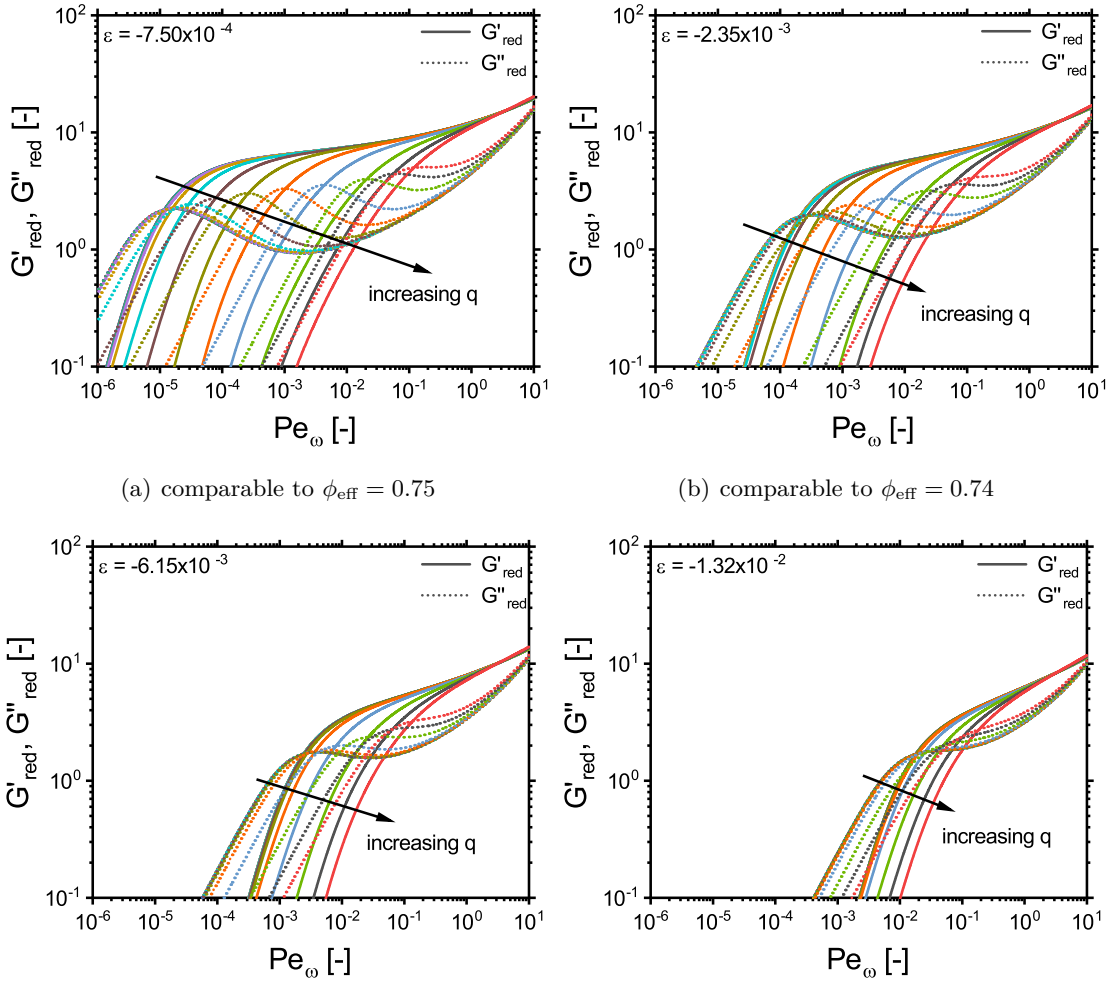

(a) comparable to $\phi_{\mathrm{eff}} = 0.75$

(b) comparable to $\phi_{\mathrm{eff}} = 0.74$

(c) comparable to $\phi_{\mathrm{eff}} = 0.73$

(d) comparable to $\phi_{\mathrm{eff}} = 0.71$

Figure 6.8: MCT predictions of the influence of qR on the linear response of colloidal suspensions in the supercooled state for a qR-range of 7.81×10^{-4} to 3.20. The deviations from the macroscopic limit of $qR \to 0$ are more pronounced for higher qR-values, at lower Pe_ω and at lower ϵ.

The Pe_ω-dependence of G'_{red} and G'''_{red} from experiments at different ϕ_{eff} below ϕ_{g} measured with cone-plate and plate-plate geometries with different plate diameters ranging from 25 mm to 50 mm are depicted in Figure 6.9. The experimental findings do not show a difference between the moduli measured with cone-plate and plate-plate geometries. In parallel plate geometries, the strain and the shear rate increase linearly along the

radius[135,136] leading to an inhomogeneous flow field, while in cone-plate geometries the flow field is homogeneous. In the linear regime, the differences between the results obtained from plate-plate measurements and those obtained from cone-plate measurements are expected to be negligible, which is consistent with the experimental findings. Additionally, it is expected, that the plate diameter does not have an influence on the measurement results. In contrast, the experimental results show an influence of the plate diameter on the moduli. A decrease in diameter has a similar effect on the measured moduli as an increase in qR has on the predicted moduli.

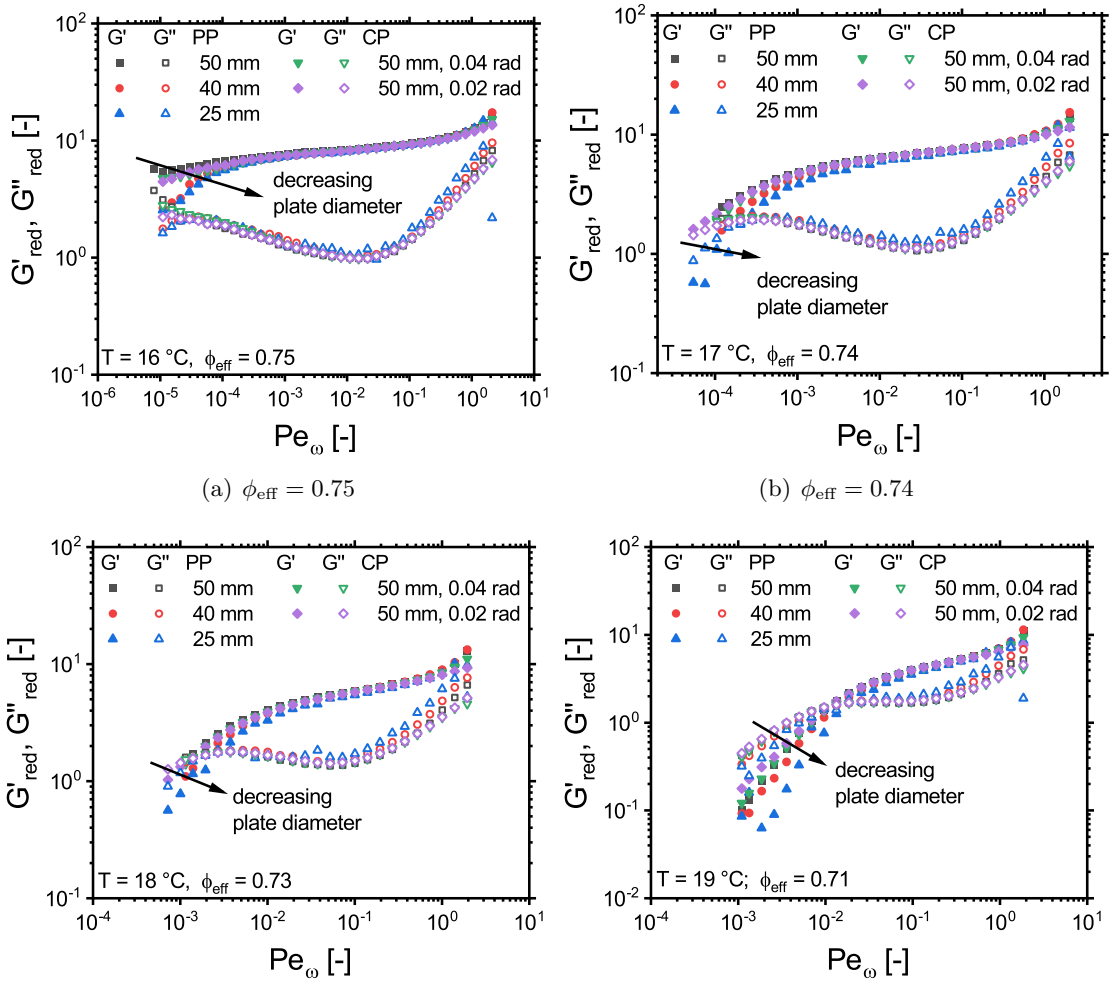

(a) $\phi_{\text{eff}} = 0.75$ (b) $\phi_{\text{eff}} = 0.74$

(c) $\phi_{\text{eff}} = 0.73$ (d) $\phi_{\text{eff}} = 0.71$

Figure 6.9: Influence of the geometry on the linear rheology of the sample. Close to the crossover point of G'_{red} and G''_{red}, G'_{red} is smaller for smaller plate diameters. MCT predicts similar deviations from the macroscopic limit of $qR \to 0$ for increasing qR. Differences between plate-plate and cone-plate geometries are not present. Be aware, that the graphs do not have the same scaling for a better visibility of the geometry effects.

For Pe_ω in the predominantly elastic regime with a large distance (2 decades) to the crossover point of G'_{red} and G''_{red}, G'_{red} does not depend on the diameter of the geometry. In contrast, for Pe_ω close to and below the crossover point, G'_{red} decreases for decreasing diameter of the geometry. This effect is more pronounced for the terminal regime below the crossover point compared to the regime at higher Pe_ω. In addition, this effect is more pronounced for samples with longer relaxation times, that is, with ϕ_{eff} closer to ϕ_{g}.

The differences in the moduli depending on the diameter of the geometry found in the experiment are not as pronounced as the deviations of the moduli at high qR compared to the macroscopic limit from the MCT predictions. This is, because the variation of the diameter of the geometries is limited to 25 mm to 50 mm due to the torque sensitivity and the availability of the geometries, while in the theoretical calculations, qR can be varied over several orders of magnitude. In the measurements at the lowest investigated $\phi_{\text{eff}} = 0.71$ using the PP25 mm geometry, for $Pe_0 \leq 3.59 \times 10^{-3}$, the measured oscillation torque of $M \leq 3.89 \times 10^{-8}\,\text{N m}$ is already below the lower torque limit in oscillation of $5 \times 10^{-8}\,\text{N m}$ of the used instrument[137].
The differences depending on qR and the diameter of the geometry may arise from long-range stress correlations, which are present in supercooled colloidal suspensions close to the glass transition volume fraction. In the experiment, this is influenced by the boundaries of the system.

6.3 Yielding Under Steady Shear

Above ϕ_{g}, the colloidal suspensions show a solid-like behavior under rest as seen in Figure 6.3 on page 80 as the α-relaxation time of the particles exceeds the investigation time $t = \frac{1}{\omega_1} \approx 3\,\text{h}$. The particles are trapped in the cages build by the surrounding particles for long times ($t > 10\,\text{h}$). The particles are immobilized, wherefore the flow of the material is hindered. The application of a $\sigma > \sigma_{\text{y}}$, leads to a flow of the material. This yielding occurs, because the shear leads to an ordering of the particles resulting in the possibility to flow. In the following, first steady state stress (σ_{st}) reached after this ordering is examined and then the transient stress during the ordering process is investigated. Finally, the differences between dynamic yield stress (σ_{dyn}) and static yield stress (σ_{stat}) are discussed.

6.3.1 Steady State Stress

The reduced steady state shear stresses as a function of the normalized shear rates of the bimodal mixture with $w = 8.30\,\text{wt\%}$ are shown in Figure 6.10(a) for ϕ_{eff} below and above ϕ_{g}, determined by oscillatory shear measurements. Similar to the oscillatory shear measurements, the measured data were double normalized as described in Section 6.1.2. Note, that the measurement covers 7 decades in Pe_0, respective in $\dot{\gamma}$. For this, the evaporation of the dispersion medium, water, had to be slowed down considerably, which was enabled by sealing the gap of the geometry with silicon oil. The selection of a suitable silicon oil is described in the Appendix in A.3.2.2.
For the lowest investigated volume fraction of $\phi_{\text{eff}} = 0.70$ at low Pe_0, σ_{red} is directly proportional to Pe_0, i.e. the viscosity η of the material is constant (see Figure 6.10(b)). The materials exhibit a first Newtonian plateau as the particles normalized α-relaxation time is lower than the inverse of Pe_0 leading to free diffusion of the particles. Increasing Pe_0 leads to a sub-linear increase in σ_{red} showing that the material is shear-thinning. Note that this happens already at Pe_0 far less than unity showing that the relaxation times of the colloids in the supercooled state are about at least 2 to 4 magnitudes (depending on ϕ_{eff}) higher than the relaxation time in dilution τ_0.

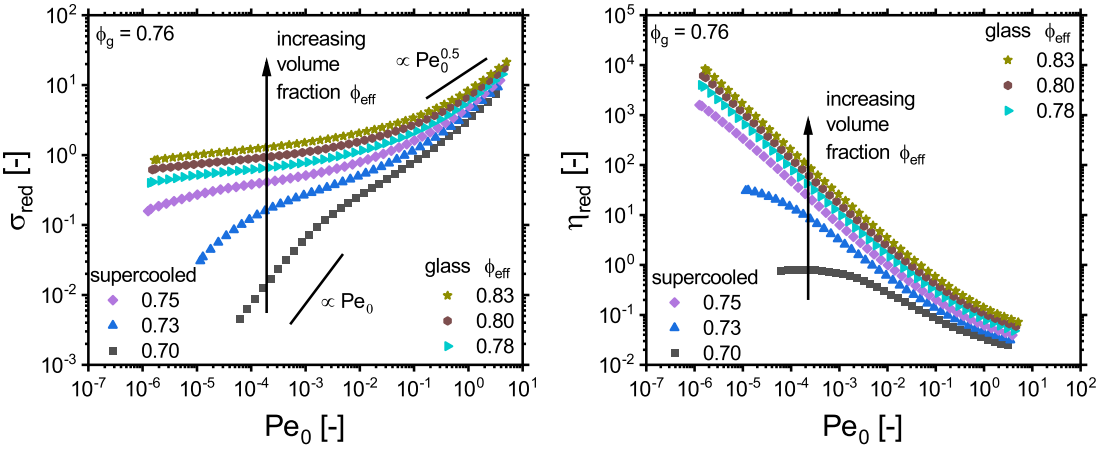

(a) (b)

Figure 6.10: Dependence of **(a)** the reduced stress σ_{red} and **(b)** the reduced viscosity (η_{red}) on the reduced shear rate Pe_0 of the bimodal mixture for ϕ_{eff} above and below ϕ_g. The reduced stress approaches a yield stress plateau for the samples in the glassy state. For the sample with ϕ_{eff} = 0.70, σ_{red} shows a direct proportionality of $\sigma_{red} \propto Pe_0$ at low Pe_0, and respectively the viscosity η is constant.

Further increasing Pe_0 leads to a steeper increase in σ_{red} with approximately $\sigma_{red} \propto Pe_0^{0.5}$ predicted for soft particles and associated to interparticle slippage[138–140]. For increasing ϕ_{eff}, the first Newtonian plateau shifts to lower Pe_0, disappearing from the experimental window for $\phi_{eff} > 0.73$. For samples with a volume fraction of $\phi_{eff} > 0.78$, the reduced stress approaches a constant plateau at low Pe_0. At these volume fractions, the α-relaxation is slowed down to the point where the particles are unable to diffuse out of their cages within the investigation times of $\frac{1}{\dot{\gamma}} = 3\,\text{h}$. The disturbance due to an external stress of at least the same magnitude as this plateau value, which is defined as the yield stress, leads to a flow of the material. This yield stress plateau was encountered first at $\phi_{eff} > 0.78$, close to the experimentally determined glass transition at $\phi_g = 0.76$. For higher Pe_0, the increase in σ_{red} with Pe_0 becomes steeper, showing that the shear thinning becomes less pronounced. These flow curves are similar to other investigations on comparable systems of dense colloidal suspensions below and above the glass transition volume fraction[17,113,141].

6.3.2 Transient Stress

Before reaching the steady state stress, an ordering of the particles in suspension occurs, which can be analyzed using the transient stress. The transient stress of the suspension at the onset of flow is analyzed for $\dot{\gamma} = 1.00 \times 10^{-2}\,\text{s}^{-1}$ and $3.73 \times 10^{-3}\,\text{s}^{-1}$ for different waiting times (t_w) after a preshear of $\dot{\gamma} = 100\,\text{s}^{-1}$ for 2 min at $\phi_{eff} = 0.83$ (see Figures 6.11(a) and 6.11(b)). The material shows an overshoot in the stress, which is the stress needed to initiate the flow of the material at the specific $\dot{\gamma}$. Similar to this stress overshoot behavior under steady shear, G'' shows an overshoot in lage amplitude oscillatory shear measurements as discussed in more detail in Section 7.1.2.

The shear causes an ordering of the particles to a lamellar structure, which facilitates the flow. After this lamellar structure is completely built, a steady state is reached resulting in

a plateau in σ called steady state stress (σ_{st}). This stress is needed to maintain the flow of the material at the specific $\dot{\gamma}$.

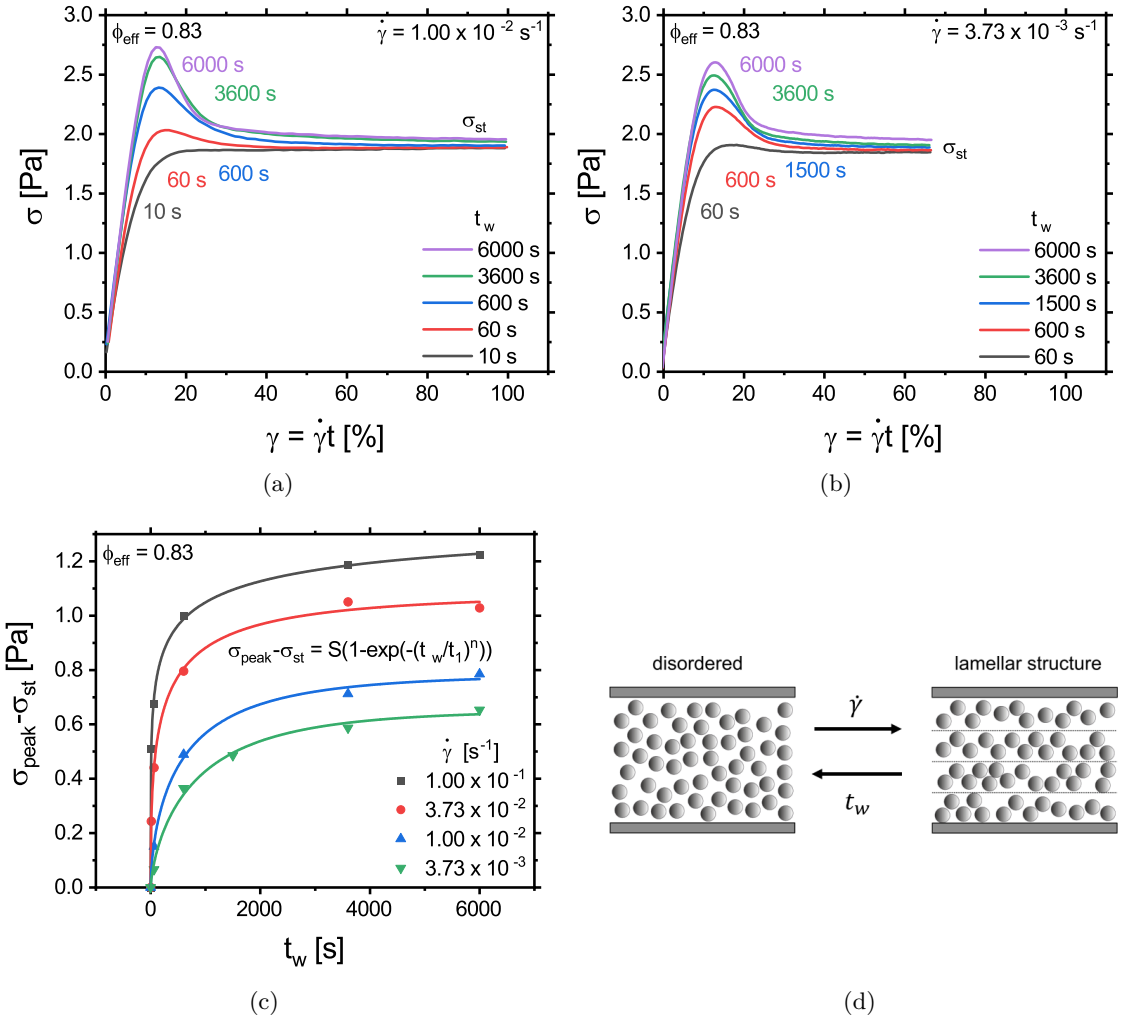

Figure 6.11: Influence of t_w on the transient stress at the onset of steady shear flow for $\phi_{eff} = 0.83$ at **(a)** $\dot{\gamma} = 1.00 \times 10^{-2}\,s^{-1}$, **(b)** $\dot{\gamma} = 3.73 \times 10^{-3}\,s^{-1}$ for $t_w = 10\,s$ to $6000\,s$. **(c)** The relative overshoot of the stress $\sigma_{peak} - \sigma_{st}$ in dependence on t_w showing a saturation. The lines depict the fit of the saturation process with a stretched exponential. **(d)** Scheme of the ordering of the disordered microstructure to a lamellar structure resulting from the steady shear motion and the recovery of the structure due to Brownian motion.

The overshoot stress (σ_{peak}) is increasing with increasing t_w as the rebuilding of the disordered microstructure is progressing with time after preshear. In contrast, the steady state stress remains the same (within the typical uncertainties of the stress obtained from rheological measurements of approx. 10 %) regardless of t_w because the shear induced ordering to the lamellar structure is complete in the steady state, and is therefore independent of the previous state of the sample. The slight increase of about 4 % to 5 % arises from slight differences in the effective volume fraction ($\Delta\phi_{eff} = 0.002$) due to evaporation of the dispersion medium water during the measurements. Note that the evaporation was already considerably slowed down by sealing the gap with silicon oil. The selection of a suitable silicon oil is described in the Appendix in A.3.2.2.

The rebuilding of the disordered microstructure is a relaxation process, which is monitored by the increase of σ_{peak} with t_{w}. The microstructure is completely rebuilt for $t_{\mathrm{w}} \to \infty$, thus σ_{peak} extrapolated to $t_{\mathrm{w}} \to \infty$ is the stress needed to initiate the flow of the material at the specific $\dot{\gamma}$ for the quiescent equilibrated state of the sample and referred to as the plateau of the overshoot stress (σ_{P}) in the following.
As the steady state stress is slightly increasing ($\frac{\Delta\sigma_{\mathrm{st}}}{\sigma_{\mathrm{st}}} \approx 5\,\%$) for increasing t_{w} due to evaporation effects, the dependence of the relative overshoot stress ($\sigma_{\mathrm{peak}} - \sigma_{\mathrm{st}}$) on t_{w} is investigated instead of the dependence of the absolute overshoot stress σ_{peak}.
In Figure 6.11(c) on page 93, the dependence of the relative overshoot stress on t_{w} is shown for $\dot{\gamma} = 1.00 \times 10^{-1}\,\mathrm{s}^{-1}$, $3.73 \times 10^{-2}\,\mathrm{s}^{-1}$, $1.00 \times 10^{-2}\,\mathrm{s}^{-1}$ and $3.73 \times 10^{-3}\,\mathrm{s}^{-1}$. It is saturating for high t_{w}. This saturation process is fitted using a stretched exponential

$$\sigma_{\mathrm{peak}} - \sigma_{\mathrm{st}} = S\left(1 - \exp\left(-\left(\frac{t_{\mathrm{w}}}{t_1}\right)^n\right)\right) \tag{6.9}$$

with the relaxation time (t_1), the stretching exponent (n) and the plateau value of the overshoot stress at high t_{w} ($S = \sigma_{\mathrm{P}} - \sigma_{\mathrm{st}}$). From S, the plateau value of the overshoot stress (σ_{P}) is calculated according to $\sigma_{\mathrm{P}} = S + \sigma_{\mathrm{st}}$. The obtained parameters are depicted in Table 6.3.
The relaxation time and the stretching exponent are strongly dependent on $\dot{\gamma}$ due to the nonlinearity of the shear process and are therefore not only sample specific. The $\sigma_{\mathrm{peak}}(t_{\mathrm{w}} = 6000\,\mathrm{s})$ deviates maximal 5.5 % from the plateau value σ_{P}, which is less than the typical uncertainty of rheological measurements of 10 %. Thus, in the following, the $\sigma_{\mathrm{peak}}(t_{\mathrm{w}} = 6000\,\mathrm{s})$ will be analyzed instead of σ_{P}. Note that for decreasing shear rate the assumption that $\sigma_{\mathrm{peak}}(t_{\mathrm{w}} = 6000\,\mathrm{s}) \approx \sigma_{\mathrm{P}}$ becomes less precise as t_1 increases with decreasing shear rate.

Table 6.3: The fit parameters of the stretched exponential for obtaining the plateau value of the overshoot stress σ_{P}. Additionally, $\sigma_{\mathrm{peak}}(t_{\mathrm{w}} = 6000\,\mathrm{s})$ is depicted, which shows only deviations $< 6\,\%$ from σ_{P}. The relaxation time t_1 and the stretching exponent n are not only sample specific, but highly depend on $\dot{\gamma}$ as the shearing is a nonlinear process.

$\dot{\gamma}$ [s^{-1}]	S [Pa]	σ_{P} [Pa]	$\sigma_{\mathrm{peak}}(t_{\mathrm{w}} = 6000\,\mathrm{s})$ [Pa]	t_1 [s]	n [−]
1.00×10^{-1}	1.36	4.21	4.08	217	0.257
3.73×10^{-2}	1.08	2.73	2.73	284	0.415
1.00×10^{-2}	0.783	2.60	2.52	662	0.615
3.73×10^{-3}	0.652	2.17	2.05	909	0.710

In Figure 6.12(a) the influence of $\dot{\gamma}$ on the transient stress is depicted for $\phi_{\mathrm{eff}} = 0.83$ and 0.80 at $t_{\mathrm{w}} = 6000\,\mathrm{s}$. The overshoot stress and the steady state stress increase for increasing shear rate as initiating and maintaining a flow with higher shear rates requires a higher stress. The difference between the overshoot stress and the steady state stress are decreasing for decreasing shear rate. The stress overshoot is located at $\gamma = 7\,\%$ to 15 % and the steady state stress is reached after $\gamma = 20\,\%$ to 40 %. The particles need to be sheared less than half a particle diameter to reach steady state flow.

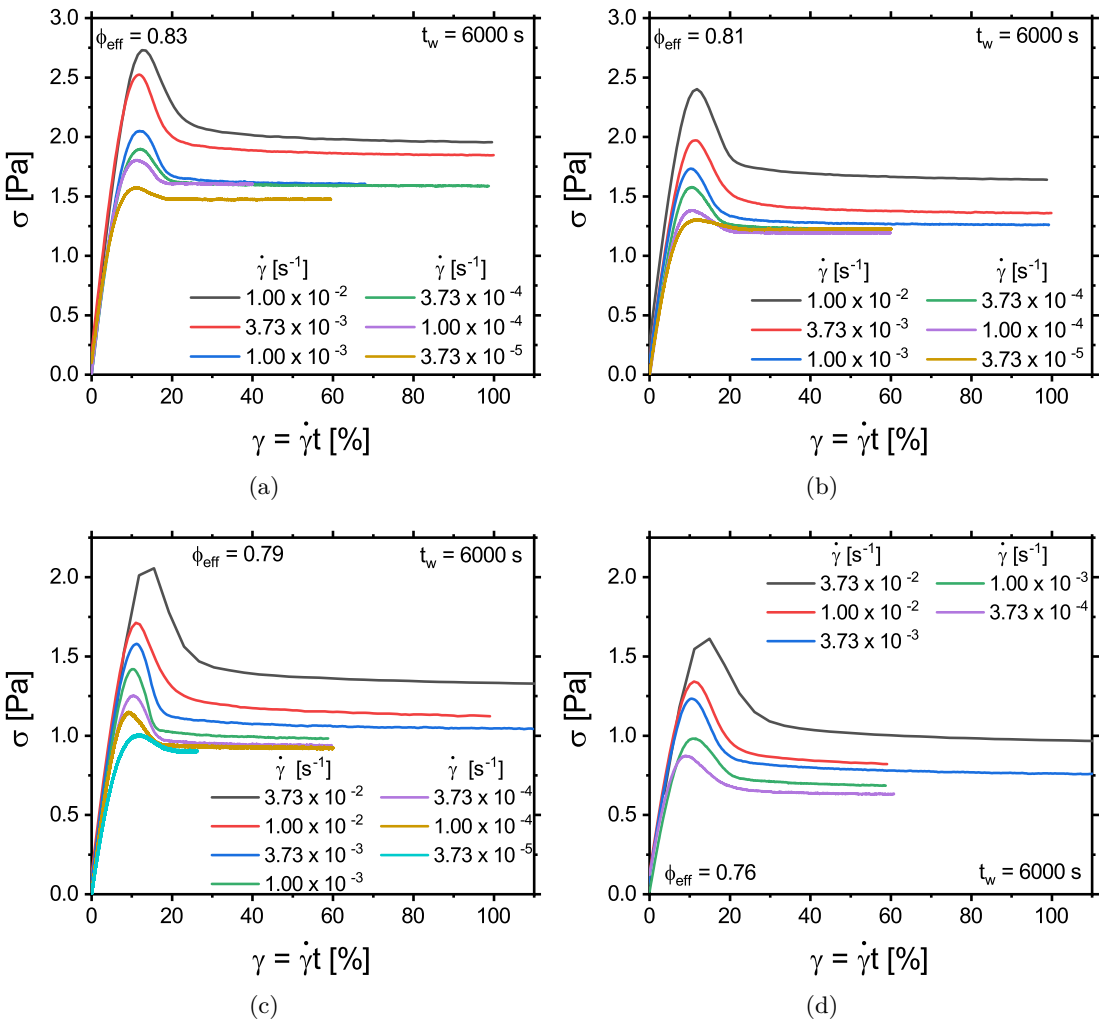

Figure 6.12: Influence of $\dot{\gamma}$ on the transient stress at the onset of steady shear flow for **(a)** $\phi_{\text{eff}} = 0.83$, **(b)** $\phi_{\text{eff}} = 0.81$, **(c)** $\phi_{\text{eff}} = 0.79$ and **(d)** $\phi_{\text{eff}} = 0.76$ for $t_{\text{w}} = 6000\,\text{s}$. The σ_{peak} and σ_{st} decrease for decreasing $\dot{\gamma}$ and decreasing ϕ_{eff}. Furthermore, the difference between σ_{peak} and σ_{st} diminishes with decreasing $\dot{\gamma}$.

Comparison to Flow Curve Measurements

In Figure 6.13, the overshoot stress and the steady state stress from the transient stress measurements are compared to the steady state stress obtained by making a flow curve measurement. For this measurement, the rheometer is only collecting the stress signal in the steady state instead of measuring the transient stress. The transient stress measurements (shown in Figure 6.12) were conducted with a waiting time $t_{\text{w}} = 6000\,\text{s}$ after preshear. The steady state stresses from the transient stress measurements coincide with the steady state stresses of the flow curve measurement for $\dot{\gamma}$ larger than a certain threshold, which is in the range of $3.73 \times 10^{-3}\,\text{s}^{-1}$ to $3.73 \times 10^{-4}\,\text{s}^{-1}$ depending on ϕ_{eff}. Below that, the σ_{st} values obtained from the transient measurement are higher compared to the ones obtained from flow curve measurement. The step time between the different data points in the flow curve measurement is not high enough to reach a strain of $\gamma = 20\,\%$ for the lower shear rates. From this, it can be concluded, that the steady state was not reached in the flow curve measurements although the appropriate measuring conditions were chosen in the software.

Therefore, for the investigation of the dynamic yield stress in Section 6.3.3, the σ_{st} values obtained from the transient measurements are used for $\dot{\gamma} < 1.00 \times 10^{-2}\,\mathrm{s}^{-1}$.

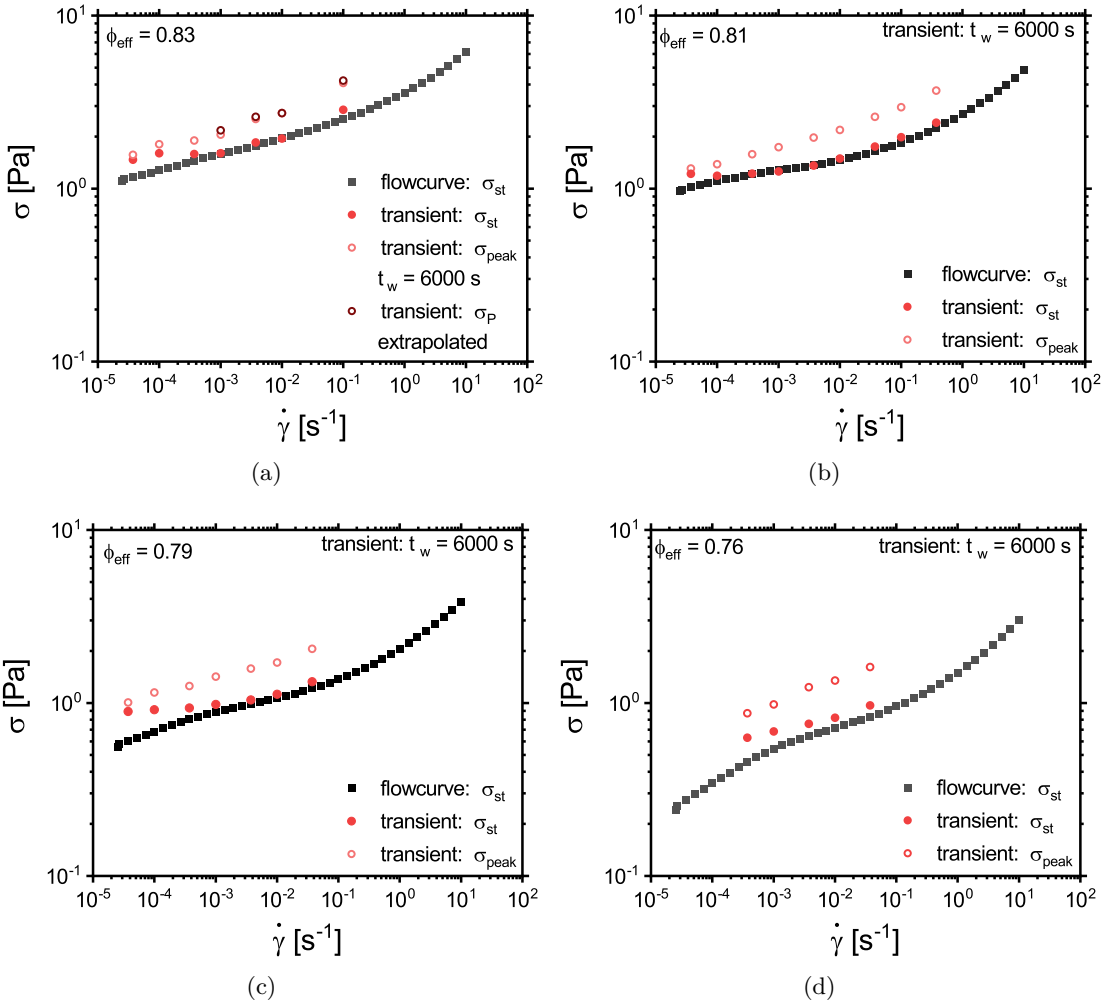

Figure 6.13: Dependence of the different stresses on $\dot{\gamma}$, namely the stress overshoot σ_{peak} obtained from the transient stress measurement for $t_w = 6000\,\mathrm{s}$ after preshear (red open dot), the steady state stress σ_{st} obtained from the transient stress measurement for $t_w = 6000\,\mathrm{s}$ (red closed dot) and the steady state stress σ_{st} obtained from the flow curve measurement (black closed squares) for **(a)** $\phi_{eff} = 0.83$, **(b)** $\phi_{eff} = 0.81$, **(c)** $\phi_{eff} = 0.79$ and **(b)** $\phi_{eff} = 0.76$. In **(a)** the plateau value of the stress at $\sigma_P = \lim_{t_w \to 0} \sigma_{peak}$ is depicted coinciding with σ_{peak} at $t_w = 6000\,\mathrm{s}$. Therefore, for the other $\dot{\gamma}$ and ϕ_{eff} the transient stress measurements (shown in Figure 6.12) were conducted with $t_w = 6000\,\mathrm{s}$ after preshear. The steady state stresses σ_{st} obtained from the transient stress measurements coincide with the steady state stresses obtained from the flow curve measurement for $\dot{\gamma}$ larger than a certain threshold, which depends on ϕ_{eff}. Below that, in the flow curve measurement the steady state was not reached although the appropriate measuring conditions were chosen in the software (for further information see the text). The peak stresses are higher than the steady state stresses, and the difference between σ_{peak} and σ_{st} is decreasing for decreasing shear rate.

The peak stresses are higher than the steady state stresses as the stress required for initiating flow is higher than the stress required for maintaining flow at a certain $\dot{\gamma}$ comparable to static friction and sliding friction in macroscopic materials. The difference between σ_{peak} and σ_{st} is decreasing for decreasing shear rate.

6.3.3 Static and Dynamic Yield Stress

The static and the dynamic yield stress are the minimum stress required to initiate and maintain flow, respectively. Consequently, the static yield stress (σ_{stat}) can be obtained by extrapolating σ_{P} to infinite low shear rates, while the dynamic yield stress (σ_{dyn}) can be obtained by extrapolating σ_{st} to infinite low shear rates. As described earlier, σ_{peak} at a waiting time $t_{\mathrm{w}} = 6000\,\mathrm{s}$ deviates only about 5.5 % from σ_{P}. Therefore, σ_{peak} at $t_{\mathrm{w}} = 6000\,\mathrm{s}$ is used for the analysis of the static yield stress. The σ_{peak} is related to the stress needed to build the lamellar structure of the particles, which leads to the flow of the material.

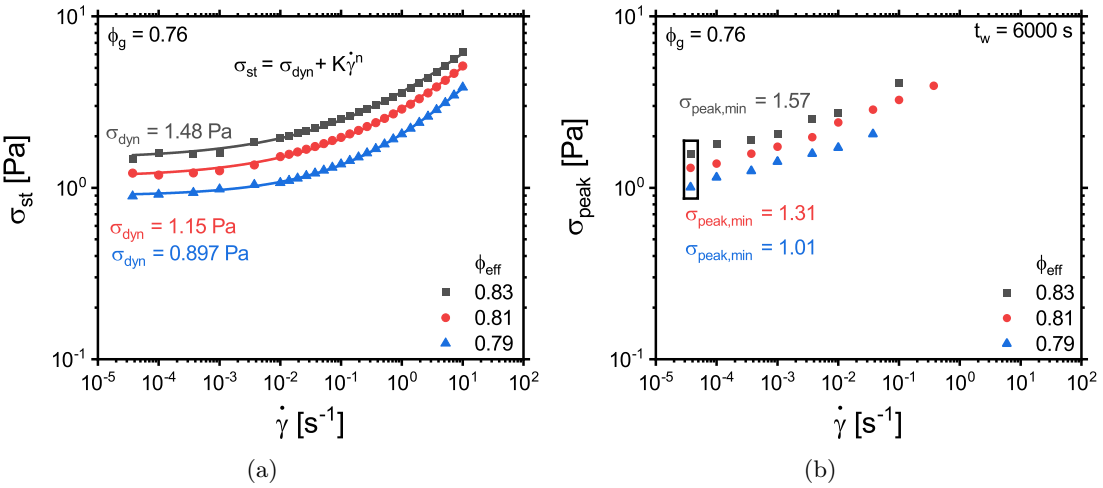

Figure 6.14: Dependence of the **(a)** steady state stress and the **(b)** overshoot stress on the shear rate. In **(a)** the steady state stress is fitted with a Herschel-Bulkley[66] fit to obtain σ_{dyn}. The σ_{peak} does not show a plateau for the measured $\dot{\gamma}$. Therefore, a Herschel-Bulkley fit would underestimate σ_{stat}. Instead, the minimum of the peak value at $\dot{\gamma} = 3.73 \times 10^{-5}\,\mathrm{s}^{-1}$ is used to compare it to steady state stress at this shear rate.

The dynamic yield stress is obtained by extrapolating the steady state stresses (Figure 6.14(a)) to vanishing shear rate by fitting with the Herschel-Bulkley[66] equation

$$\sigma_{\mathrm{st}} = \sigma_{\mathrm{dyn}} + K\dot{\gamma}^{n} \tag{6.10}$$

with the fit parameters K and n. Note that the unit of the parameter K depends on the power law factor n. The fit parameters are depicted in Table 6.4.

Table 6.4: Dynamic yield stress (σ_{dyn}) of the bimodal mixture at different ϕ_{eff} obtained from a Herschel-Bulkley fit and the fit parameters K and n. Note that the unit of the parameter K depends on the power law factor n.

ϕ_{eff} [−]	σ_{dyn} [Pa]	K [Pas^n]	n [−]
0.83	1.48	2.15	0.331
0.81	1.15	1.75	0.349
0.79	0.897	1.16	0.400

The σ_{peak} does not show a plateau within the measured $\dot{\gamma}$ range. Therefore, obtaining σ_{stat} with the Herschel-Bulkley equation would underestimate σ_{stat}. Thus, the minimum of the peak value at $\dot{\gamma} = 3.73 \times 10^{-5}\,s^{-1}$ is compared to the steady state stress at this shear rate, instead of determining a σ_{stat}. The ratio of the $\sigma_{peak,min}$ to the $\sigma_{st,min}$ is ranging from 1.07 to 1.10.

The decreasing difference between σ_{peak} and σ_{st} (seen in Figure 6.13 on page 96) suggests, that they would coincide for infinite low $\dot{\gamma}$, resulting in $\sigma_{stat} = \sigma_{dyn}$. Note that for decreasing shear rate the assumption that $\sigma_{peak,tw=6000s} \approx \sigma_P$ becomes less precise. For $\dot{\gamma} \leq 3.73 \times 10^{-4}\,s^{-1}$, the relaxation time $t_1 > 14\,000\,s$ exceeds the waiting time of $t_w = 6000\,s$ as shown in the Appendix in A.3.2.5 in Figure A.3.12 on page 159. A conclusive statement would therefore require further investigations on a system where the evaporation of the dispersion medium does not limit the measurement time. This would allow measurements with longer waiting times after pre-shearing of the material to ensure complete equilibration of the microstructure in the quiescent state.

In the literature, there is a discrepancy between molecular dynamics simulations expecting $\sigma_{stat} = 1.2\sigma_{dyn}$ for colloidal glasses[142], and experiments, which could not detect a difference in the yield stresses for similar systems[28] as investigated within this work. More recent findings show that there is no difference in the static and the dynamic yield stress of simple yield stress fluids[143,144].

Table 6.5: Dynamic yield stress of the bimodal mixture at different ϕ_{eff} obtained with a Herschel-Bulkley fit. The static yield stress cannot be determined as the measurable $\dot{\gamma}$ is not sufficiently small to reach a plateau in σ_{peak}. Therefore, the ratio of the minimum of σ_{peak} to the minimum in σ_{st}, which are both at the same $\dot{\gamma}$ of $3.73 \times 10^{-5}\,s^{-1}$, is depicted instead.

ϕ_{eff} [−]	σ_{dyn} [Pa]	$\sigma_{peak,min}$[Pa]	$\frac{\sigma_{peak,min}}{\sigma_{st,min}}$[−]
0.83	1.48	1.57	1.07
0.81	1.15	1.31	1.07
0.79	0.897	1.01	1.10

6.4 Influence of Steady Shear on the Relaxation Times

Above ϕ_g, the colloidal suspensions show a solid-like behavior under rest, as shown in Figure 6.3 on page 80. The α-relaxation time of the particles exceeds the investigation time, causing the particles to be trapped in their cages for this time. The particles are immobilized, wherefore the flow of the material is hindered.

The application of a stress, which is higher than the yield stress, or of a constant shear rate leads to a flow of the material, as described in Section 6.3. This yielding occurs, because the shear favors the relaxation of the particles, resulting in a change of the relaxation times. To test how the steady shear motion affects the relaxation times of colloids in the suspension, an oscillatory shear with a strain amplitude in the sample's linear regime is superimposed on the steady shear motion. The resulting time dependent shear rate is shown in Equation 6.11.

$$\dot{\gamma}(t) = \dot{\gamma}_c + \gamma_0 \omega_1 \cos(\omega_1 t) \tag{6.11}$$

$\dot{\gamma}_c$ is the constant shear rate applied to yield the material, while the second term is the oscillatory shear motion applied to test the rheological behavior and relaxation times of the material.

The resulting G' and G'' in dependence on ω_1 are shown exemplary in Figures 6.15(a) and 6.15(b) for $\phi_{\text{eff}} = 0.86$ and 0.73 without steady shear (black squares) and with a constant shear rate of $5 \times 10^{-3}\,\text{s}^{-1}$ to $5\,\text{s}^{-1}$. The measurements are conducted on the bimodal mixture with a mass fraction of $w = 8.62\,\text{wt}\%$. For different ϕ_{eff}, the same shear rate results in different Pe_0 because ϕ_{eff} is varied by changing T and respective R_{H} of the particles. The corresponding measurement temperatures and normalization constants are depicted in the Appendix in A.3.2.1 in Table A3.

G'' shows the power law slope of 1 consistent with Brownian dynamic simulations[109], which predict Maxwell type terminal flow of sheared colloidal suspensions (see Figures 6.15(a) and 6.15(b)). G' shows a power law increase with a higher slope than 2 and negative values typical for the parallel superposition elastic modulus and already found in the first experimental analysis of parallel superposition moduli G' and G'' in 1966 in Booij[145]. Later the high slope and the negative values could be predicted theoretically[146] and could be attributed to the coupling of the steady and the oscillatory shear motion.

The crossover point between G' and G'' correlated to the α-relaxation time (τ_α) and the minimum in $\tan(\delta)$ correlated to the transition of the α- to the β-relaxation process (t_{min}) shift to higher ω_1 for increasing shear rates.

The α-relaxation time τ_α and the characteristic time t_{min} normalized to the relaxation time in dilution τ_0 for the different ϕ_{eff} are depicted in Figure 6.15(c) in dependence on Pe_0. The normalized α-relaxation time $\frac{1}{Pe_\omega(G'=G'')} = \frac{\tau_\alpha}{\tau_0}$ is inverse proportional to Pe_0, while $\frac{t_{\text{min}}}{\tau_0}$ shows a power law dependence on with $\frac{t_{\text{min}}}{\tau_0} \propto Pe_0^{-0.55}$. The direct proportionality of $\frac{\tau_\alpha}{\tau_0}$ on Pe_0 shows that the microscopic mechanism of flow is a convective cage release[109] and is in line with confocal microscopy experiments[147] and MCT predictions[13,26,97]. A comparison between the experimental results and the predictions obtained with the new MCT approach used in this work is provided in the following section.

Interestingly, the normalized α-relaxation time is superimposing for all measured ϕ_{eff} in the supercooled regime below and in the glassy regime above $\phi_{\text{g}} = 0.76$. The normalized out-of-cage relaxation time is independent of ϕ_{eff} in a sheared system in the supercooled as well as in the glassy state. This is in agreement with the work of Jacob *et al.*[109], who observed this indenpendence in the glassy state for distinct $\dot{\gamma}$ values. They interpret that the α-relaxation time is not changing with ϕ_{eff} in the glassy state. Since it was found in this work that even in the supercooled regime the normalized α-relaxation time is superimposing, where in the quiescent state the crossover angular frequency is accessible experimentally and depends on ϕ_{eff}, it can be concluded, that the independence of ϕ_{eff} holds only for a sheared system. No conclusions about the quiescent state can be drawn from the sheared state.

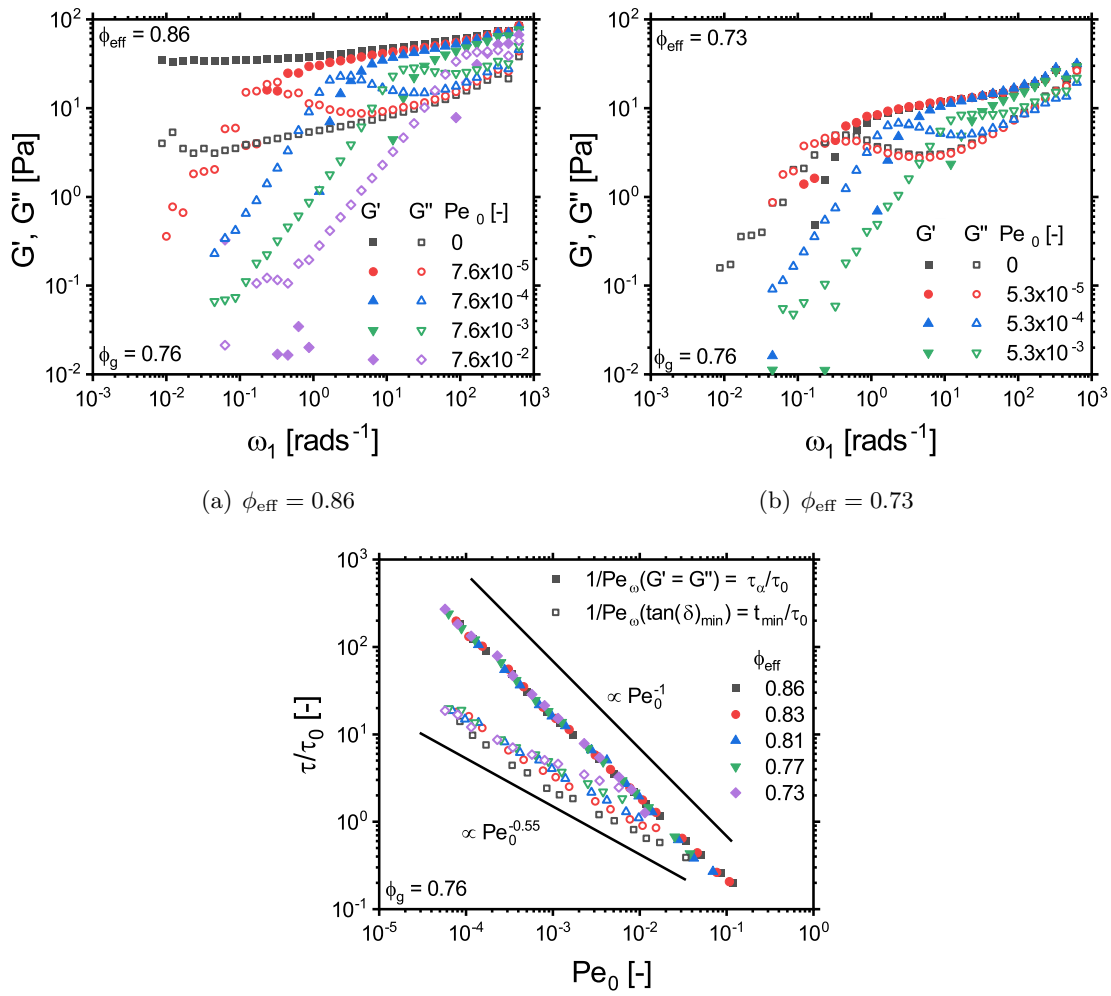

(a) $\phi_{\text{eff}} = 0.86$

(b) $\phi_{\text{eff}} = 0.73$

(c) normalized relaxation times

Figure 6.15: Influence of a steady shear excitation with $\dot{\gamma} = 5 \times 10^{-3}\,\text{s}^{-1}$ to $5\,\text{s}^{-1}$ on the linear rheological response of the colloidal suspension measured at $w = 8.62\,\text{wt\%}$ at **(a)** $\phi_{\text{eff}} = 0.86$ and **(b)** $\phi_{\text{eff}} = 0.73$. As the effective volume fraction of the sample was varied by adjusting R_{H} by changing T, the same $\dot{\gamma}$ results in different Pe_0 values for the different ϕ_{eff}. **(c)** Influence of the steady shear motion on the normalized relaxation times finding $\frac{\tau_\alpha}{\tau_0} \propto Pe_\omega^{-1}$ and $\frac{t_{\text{min}}}{\tau_0} \propto Pe_\omega^{-0.55}$. Interestingly, the normalized α-relaxation times superimpose for all measured ϕ_{eff} in the supercooled and the glassy regime. The out-of-cage relaxation time in a sheared system does not depend on the effective volume fraction.

6.4.1 Comparison to Mode Coupling Theory Predictions

The approach used for the MCT predictions of the linear response of the colloidal suspensions in a state, where the system is perturbed due to a nonlinear steady shear motion, combines the ISHSM model described in Section 4.4.3 and the linear response theory described in Section 4.4.2. The moduli are calculated according to the same equations as in linear response, but with a more complex memory function as the nonlinear steady shear motion is introduced via the memory function, thus $C_{xyxy}^{(\sigma)}(\vec{q}, t - t')$ becomes a function of the shear rate $C_{xyxy}^{(\sigma)}(\vec{q}, t - t', \dot{\gamma}_{\text{c}})$. The memory function is derived from the ISHSM model. The influence of a steady shear motion in a Pe_0 range of 7.70×10^{-8} to 3.68×10^{-1} on the moduli predicted by this approach is depicted exemplary for $\epsilon = 1.55 \times 10^{-5}$ in

Figure 6.16(a). The MCT predictions shows a similar influence of the shear rate on the moduli as the experiments. The crossover of G'_{red} and G''_{red} and the minimum in G''_{red} shift to higher Pe_ω. The material is liquified due to the steady shear motion. In contrast to the experimental results, in the MCT calculations the minimum in G''_{red} becomes sharper and G'_{red} shows an overshoot for high Pe_0.

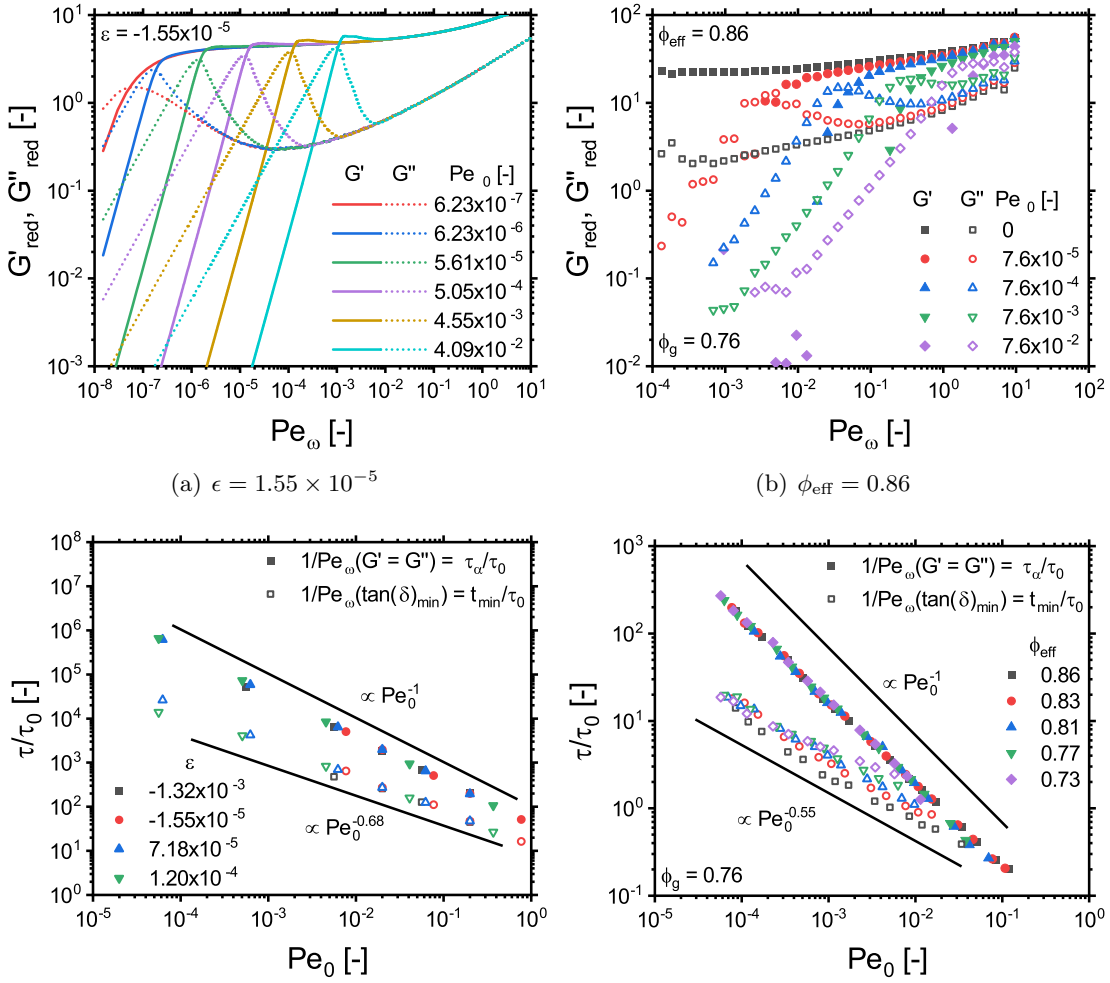

(a) $\epsilon = 1.55 \times 10^{-5}$

(b) $\phi_{\mathrm{eff}} = 0.86$

(c) normalized relaxation times MCT

(d) normalized relaxation times experiment

Figure 6.16: Influence of a steady shear excitation on the linear rheological response of the colloidal suspension **(a)** predicted by MCT and **(b)** obtained from rheological experiments. Both, experiment and MCT show a liquidification of the colloidal suspension. The influence of Pe_0 on the normalized relaxation times $\frac{\tau_\alpha}{\tau_0}$ and $\frac{t_{\mathrm{min}}}{\tau_0}$ are depicted for **(c)** the MCT predictions and **(d)** the experiments obtained from the crossover point and the minimum in $\tan(\delta)_{\mathrm{min}}$ in **(a)** and **(b)** and spectra at other ϵ and ϕ_{eff} not shown here. The normalized α-relaxation time shows the same power law dependence in theory and experiment $\frac{\tau_\alpha}{\tau_0} \propto Pe_\omega^{-1}$, whereas the exponent of the normalized characteristic time $\frac{t_{\mathrm{min}}}{\tau_0} \propto Pe_\omega^{-d}$ is $d = 0.68$ in theory and $d = 0.55$ in the experiment. Be aware of the different x- and y-scalings.

The Pe_ω at the crossover and at the minimum of $\tan(\delta)$ depicts the characteristic timescales of the colloidal suspension normalized to the timescale of diffusion under high dilution. The normalized α-relaxation time shows an antiproportionality to Pe_0 as $\frac{\tau_\alpha}{\tau_0} \propto Pe_\omega^{-1}$ consistent with the experiment, whereas the scaling law for the characteristic time t_{min} obtained from

theory shows $\frac{t_{\min}}{\tau_0} \propto Pe_\omega^d$ with $d = -0.68$, while in experiments a power law dependence with $d = -0.55$ was found.
The MCT predictions show the independence of the normalized relaxation times on the effective volume fraction in the supercooled and the glassy state in the sheared systems as found in the experiments. This supports the findings, that no conclusions about the quiescent state can be drawn from the sheared state.

6.5 Summary

This chapter provided the rheological characterization of the bimodal mixture used as a model system for glass-forming colloidal suspensions under linear oscillatory shear and under steady shear and comparison of the rheological results to MCT predictions. The rheological investigations include the characterization of the relaxation times in the quiescent state and their dependence on the effective volume fraction, an estimation of the hardness of the interaction potential of the particles, the yielding behavior under steady shear including the transient behavior at the onset of flow, and the influence of steady shear on the relaxation times of the system.
The effective volume fraction of the system was determined by investigating the relative zero-shear viscosity of a series of suspensions with different mass fractions at 20 °C, see Figure 6.1 on page 76. By fitting the obtained results with the Krieger-Dougherty equation[87] the proportionality factor of $k\,(20\,^\circ\mathrm{C}) = 0.08462$ between w and ϕ_{eff} was determined. This scaling factor was used to derive $\phi_{\mathrm{eff}}(20\,^\circ\mathrm{C})$ of a sample with a chosen mass fraction. The ϕ_{eff} for further T was determined by rescaling $\phi_{\mathrm{eff}}(20\,^\circ\mathrm{C})$ with $R_{\mathrm{H}}(T)$ derived from DLS measurements. Furthermore, the normalization factors are calculated from this R_{H}. These normalization factors are needed to scale the moduli and stresses to the characteristic energy scale of the particles and the shear rate and angular frequency to the characteristic time scale of the particles. This normalization is required for the comparison of the rheological results of particles of different sizes as well as for the comparison to theoretical predictions. The glass transition volume fraction $\phi_{\mathrm{g}} = 0.76$ was determined from the mechanical behavior of the sample, see Figure 6.2 on page 79. It was defined to be at the ϕ_{eff}, where no decrease of G' from its plateau value was observed within the investigation time of $\frac{1}{\omega_1} \approx 3\,\mathrm{h}$.
To investigate the principle equilibrium rheological behaviour, SAOS experiments were conducted, see Figure 6.3 on page 80. In the quiescent state, in the glassy regime, the colloidal suspensions exhibit solid-like behavior for the whole investigated angular frequency region of $10^{-4}\,\mathrm{rad\,s^{-1}}$ to $10^{2}\,\mathrm{rad\,s^{-1}}$ with $G'_{\mathrm{P}} \approx 15\,\mathrm{Pa}$ to $26\,\mathrm{Pa}$ and $G'_{\mathrm{red,P}} \approx 9$ to 18 depending on ϕ_{eff}. In the supercooled regime, the suspension exhibits solid-like behavior at high Pe_ω and liquid-like behavior at low Pe_ω. The Pe_ω at which this transition from solid-like to liquid-like behavior occurs depends on the effective volume fraction. This behavior in the glassy and the supercooled regime is typical for colloidal glasses[7,17,74,75,113] and confirms the suitability of the model system for investigating the rheological behavior of colloidal glasses.

The normalized time scale of the α-relaxation ($\frac{\tau_\alpha}{\tau_0}$) and of the transition from the α-relaxation to the β-relaxation ($\frac{t_{\min}}{\tau_0}$) show a strong dependence on ϕ_{eff} with $\frac{\tau_\alpha}{\tau_0} \propto \phi_{\text{eff}}^m$ with $m \approx 124 \pm 7$ and of $\frac{t_{\min}}{\tau_0} \propto \phi_{\text{eff}}^n$ with $n \approx 44.7 \pm 3.8$, see Figure 6.4 on page 82).
The MCT predictions of the linear response modulus G'_{red} of the glass-forming colloidal suspension is in agreement with the experiment both in the supercooled and in the glassy state, see Figure 6.5 on page 84. However, G''_{red} is only matched sufficiently in the supercooled region with a certain distance to the glass transition volume fraction. Close to the glass transition volume fraction of 0.76 at $\phi_{\text{eff}} = 0.75$ the experimentally determined G''_{red} shows a smoother transition from the maximum to the minimum in G''_{red}. This is due to the broadening of the α-relaxation time distribution for particles of different sizes resulting from the heterogeneities in structure arising close to ϕ_{g} and due to the softness of the particles. Both cannot be depicted by MCT as the predictions are based on monodisperse hard sphere particles, which all exhibit the same α-relaxation time. In the glassy state in the low Pe_ω regime, the MCT predictions of G''_{red} do not agree with the experimental results as in MCT predictions the α-relaxation of the colloids vanishes completely in the glassy state, while it only slows down considerably in the real system.
To match the amplitude of G'_{red} and G''_{red} of the MCT predictions to the experiment, the moduli derived from theory have to be multiplied by a fudge parameter as known from literature[17,113]. This arises from the increase in G'_{red} and G''_{red} in experiment, which is not predicted by the MCT calculations. This increase directly arises from the interaction potential of the particles. The power law increase of $G'_{\text{red}} \propto \phi_{\text{eff}}^m$ with $m \approx 13.6$ in the supercooled and $m \approx 7.6$ in the glassy regime, see Figure 6.6 on page 86, is used to derive an approximation of the hardness of the interaction potential of the particles. The core-shell particles have an interaction potential closer to the interaction potential of PMMA hard sphere particles than to the one of ultra-soft star-like micelles[20,108], see Figure 6.7 on page 88.
The new MCT approach takes into consideration the q-dependence of the autocorrelation of density fluctuations in glass-forming colloids. It predicts an unexpected q-dependence of the moduli in the linear regime on ϕ_{eff} close to ϕ_{g}, see Figure 6.8 on page 89. Experiments with varying plate diameters result in the same dependence of the moduli on the plate diameter as derived from theory for the q-dependence, see Figure 6.9 on page 90. This dependence may arise from long-range stress correlations, which are present in supercooled colloidal suspensions close to the glass transition volume fraction and depend on the boundaries of the system.
Moreover, the yielding behavior under steady shear was investigated. The overshoot in the transient stress at $\gamma \approx 7\,\%$ to $15\,\%$ can be attributed to the formation of a lamellar microstructure which increases the flowability of the system. When the lamellar microstructure is completely build, a steady state stress is reached, which is at total strains of $\gamma \approx 20\,\%$ to $40\,\%$. The amplitude of the overshoot stress σ_{peak} and the steady state stress σ_{st} depend on the shear rate and the ϕ_{eff}. For the measurements parameter ranging from $\dot{\gamma} = 2 \times 10^{-5}\,\text{s}^{-1}$ to $10\,\text{s}^{-1}$ and $\phi_{\text{eff}} = 0.76$ to 0.83, they are between σ_{peak} $\approx 9 \times 10^{-1}\,\text{Pa}$ to $4\,\text{Pa}$ and $\sigma_{\text{st}} \approx 6 \times 10^{-1}\,\text{Pa}$ to $3\,\text{Pa}$, see Figure 6.12 on page 95. The

overshoot stress depends on the waiting time after the preshear of the material as the rebuilding of the disorder microstructure from the lamellar structure is not immediate, see Figure 6.11 on page 93. The relaxation time t_1 obtained from fitting the relative stress overshoot in dependence on the waiting time is not only sample specific, but increases with decreasing shear rate.

The dynamic yield stress obtained from a Herschel-Bulkley fit of the steady state stress increases from 0.90 Pa to 1.48 Pa with increasing ϕ_{eff} from 0.79 to 0.83, see Figure 6.14 on page 97. The static yield stress could not be obtained as the accessible shear rate range was restricted. The decreasing difference between the overshoot stress and the steady state stress with decreasing $\dot{\gamma}$, see Figure 6.13 on page 96, suggests that $\sigma_{\text{dyn}} = \sigma_{\text{stat}}$. However, this evidence is not conclusive as the assumption that $\sigma_{\text{peak,tw=6000s}} = \sigma_{\text{P}}$ was made, which becomes less accurate for lower shear rates as t_1 increases for decreasing shear rate, see Table 6.3 on page 94.

Finally, the influence of a steady shear motion on the relaxation times was investigated by applying parallel superposition of steady and oscillatory shear. The steady shear motion leads to a liquidification of both the glassy and the supercooled state, see Figure 6.15 on page 100. A direct antiproportionality of the normalized α-relaxation time on the normalized shear rate of $\frac{\tau_\alpha}{\tau_0} \propto Pe_0^{-1}$ was found in both experiment and MCT predictions. Additionally, the normalized characteristic time of the transition from α- to β-relaxation shows a power law decrease of $\frac{t_{\min}}{\tau_0} \propto Pe_\omega^{-d}$ with $d = 0.55$ in experiment and $d = 0.68$ in the MCT predictions. Experiment and MCT predictions both show an independence of the α-relaxation time and the characteristic time on ϕ_{eff} for a sheared sample in the supercooled as well as in the glassy state, see Figure 6.16 on page 101. This is in agreement with the work of Jacob *et al.*[109], who observed this indenpendence in the glassy state for distinct $\dot{\gamma}$ values. In contrast to their interpretations, from the experiments conducted within this work it is concluded that the independence of ϕ_{eff} holds only for a sheared system. No conclusions about the quiescent state can be drawn from the sheared state.

7 Medium and Large Amplitude Oscillatory Shear Investigations

In this Chapter, the rheological response of the bimodal glass-forming colloidal model system to a nonlinear oscillatory shear excitation is investigated and compared to mode coupling theory (MCT) predictions. First, the strain amplitude dependence of the moduli and the relative intensity of the third harmonic, used as a quantification of the anharmonicity of the suspension are investigated in the glassy and the supercooled state. Additionally, the onset of local and macroscopic yielding is analyzed. Moreover, the frequency dependence of the intrinsic anharmonicity parameter is investigated in the glassy and the supercooled state and compared to MCT predictions kindly provided by Leonhard Lang from the university of Konstanz and from literature[29].

The content of this Chapter and the corresponding sections in the Appendix have been published in the Journal of Rheology from the American Institute of Physics (AIP)[120] and have been adapted with permission. Lea Fischer is the first author of this article.

The focus of this chapter is to answer a question raised by a previous comparison of Fourier transform (FT) rheological results to mode coupling theory (MCT)[29]. There, the strong growth of the third harmonic response when approaching the glass transition was observed in large amplitude oscillatory shear (LAOS) measurements, while theory even predicts its divergence[29]. The behavior in the glass state was neither addressed in the experiments nor in the MCT predictions. Additionally, only the high frequency scaling in the supercooled state could be verified, while the scaling in the low and medium frequency regime could neither be confirmed nor disproven. To fill this gap, in this thesis the strain amplitude and frequency dependence of the anharmonicity of the response of the colloidal model system in the supercooled and in the glassy state are extensively investigated.

7.1 Strain Amplitude Dependence of the Nonlinear Response

In this section, the strain amplitude dependence of the nonlinear and anharmonic response in the supercooled and in the glassy state is investigated. The strain amplitude (γ_0) dependence of the storage modulus (G'), the loss modulus (G'') and the relative intensity of the third harmonic ($I_{3/1}$) are depicted in Figure 7.1 at two different effective volume fraction (ϕ_{eff}) in the supercooled regime $\phi_{\text{eff}} < \phi_{\text{g}}$. In Figure 7.3 on page 108 the same is shown at two ϕ_{eff} in the glassy regime. Additionally, the linear rheological response at the distinct ϕ_{eff} are depicted.

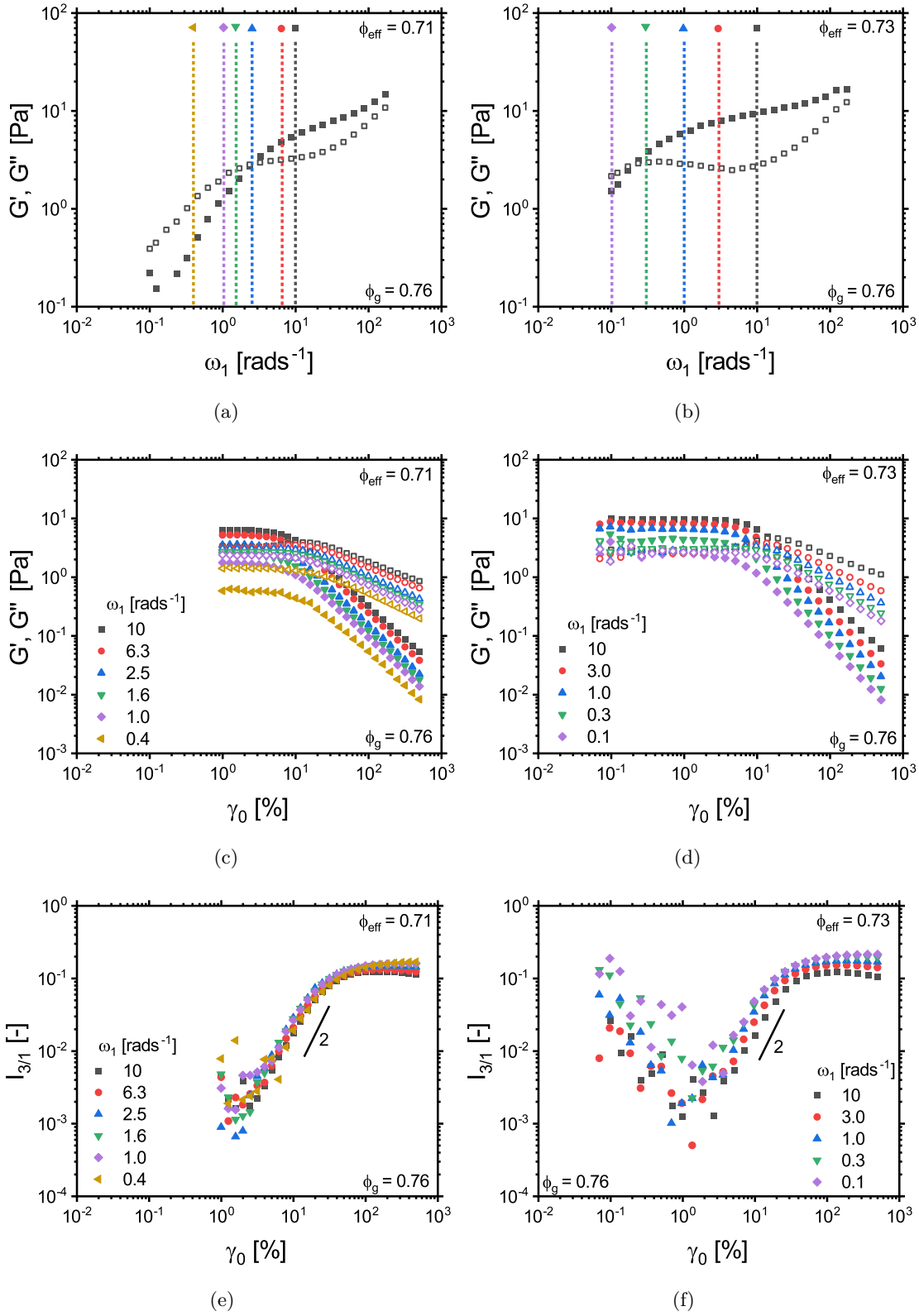

Figure 7.1: Dependence of G' and G'' on the angular frequency in the linear regime of the samples **(a)** and **(b)**, G' and G'' in dependence on the amplitude ranging from the linear to the nonlinear regime **(c)** and **(d)**, and $I_{3/1}$ as a function of the strain amplitude **(e)** and **(f)** from the same strain sweeps at two different volume fractions in the supercooled region of the sample ($\phi_{\text{eff}}<\phi_{\text{g}}$). $I_{3/1}$ shows the proportionality of γ_0^2 in the asymptotic regime. The colored vertical lines and symbols in **(a)** and **(b)** indicate the ω_1 at which G', G'' and $I_{3/1}$ were measured.

7.1.1 Third Order Anharmonic Response

For all investigated volume fractions in both the glassy and the supercooled regime, $I_{3/1}$ shows a monotonic increase with the strain amplitude. The predicted proportionality $I_{3/1} \propto \gamma_0^2$ (see Equation 3.36 on page 31) is observed for medium strain amplitudes. This region is defined as the scaling region or medium amplitude oscillatory shear (MAOS) regime and is followed by a leveling off to a plateau value.

For the lowest investigated ϕ_{eff} of 0.71, most of the investigated angular frequency are intentionally chosen to be in the range where the sample shows predominantly viscous behavior. For these ω_1, the strain amplitude of the onset of anharmonicities (defined by extrapolation of the scaling region of $I_{3/1} \propto \gamma_0^2$ to 0.5 %) decreases from $\gamma_0 = 5.2\,\%$ to 4.1 % as ω_1 increases from $0.4\,\text{rad}\,\text{s}^{-1}$ to $1.6\,\text{rad}\,\text{s}^{-1}$, because the maximum shear rate attained during an oscillation cycle increases for increasing ω_1. The maximum shear rate is equal to the product of the strain amplitude and the angular frequency $\dot{\gamma}_{\text{max}} = \gamma_0\omega_1$. The anharmonicity levels off to a plateau value of $I_{3/1} = 11\,\%$ to 16 % depending on ω_1 (see Figure 7.2). This decrease of $I_{3/1}$ from the plateau value in the LAOS regime is seen for the other three volume fractions as well and is in agreement with model predictions[75] and experimental findings on a similar system. It can be rationalized by the transformation of the sample from a viscoelastic solid to a viscoelastic liquid at the yielding point[108].

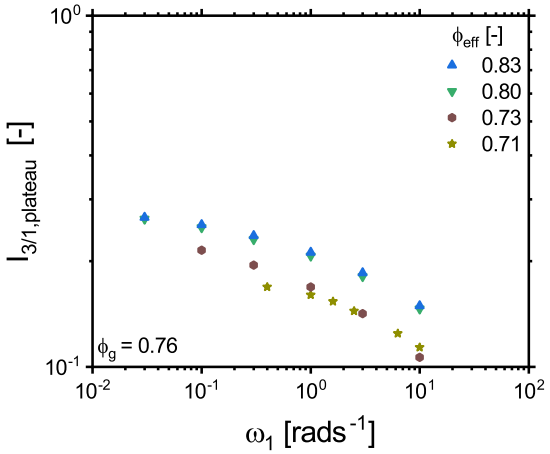

Figure 7.2: Dependence of the plateau values of $I_{3/1}$ on ω_1 for different ϕ_{eff} in the supercooled and the glassy regime obtained from the data shown in Figures 7.1(e), 7.1(f), 7.3(e) and 7.3(f). The plateau value decreases for increasing ω_1 and for decreasing ϕ_{eff}.

The plateau value of $I_{3/1}$ is higher for the glassy samples (e.g., around 21 % for $\omega_1 = 1\,\text{rad}\,\text{s}^{-1}$) than for the samples in the supercooled regime (e.g., around 16 % for $\omega_1 = 1\,\text{rad}\,\text{s}^{-1}$). The findings of the soft core-shell systems are in agreement with the findings of Poulos *et al.*[21] on ultra-soft star-like micelles. It differs from the behavior of hard sphere glasses, where the plateau value and the general course of $I_{3/1}$ show a stronger dependence on the frequency as seen in Fig. 5 of Poulos *et al.*[21], where the decrease of the plateau value of $I_{3/1}$ is present at low volume fractions for the samples in the supercooled regime and becomes even more pronounced for glassy samples. Additionally, the glassy sample in Fig. 5 of Poulos *et al.*[21] displays a peak in $I_{3/1}$, which has been attributed to the phenomenon of two-step yielding that is observed in hard sphere glasses[20,21].

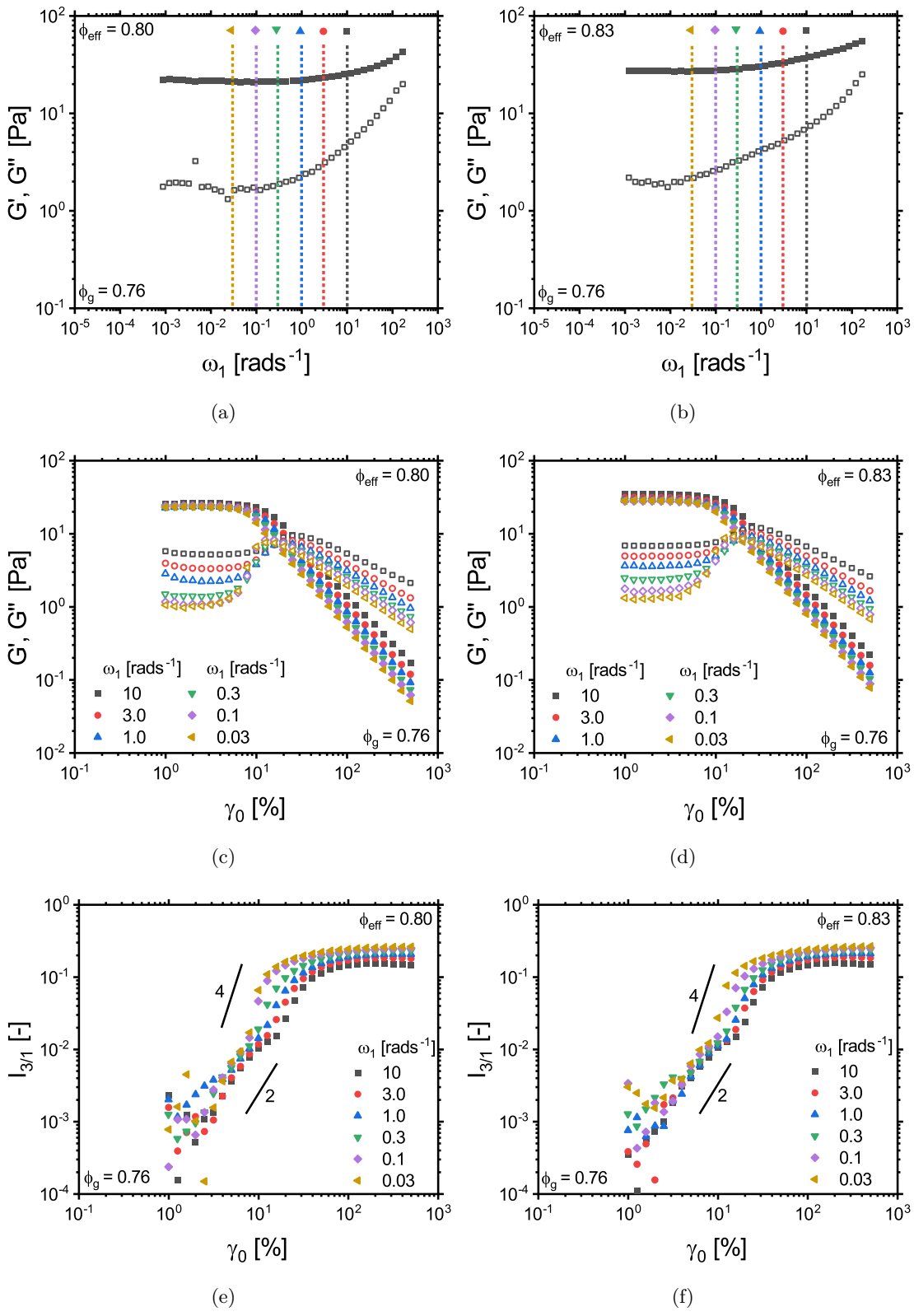

Figure 7.3: Dependence of G' and G'' on the angular frequency in the linear regime of the samples **(a)** and **(b)**, G' and G'' in dependence on the amplitude ranging from the linear to the nonlinear regime **(c)** and **(d)**, and $I_{3/1}$ as a function of the strain amplitude **(e)** and **(f)** from the same strain sweeps at two different volume fractions in the solid-like region ($\phi_{\text{eff}} > \phi_{\text{g}}$). $I_{3/1}$ shows a quadratic increase with γ_0, which changes to a scaling of $I_{3/1} \propto \gamma_0^4$ at $\gamma_0 \approx 10\,\%$ to $15\,\%$. For further information, see the main text. The colored vertical lines and symbols in **(a)** and **(b)** indicate the angular frequencies at which G', G'' and $I_{3/1}$ were measured.

For the other three volume fractions, the investigated frequencies are chosen to be in the range where the sample exhibits predominantly elastic behavior (see Figures 7.1(b), 7.3(a) and 7.3(b) on page 106 and 108). Here, the onset of anharmonicities (defined by extrapolation of the scaling region of $I_{3/1} \propto \gamma_0^2$ to 0.5 %) shifts to slightly lower γ_0 as ω_1 decreases (e.g., for $\phi_{\text{eff}} = 0.73$ from $\gamma_0 = 5.0\,\%$ to 2.7 % for decreasing ω_1 from 10 rad s^{-1} to 0.1 rad s^{-1}), similar to the decrease of the yield strain (γ_y) with decreasing ω_1. This will be discussed in Section 7.1.3. For the two samples in the glassy regime (Figure 7.3), the scaling is first $I_{3/1} \propto \gamma_0^2$, but changes to a scaling of $I_{3/1} \propto \gamma_0^4$ shortly before reaching the plateau for the two lowest angular frequencies. This transition falls in a similar range as the yield strain (see the following section) and the stress overshoot observed at the onset of flow in steady shear measurements as discussed in more detail in Section 6.3.2. This behavior is also observed in polymeric glasses, when the sample deforms plastically and the deformation of the sample becomes localized*. In the colloidal glass, this transition point shifts to lower strain amplitudes for decreasing angular frequencies.

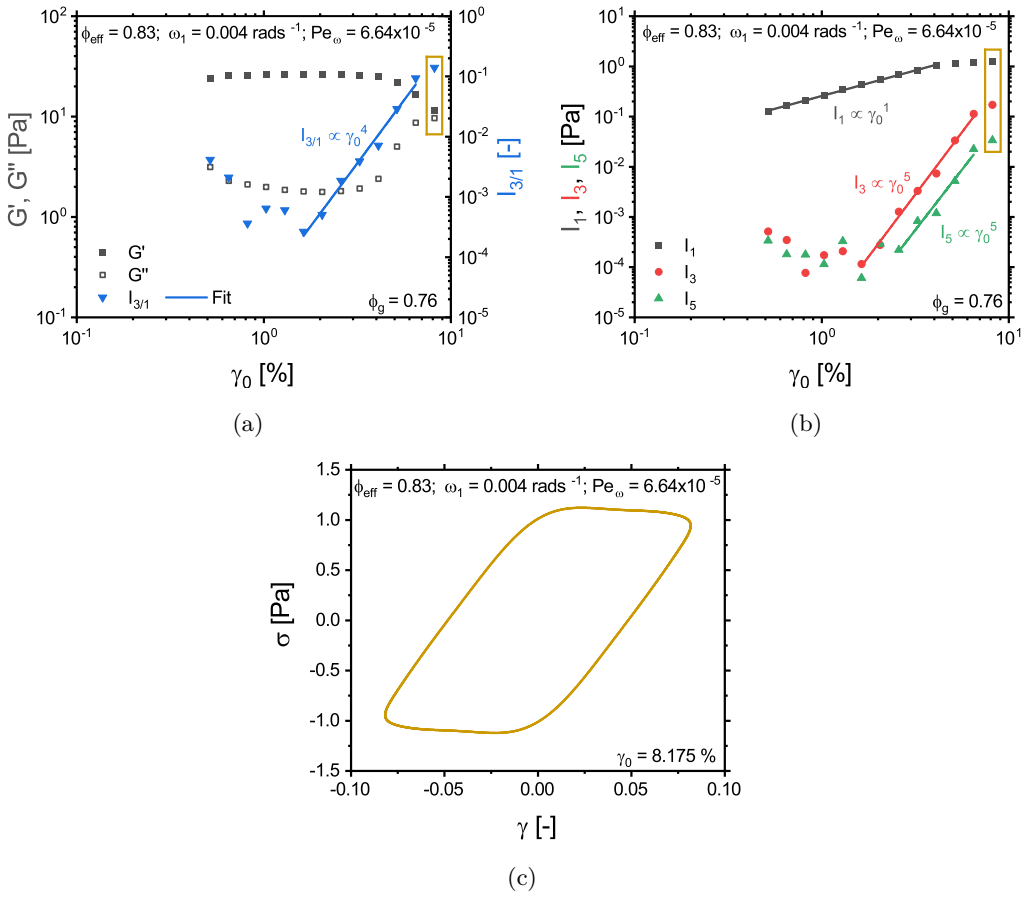

Figure 7.4: **(a)** The strain amplitude dependence of G', G'' (left axis) and $I_{3/1}$ (right axis) for a glassy sample at low ω_1 showing an unexpected proportionality of $I_{3/1} \propto \gamma_0^4$. This may be due to localization of deformation at low deformation frequencies as found in polymeric glasses*, see p. 109. **(b)** The γ_0 dependence of the fundamental and of the third and fith harmonics and linear fits of them showing the power law dependence $I_1 \propto \gamma_0^1$, $I_3 \propto \gamma_0^5$ and $I_5 \propto \gamma_0^5$. **(c)** The Lissajous-Bowditch figure at $\gamma_0 = 8.175\,\%$ visualizes the nonlinear behavior of the sample. This strain amplitude is highlighted with a yellow box in both **(a)** and **(b)**.

*Private communication with Valerian Hirschberg related to Hirschberg *et al.*[148]

In Figure 7.4(a), the strain amplitude dependence of $I_{3/1}$ for the highest volume fraction is shown at the lowest frequency measured. Here, just the substantial increase in $I_{3/1}$ with the dependence of $I_{3/1} \propto \gamma_0^4$ is observed as the proportionality of $I_{3/1} \propto \gamma_0^2$ vanishes at low strain amplitudes into the region where I_3 is experimentally too small to be detected above the noise.
In Figure 7.4(b), the absolute stress signals of the fundamental and the harmonics are shown for a high volume fraction. The third harmonic of the stress signal shows a power law of $I_3 \propto \gamma_0^5$ instead of the expected power law of $I_3 \propto \gamma_0^3$, while the first and the fifth harmonic still show the expected power laws of $I_1 \propto \gamma_0^1$ and $I_5 \propto \gamma_0^5$, confirming that this increase arises from the increase in I_3 rather than from a decrease of I_1. This suggests that additional nonlinear processes besides the predicted homogeneous nonlinear viscoelasticity are involved, leading to the observed increase. This amplification might be attributed to the same localization effect of deformation seen in polymeric glasses, where a change of the scaling of $I_{3/1} \propto \gamma_0^2$ to $I_{3/1} \propto \gamma_0^4$ is observed when the deformation of the sample becomes localized*, see p. 109.
To the best of our knowledge an increase with a higher exponent than $I_{3/1} \propto \gamma_0^2$ was never found before in suspensions. Only recently lower noninteger exponents were found[149,150] and attributed to the particle contact dynamics of attractive suspension networks[150].

7.1.2 Storage and Loss Moduli

The samples in the predominantly elastic regime show an overshoot in G'' as function of γ_0 without showing an overshoot in G', which is "type III" behavior according to Hyun *et al.*[73] and is typical for soft glassy materials as concentrated emulsions[11,151], suspensions[25,152], and colloidal glasses[21,74–76]. Similar to this behavior, in steady shear a stress overshoot is observed at the onset of flow discussed more in detail in Section 6.3.2.
Recently, Donley *et al.*[153] could gain more insight into this yielding behavior of type III materials by distinguishing between solid-like and fluid-like contributions to the total energy dissipation combining strain-controlled oscillatory shear with stress-controlled recovery tests. Zero-stress recovery tests[154] allow for distinguishing between the recoverable and unrecoverable energy dissipation. They could show, that the overshoot in G'' comes with a continuous transition from predominantly solid-like to predominantly fluid-like dissipation by showing, that the deformations transition from predominantly recoverable to predominantly unrecoverable. In colloidal glasses, a significant recoverable component was observed at flow reversal, at strain amplitudes, where G' and G'' already crossed[155] in accordance with Donley *et al.*[156] finding large correlations in the microstructure before and after yielding.
Based on these findings, a microstructural interpretation of the processes during this yielding process can be made. In the low strain region where G' and G'' are still constant, the strain amplitude is not sufficient to break or irreversibly deform or modify the shape of the local cages of the glassy structure. The increase in G'' and decrease of G' for type III materials is directly accompanied by an increase of the unrecoverable strain[153], which characterizes the extent of microscopic changes[156], as the shear amplitude is sufficient to locally deform

the cages, but the reformation of the cages is faster than the destruction of the cages. While further increasing the strain amplitude, the destruction of the cages becomes more dominant, leading to a higher unrecoverable strain component than recoverable component. The maximum in G'' is correlated to the dissipation of energy due to the breaking of the cages for colloidal glasses[75]. This is more pronounced in soft sphere glasses compared to hard sphere glasses due to the deformability and elasticity of the particles. The peak value of G'' slightly decreases for decreasing frequencies, i.e. the dissipation energy resulting from breaking the cages slightly decreases, as the Brownian motion of the particles supports the opening of the cages[18].

7.1.3 Macroscopic and Local Yield Strain

Several methods of the determination of the yield strain γ_y from oscillatory shear measurements are frequently used, such as the strain at the crossover point of G' and G'', at the maximum in G'', at the deviation of G'' from its linear plateau value or at the intersection between a horizontal line through the plateau modulus with a power law fit of the high strain behavior of G'. Another method to determine the yield strain is to plot σ vs γ_0 on logarithmic coordinates and find the intersection of a line with unit slope at low strains (corresponding to the linear regime) with a power law fit of the high strain behavior. Those methods were recently compared for different materials[157–160] finding the obtained values for the yield strain and the yield stress to vary about 3 orders of magnitude with the yield strain at the crossover of G' and G'' being the highest. Furthermore, these studies have demonstrated that defining a single yield strain is uncertain. During an oscillation cycle, the material yields and unyields depending on the strain currently applied[158,161].
By looking into the transient behavior during a cycle of oscillation Donley *et al.*[158] found the G'_t and G''_t values to show a time dependency as soon as the averaged moduli G' and G'' show deviations from the linear viscoelastic regime. Additionally, they found that the strain amplitude at which the transient behavior crosses the line of $G'_t = G''_t$ for the first time is close to the strain at the maximum of G''. Therefore, they interpret the strain at which G' decreases and G'' increases simultaneously as the strain at which small fractions of the material already yield[162], while the material as a whole yields close to the maximum of G''[158]. Aime *et al.*[163] found a transition from a slow relaxation mode to a fast relaxation mode in concentrated microgels between the maximum of G'' and the crossover of G' and G'' associated with yielding. Recently, Kamani *et al.*[161,164] developed a model with only a single yield stress, that can depict the characteristics of the whole amplitude sweep by allowing for a rate-dependent relaxation time and plastic viscosity.
According to Donley *et al.*[158], the onset of local and the onset of macroscopic yielding are defined as the strain at which G'' deviates 5 % from its plateau value in the linear regime and the strain at the maximum of G'', respectively. In Figure 7.5(a) the frequency dependence of the onset of macroscopic yielding at the yield strain ($\gamma_y = \gamma_0(G''_{max})$) and in Figure 7.5(b) the onset of local yielding at the yield strain ($\gamma_y = \gamma_0(G'' > 1.05G''_{lin})$) are shown. The onset of local yielding is in a strain amplitude range of 3 % to 8 %, while the macroscopic yielding occurs at strain amplitudes of 7 % to 28 %, depending on the

angular frequency. Note that both metrics may be based on the same underlying physics as a model with a single yield stress can depict both rheological characteristics[161,164]. In steady shear the stress overshoot observed at the onset of flow is in a similar γ-range of 7 % to 15 % (see Section 6.3.2) as the maximum in G''.

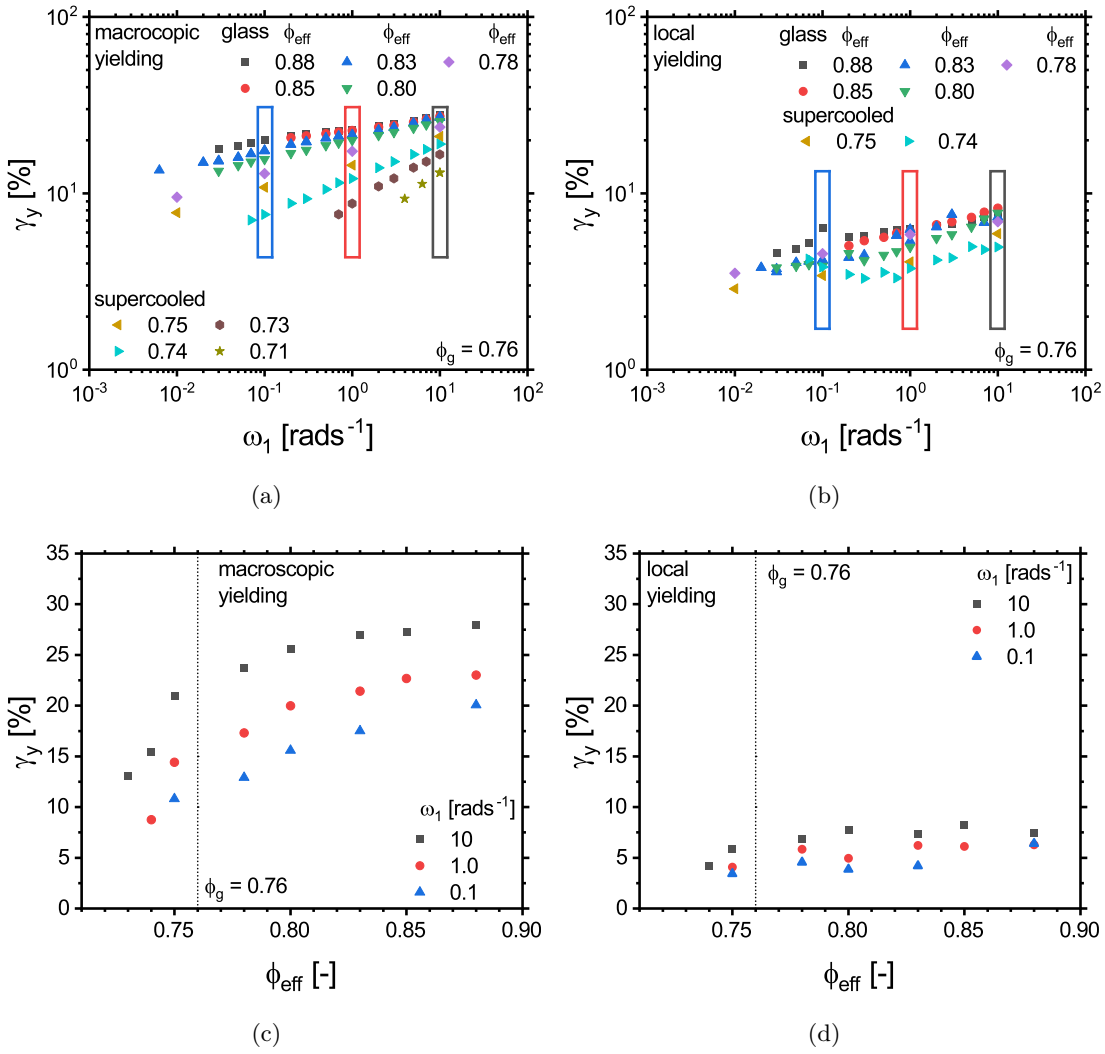

Figure 7.5: Yield strain as a function of ω_1 for different volume fractions in the supercooled and in the glassy regime for **(a)** macroscopic yielding ($\gamma_y = \gamma_0(G''_{max})$), where the material as a whole yields, and **(b)** local yielding ($\gamma_y = \gamma_0(G'' > 1.05G''_{lin})$), where small fractions of the material already yield, showing an increase of the yield strain for increasing angular frequencies. Yield strain of macroscopic **(c)** and local **(d)** yielding as a function of ϕ_{eff} for three different angular frequencies (marked in **(a)** and **(b)** with the black, red and blue box). The macroscopic yield strain shows an increase of the yield strain with increasing volume fraction. The local yield strain shows higher scattering of the data compared to the macroscopic yield strain. This is because determining the deviation from a plateau value is less accurate than determining a maximum.

For increasing ω_1, an increase in γ_y is observed in accordance with previous experimental findings in soft and hard sphere glasses[15,75,108,165]. This can be rationalized by the cage effect, which is present for parameters, where in the linear regime $G' > G''$. At low applied ω_1 the Brownian motion of the particles supports the escape from the cages. At higher ω_1, the particles have less time to escape the cage, i.e. a higher strain amplitude is necessary

to break the cage. The suspension behaves still linear at higher strain amplitudes than it does at lower frequencies.
In Figures 7.5(c) and 7.5(d) the volume fraction dependence of the yield strain amplitude is shown for three different angular frequencies. It is observed that the yield strain increases with increasing effective volume fraction in accordance with findings of Koumakis *et al.*[105] on soft core-shell particles.
In contrast, for hard sphere glasses a maximum in the yield strain in dependence on the volume fraction determined from creep and recovery measurements for hard sphere glasses. Note that different methods for the determination of γ_y do not necessarily yield the same values, but Dinkgreve *et al.*[157] found the same qualitative behavior for different simple yield stress fluids in dependence on ϕ_{eff} for different methods. Therefore, a qualitative comparison of the yield strains can be made, but a quantitative comparison between the yield strains obtained with different yielding criteria such as $\gamma_y = \gamma_0(G'' > 1.05G''_{\text{lin}})$ and $\gamma_y = \gamma_0(G''_{\text{max}})$ with the values from literature at $\gamma_y = \gamma_0(G' = G'')$[7,105] or from creep and recovery measurements[107,108] is not reasonable.
The maximum in the yield strain observed in hard sphere glasses[105,108] was attributed to two competitive effects. In the glassy regime, the distance between particles decreases while increasing the effective volume fraction approaching random close packing. This results in a decreased strain required to break the cages. Additionally, the yield strain tends towards zero at the liquid-to-glass transition as particles are not permanently caged in the supercooled state causing the yield strain to decrease for decreasing volume fraction starting from the maximum.
The increase in the yield strain of soft particle glasses for increasing volume fraction below the glass transition volume fraction can be attributed to the same effect of the emergence of the cage effect as in hard sphere glasses. The increase above the glass transition volume fraction is attributed to the particle softness, which dampens the cage relaxation partially[105,108].

7.2 Frequency Dependence of the Anharmonic Response

7.2.1 Validation of the Frequency Sweep MAOS

To reduce the measurement time for investigating the frequency dependence of the intrinsic anharmonicity Q_0, the measurements can be conducted as a frequency sweep instead of several strain amplitude sweeps as described in Section 3.4. To determine the minimum and maximum strain amplitude thresholds for the MAOS region at various frequencies, the strain sweeps depicted in Figures 7.1(e), 7.1(f), 7.3(e) and 7.3(f) on page 106 and 108 were utilized.
For the effective volume fractions of $\phi_{\text{eff}} = 0.71$ and $\phi_{\text{eff}} = 0.73$, the sample is in the range of $De < 1$ for the low angular frequencies. However, there is still no shift in the strain amplitude range of asymptotic behavior. For the higher volume fractions $\phi_{\text{eff}} = 0.80$ and $\phi_{\text{eff}} = 0.83$ in the glassy regime, the sample is in the region of $De > 1$ for all investigated

angular frequencies as shown in the linear frequency sweeps shown in Figure 6.3 on page 80 and in Figures 7.3(a) and 7.3(b).

In the regime, where the sample is more elastic than viscous ($\phi_{\text{eff}} = 0.73$ and $\omega_1 > 0.2\,\text{rad}\,\text{s}^{-1}$; $\phi_{\text{eff}} = 0.80$ and $\phi_{\text{eff}} = 0.83$ for all investigated ω_1), there is a slight shift in the strain amplitude boundaries for asymptotic behavior to lower strains at lower frequencies, as previously described. But it is still evident that for all volume fractions a fixed strain amplitude can be utilized for the frequency sweep MAOS. The strain amplitude was selected between $\gamma_0 = 7\,\%$ to $10\,\%$, depending on the volume fraction. Strain sweeps at lower frequencies were conducted within a shortened measurement window to confirm whether the selected strain amplitude is still within the MAOS regime for those low angular frequencies. Note that for low angular frequencies ($\omega_1 < 0.01\,\text{rad}\,\text{s}^{-1}$), the region, where $I_{3/1}$ scales quadratically with γ_0 could not be detected as described in Section 7.1.1 with Figure 7.4 on page 109. Therefore, the investigation of Q_0 is limited to an angular frequency range of $0.01\,\text{rad}\,\text{s}^{-1}$ to $10\,\text{rad}\,\text{s}^{-1}$.

To further evaluate the suitability of the frequency sweep MAOS and strain amplitude for the colloidal suspension, a comparison between a frequency sweep at a fixed strain amplitude of $\gamma_0 = 10\,\%$ and different strain sweeps is shown in Figure 7.6 for a volume fraction of $\phi_{\text{eff}} = 0.73$.

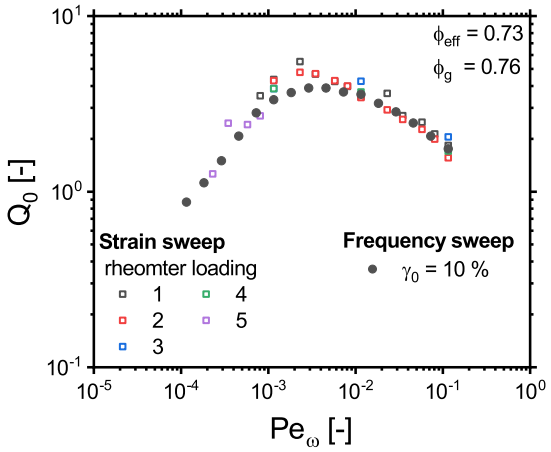

Figure 7.6: Comparison of the frequency dependence of the intrinsic anharmonicity Q_0 obtained from the frequency sweep MAOS measurements with a strain amplitude of $\gamma_0 = 10\,\%$ and from strain sweep MAOS measurements showing agreement (ca. $20\,\%$ deviation of the $Q_{0,\text{max}}$ values) of the results confirming that the frequency sweep MAOS is a suitable alternative to the strain sweep MAOS.

The Q_0 values observed from the frequency sweep and the strain sweep show the same trend and, especially in the high and low Pe_ω-region, the data superimpose. Just in the region around the maximum, the Q_0 value determined from the frequency sweep MAOS deviates slightly from the value determined from the strain sweep MAOS. Note that the strain sweep data scatter, while the frequency sweep data are quite smooth. By using a fixed amplitude, scattering of the $I_{3/1}$ data is reduced, resulting in small deviations from the actual value. However, the values are consistent with each other.

The reduction in measurement time when using the frequency sweep MAOS instead of the strain sweep MAOS methodology depends significantly on the measurement parameters,

such as the investigated ω_1 range, the point density in ω_1 space, and the number of points used in the strain sweeps. For a ω_1 range of $10^2\,\mathrm{rad\,s^{-1}}$ to $10^{-3}\,\mathrm{rad\,s^{-1}}$ with 5 points per decade and 10 points measured per strain sweep, the measurement time can be reduced from 83 h to 34 h by using the frequency sweep MAOS instead of the strain sweep MAOS, a reduction by a factor of 2.4. The calculated measurement time for the frequency sweep MAOS includes the time for a γ_0-sweep at the highest and lowest investigated ω_1.

7.2.2 Anharmonic Response in the Supercooled State

By using the time efficient method of the frequency sweep MAOS, the intrinsic anharmonicity Q_0 for a large frequency window and with a high point density in frequency space was investigated, both in the supercooled and the glassy regime while reducing measurement artifacts from water evaporation. Note that determining critical spectra requires wide frequency ranges. In Figure 7.7(a), the dependence of Q_0 of the sample in the supercooled states on the rescaled frequency Pe_ω is depicted. The $Q_0\,(Pe_\omega)$ curves of the different volume fractions superimpose in the high frequency regime and exhibit a maximum in Q_0, which increases from $Q_0 = 2$ to 6 and its position shifts from $Pe_\omega = 4.2\times10^{-2}$ to 6.2×10^{-4} for increasing ϕ_{eff} from $= 0.70$ to 0.74.

MCT predictions of Q_0 in the supercooled regime for different separation parameter $\epsilon = \frac{\phi_{\mathrm{eff}}-\phi_{\mathrm{g}}}{\phi_{\mathrm{g}}}$ are depicted in Figure 7.7(b). The separation parameter (ϵ) is a measure for the distance to the glass transition $\epsilon = \frac{\phi_{\mathrm{eff}}-\phi_{\mathrm{g}}}{\phi_{\mathrm{g}}}$. The supercooled regime is denoted by $\epsilon < 0$, while $\epsilon > 0$ denotes the glassy regime. The MCT predictions were kindly provided by Leonhard Lang from the group of Prof. Fuchs from the university of Konstanz. The schematic model introduced in Section 4.4.4 is used for the predictions, which are in qualitative agreement with the experimental data.

The intrinsic anharmonicity parameter superimposes for different ϕ_{eff} in the high frequency regime. A maximum in Q_0 is observed, which increases from 1 to 150 in amplitude and shifts to lower Pe_ω from 4 to 3×10^{-10} for increasing ϵ from 10^{-2} to 10^{-6}, i.e. for ϕ_{eff} closer to the glass transition volume fraction.

The principle Pe_ω dependence of Q_0 obtained from experiment and MCT predictions are in agreement, while the absolute values of Q_0 and the position of the curves in Pe_ω space do not align. This discrepancy arises because the MCT predictions are based on arbitary input parameters. To obtain agreement in Pe_ω space and absolute Q_0 values, MCT predictions, which are based on input parameters obtained from the linear rheological results of the experimentally investigated bimodal model system, are needed.

Due to the inhomogeneity of the flow field in parallel plate geometries adjustments of the nonlinear rheological results have to be made to match the results to the data from cone-plate and plate-plate experiments. Wilhelm *et al.*[70] adjusted by multiplying the strain amplitude values of the plate-plate measurements by 0.75, whereas Wagner *et al.*[166] and Giacomin *et al.*[167] multiplied the $I_{3/1}$ values obtained from parallel plate experiments by 1.5, yielding similar correction factors for Q.

A comparison between $I_{3/1}$ measured with a plate-plate and a cone-plate geometry seen in Figure 7.8 leads to the conclusion that a multiplication of γ_0 of the plate-plate measurements

by 0.75 leads to agreement between the plate-plate and the cone-plate results. From this, a correction of approx. $Q_{0,\mathrm{CP}} = 1.78 Q_{0,\mathrm{PP}}$ results. A direct multiplication of the $I_{3/1}$ values is not reasonable in this thesis, as the plateau value of $I_{3/1}$ is almost independent of the used geometry. The adjusted values of Q_0 are presented in Figure 7.7(c). Additionally, predictions from MCT from Seyboldt *et al.*[29] are shown. The absolute predicted Q_0 values based on input parameter from the linear rheology of a disperse system are illustrated as a dashed line, whereas the predicted scaling laws for the low, medium and high frequency behavior, which are universal for glass-foming colloids, are shown as solid lines.

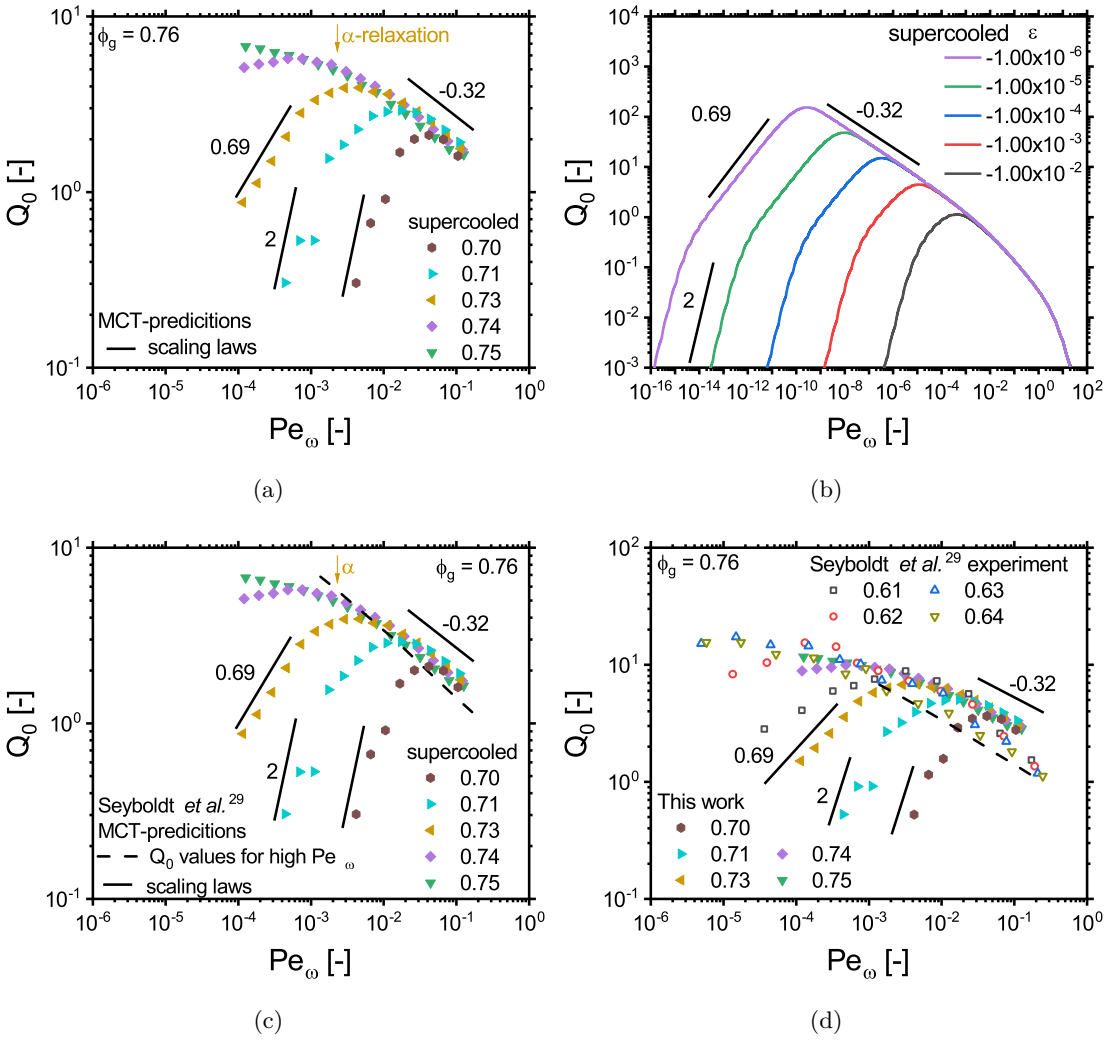

Figure 7.7: **(a)** Q_0 obtained from frequency sweep MAOS measurements with a plate-plate geometry in the supercooled regime. The scaling laws of Q_0 show agreement with the predictions from MCT depicted by the black lines. **(b)** Q_0 obtained from the MCT calculations of Leonhard Lang showing the same qualitative trends as the experimental data and the same scaling laws. **(c)** Q_0 values from the same measurements as in **(a)** and the MCT predictions of the Q_0 values and the scaling laws. The dashed line depicts the MCT results of Fig. 2 from Seyboldt *et al.*[29]. **(d)** Q_0 values from the same measurements (closed symbols), corrected for the inhomogeneity of the shear field in plate-plate geometries and the experimental data (open symbols) from Seyboldt *et al.*[29]. The scaling laws and absolute predicted values are identical to those presented in **(c)**.

In Figure 7.7(c), the experimental findings published in Seyboldt *et al.*[29] are displayed additionally. Agreement between the two data sets is observed for the high frequency flank

with deviations of 6 % to 45 % between them. Deviations between this work and Seyboldt *et al.'s*[29] may be accounted for by the different particle size distributions and modalities, as Seyboldt *et al.*[29] investigated a polydisperse monomodal system.

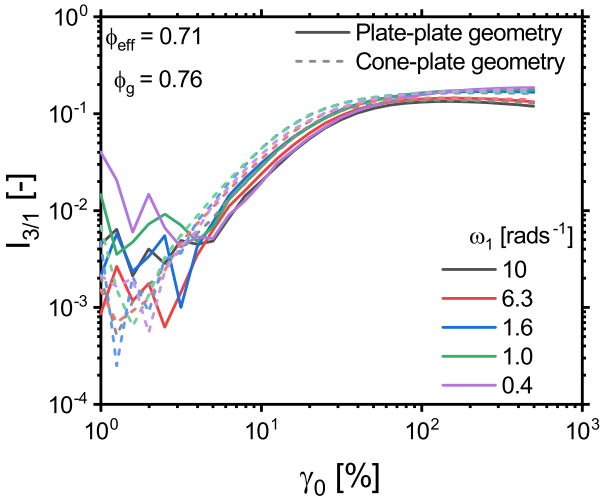

Figure 7.8: Comparison of $I_{3/1}$ obtained from plate-plate and cone-plate measurements leading to the conclusion that multiplying the strain of the plate-plate results by 0.75 leads to agreement between the measurements. A direct multiplication of the $I_{3/1}$ values is not reasonable because the plateau value of $I_{3/1}$ is independent of the geometry used.

7.2.2.1 Scaling Laws of the Anharmonicity in the Supercooled State

The MCT predicts three different regimes with different dependence of Q_0 on the rescaled frequency Pe_ω. The predicted scaling $Q_0 \propto Pe_\omega^{-a}$ with $a = 0.32$ in the high frequency regime and the scaling in the intermediate frequency regime $Q_0 \propto Pe_\omega^{-b}$ with $b = 0.69$ agree with the experimental findings, see Figure 7.7 on page 116. Additionally, a first indication of the predicted quadratic behavior in the low frequency regime $Q_0 \propto Pe_\omega^2$ is observed. The region with the scaling of $Q_0 \propto Pe_\omega^{-b}$ with $b = 0.69$ vanishes for low ϕ_{eff} in the experiments consistent with the MCT predictions, where it vanishes for low ϵ. Note that the high frequency regime in $Q_0\,(Pe_\omega)$ in monodisperse polymer melts shows similar scaling laws and the low frequency regime the same scaling law as in colloidal suspensions, so an exponent of 0.35 and 2. In polymer melts the exponent of the low frequency regime highly depends on the dispersity of the molecular weight of the system[79].
The different regimes shift to lower angular frequencies, respectively lower Pe_ω, for higher volume fractions consistent with MCT predictions as the relaxation times of the sample are increasing for increasing volume fractions.
For high Pe_ω, MCT predicts Q_0 to superimpose for different ϕ_{eff}. The experimental findings validate this and coincide with Seyboldt *et al.'s*[29] on a similar system. Note that the data shown in Seyboldt *et al.*[29] show the expected scaling law in the high frequency region only for the highest investigated volume fraction ϕ_{eff}, while the experimental data from this thesis show the dependence for all investigated volume fractions. Additionally, in this thesis the low and the medium frequency regime scalings could be found for at least one ϕ_{eff}. The scaling laws could be confirmed because of the higher point density in the frequency domain

and a more suitable selection of the investigated volume fractions in the supercooled region compared to the work of Seyboldt *et al.*[29]. Furthermore, the experimental results in this thesis show reduced scattering compared to the data of Seyboldt *et al.*[29] due to the use of the time efficient frequency sweep MAOS instead of using strain sweep MAOS.
The deviations of the experimental results from the absolute predicted values from MCT (depicted as dashed line in Figures 7.7(c) and 7.7(d) on page 116) can be explained by the difference in the particle size distribution, as Seyboldt *et al.*[29] investigated a monomodal, but disperse suspension with a relative standard deviation of the radius distribution of $\sigma_{\mathrm{rel}} = 17\,\%$, i.e. the input parameter of the MCT predictions were based on the linear rheology of this system. In contrast, the experimentally investigated system in this work is bimodal.
As described earlier, the scaling laws of the Pe_ω dependence of Q_0 obtained from experiment and MCT predictions show agreement, while the absolute values of Q_0 and the position in Pe_ω space vary as the MCT predictions are based on arbitary input parameters. In Figure 7.9, the experimental results for $Q_0(Pe_\omega)$ at $\phi_{\mathrm{eff}} = 0.73$, corrected for the inhomogeneity of the shear field in plate-plate geometries and the MCT predictions shown in Figure 7.7(b) shifted to the high frequency flank of the experimental results, are shown. The course of the Pe_ω dependence of Q_0 obtained from experiment and MCT predictions superimposes for the whole investigable frequency region.

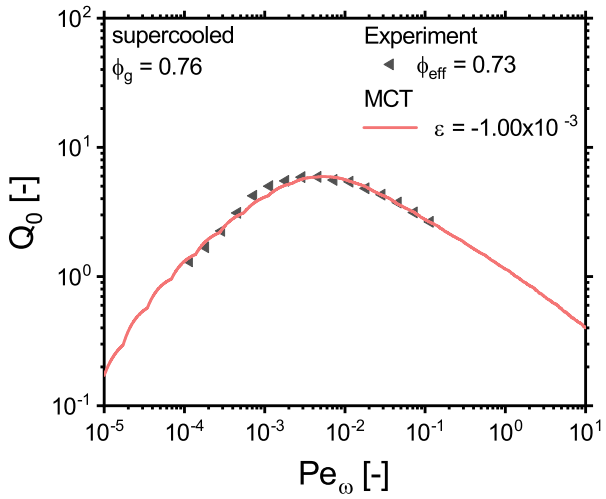

Figure 7.9: Direct comparison of Q_0 obtained from experiment at $\phi_{\mathrm{eff}} = 0.73$, corrected for the inhomogeneity of the shear field in plate-plate geometries and the MCT predictions shown in Figure 7.7(b) shifted to the high frequency flank of the experimental results. The general course of the Pe_ω dependence of Q_0 in experiment and MCT predictions superimposes.

The agreement between the experimental findings and the MCT predictions support the capability of MCT to predict the rheological behavior of glass-forming colloidal suspensions. Additionally, it implies the need for further scrutiny of MCT predictions, which are based on input parameters from the linear rheology of the bimodal system. With these MCT predictions, comparison between the absolute Q_0 values and the position in Pe_ω space would be feasible. In addition, the qualitative agreement between the MCT predictions, which were often used to describe hard sphere glass-forming colloids, and the experimental results

of soft core-shell systems further supports the independence of the anharmonicity from the particle interactions, which was proposed by Poulos *et al.*[21]. They found qualitative agreement of the anharmonicity of the two more extreme cases of ultra-soft star-like micelles and hard sphere glasses.

7.2.3 Anharmonic Response in the Glassy State

The experimental results of Q_0 in dependence on Pe_ω for the colloidal suspension in the supercooled and the glassy states determined from the frequency sweep MAOS via $Q_0 = \frac{I_{3/1}}{\gamma_0^2}$ are depicted in Figure 7.10(a). The glassy samples show the scaling $Q_0 \propto Pe_\omega^{-a}$ with the critical exponent $a = 0.32$ in the high frequency regime in quantitative agreement with the samples in the supercooled regime and as predicted by MCT, see Figure 7.10(b). The Q_0 values of the samples in the supercooled regime superimpose, whereas in the glassy regime Q_0 decreases for increasing volume fractions. This decrease is not expected from the MCT predictions shown in Figure 7.10(b). From theory, still a collapse in the high frequency regime is expected. Note that the oscillations in Q_0 (and $[I_3]$, see Figure 7.10(d)) at low Pe_ω arise from discretization and are a known uncertainty of MCT[168].
To analyze if the decrease arises from a decrease in the intrinsic third anharmonicity $[I_3] = \frac{I_3}{\gamma_0^3}$ or an increase in the intrinsic fundamental $[I_1] = \frac{I_1}{\gamma_0^1} = |G^*|$, in Figures 7.10(c) and 7.10(e) $[I_3]$ and $[I_1]$ are depicted for different ϕ_{eff}. They can be used as an internal comparison, since the samples are measured with the same rheometer, and thus with the same torque sensitivity.
Note that the intrinsic third harmonic and the intrinsic fundamental are defined as the extrapolation of the scaling regions $[I_3] = \lim_{\gamma_0 \to 0} \frac{I_3}{\gamma_0^3}$ and $[I_1] = \lim_{\gamma_0 \to 0} \frac{I_1}{\gamma_0}$. The measurements are conducted in the regime, where I_3 and I_1 show these scalings with $I_3 \propto \gamma_0^3$ and $I_1 \propto \gamma_0$. Hence, $\frac{I_3}{\gamma_0^3}$ and $\frac{I_1}{\gamma_0}$ are plateau values in this region. Therefore, rather than extrapolating the amplitude dependence of I_3 and I_1, the intrinsic third harmonic and fundamental can be calculated from one value of I_3 and I_1 according to $[I_3] = \frac{I_3}{\gamma_0^3}$ and $[I_1] = \frac{I_1}{\gamma_0^1} = |G^*|$, respectively.
The intrinsic third harmonic $[I_3]$ of the sample in the glassy regime shows a collapse in the high frequency regime as expected from the MCT predictions, while $[I_1] = |G^*| = \frac{I_1}{\gamma_0}$ increases with increasing ϕ_{eff} (see Figures 7.10(c) and 7.10(e)). It can be concluded that the decrease in Q_0 is due to the increase of the intrinsic fundamental $[I_1] = |G^*|$ rather than a decrease of the intrinsic third harmonic $[I_3]$. $[I_3]$ and $[I_1]$ increase with the volume fraction ϕ_{eff} in the supercooled region, whereas in the glass this increase vanishes for $[I_3]$ while $[I_1]$ still scales with the volume fraction ϕ_{eff}. Consequently, the decrease of the intrinsic anharmonicity Q_0 is caused by the higher linear elasticity of the sample approaching higher volume fractions rather than a decrease of the intrinsic third harmonic $[I_3]$.
Furthermore, in the MCT predictions a wider range in Pe_ω space is accessible than in the experiments. The MCT predictions of the Pe_ω dependence of Q_0 at the glass transition with $\epsilon = 0.00$ shows a decrease of Q_0 with increasing Pe_ω for the whole Pe_ω region. In contrast, at higher ϵ, i.e. deeper in the glassy state, Q_0 levels off to a plateau value in Q_0 for low Pe_ω, which decreases from 239 to 0.38 for increasing ϵ from 10^{-6} to 10^{-1}.

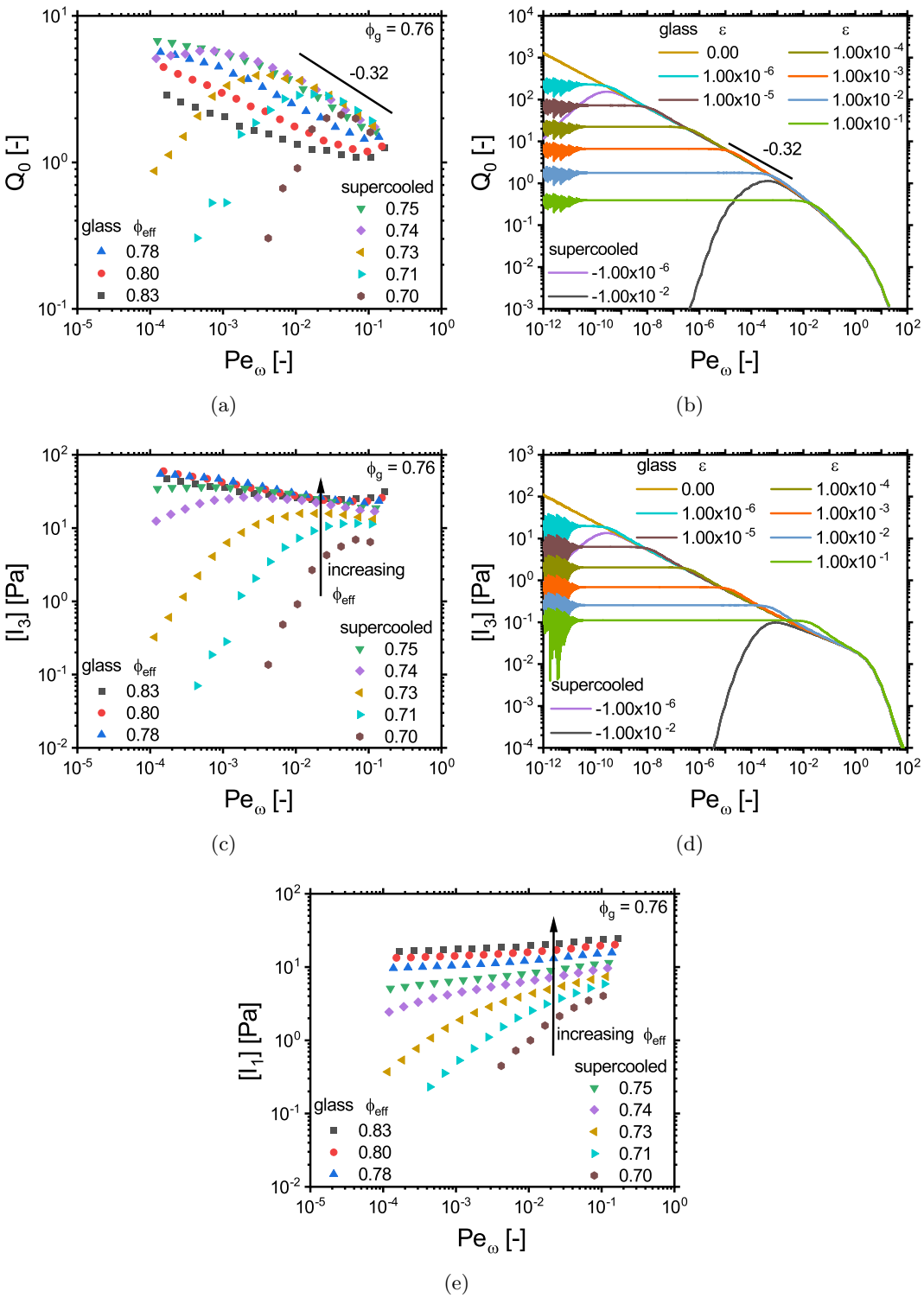

Figure 7.10: **(a)** Q_0 obtained from frequency sweep MAOS measurements for the sample in the glassy and supercooled regime. In the glassy regime Q_0 decreases with increasing Pe_ω. **(b)** The MCT predictions in the glass show a collapse of Q_0 for varying ϕ_{eff} in the high Pe_ω regime with a scaling law of $Q_0 \propto Pe_\omega^{-0.32}$. Additionally, the samples in the supercooled regime at the highest and the lowest ϵ investigated are displayed to show the relative position of Q_0 in the glass with respect to Q_0 in the supercooled regime. **(c)** The intrinsic third harmonics $[I_3]$ obtained from the same measurements as in **(a)** do not show a decrease for the glassy samples, confirming that the decrease in Q_0 arises from the normalization to the fundamental $[I_1]$, which increases with increasing ϕ_{eff} shown in **(e)**. **(d)** MCT predictions of the intrinsic third harmonic $[I_3]$ in the glass, showing the same collapse as observed in the experiment.

7.2.4 Comparison of the Frequency Dependence of the Anharmonic and Linear Response

In Figure 7.11 the volume fraction dependence of Pe_ω of the characteristic linear and nonlinear mechanical properties is shown. The minimum in the loss factor $\tan(\delta)_{min}$ and in G'' extracted from the linear frequency sweeps (see Section 6.2.1, Figure 6.3 on page 80) show different scaling laws in the supercooled and in the glassy state. The maximum in Q_0 obtained from the frequency sweep MAOS measurements, see Figure 7.7(c) on page 116, is located in the region of the α-relaxation process and scales accordingly. The maximum in Q_0 of about 2 to 6 is about 2 decades higher in amplitude than that found in linear and sparsely branched polymer melts[79]. This is in agreement with findings on soft colloidal star polymer systems[169] and is attributed to the difference in the onset of anharmonicities. Polymer melts behave linear over a wider range of strain amplitudes ($\gamma_y \approx 100\,\%$) than colloidal suspensions ($\gamma_y \approx 10\,\%$) resulting in lower maximal Q_0 values compared to colloidal suspensions. The Q_0 value is lower for a system, that exhibits linear behavior over a wide range of strain amplitudes compared to a system, where the onset of anharmonicities occurs at smaller strain amplitudes.

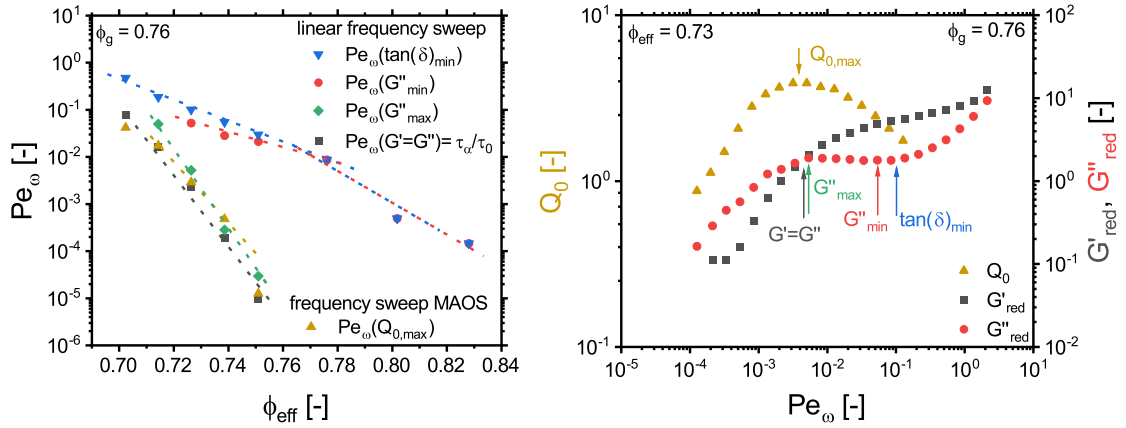

Figure 7.11: (a) Comparison of the volume fraction dependence of the position in Pe_ω of the characteristic linear and nonlinear rheological behavior, as the crossover point of G' and G'', the minimum in the loss factor $\tan(\delta)_{\text{min}}$ and in G'' and the maximum in G'', as well as the position in Pe_ω of the maximum in intrinsic anharmonicity Q_0. The results show that the maximum in Q_0 is located in the region of the α-relaxation ($Pe_\omega(G' = G'')$) and scales accordingly. The dotted lines are as guide for the eye. In **(b)**, it is illustrated how these characteristics are extracted from the linear rheological response and from the Pe_ω dependence of Q_0.

In this work, an increase of Q_0 is found for samples in the supercooled state in the frequency range where the sample shows a predominantly viscous behavior in the linear regime, and a decrease for frequencies in the range where the sample shows a predominantly elastic behavior in the linear regime, in agreement with the literature[21]. This behavior can be explained by the increasing shear rates reached during a cycle of oscillation. For supercooled samples this leads to stronger shear thinning, resulting in an increase of the anharmonicities. In contrast, for solid-like samples this leads to a transition from elastic to plastic flow, and therefore to a decrease of anharmonicities as the material cannot follow the applied external shear rate[21]. The intrinsic anharmonicity Q_0 is closely related to the

linear frequency dependent behavior, as it describes the anharmonicity of the sample in the limit of vanishing strain amplitude $Q_0 = \lim_{\gamma_0 \to 0} \frac{I_{3/1}}{\gamma_0^2}$.
For volume fractions in the glassy state, no maximum in Q_0 is observed supporting the MCT predictions of a power law divergence for low frequencies at the glass transition.

7.3 Summary

This chapter provided the characterization of the nonlinearity and anharmonicity of the bimodal colloidal model system under nonlinear oscillatory shear at different ϕ_{eff} in the supercooled and glassy state using frequency and strain sweep MAOS. Additionally, the frequency dependence of the anharmonicity was compared to MCT predictions.
Using strain sweep MAOS, it was found that the core-shell particles feature a constant plateau value of $I_{3/1}$ at $\gamma_0 > 50\,\%$, which decreases from 27 % to 11 % by increasing ω_1 from $3 \times 10^{-2}\,\text{rad}\,\text{s}^{-1}$ to $10\,\text{rad}\,\text{s}^{-1}$ and decreasing ϕ_{eff} from 0.83 to 0.71, see Figure 7.2 on page 107. The soft core-shell particles behave similarly to the ultra-soft system studied by Poulos *et al.*[21]. Their study investigated the anharmonic behavior of ultra-soft star-like micelles and hard sphere glasses. In contrast to the ultra-soft systems and the core-shell particles studied in this thesis, the hard sphere glass-forming colloids show a significant drop of the plateau value in the glassy regime.
In this work, additionally, a substantial increase of $I_{3/1}$ at low ω_1 with a dependence of $I_{3/1} \propto \gamma_0^4$ in colloidal glasses was observed, see Figure 7.4 on page 109. This behavior is similar to that observed in amorphous polymeric materials when the deformation of the sample becomes localized[170].
The oscillatory local and macroscopic yield strain amplitude were obtained from the strain at which G'' deviates 5 % from its plateau value and the strain at the maximum in G'', respectively. The macroscopic yield strain amplitude increases from 7 % to 28 % for increasing the frequency from $10^{-2}\,\text{rad}\,\text{s}^{-1}$ to $10\,\text{rad}\,\text{s}^{-1}$ and for increasing the volume fraction from 0.71 to 0.88, see Figure 7.5 on page 112. The increase in yield strain for increasing frequencies can be attributed to the reduced time the particles have to escape from their cages. Thus, higher strain amplitudes are required to break the cages. Note that the position of the stress overshoot observed in steady shear measurements in Section 6.3.2 is in a comparable range of total strains of 7 % to 15 % as the overshoot in G'', see Figure 6.12 on page 95.
Additionally, the findings of Singh *et al.*[81] that utilizing frequency sweep MAOS is a viable and more time-efficient alternative to strain sweep MAOS to obtain the frequency-dependent anharmonic characteristics of colloidal glasses was supported by this thesis. The reduction of the measurement time when using the frequency sweep MAOS instead of the strain sweep MAOS methodology depends significantly on the measurement parameters, such as the investigated ω_1 range, the point density in ω_1 space and the number of points used in the strain sweeps. For example, for a ω_1 range of $10^2\,\text{rad}\,\text{s}^{-1}$ to $10^{-3}\,\text{rad}\,\text{s}^{-1}$ with 5 points per decade and 10 points measured per strain sweep, the measurement time can be reduced by a factor of 2.4.

By using frequency sweep MAOS instead of strain sweep MAOS, the anharmonicity of glass-forming colloidal suspensions in a broad frequency and volume fraction regime with a high point density in frequency space was determined, which makes a thorough comparison to MCT predictions possible. In the experiments in the supercooled regime of the sample, Q_0 superimposes in the high frequency regime, see Figure 7.7 on page 116. This supports the MCT prediction of a power law rise of the anharmonicity with decreasing frequency that is independent of the distance to the glass transition.
Furthermore, the findings reveal that Q_0 exhibits the scaling laws predicted by MCT in the three different Pe_0 regions of $Q_0 \propto Pe^2$ in the low, $Q_0 \propto Pe^{0.69}$ in the medium and $Q_0 \propto Pe^{-0.32}$ in the high frequency regime. The frequencies at which these scaling laws occur depend on the radius and volume fraction of the particles. The agreement between the scaling laws and the principle course of the Pe_ω dependence of Q_0 obtained from MCT predictions and obtained from rheological experiments of the bimodal system shows the universality of the critical anharmonicity at the MCT glass transition.
It was demonstrated that Q_0 reaches a maximum of 2 to 6 depending on ϕ_{eff} for the samples below ϕ_{g}, which lies in the region of the α-relaxation, and its position scales accordingly. As the sample becomes more fluidized, the material becomes more Newtonian, leading to a decrease of the intrinsic anharmonicity Q_0. In contrast, in the solid-like regime the higher shear rates reached during a cycle of oscillation leads to a transition from predominantly elastic to predominantly viscous flow, which leads to a decrease of the anharmonicity.
The glassy samples still show the scaling of $Q_0 \propto Pe_\omega^{-0.32}$ in the high frequency regime as predicted by MCT, see Figure 7.10 on page 120. In the high frequency limit, the intrinsic anharmonicity Q_0 is not a function of the volume fraction in the supercooled regime, whereas it decreases with volume fraction in the glassy regime. In contrast, the intrinsic third harmonic of the stress signal $[I_3] = \lim_{\gamma_0 \to 0} \frac{I_3}{\gamma_0^3}$ increases in the supercooled regime, whereas above ϕ_{g} it is no longer a function of the volume fraction, while the intrinsic fundamental $[I_1] = \lim_{\gamma_0 \to 0} \frac{I_1}{\gamma_0^1}$ and consequently σ, increases with increasing volume fraction. Consequently, the decrease of the intrinsic anharmonicity Q_0 is caused by the higher elasticity of the sample approaching higher volume fractions rather than a decrease of the intrinsic third harmonic. The collapse of $[I_3]$ in the glass is in agreement with the MCT predictions.
In summary, it was shown that several characteristics of the Pe_ω dependence of the intrinsic anharmonicity, predicted by MCT, are consistent with the rheological results, such as the principle course of Q_0, the determined scaling laws, the collapse of Q_0 for different ϕ_{eff} in the supercooled state, and the collapse of the intrinsic third harmonic $[I_3]$ for different ϕ_{eff} in the glassy state in the high frequency regime. This agreement between rheological and predicted results supports the capability of MCT to predict the intrinsic anharmonicity of glass-forming colloidal suspensions.

8 Conclusion and Outlook

Conclusion

The objective of this work is to give a thorough picture of the dynamics and rheological properties of glass-forming colloidal suspensions covering the range from the supercooled to the glassy state. Accordingly, a bimodal core-shell model system was developed and fully characterized. Linear and nonlinear oscillatory rheology as well as the yielding behavior were investigated and compared to mode coupling theory (MCT) predictions, to give a detailed picture of the glass-forming colloidal suspension.

A model systen was developed fulfilling the boundary conditions defined by the scope of this thesis. The particles need to be of spherical shape, exhibit an easy adjustable volume fraction as well as an interaction potential close to hard spheres. Additionally, the particle crystallization has to be suppressed to obtain a stable glassy state.

To meet the criterion of a precisely adjustable effective volume fraction (ϕ_{eff}), thermoresponsive polymer based core-shell particles were chosen as a model system. A previously developed synthesis of colloidal suspensions of thermoresponsive PS-PNIPAm core-shell particles[119] was scaled-up to a total volume of $V = 1.8\,\mathrm{L}$ of the suspension to allow for enough material for a detailed characterization of the rheological properties of the model system. Imaging the core-shell particles with TEM confirmed the spherical core-shell structure of the chosen model systems, see Figure 5.10 on page 59, while DCS confirmed its narrow radius distribution with a relative standard deviation below 6 %. However, due to the narrow radius distribution, the model system was prone to particle crystallization. Previous studies[17,22,28] used monomodal samples with a high dispersity of the radius to suppress particle crystallization. In contrast to these studies, in this thesis a binary mixture with a size ratio of approx. 0.58 in radii and a mass ratio of large ($R_{\mathrm{H}}(15\,^{\circ}\mathrm{C}) = 139.9\,\mathrm{nm}$) to small ($R_{\mathrm{H}}(15\,^{\circ}\mathrm{C}) = 81.4\,\mathrm{nm}$) particle of 90:10 was investigated. Both core-shell particles chosen for the mixture had well-characterized, narrow radius distributions. This improves comparability to MCT predictions as they were tailored to monodisperse suspensions. However, they can be extended to well-defined binary mixtures[171,172]. Time-dependent rheological investigations confirmed that particle crystallization is suppressed for at least 26 h, see Figure A.3.9 on page 156, which exceeds the time scales of the rheological investigations. The expected temperature dependence of R_{H} of the chosen core-shell model system was confirmed using DLS, see Figure 5.15 on page 69. In agreement with the work of Crassous *et al.*[113], R_{H} followed a linear decrease with increasing temperature in the temperature range of 10 °C to 25 °C with thermal expansion coefficients between $-0.5\,\mathrm{nm\,^{\circ}C^{-1}}$ to

$-1.0\,\mathrm{nm\,°C^{-1}}$ depending on the effective crosslinking density and the shell thickness. This linear decrease in R_H is followed by a sharp drop at $T_\mathrm{LCST} = 32\,°\mathrm{C}$ and a leveling off.
The synthesis path of the core-shell particles led to charges on the particle surface due to the use of a charged initiator. To meet the criterium of a hard sphere interaction potential, these surface charges were screened by the addition of KCl with $c_\mathrm{KCl} = 0.05\,\mathrm{mol\,L^{-1}}$ leading to a Debye length of $\lambda_\mathrm{D} = 1.3\,\mathrm{nm}$. It was shown, that the system with added salt is colloidally stable below T_LCST, but loses colloidal stability above this temperature, see Figure 5.13 on page 63. Therefore, the rheological characterization was limited to $T < T_\mathrm{LCST} = 32\,°\mathrm{C}$, which was sufficient to study effective volume fraction in both the supercooled as well as the glassy state.
In the second part of the thesis, the rheological behavior and dynamics of the glass-forming colloidal suspension in linear response using SAOS experiments and during yielding using steady shear experiments was investigated. The linear rheological behavior typical for colloidal glasses[7,17,74,75,113] was found for the model system used, see Figure 6.3 on page 80, and thus confirmed its suitability for the conducted studies. The normalized time scale of the α-relaxation of the colloidal suspension shows a strong dependence on the volume fraction $\frac{\tau_\alpha}{\tau_0} \propto \phi_\mathrm{eff}^m$ with $m \approx 124$, see Figure 6.4 on page 82.
The power law increase of $G'_\mathrm{red} \propto \phi_\mathrm{eff}^m$ with $m \approx 13.6$ in the supercooled and $m \approx 7.6$ in the glassy regime, see Figure 6.6 on page 86, allows for an estimation of the hardness of the interaction potential between the particles. Comparison to power law increases of ultra-soft and hard particles found in literature[20,108] reveals that the interaction potential of the model system used within this thesis is close to the interaction potential of the hard particles, see Figure 6.7 on page 88. This shows that the model system fulfills the requirement of an interaction potential close to hard spheres, although particles with a polymeric shell were used as model system, which allow for a precise adjustment of the effective volume fraction.
The MCT predictions of the linear response modulus G'_red of the glass-forming colloids is in agreement with the experiment in both the supercooled and the glassy state, see Figure 6.5 on page 84. However, G''_red is only matched sufficiently in the supercooled region with a certain distance of $\Delta\phi_\mathrm{eff} \geq 0.02$ to the glass transition volume fraction. Close to ϕ_g, the distribution of α-relaxation times broadens for increasing ϕ_eff for particles of different sizes due to heterogeneities in the structure, resulting in a smoother transition from the minimum to the maximum in G''_red. Additionally, the softness of the particles contributes to this smoother transition. Both the softness and the distribution of the α-relaxation time of the particles cannot be depicted by MCT as the predictions are based on monomodal hard sphere systems with a sharp relaxation time. In the glassy state the behavior of the suspension in the low frequency regime is not matched as the α-relaxation vanishes completely in the MCT predictions, while it only slows down considerably in the real system.
Furthermore, the MCT predictions were made with a variant wave vector q showing an unexpected q-dependence of the moduli close to the glass transition volume fraction, see Figure 6.8 on page 89. The same behavior was observed in experiments with increasing

the plate diameter of the used geometry, see Figure 6.9 on page 90. The deviations in the moduli depending on q or the diameter of the geometry may arise from long-range stress correlations, which depend on the boundaries of the system.

In addition to the linear rheological characterization using SAOS, the yielding behavior of the colloidal suspension in the glassy state under steady shear was investigated. The overshoot in transient stress at $\gamma \approx 7\,\%$ to $15\,\%$ can be attributed to the formation of a lamellar microstructure which increases the flowability of the system in the steady state, see Figure 6.11 on page 93. The amplitude of the overshoot stress σ_{peak} and the steady state stress σ_{st} depend on the shear rate and the ϕ_{eff}. For the measurement parameters ranging from $\dot{\gamma} = 2 \times 10^{-5}\,\mathrm{s}^{-1}$ to $10\,\mathrm{s}^{-1}$ and $\phi_{\mathrm{eff}} = 0.76$ to 0.83, they are between $\sigma_{\mathrm{peak}} \approx 9 \times 10^{-1}\,\mathrm{Pa}$ to $4\,\mathrm{Pa}$ and $\sigma_{\mathrm{st}} \approx 6 \times 10^{-1}\,\mathrm{Pa}$ to $3\,\mathrm{Pa}$, see Figure 6.12 on page 95. No conclusive evidence about the ratio between the static and the dynamic yield stress could be drawn. The time to rebuild the disordered microstructure after preshear exceeded the waiting time $t_1 > 14\,000\,\mathrm{s} > t_{\mathrm{w}} = 6000\,\mathrm{s}$ for low shear rates $\dot{\gamma} < 3.73 \times 10^{-4}\,\mathrm{s}^{-1}$. Although, the evaporation of the aqueous suspending fluid was minimized by sealing the gap of the geometry with silicon oil, the total measurement time was restricted due to evaporation at long time scales, see Figure A.3.9 on page 156.

The influence of a steady shear motion on the relaxation times of the colloidal suspension in the glassy and the supercooled state was investigated by applying parallel superposition of steady and oscillatory shear. The steady shear leads to a liquidification of the colloidal suspension. An inverse proportionality of the normalized α-relaxation time on the normalized shear rate, $\frac{\tau_\alpha}{\tau_0} \propto Pe_0^{-1}$, was found in both experiment and MCT predictions. The normalized characteristic time shows a power law decrease of $\frac{t_{\mathrm{min}}}{\tau_0} \propto Pe_\omega^{-d}$ with $d = 0.55$ in experiment and $d = 0.68$ in MCT predictions.

Experiment and MCT predictions both show an independence of the α-relaxation on ϕ_{eff} for a sheared sample in the supercooled as well as in the glassy state, see Figure 6.16 on page 101. This is in agreement with the work of Jacob *et al.*[109], who observed this independence in the glassy state for distinct $\dot{\gamma}$ values. In contrast to their interpretations, within this thesis it is concluded that the independence of ϕ_{eff} holds only for a sheared system. No conclusions about the quiescent state can be drawn from the sheared state.

In the third part of the thesis, the response of the glass-forming colloidal suspension in the supercooled and the glassy state to a nonlinear oscillatory shear deformation was investigated. The focus of the investigation was the characterization of the frequency dependence of the anharmonicity of the stress response. Using the frequency sweep MAOS introduced by Singh *et al.*[81], the anharmonicity of a glass-forming colloidal suspension was determined over a wide range of frequencies and volume fractions, allowing a thorough comparison with MCT predictions.

In the supercooled region, Q_0 shows a maximum of 2 to 6 depending on ϕ_{eff}. Futhermore, Q_0 collapses for different ϕ_{eff} in the high frequency region and shows a scaling of $Q_0 \propto Pe_\omega^{-0.32}$ both in experiment and MCT predictions. The experimental data support the MCT prediction of a power law increase of the anharmonicity with decreasing frequency that is independent of the distance to the glass transition. The data of Seyboldt *et al.*[29]

suggested the same finding, however high scattering complicated the interpretation of the data. Furthermore, the findings of this thesis reveal that Q_0 exhibits the scaling laws predicted by MCT in the three different frequency regions of $Q_0 \propto Pe_\omega^2$ in the low, $Q_0 \propto Pe_\omega^{0.69}$ in the medium and $Q_0 \propto Pe_\omega^{-0.32}$ in the high frequency regime, see Figure 7.7 on page 116. Additionally, the principle course of $Q_0(Pe_\omega)$ obtained from experiment and MCT superimposes completely, see Figure 7.9 on page 118.

Moreover, for the first time, the frequency dependence of the anharmonicity in the glassy state was thouroughly investigated with experiments and MCT predictions. The MCT predictions of Q_0 in the glassy state show the same scaling of $Q_0 \propto Pe_\omega^{-0.32}$ in the high frequency regime as Q_0 in the supercooled state. This predicted scaling is revealed by the experimental results. Furthermore, the MCT predictions of Q_0 collapse for different ϕ_{eff} ranging from the supercooled to the glassy state. In contrast, in the experiments a decrease of Q_0 with increasing ϕ_{eff} was observed, see Figure 7.10 on page 120.

Since Q_0 is defined as $\lim_{\gamma_0 \to 0} \frac{I_3}{I_1 \gamma_0^2}$ this decrease can either be caused by a decrease of the third harmonic or an increase of the fundamental of the sample with ϕ_{eff}. The intrinsic third harmonic $[I_3] = \lim_{\gamma_0 \to 0} \frac{I_3}{\gamma_0^3}$ shows a collapse in experiment and MCT predictions, while the intrinsic fundamental $[I_1] = \lim_{\gamma_0 \to 0} \frac{I_1}{\gamma_0}$ increases for increasing ϕ_{eff} in the experiment. The decrease in Q_0 arises from the higher elasticity of the sample, which is not captured by MCT, rather than by a decrease in the intrinsic third harmonic.

The frequency dependence was investigated in the entire frequency range in which Q_0 was accessible. For lower frequencies, an unexpected increase in $I_{3/1} \propto \gamma_0^4$ was observed, see Figure 7.4 on page 109, which may be attributed to the localization of the deformation of the sample. Since Q_0 is based on a quadratic scaling of $I_{3/1}$, this unexpected increase causes that Q_0 cannot be determined.

This work provided an extensive dataset on the rheological behavior of a glass-forming colloidal suspension in both the supercooled and glassy regime. It was shown, that several rheological results are consistent with the predictions of MCT. This agreement between rheological and predicted results confirms MCT to be a powerful tool for predicting the rheological behavior of glass-forming colloidal suspensions.

Outlook

The extensive data set of the rheological behavior of a glass-forming colloidal model system under various shear deformations provided by this work can serve as a foundation for future studies using MCT. The detailed measurements for various effective volume fractions in the glassy and supercooled states, across broad angular frequency ranges of $10^{-4}\,\text{rad}\,\text{s}^{-1}$ to $10^{2}\,\text{rad}\,\text{s}^{-1}$ and broad shear rate ranges of $10^{-4}\,\text{s}^{-1}$ to $10^{2}\,\text{s}^{-1}$, allowed and continue to allow for detailed comparisons to MCT predictions. Especially, MCT predictions of the transient stress at the onset of flow would be beneficial and would additionally allow for comparison to the steady state behavior and the static and dynamic yield stress of the colloidal suspension.

The agreement between the MCT predictions and the experimental results of the bimodal system of the principle characteristics and the scaling laws of Q_0 shows the universality

of the critical nonlinearity at the MCT glass transition. In future work, a more detailed analysis of MCT predictions, with input parameters obtained from the measured linear rheology of the bimodal system, would allow a comparison between the absolute Q_0 values obtained from MCT predictions and experiment.

A limiting factor in the quality of the conducted studies was the evaporation of the aqueoues dispersion medium. For future works, it would be beneficial to develop a model system with a non-evaporating suspending fluid. A possible model system could be PMMA particles dispersed in a solvent with low vapour pressure, for example *cis*-decalin or octadecane/bromonaphthalene mixtures. A model system like this would allow the investigations of further open scientific questions. For one, the open question of the ratio between the dynamic and the static yield stress in colloidal suspensions could be addressed. Secondly, with this model system, orthogonal superposition (OSP) of oscillatory and steady shear motion would be possible. This rheological experiment would prevent the artifacts from the coupling of the oscillatory shear motion and the steady shear motion observed in parallel superposition rheology. However, this measurement technique requires a specific geometry, in which the evaporation of the dispersion medium could not be controlled within this thesis. Therefore, this experiment could not be conducted. Third, the non-evaporating model system could be used to extend the experiments to other deformation types like extension, which can be applied with a capillary breakup extensional rheometer. In this experimental set-up, the sample is put in between two plates, which are moved apart to apply the extensional deformation and investigate the capillary build between the plates. Sealing with silicon oil is not possible in this set-up and evaporation intervenes stronger than in the shear rheological measurements as the surface to volume ratio is high.

Furthermore, the PMMA particles exhibit a harder interaction potential between the particles compared to the PS-PNIPAm core-shell particles utilized as model system in this thesis. Comparing the rheological response of the PMMA particles with that of the PS-PNIPAm particles would allow an investigation of the effect of particle softness on the rheological results.

Moreover, rheological measurements provide only insights in the macroscopic average shear response. To gain a deeper understanding of the local dynamics within the glass-forming suspension, spatially resolved techniques are required. For instance, combining rheology with confocal microscopy or velocimetry could provide further understanding. Observing the motion of fluorescent tracer particles in the suspension using microscopy could provide the mean square displacement of the tracer particles in the quiescent state. By using a shear cell or a coupling with a rheometer, this could be extended to sheared states. These findings could then be compared with predictions from MCT and results from Brownian dynamic simulations.

Bibliography

[1] Israelachvili, J. N., *Intermolecular and Surface Forces*, 3rd ed.; Elsevier: Amsterdam, Netherlands, 2011.

[2] Jones, R. G.; Kahovec, J.; Stepto, R.; Wilks, E. S.; Hess, M.; Kitayama, T.; Metanomski, W. V. *Chemistry International – Newsmagazine for IUPAC* **2009**, *31*, 32–33.

[3] Stepto, R. F. T. *Pure. Appl. Chem.* **2009**, *81*, 351–353.

[4] Forrest, S. R.; Thompson, M. E. *Chem. Rev.* **2007**, *107*, 923–925.

[5] Hüttner, S.; Sommer, M.; Steiner, U.; Thelakkat, M. *Appl. Phys. Lett.* **2010**, *96*, 073503.

[6] Ediger, M. D.; Angell, C. A.; Nagel, S. R. *J. Phys. Chem.* **1996**, *100*, 13200–13212.

[7] Koumakis, N.; Schofield, A. B.; Petekidis, G. *Soft Matter* **2008**, *4*, 2008.

[8] Phan, S.-E.; Russel, W. B.; Zhu, J.; Chaikin, P. M. *J. Chem. Phys.* **1998**, *108*, 9789–9795.

[9] Gasser, U. *J. Phys.: Condens. Matter* **2009**, *21*, 203101.

[10] Pusey, P. N.; van Megen, W. *Phys. Rev. Lett.* **1987**, *59*, 2083–2086.

[11] Mason, T. G.; Bibette, J.; Weitz, D. A. *Phys. Rev. Lett.* **1995**, *75*, 2051–2054.

[12] Senff, H.; Richtering, W.; Norhausen, C.; Weiss, A.; Ballauff, M. *Langmuir* **1999**, *15*, 102–106.

[13] Fuchs, M.; Cates, M. E. *Phys. Rev. Lett.* **2002**, *89*, 248304.

[14] Heymann, L.; Peukert, S.; Aksel, N. *J. Rheol.* **2002**, *46*, 93–112.

[15] Petekidis, G.; Vlassopoulos, D.; Pusey, P. N. *Farad. Disc.* **2003**, *123*, 287–302.

[16] Besseling, R.; Weeks, E. R.; Schofield, A. B.; Poon, W. C. K. *Phys. Rev. Lett.* **2007**, *99*, 028301.

[17] Siebenbürger, M.; Fuchs, M.; Winter, H.; Ballauff, M. *J. Rheol.* **2009**, *53*, 707–726.

[18] Brader, J. M.; Siebenbürger, M.; Ballauff, M.; Reinheimer, K.; Wilhelm, M.; Frey, S. J.; Weysser, F.; Fuchs, M. *Phys. Rev. E* **2010**, *82*, 1–20.

[19] Van der Vaart, K.; Rahmani, Y.; Zargar, R.; Hu, Z.; Bonn, D.; Schall, P. *J. Rheol.* **2013**, *57*, 1195–1209.

[20] Koumakis, N.; Brady, J. F.; Petekidis, G. *Phys. Rev. Lett.* **2013**, *110*, 178301.

[21] Poulos, A. S.; Renou, F.; Jacob, A. R.; Koumakis, N.; Petekidis, G. *Rheol. Acta.* **2015**, *54*, 715–724.

[22] Siebenbürger, M.; Fuchs, M.; Ballauff, M. *Soft Matter* **2012**, *8*, 4014.

[23] Amann, C. M.; Siebenbürger, M.; Ballauff, M.; Fuchs, M. *J. Phys.: Condens. Matter* **2015**, *27*, 194121.

[24] Kallus, S.; Willenbacher, N.; Kirsch, S.; Distler, D.; Neidhöfer, T.; Wilhelm, M.; H.W., S. *Rheol. Acta.* **2001**, *40*, 552–559.

[25] Klein, C. O.; Spiess, H. W.; Calin, A.; Balan, C.; Wilhelm, M. *Macromolecules* **2007**, *40*, 4250–4259.

[26] Fuchs, M.; Cates, M. E. *J. Rheol.* **2009**, *53*, 957–1000.

[27] Brader, J. M.; Cates, M. E.; Fuchs, M. *Phys. Rev. Lett.* **2008**, *101*, 138301.

[28] Siebenbürger, M.; Ballauff, M.; Voigtmann, T. *Phys. Rev. Lett.* **2012**, *108*, 255701.

[29] Seyboldt, R.; Merger, D.; Coupette, F.; Siebenbürger, M.; Ballauff, M.; Wilhelm, M.; Fuchs, M. *Soft Matter* **2016**, *12*, 8825–8832.

[30] Matyjaszewski, K.; Spanswick, J. *Mater. Today.* **2005**, *8*, 26–33.

[31] Davis, T. P.; Matyjaszewski, K., *Handbook of Radical Polymerization*; Wiley-Interscience: Hoboken, NJ, USA, 2002.

[32] Biederbick, K., *Kunststoffe*, 4th ed.; Vogel-Verlag: Würzburg, Germany, 1977.

[33] Obrecht, W.; Lambert, J.; Happ, M.; Oppenheimer-Stix, C.; Dunn, J.; Krüger, R. In *Ullmann's Encyclopedia of Industrial Chemistry*; Wiley: Hoboken, NJ, USA, 2003.

[34] Hefter, G. T. Solubility of Styrene in Water `https://srdata.nist.gov/solubility/IUPAC/SDS-38/SDS-38-pages\_1.pdf` (accessed 08/15/2023).

[35] Smith, W. V.; Ewart, R. H. *J. Chem. Phys.* **1948**, *16*, 592–599.

[36] Wang, A.; Wang, W. In *Kirk-Othmer Encyclopedia of Chemical Technology*; John Wiley & Sons, Inc: Hoboken, NJ, USA, 2000.

[37] Fitch, R. M.; Prenosil, M. B.; Sprick, K. J. *J. Polym. Sci. Pol. Sym.* **1969**, *27*, 95–118.

[38] Lovell, P. A.; Schork, F. J. *Biomacromolecules* **2020**, *21*, 4396–4441.

[39] Wang, Q.; Fu, S.; Yu, T. *Prog. Polym. Sci.* **1994**, *19*, 703–753.

[40] Odian, G., *Principles of Polymerization*; John Wiley & Sons: Hoboken, NJ, USA, 2004.

[41] Hansen, F. K.; Ugelstad, J. *J. Polym. Sci. Pol. Chem.* **1978**, *16*, 1953–1979.

[42] Pusch, J.; van Herk, A. M. *Macromolecules* **2005**, *38*, 6909–6914.

[43] Modena, M. M.; Rühle, B.; Burg, T. P.; Wuttke, S. *Adv. Mater.* **2019**, *31*.

[44] Stokes, D., *Principles and Practice of Variable Pressure/Environmental Scanning Electron Microscopy (VP-ESEM)*; John Wiley & Sons: Chichester, UK, 2008.

[45] Arndt, K.-F.; Müller, G., *Polymer Charakterisierung*; Carl Hanser Verlag: München, Germany, 1996.

[46] Stetefeld, J.; McKenna, S. A.; Patel, T. R. *Biophys. Rev.* **2016**, *8*, 409–427.

[47] Goldstein, J. I.; Newbury, D. E.; Michael, J. R.; Ritchie, N. W.; Scott, J. H. J.; Joy, D. C., *Scanning Electron Microscopy and X-Ray Microanalysis*; Springer: New York, NY, USA, 2018.

[48] Butt, H.-J.; Graf, K.; Kappl, M., *Physics and Chemistry of Interfaces*, 4th ed.; Wiley-VCH: Weinheim, Germany, 2023.

[49] Derjaguin, B. V. and Landau, L. D. *Acta. Physico. Chim.* **1941**, *14*, 633.

[50] Verwey, E. J. W. and Overbeek, J. Th. G., *Theory of the Stability of Lyophobic Colloids*; Elsevier/Academic Press: Amsterdam, Netherlands, 1948.

[51] Bhattacharjee, S.; Elimelech, M.; Borkovec, M. *Croat. Chem. Acta.* **1998**, *71*, 883–903.

[52] Randall, C.; van Tassel, J. *Encyclopedia of Materials: Science and Technology* **2001**, 2733–2738.

[53] Fernández-Barbero, A.; Martın-Rodrıguez, A.; Callejas-Fernández, J.; Hidalgo-Alvarez, R. *J. Colloid. Interf. Sci.* **1994**, *162*, 257–260.

[54] Dealy, J. M.; Read, D. J.; Larson, R. G., *Structure and Rheology of Molten Polymers: From Structure to Flow Behavior and Back Again*; Hanser Verlag: München, Germany, 2006.

[55] Barnes, H. A., *Handbook of Elementary Rheology*; University of Wales - Institute of Non-Newtonian Fluid Mechanics: Aberystwyth, UK, 2000.

[56] Haynes, W. M., *CRC Handbook of Chemistry and Physics*, 95th ed.; CRC Press Taylor & Francis Group: Boca Raton, USA, 2014.

[57] Mezger, T. G., *Applied Rheology: With Joe Flow on Rheology Road*, 10th ed.; Anton Paar GmbH: Graz, Austria, 2023.

[58] Malkin, A. Y., *Rheology Fundamentals*; ChemTec Publ: Toronto, Canada, 1994.

[59] Crandall, S. H.; Dahl, N. C.; Lardner, T. J.; Sivakumar, M. S., *An Introduction to Mechanics of Solids*, 3rd ed.; Tata McGraw-Hill Education Private Limited: New Dehli, India, 2012.

[60] Pries, A. R.; Neuhaus, D.; Gaehtgens, P. *Am. J. Physiol.-Heart. C.* **1992**, *263*, H1770–H1778.

[61] Yanniotis, S.; Skaltsi, S.; Karaburnioti, S. *J. Food. Eng.* **2006**, *72*, 372–377.

[62] Ostwald, W. *Kolloid. Z.* **1925**, *36*, 157–167.

[63] Cross, M. M. *Rheol. Acta.* **1979**, *18*, 609–614.

[64] Yasuda, K.; Armstrong, R. C.; Cohen, R. E. *Rheol. Acta.* **1981**, *20*, 163–178.

[65] Bingham, E. C., *An Investigation of the Laws of Plastic Flow*; 278; US Government Printing Office: Washington D.C., USA, 1917.

[66] Herschel, W. H.; Bulkley, R. *Kolloid. Z.* **1926**, *39*, 291–300.

[67] Larson, R. G., *The Structure and Rheology of Complex Fluids*; Oxford University Press: New York, NY, USA, 1999.

[68] Morrison, F. A., *Understanding Rheology*; Topics in Chemical Engineering; Oxford University Press: New York, NY, USA, 2001.

[69] Wilhelm, M.; Maring, D.; Spiess, H.-W. *Rheol. Acta.* **1998**, *37*, 399–405.

[70] Wilhelm, M.; Reinheimer, P.; Ortseifer, M. *Rheol. Acta.* **1999**, *38*, 349–356.

[71] Wilhelm, M.; Reinheimer, P.; Ortseifer, M.; Neidhöfer, T.; Spiess, H.-W. *Rheol. Acta.* **2000**, *39*, 241–246.

[72] Hyun, K.; Wilhelm, M. *Macromolecules* **2009**, *42*, 411–422.

[73] Hyun, K.; Wilhelm, M.; Klein, C. O.; Cho, K. S.; Nam, J. G.; Ahn, K. H.; Lee, S. J.; Ewoldt, R. H.; McKinley, G. H. *Prog. Polym. Sci.* **2011**, *36*, 1697–1753.

[74] Mason T. G., a. D. A. W. *Phys. Rev. Lett.* **1995**, *75*, 2770–2773.

[75] Carrier, V.; Petekidis, G. *J. Rheol.* **2009**, *53*, 245–273.

[76] Pham, K. N.; Petekidis, G.; Vlassopoulos, D.; Egelhaaf, S. U.; Pusey, P. N.; Poon, W. C. K. *Europhys. Lett.* **2006**, *75*, 624–630.

[77] Wilhelm, M. *Macromol. Mater. Eng.* **2002**, *287*, 83–105.

[78] Sagis, L. M.; Ramaekers, M.; van der Linden, E. *Phys. Rev. E.* **2001**, *63*, 051504.

[79] Cziep, M. A.; Abbasi, M.; Heck, M.; Arens, L.; Wilhelm, M. *Macromolecules* **2016**, *49*, 3566–3579.

[80] Pusey, P. N. *Les Houches* **1991**, *51*.

[81] Singh, P. K.; Soulages, J. M.; Ewoldt, R. H. *J. Rheol.* **2018**, *62*, 277–293.

[82] Astarita, G.; Jongschaap, R. *J. Non-Newton. Fluid.* **1978**, *3*, 281–287.

[83] Mewis, J.; Wagner, N. J., *Colloidal Suspension Rheology*, 1st ed.; Cambridge University Press: Cambridge, UK, 2012.

[84] Einstein, A. *Ann. Phys.* **1906**, 289–306.

[85] Einstein, A. *Ann. Phys.* **1911**, *34*, 591–592.

[86] Batchelor, G. K. *J. Fluid Mech.* **1977**, *83*, 97–117.

[87] Krieger, I. M.; Dougherty, T. J. *T. Soc. Rheol.* **1959**, *3*, 137–152.

[88] Krieger, I. M. *Adv. Colloid. Interfac.* **1972**, *3*, 111–136.

[89] Quemada, D. *Rheol. Acta.* **1977**, *16*, 82–94.

[90] Quemada, D. *Rheol. Acta.* **1978**, *17*, 643–653.

[91] Maron, S. H.; Pierce, P. E. *J. Colloid. Sci.* **1956**, *11*, 80–95.

[92] Einstein, A. *Ann. Phys.* **1905**, *322*, 549–560.

[93] Hunter, G. L.; Weeks, E. R. *Rep. Prog. Phys.* **2012**, *75*.

[94] Merger, D. *Large Amplitude Oscillatory Shear Investigations of Colloidal Systems: Experiments and Constitutive Model Predictions*, Karlsruhe, Germany, Karlsruhe Institute of Technology, PhD thesis, **2015**.

[95] Bengtzelius, U.; Götze W. and Sjölander, A. *J. Phys. C. Solid. State.* **1984**, *17*, 5915–5934.

[96] Götze, W. *Z. Phys. B. Con. Mat.* **1985**, *60*, 195–203.

[97] Fuchs, M.; Cates, M. E. *Farad. Disc.* **2003**, *123*, 267–286.

[98] Brader, J. M.; Voigtmann, T.; Fuchs, M.; Larson, R. G.; Cates, M. E. *P. Natl. Acad. Sci. USA.* **2009**, *106*, 15186–15191.

[99] Van Megen, W.; Pusey, P. N. *Phys. Rev. A.* **1991**, *43*, 5429–5441.

[100] Willenbacher, N.; Vesaratchanon, J. S.; Thorwarth, O.; Bartsch, E. *Soft Matter* **2011**, *7*, 5777.

[101] Henrich, O.; Weysser, F.; Cates, M. E.; Fuchs, M. *Philos. T. Roy. Soy. A.* **2009**, *367*, 5033–5050.

[102] Zwanzig, R.; Mountain, R. D. *J. Chem. Phys.* **1965**, *43*, 4464–4471.

[103] Mori, H. *Prog. Theor. Phys.* **1965**, *33*, 423–455.

[104] Vogel, F.; Fuchs, M. *Eur. Phys. J. E* **2020**, *43*, 70.

[105] Koumakis, N.; Pamvouxoglou, A.; Poulos, A. S.; Petekidis, G. *Soft Matter* **2012**, *8*, 4271.

[106] Petekidis, G.; Moussaïd, A.; Pusey, P. N. *Phys. Rev. E.* **2002**, *66*, 051402.

[107] Petekidis, G.; Vlassopoulos, D.; Pusey, P. N. *J. Phys.-Condens. Mat.* **2004**, *16*, 3955–3963.

[108] Le Grand, A.; Petekidis, G. *Rheol. Acta.* **2008**, *47*, 579–590.

[109] Jacob, A. R.; Poulos, A. S.; Kim, S.; Vermant, J.; Petekidis, G. *Phys. Rev. Lett.* **2015**, *115*, 218301.

[110] Bryant, G.; Williams, S. R.; Qian, L.; Snook, I. K.; Perez, E.; Pincet, F. *Phys. Rev. E.* **2002**, *66*, 060501.

[111] Deike, I.; Ballauff, M.; Willenbacher, N.; Weiss, A. *J. Rheol.* **2001**, *45*, 709–720.

[112] Crassous, J. J.; Siebenbürger, M.; Ballauff, M.; Drechsler, M.; Henrich, O.; Fuchs, M. *J. Chem. Phys.* **2006**, *125*, 204906.

[113] Crassous, J. J.; Siebenbürger, M.; Ballauff, M.; Drechsler, M.; Hajnal, D.; Henrich, O.; Fuchs, M. *J. Chem. Phys.* **2008**, *128*, 204902.

[114] Halperin, A.; Kröger, M.; Winnik, F. M. *Angew. Chem.-Ger. Edit.* **2015**, *127*, 15558–15586.

[115] Hyun, K.; Nam, J. G.; Wilhellm, M.; Ahn, K. H.; Lee, S. J. *Rheol. Acta.* **2006**, *45*, 239–249.

[116] *Methods for Determination of Particle Size Distribution Part 8: Photon Correlation Spectroscopy*; Standard; Geneva, Switzerland: International Organization for Standardization, 1996.

[117] Russel, W. *J. Rheol.* **1980**, *24*, 287–317.

[118] Bartlett, P.; Ottewill, R. H.; Pusey, P. N. *J. Chem. Phys.* **1990**, *93*, 1299–1312.

[119] Dingenouts, N.; Norhausen, C.; Ballauff, M. *Macromolecules* **1998**, *31*, 8912–8917.

[120] Fischer, L.; Maier, M.; Dingenouts, N.; Hirschberg, V.; Wittemann, A.; Fuchs, M.; Wilhelm, M. *J. Rheol.* **2024**, *68*, 709–729.

[121] Dyre, J. C. *Rev. Mod. Phys.* **2006**, *78*, 953–972.

[122] Schweizer, K. S.; Saltzman, E. J. *J. Chem. Phys.* **2003**, *119*, 1181–1196.

[123] Woodcock, L. V. *Ann. NY Acad. Sci.* **1981**, *371*, 274–298.

[124] Pusey, P. N.; van Megen, W. *Nature* **1986**, *320*.

[125] Gotze, W.; Sjorgen, L. *Rep. Prog. Phys.* **1992**, 241–376.

[126] Donev, A.; Torquato, S.; Stillinger, F. H. *Phys. Rev. E.* **2005**, *71*, 011105.

[127] Buscall, R.; Goodwin, J. W.; Hawkins M. W. and Ottewill, R. H. *J. Chem. Soc. Farad. T. 1* **1982**, *78*, 2889–2899.

[128] Wagner, N. J. *J. Colloid. Interf. Sci.* **1993**, *161*, 169–181.

[129] Raynaud, L.; Ernst, B.; Verge, C.; Mewis, J. *J. Colloid. Interf. Sci.* **1996**, *181*, 11–19.

[130] Paulin, S. E., Ackerson, B. J. and Wolfe, M. S. *J. Colloid. Interf. Sci.* **1996**, *178*, 251–262.

[131] Lennard-Jones, J. E. *P. Phys. Soc.* **1931**, *43*, 461–482.

[132] Fischer, J.; Wendland, M. *Fluid. Phase. Equilibr.* **2023**, *573*, 113876.

[133] Ozon, F.; Petekidis, G.; Vlassopoulos, D. *Ind. Eng. Chem. Res.* **2006**, *45*, 6946–6952.

[134] Stieger, M.; Pedersen, J. S.; Lindner, P.; Richtering, W. *Langmuir* **2004**, *20*, 7283–7292.

[135] Macosko, C. W., *Rheology: Principles, Measurements and Applications*; Wiley: Hoboken, NJ, USA, 1994.

[136] Giacomin, A. J.; Dealy, J. M., *Using Large-Amplitude Oscillatory Shear*, 2nd ed.; Collyer, A. A., Clegg, D. W., Eds.; Springer: Dordrecht, Netherlands, 1998.

[137] TA Instruments. ARES-G2 Specifications `https://www.tainstruments.com/ares-g2/` (accessed 05/27/2024).

[138] Seth, J. R.; Mohan, L.; Locatelli-Champagne, C.; Cloitre, M.; Bonnecaze, R. T. *Nat. Mater.* **2011**, *10*, 838–843.

[139] Meeker, S. P.; Bonnecaze, R. T.; Cloitre, M. *J. Rheol.* **2004**, *48*, 1295–1320.

[140] Cloitre, M.; Borrega, R.; Monti, F.; Leibler, L. *Phys. Rev. Lett.* **2003**, *90*, 068303.

[141] Fuchs, M.; Ballauff, M. *J. Chem. Phys.* **2005**, *122*, 094707.

[142] Varnik, F.; Bocquet, L.; Barrat, J.-L. *J. Chem. Phys.* **2004**, *120*, 2788–2801.

[143] Balmforth, N. J.; Frigaard, I. A.; Ovarlez, G. *Annu. Rev. Fluid Mech.* **2014**, *46*, 121–146.

[144] Coussot, P. *J. Non-Newton. Fluid.* **2014**, *211*, 31–49.

[145] Booij, H. C. *Rheol. Acta.* **1966**, *5*, 215–221.

[146] Vermant, J.; Walker, L.; Moldenaers, P.; Mewis, J. *J. Non-Newton. Fluid.* **1998**, *79*, 173–189.

[147] Eisenmann, C.; Kim, C.; Mattsson, J.; Weitz, D. A. *Phys. Rev. Lett.* **2010**, *104*, 035502.

[148] Hirschberg, V.; Faust, L.; Rodrigue, D.; Wilhelm, M. *Macromolecules* **2020**, *53*, 5572–5587.

[149] Natalia, I.; Ewoldt, R. H.; Koos, E. *J. Rheol.* **2020**, *64*, 625–635.

[150] Natalia, I.; Ewoldt, R. H.; Koos, E. *J. Rheol.* **2022**, *66*, 17–30.

[151] Bower, C.; Gallegos, C.; Mackley, M. R.; Madiedo, J. M. *Rheol. Acta.* **1999**, *38*, 145–159.

[152] Bossard, F.; Moan, M.; Aubry, T. *J. Rheol.* **2007**, *51*, 1253–1270.

[153] Donley, G. J.; Singh, P. K.; Shetty, A.; Rogers, S. A. *P. Natl. Acad. Sci. USA* **2020**, *117*, 21945–21952.

[154] Lee, J. C.-W.; Hong, Y.-T.; Weigandt, K. M.; Kelley, E. G.; Kong, H.; Rogers, S. A. *J. Rheol.* **2019**, *63*, 863–881.

[155] Poulos, A. S.; Stellbrink, J.; Petekidis, G. *Rheol. Acta.* **2013**, *52*, 785–800.

[156] Donley, G. J.; Narayanan, S.; Wade, M. A.; Park, J. D.; Leheny, R. L.; Harden, J. L.; Rogers, S. A. *P. Natl. Acad. Sci. USA* **2023**, *120*.

[157] Dinkgreve, M.; Paredes, J.; Denn, M. M.; Bonn, D. *J. Non-Newton. Fluid.* **2016**, *238*, 233–241.

[158] Donley, G. J.; Hyde, W. W.; Rogers, S. A.; Nettesheim, F. *Rheol. Acta.* **2019**, *58*, 361–382.

[159] Griebler, J. J.; Rogers, S. A. *Phys. Fluids.* **2022**, *34*, 023107.

[160] Fernandes, R. R.; Andrade, D. E. V.; Franco, A. T.; Negrão, C. O. R. *J. Rheol.* **2017**, *61*, 893–903.

[161] Kamani, K. M.; Donley, G. J.; Rao, R.; Grillet, A. M.; Roberts, C.; Shetty, A.; Rogers, S. A. *J. Rheol.* **2023**, *67*, 331–352.

[162] Park, J. D.; Rogers, S. A. *Phys. Fluids.* **2020**, *32*, 063102.

[163] Aime, S.; Truzzolillo, D.; Pine, D. J.; Ramos, L.; Cipelletti, L. *Nat. Phys.* **2023**, *19*, 1673–1679.

[164] Kamani, K.; Donley, G. J.; Rogers, S. A. *Phys. Rev. Lett.* **2021**, *126*, 218002.

[165] Helgeson, M. E.; Wagner, N. J.; Vlassopoulos, D. *J. Rheol.* **2007**, *51*, 297–316.

[166] Wagner, M. H.; Rolón-Garrido, V. H.; Hyun, K.; Wilhelm, M. *J. Rheol.* **2011**, *55*, 495–516.

[167] Giacomin, A. J.; Gilbert, P. H.; Merger, D.; Wilhelm, M. *Rheol. Acta.* **2015**, *54*, 263–285.

[168] Coupette, F. *Third Harmonic of Large Amplitude Oscillatory Shearing in Quasistatic Approximation*, Konstanz, Germany, University of Konstanz, Bachelor thesis, **2015**.

[169] Merola, M. C.; Parisi, D.; Truzzolillo, D.; Vlassopoulos, D.; Deepak, V. D.; Gauthier, M. *J. Rheol.* **2018**, *62*, 63–79.

[170] Hirschberg, V.; Lyu, S.; Schußmann, M. G. *J. Rheol.* **2023**, *67*, 403–415.

[171] Götze, W., *Complex Dynamics of Glass-Forming Liquids: A Mode-Coupling Theory*; Oxford University Press: Oxford, UK, 2009; Vol. 143.

[172] Voigtmann, T. *Europhys. Lett.* **2011**, *96*, 36006.

[173] Plüisch, C. S.; Stuckert, R.; Wittemann, A. *Nanomaterials-Basel* **2021**, *11*.

Appendix

A.1 Materials and Methods

A.1.1 Materials and Purification

A.1.1.1 Purification of Monomers

Styrene (99 %, Acros) was purified by destillation under reduced pressure ($T = 75\,^{\circ}\mathrm{C}$, $p = 50\,\mathrm{mbar}$).

A.1.1.2 Further Chemicals

Core-Shell Particles
N-isopropylacrylamide (99 %, Fisher Scientific), sodium dodecyl sulfate (98 %), potassium persulfate (≥99 %, Merck), *N,N'*-methylene bisacrylamide (99 %, Sigma-Aldrich)

Rheological Measurements
Potassium chloride (≥99 %, Merck)

Fluorescent Core-Shell Particles
Nile red (for microscopy, Sigma-Aldrich), tetrahydrofuran (99.5 %, Roth)

A.1.2 Synthesis

Core-Shell Particles
The synthesis of the PS-PNIPAm core-shell systems was conducted in a two-step synthesis procedure adapted from Dingenouts *et al.*[119]. The first synthesis step of the polystyrene (PS) core was carried out as an emulsion polymerization as a free radical polymerization and the second synthesis step of the crosslinked poly(*N*-isopropylacrylamide) (PNIPAm) shell was carried out as a sedded emulsion polymerization as a free radical polymerization.

PS-core 18.82 g *N*-isopropylacrylamide (0.166 mol) and 7.00 g sodium dodecyl sulfate (0.024 mol) were dissolved in 800 mL deionized water under a stirring speed of 500 RPM for 10 min at room temperature. 391 mL styrene (355.38 g, 3.412 mol) were added and the remaining oxygen in the emulsion removed by alternating degassing and flushing with argon three times. The reaction mixture was heated to 80 °C. A solution of 0.754 g potassium

persulfate (2.79 mmol) dissolved in 20 mL deionized water were added. The resulting mixture was stirred for 5.5 h at 80 °C. After the suspension was cooled down to 60 °C, the mixture was filtered through glass wool. The resulting colloidal suspension was dialized for 3 weeks against deionized water. The water was changed every day for the first week and every second day for the second and third week.

Table A1: Synthesis details of the core synthesis: mass of the surfactant sodium dodecyl sulfate (m_{SDS}), monomer styrene (m_{styrene}), the comonomer *N*-isopropylacrylamide (m_{NIPAm}), the initiator potassium persulfate (m_{KPS}), and the dispersion medium water, the mass fraction at which the synthesis was performed.

Core Particle	m_{SDS} [g]	m_{styrene} [g]	m_{NIPAm} [g]	m_{KPS} [g]	w [wt%]
PScore-47	7.02	353.34	18.84	0.757	33.7
PScore-40	7.02	353.34	18.85	0.760	33.7
PScore-37	14.00	356.96	18.83	0.752	34.3
PScore-33	14.10	356.96	18.92	0.750	34.3
PScore-42	7.00	355.15	18.89	0.757	33.8
PScore-51	7.01	356.96	18.83	0.764	33.9

PNIPAm-shell 7.00 g (dryweight) of the purified core suspension syntesized as described above were mixed with 0.24 g *N,N'*-methylene bisacrylamide (0.0016 mol)), 7.00 g *N*-isopropylacrylamide (0.060 mol) and 140 mL deionized water under stirring at 600 RPM. Remaining oxygen in the suspension was removed by alternating degassing and flushing with argon three times. The reaction mixture was heated to 80 °C. A solution of 0.070 g potassium persulfate (0.26 mmol) dissolved in 10 mL deionized water were added. The resulting suspension was stirred for 5 h at 80 °C. After the suspension was cooled down to 60 °C, the mixture was filtered through glass wool.

Table A2: Synthesis details of the shell synthesis: mass of the seed latex (m_{seed}), the mass fraction of the seed latex (w_{seed}) and the resulting mass of polystyrene seed (m_{PS}), mass of the monomer *N*-isopropylacrylamide, the crosslinker *N,N'*-methylenebisacrylamide (m_{MBA}), the initiator potassium persulfate (m_{KPS}), the resulting theoretical crosslinking density of the shell (DC_{theo}), the total volume (V) and the mass fraction (w) at which the synthesis was performed. Note that the seed latices have a lower mass fraction than the one at which they were synthesized, due to dilution during purification.

Core-Shell Particle	Seed Latex	m_{seed} [g]	w_{seed} [wt%]	m_{PS} [g]	m_{NIPAm} [g]	m_{MBA} [g]	DC_{theo} [mol %]	m_{KPS} [g]	w [wt%]	V [mL]
PS-37-PNIPAm-83	PScore-37	37.62	16.8	6.319	7.04	0.244	2.54	0.0703	5.6	240
PS-40-PNIPAm-86	PScore-40	321.74	20.5	65.96	66.68	2.290	2.52	0.6725	8.1	1700
PS-40-PNIPAm-89	PScore-40	322.36	20.5	66.08	68.77	2.361	2.52	0.6710	9.4	1500
PS-37-PNIPAm-75	PScore-37	392.61	16.7	65.57	66.00	2.262	2.52	0.6766	7.9	1700
PS-51-PNIPAm-131	PScore-51	138.24	26.0	35.94	97.13	3.316	2.51	0.3749	8.3	1600
PS-47-PNIPAm-106	PScore-47	342.73	15.6	53.47	79.5	2.726	2.52	0.5467	7.4	1800

A.2 Characterization Techniques

A.2.1 Dynamic Light Scattering

The DLS measurements of the core particles were performed with the ALV/CGS-3 goniometer system (ALV, Langen, Germany) at a temperature of 25 °C. The wavelength of the HeNe laser was 633 nm and the scattered light was detected at an angle of 90°. Each measurement was performed five times and the given result is the average of the five measurements. The hydrodynamic radius was determined by cumulant analysis, which is implemented in the instrument software. For the core-shell particles, the temperature dependence of the R_H are relevant. As the adjustment of the temperature and the start of the measurement has to be made manually, measuring the temperature dependence with this system is time consuming. Therefore, instead an automated system was used for measuring the temperature dependent R_H of the core-shell systems.
The temperature-dependent DLS measurements were performed with the Zetasizer Nano S (Malvern Panalytical, Malvern, United Kingdom) at the university of Düsseldorf in the group of Prof. Matthias Karg. The wavelength of the laser was 633 nm and the scattered light was detected at an angle of 173°. Measurements were performed in semi macro cuvettes (PMMA/VWR) in a temperature range from 10 °C to 50 °C in steps of 0.5 °C. The equilibration time between each step was set to 300 s. Each measurement was performed three times and the given result is the average of the three measurements. The hydrodynamic radius was determined by cumulant analysis, which is implemented in the instrument software.

A.2.2 Disc Centrifuge Sedimentation

Particle size distributions were measured by differential centrifugal sedimentation (DCS) on an analytical disc centrifuge (DC24000 UHR, CPS Instruments, Inc., Prairieville, LA, USA) at the university of Konstanz in the group of Prof. Alexander Wittemann. A density gradient was prepared from nine aqueous sucrose solutions (1.6 mL each) ranging from 8.0 wt% to 2.0 wt% inside a hollow disk rotating at 24 000 RPM. A thin layer of *n*-dodecane was deposited onto the gradient, thus minimizing evaporation of water, and extending the lifetime of the gradient. The step gradient was allowed to equilibrate for 30 min, thus yielding a continuous gradient, which is linear in volume. Each particle size measurement was calibrated using polystyrene nanospheres with a nominal size of 251 nm and a particle density of 1.054 g cm^{-3}. A volume of 100 µL of diluted suspensions of the core-shell particles and their cores (0.02 wt%) were injected into the spinning disk. During the centrifugation the particles were sedimenting at rates that depend on the actual size and density of the particles. The measured sedimentation time is in inverse relationship to the sedimentation coefficient[173]. Stokes' law and particles densities measured either on a densitometer or derived from DLS measurements were used to calculate the actual particle sizes from the sedimentation coefficients measured in the DCS experiment. The concentration of the particles arriving at the detector position were determined using light attenuation at $\lambda = 405$ nm, thus making the particle size distribution complete. Mean particle sizes and

dispersities given as weight-average diameter divided by the number-average diameter were obtained this way.

A.2.3 Scanning Electron Microscopy

The SEM images of the core and the core-shell particles were taken at the Laboratory for Electron Microscopy (LEM) at the Karlsruhe Institute of Technology (KIT) with a LEO 1530 Gemini (Zeiss, Jena, Germany) at an acceleration voltage of 5 kV at a working distance of 6 mm with a magnification of 2×10^5. The samples were dripped onto a silicon wafer, which was connected to the sample holder with silver lacquer and dried under athmosphere.

A.2.4 Environmental Scanning Electron Microscopy

The ESEM images of the core-shell particles were taken at the Laboratory for Electron Microscopy (LEM) at the Karlsruhe Institute of Technology (KIT) with a Quanta FEG 650 (FEI, Hilsboro, Oregon, United States) at an acceleration voltage of 10 kV at a working distances of 8.0 mm to 8.1 mm with magnifications of 5×10^4 to 10^5. The samples were dripped onto a silicon wafer, which was connected to the sample holder with silver lacquer and dried under athmosphere. The water pressure in the sample chamber was varied from 200 Pa to 750 Pa and the sample holder was cooled down to 4 °C to cause condensation of the water onto the sample.

A.2.5 Transmission Electron Microscopy

The TEM images of the core-shell particles were conducted in the group of Prof. Matthias Karg at the university of Düsseldorf with the JEM-2100Plus (JEOL, Akishima, Tokyo, Japan) at an acceleration voltage of 80 kV under a pressure of 10^{-4} Pa.

A.2.6 Atomic Force Microscopy

The AFM images of the core-shell particles were captured with a JPK NanoWizard 2 (Bruker, Billerica, Massachusetts, United States).

A.2.7 Rheology

If not indicated otherwise, the rheological measurements were conducted on an ARES-G2 rheometer (TA Instruments, Newcastle, USA) using a 40 mm plate-plate geometry at a gap of 1 mm on the bimodal mixture with a mass fraction of 8.3 wt%. The samples were put on the plates with a syringe and sealed with silicon oil with a viscosity of 215 mPa s to 315 mPa s for the investigated temperatures to suppress water evaporation. All the shear experiments were conducted between 20 °C to 10 °C, resulting for the mass fraction of 8.3 wt% in effective volume fractions between 0.70 to 0.83. All samples were sheared at $\dot{\gamma} = 100\,\mathrm{s}^{-1}$ for $t = 2$ min before all measurements to rejuvenate the sample.
Linear oscillatory shear was measured in an angular frequency range of $\omega_1 = 100\,\mathrm{rad\,s}^{-1}$ to down to $1.69 \times 10^{-4}\,\mathrm{rad\,s}^{-1}$ depending on the mechanical behavior of the sample at the

specific volume fraction and a strain amplitude of $\gamma_0 = 1\,\%$. The more solid the samples are, the lower the lowest angular frequency was chosen.
The steady state stress measurements were conducted in a shear rate range from $\dot{\gamma} = 300\,\mathrm{s}^{-1}$ to down to $10^{-4}\,\mathrm{s}^{-1}$ depending on the rheological behavior of the sample at the certain volume fraction.
The transient stress measurements were conducted in a shear rate range of $\dot{\gamma} = 3.73 \times 10^{-1}\,\mathrm{s}^{-1}$ to $3.73 \times 10^{-5}\,\mathrm{s}^{-1}$ with waiting times after rejuvenation ranging from $t_\mathrm{w} = 10\,\mathrm{s}$ to 92 000 s until steady state was reached.
The superposition rheology measurements were conducted using a cone-plate geometry with a diameter of 50 mm and a cone angle of 0.02 rad on the bimodal mixture with a mass fraction of 8.9 wt% in a temperature range of 20 °C to 10 °C resulting in effective volume fractions of 0.75 to 0.83. The measurements were conducted at shear rates from $\dot{\gamma} = 0\,\mathrm{s}^{-1}$ to $7\,\mathrm{s}^{-1}$ with a parallel superposition of an oscillatory measurement with angular frequencies of $628\,\mathrm{rad\,s}^{-1}$ to $4.5 \times 10^{-2}\,\mathrm{rad\,s}^{-1}$.
The LAOS measurements were conducted as strain sweeps from $\gamma_0 = 1\,\%$ to $5 \times 10^2\,\%$ for angular frequencies ranging from $\omega_1 = 10\,\mathrm{rad\,s}^{-1}$ to $3.98 \times 10^{-4}\,\mathrm{rad\,s}^{-1}$ and as frequency sweeps at a fixed strain amplitude of $\gamma_0 = 7\,\%$ or $10\,\%$ depending on the volume fraction. The frequency sweeps were conducted from $\omega_1 = 10\,\mathrm{rad\,s}^{-1}$ to $2 \times 10^{-2}\,\mathrm{rad\,s}^{-1}$ for all volume fractions.

A.3 Supporting Information

A.3.1 Colloidal Model System

A.3.1.1 Purification of the Core Particles - Dialysis

After the synthesis, the core particles are purified by dialysis against deionized water to remove the emulsifier, SDS. This is done by filling the suspension in a Nadir dialysis tube with a molecular weight range of $10^4\,\mathrm{g\,mol}^{-1}$ to $2 \times 10^4\,\mathrm{g\,mol}^{-1}$, which corresponds to a pore size of about 3.1 nm to 3.9 nm.
The purification process is parallelized by using five dialysis tubes each filled with 240 mL suspension in five beakers filled with 4500 mL deionized water at a time. The surrounding water is changed every 24 h to 96 h as the change of the water accelerates the process. Before changing the water, the electrical conductivity of the suspension and the surrounding water is measured.
The electrical conductivity κ can be used as a measure for the progress of the purification due to the charged head group of the surfactant (see Figure A.3.2(b)). In Figure A.3.2(a) the electrical conductivity κ of the suspension and the surrounding water is shown exemplary for the purification process of the core particle PScore-40.
The water and surfactant molecules are small enough to pass through the membrane, while the core particles are larger than the pores ($V_\mathrm{core} > 9V_\mathrm{pores}$) and therefore remain in the dialysis tubes. Since the concentration of surfactant molecules inside the dialysis tube is higher than in the surrounding deionized water, the chemical potential inside the dialysis

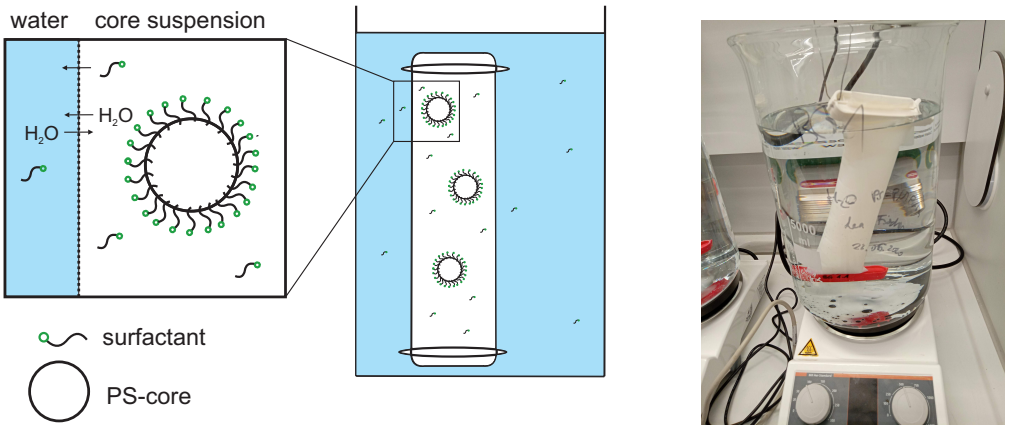

(a) (b)

Figure A.3.1: Purification of the core particles via dialysis to remove the surfactant molecules from the suspension. **(a)** Scheme of the purification process, **(b)** photo of the procedure.

tube is higher, causing the surfactant molecules to diffuse into the deionized water. In addition, water from the surroundings enters the tubes, causing them to swell.
The conductivity of the suspension before the purification process $\kappa_{\mathrm{Susp}} = 2085\,\mu\mathrm{S\,cm^{-1}}$ decays to $\kappa_{\mathrm{Susp}} = 255\,\mu\mathrm{S\,cm^{-1}}$ after the purification process. The remaining conductivity of the suspension after the dialysis is high compared to the conductivity of the used deionized water ($\kappa_{\mathrm{H2O}} = 0.3\,\mu\mathrm{S\,cm^{-1}}$). The charged end groups of the core particles shown in Figure A.3.2(b) lead to a remaining conductivity.

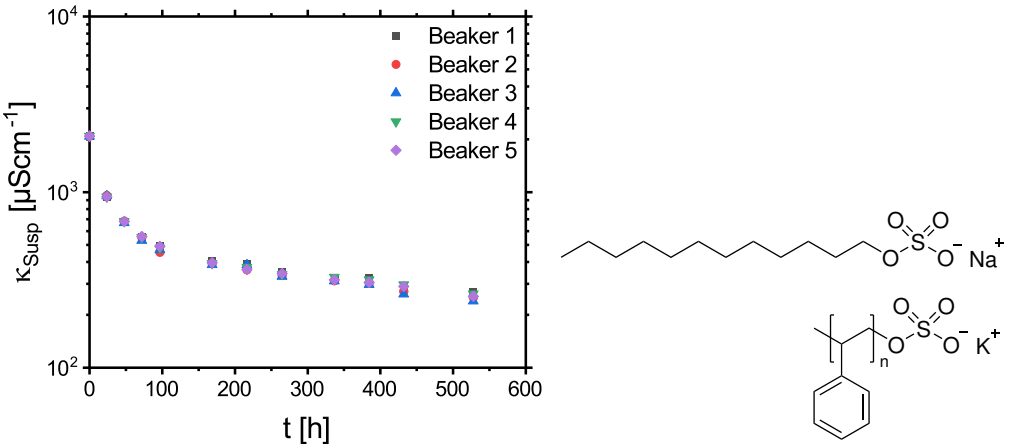

(a) (b)

Figure A.3.2: Progress of the purification of the core particles to remove the surfactant. **(a)** The conductivity of the suspension κ_{Susp} results from the charged head group of the surfactant and the charged end group of the polystyrene polymer chain in the core particles shown in **(b)**.

A.3.1.2 Structure of the Core Particles

SEM images of all synthesized core particles are given in Figure A.3.3.

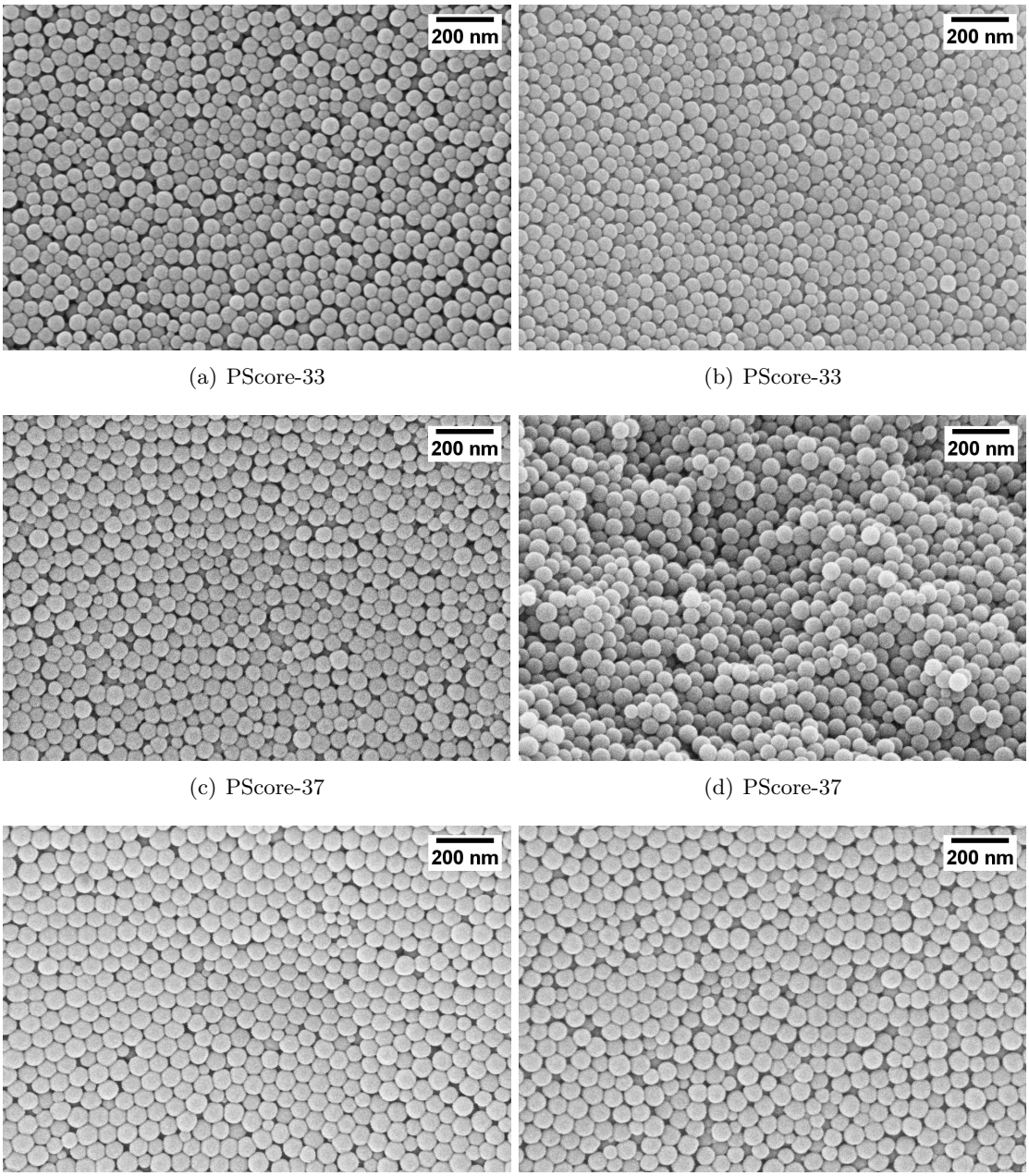

(a) PScore-33 (b) PScore-33

(c) PScore-37 (d) PScore-37

(e) PScore-40 (f) PScore-40

Figure A.3.3: Scanning electron microscopy images of the dried core particles.

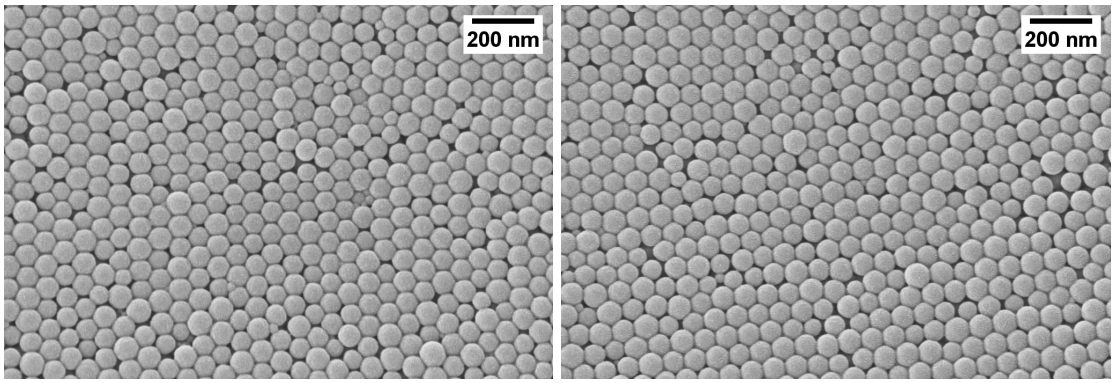

(g) PScore-42 (h) PScore-42

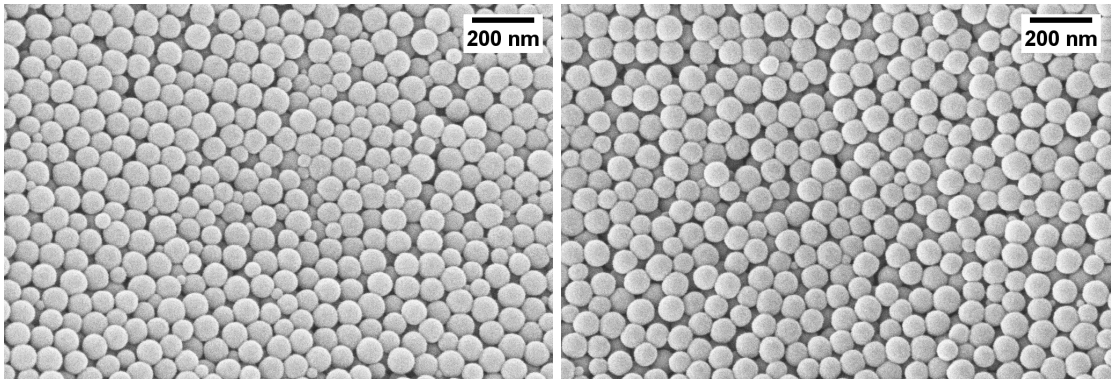

(i) PScore-47 (j) PScore-47

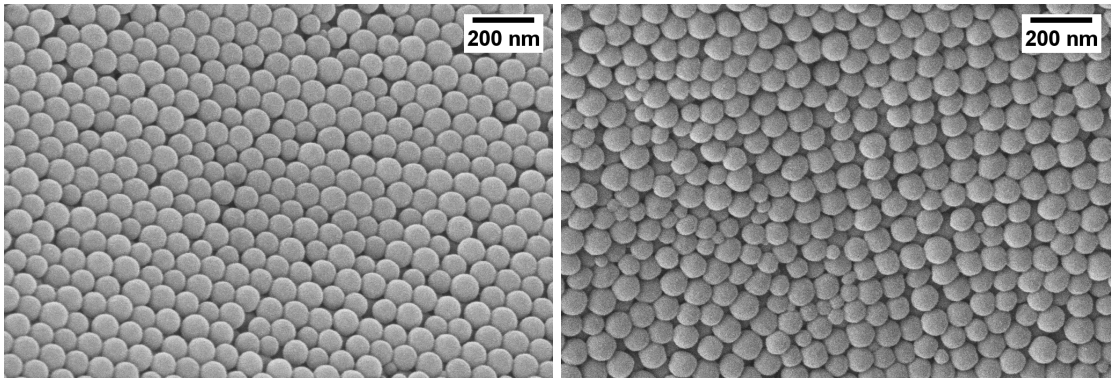

(k) PScore-51 (l) PScore-51

Figure A.3.3: Scanning electron microscopy images of the dried core particles.

A.3.1.3 Purification of the Core-Shell Particles - Ultrafiltration

Figure A.3.5 displays the construction plans for the ultrafiltration set-up used for the purification of the PS-PNIPAm core-shell particles. The set-up is based on the set-up of Prof. Wittemann of the university of Konstanz and was improved by Dr. Masood Khabazian Esfahani.

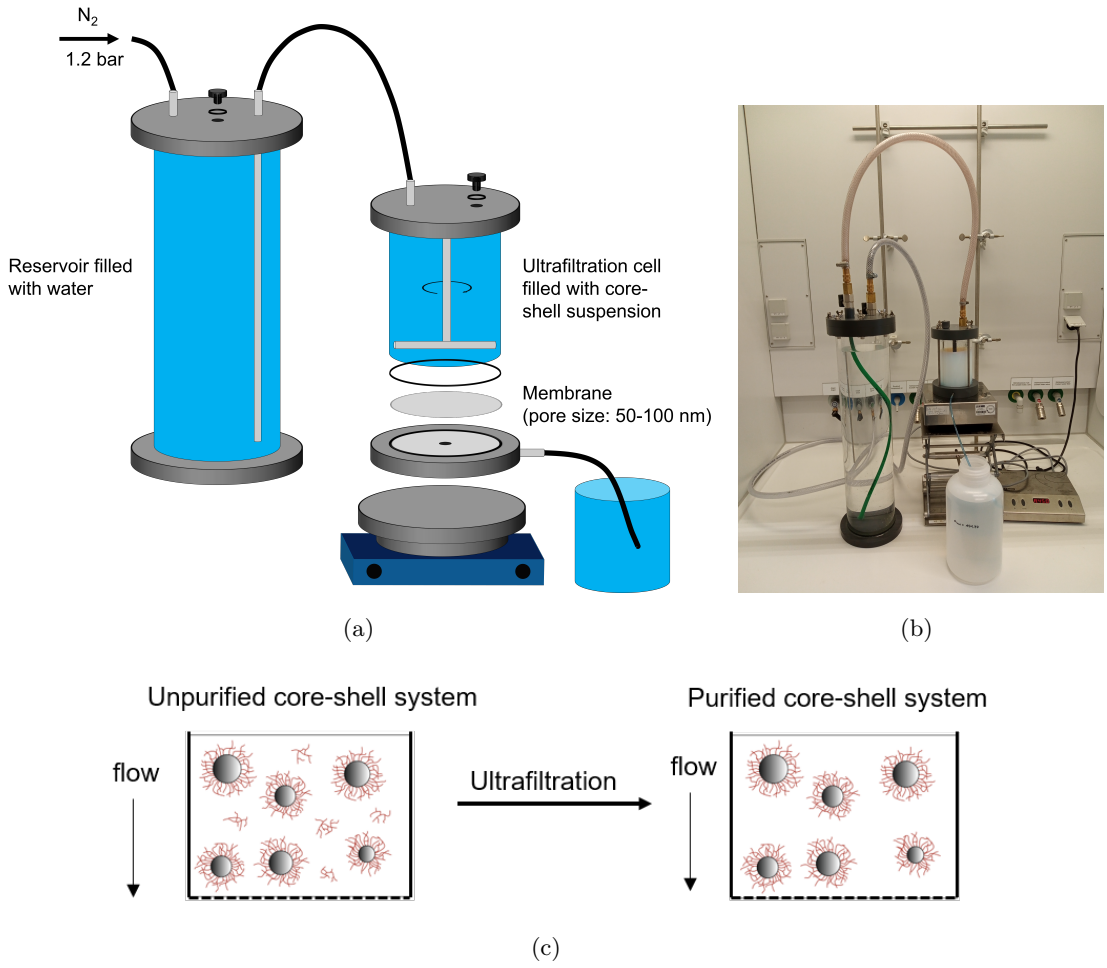

Figure A.3.4: Purification of the core-shell particles via ultrafiltration: **(a)** Scheme of the purification set-up, **(b)** photo of the procedure and **(c)** schematic illustration of the purification process.

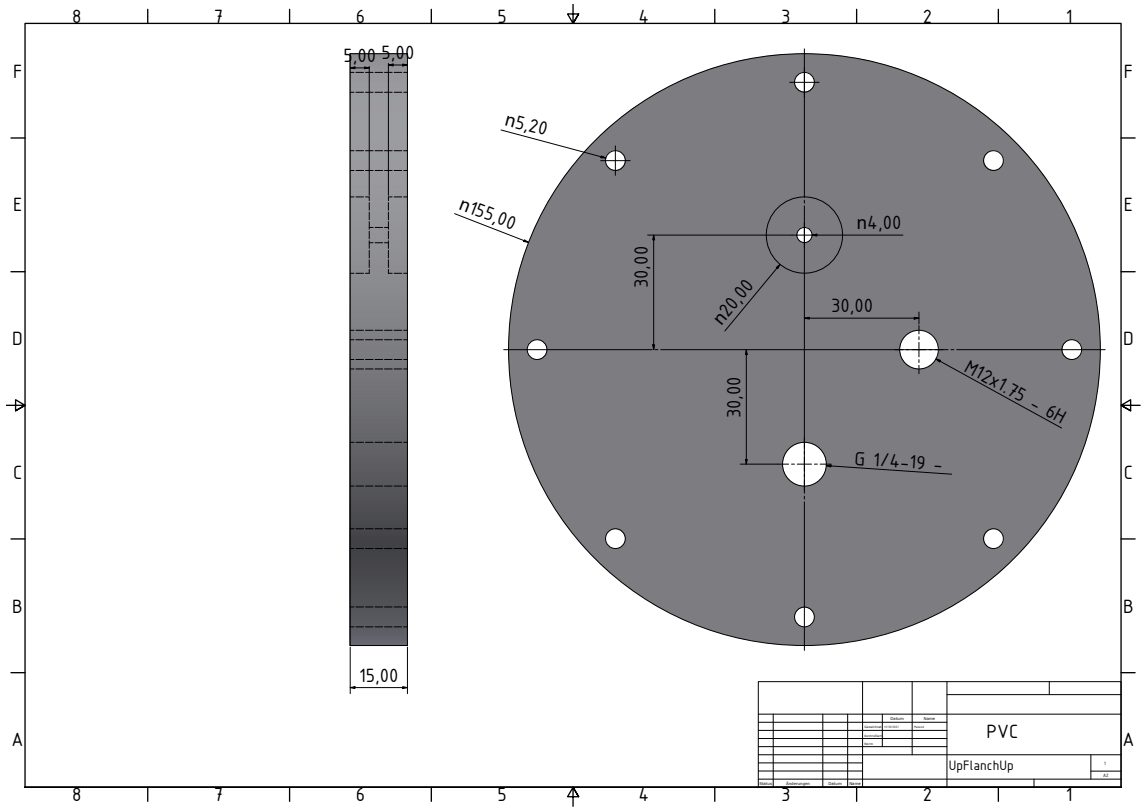

(a)

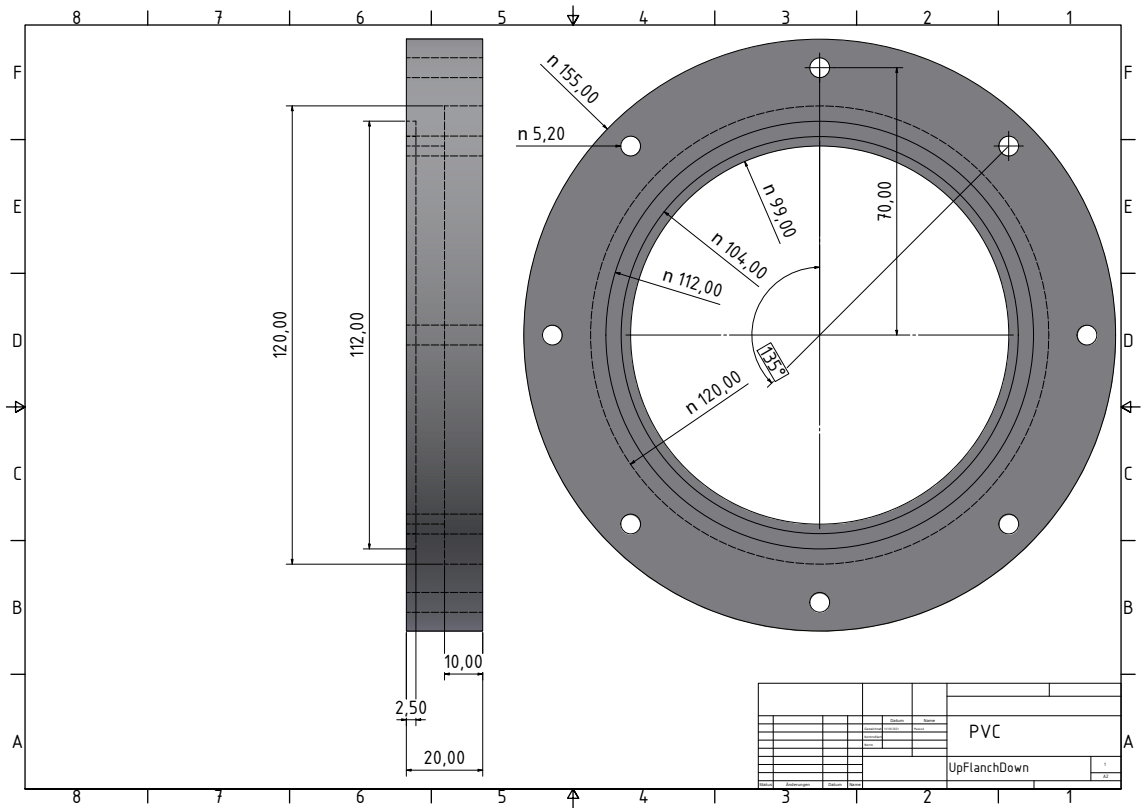

(b)

Figure A.3.5: Construction plans of the ultrafiltration set-up. The view of the upper part of the reservoir from **(a)** above and **(b)** below.

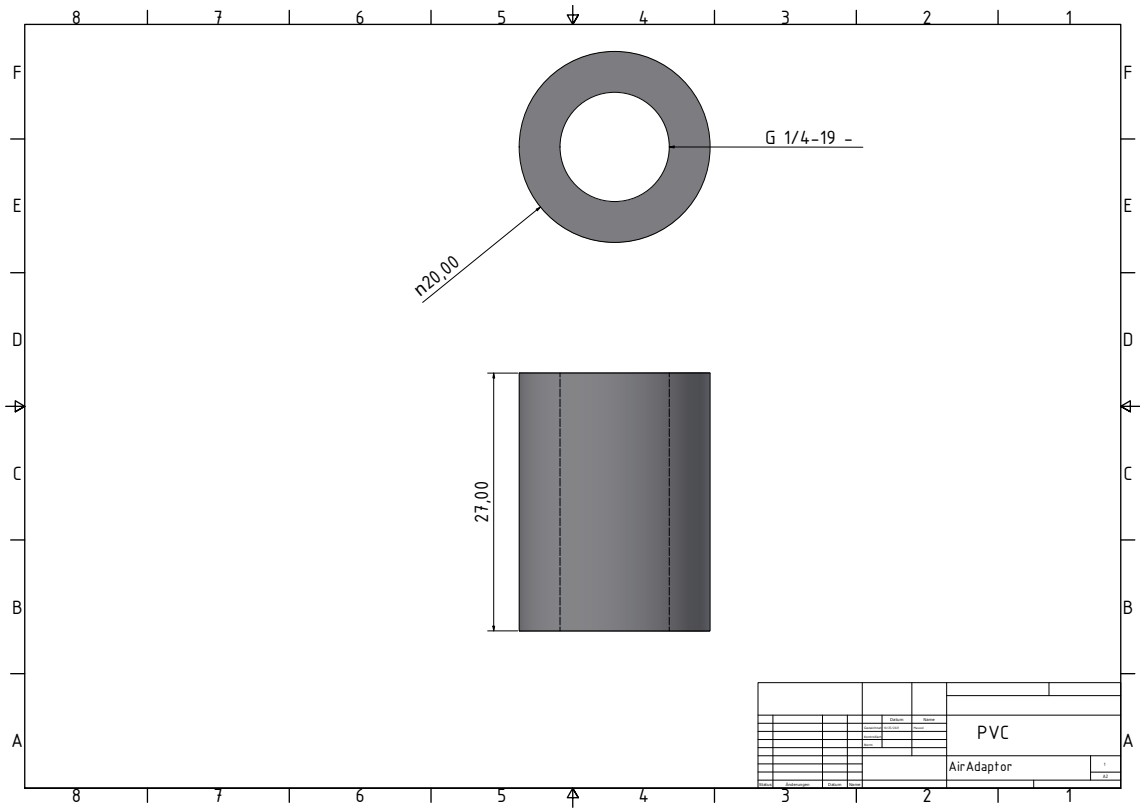

(c)

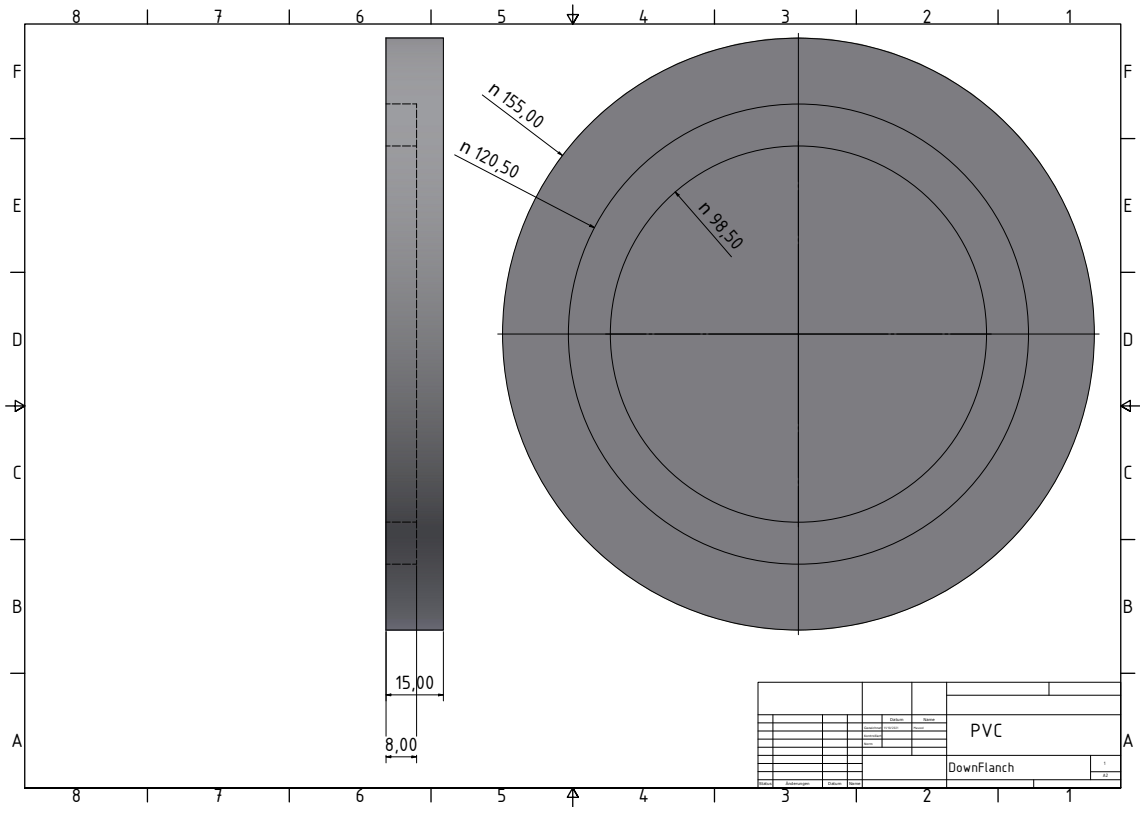

(d)

Figure A.3.5: Construction plans of the ultrafiltration set-up for **(c)** the air adapter fixed twice onto the upper part of the reservoir and additionally fixed to the upper part of the ultrafiltration cell and **(d)** the lower part of the reservoir.

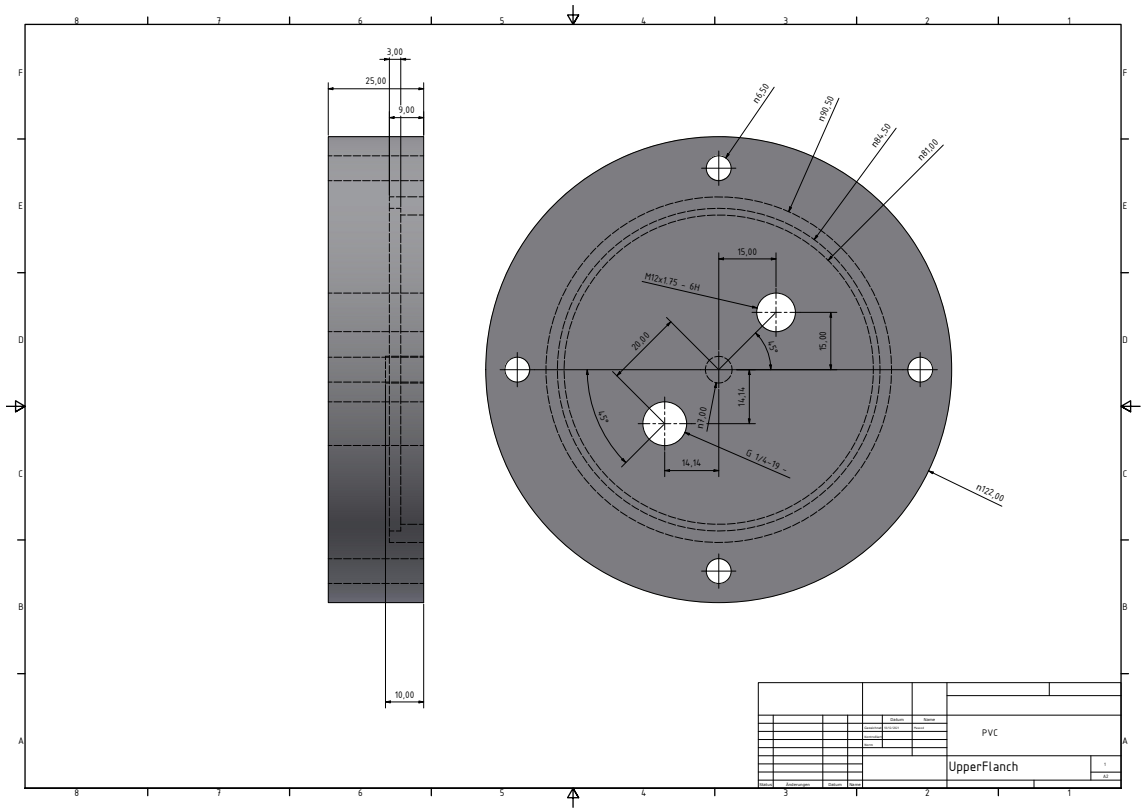

(e)

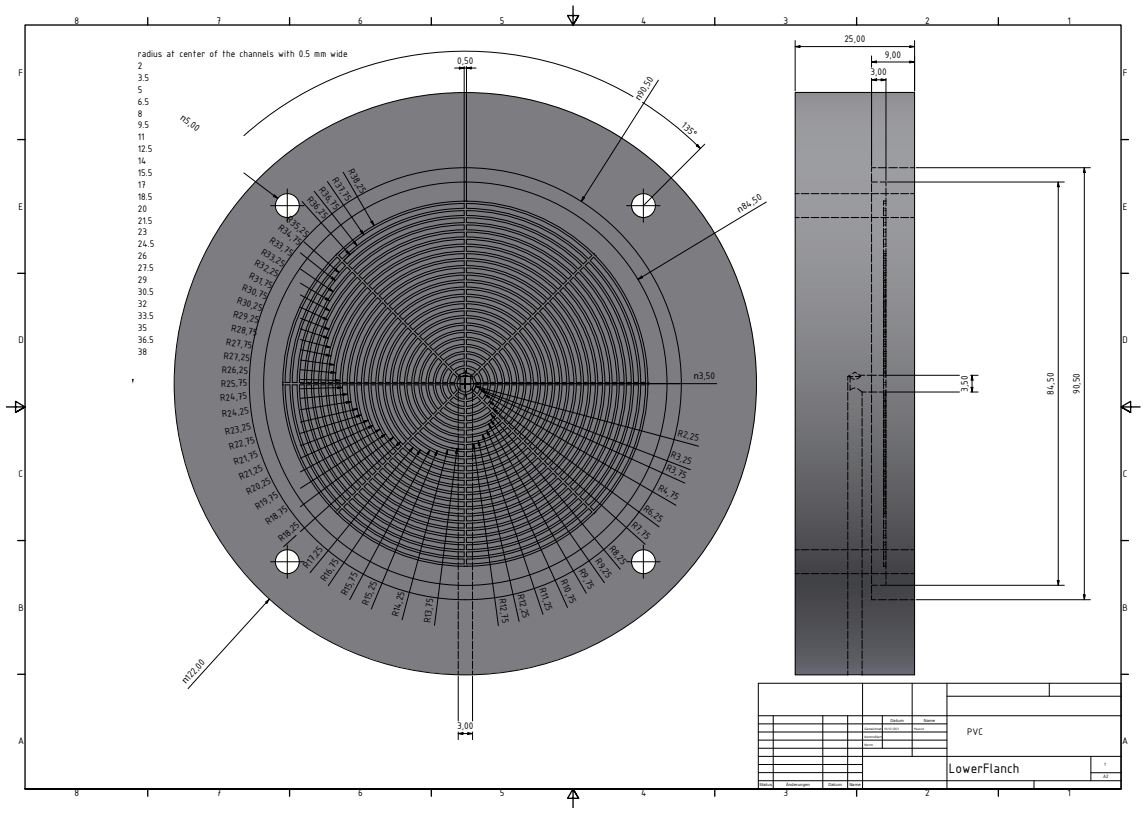

(f)

Figure A.3.5: Construction plans of the ultrafiltration set-up. The **(e)** upper part of the ultrafiltration cell and the **(f)** lower part of the ultrafiltration cell on which the membrane is placed. The lower part contains thin channels to improve water drainage.

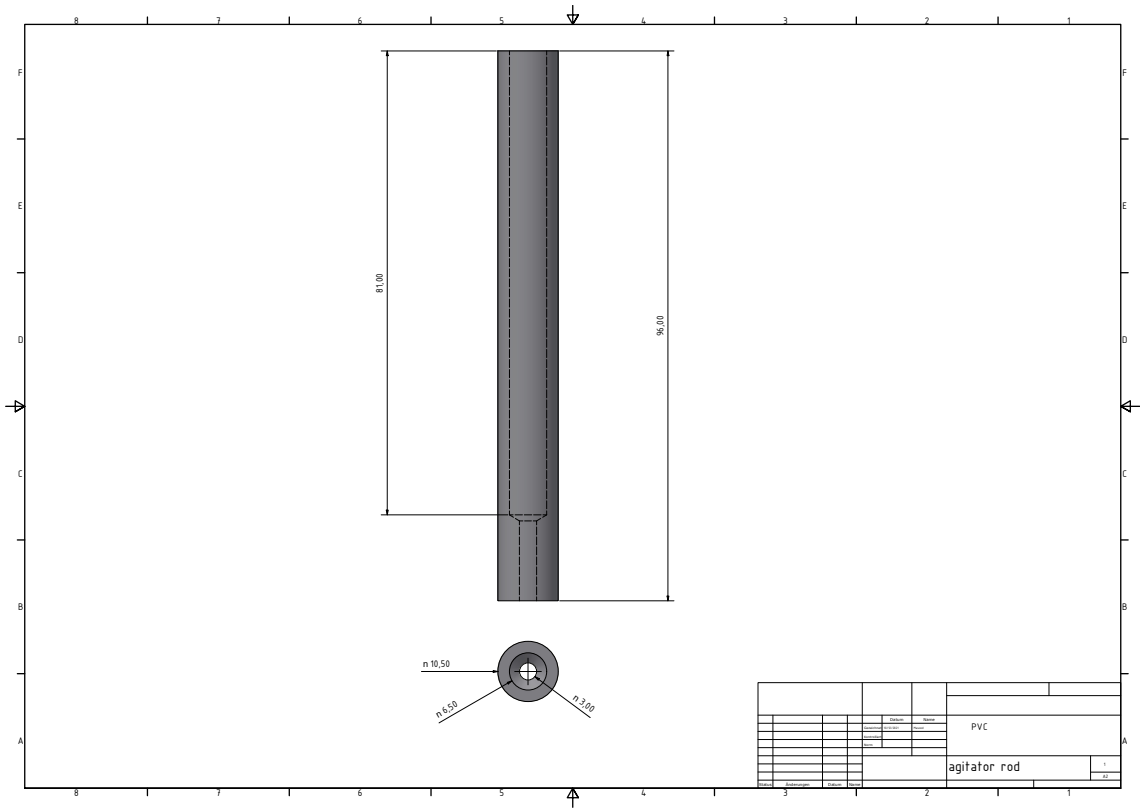

(g)

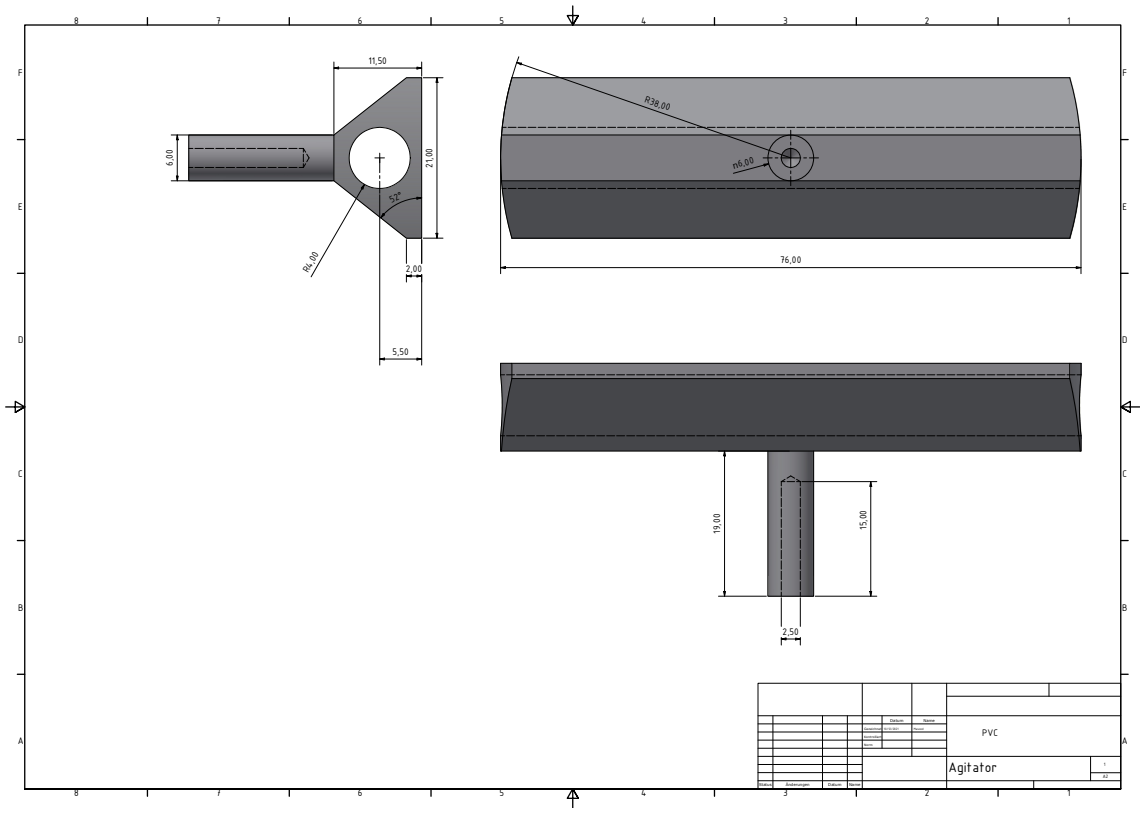

(h)

Figure A.3.5: Construction plans of the ultrafiltration set-up for **(g)** the agitator rod and **(h)** the agitator. A magnetic stirring rod is attached to the center of the agitator.

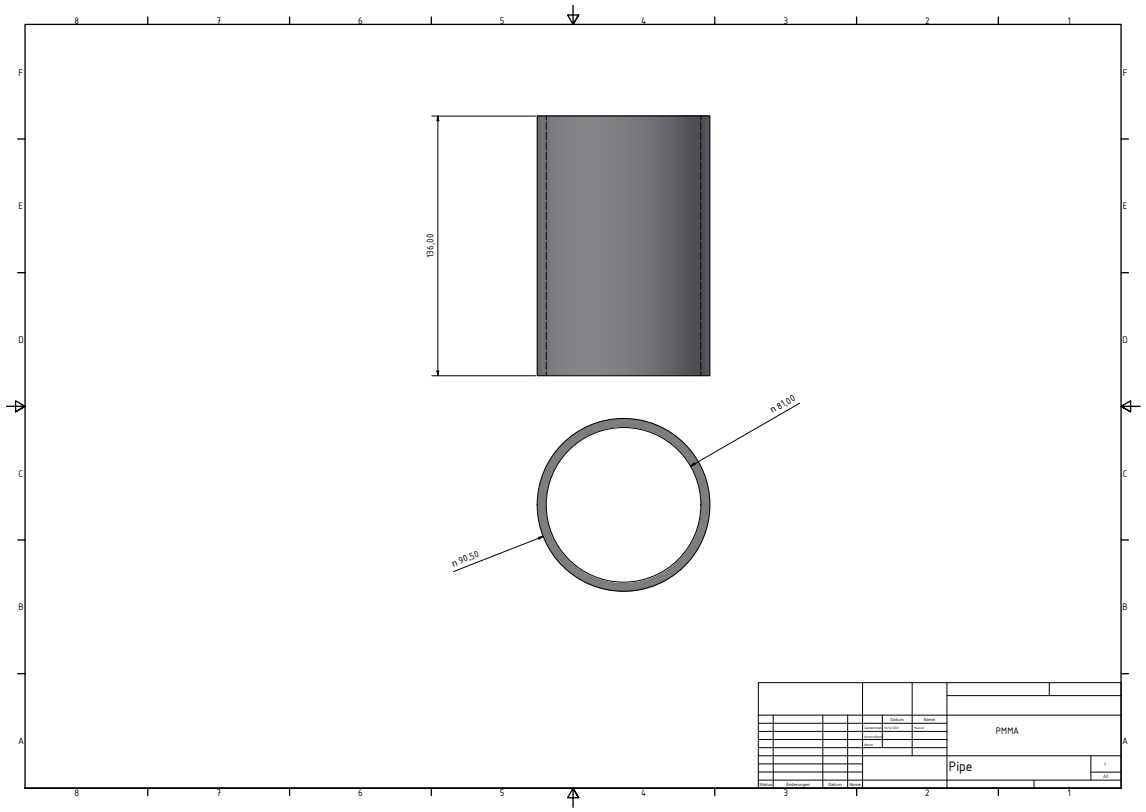

(i)

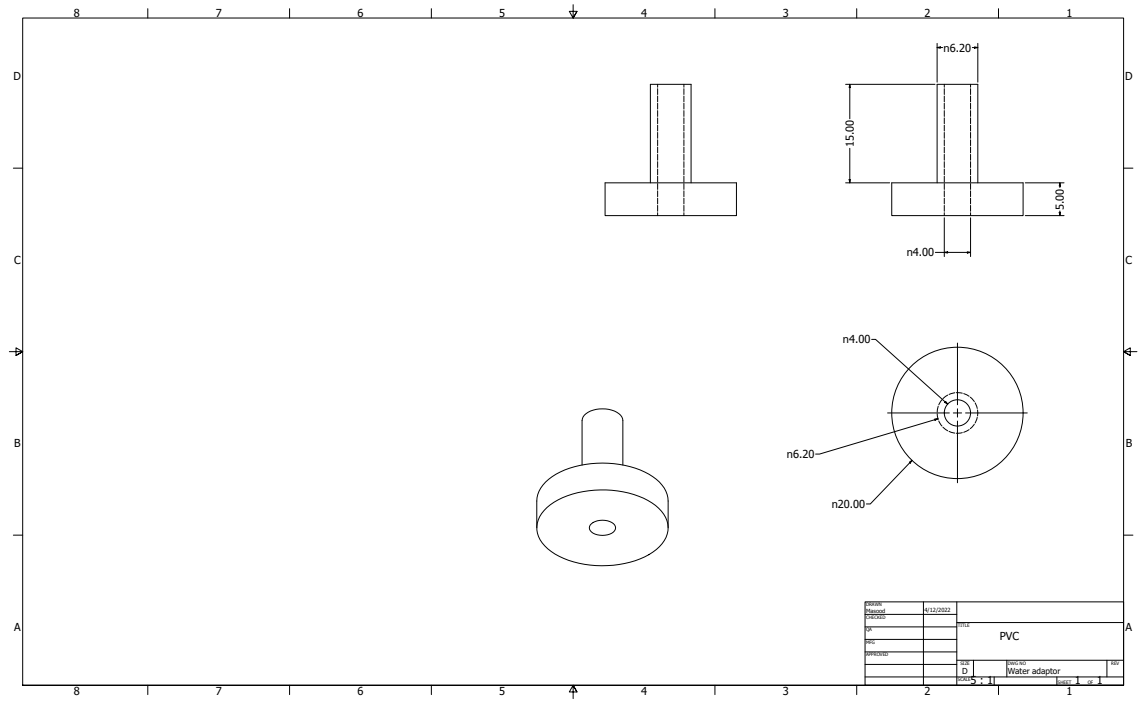

(j)

Figure A.3.5: Construction plans of the ultrafiltration set-up. **(i)** The PMMA pipe fixed between the upper and the lower part of the ultratiltration cell and **(j)** the removable locks for the upper parts of the reservoir and the ultrafiltration cell.

A.3.1.4 Characterization of the Core-Shell Particles

Swelling of the Core-Shell Particles

Environmental scanning electron microscopy allows for the analysis of a sample with a small amount of water, which can be controlled by adjusting the water pressure in the sample chamber, while the sample holder is cooled down to $T = 4\,^{\circ}\mathrm{C}$, causing water to condensate onto the sample.

In Figure A.3.6, ESEM images depict a core-shell system at various water pressures within the sample chamber. At a pressure of $p = 200\,\mathrm{Pa}$, when the sample is dry, the particles are separated from each other. At a pressure of $p = 500\,\mathrm{Pa}$, particle boundaries become less apparent and completely disappear for $p = 750\,\mathrm{Pa}$ as this pressure corresponds to 100 % humidity in the sample. At higher humidities, the shells become more swollen, causing the particles to be less separated. As the shells do not have sufficient space to fully swell, they interpenetrate each other, resulting in poorer contrast. A detailed particle size analysis is not feasible given the low resolution of the images compared to those obtained with SEM and the loss of clear boundaries due to swelling and interpenetrating of the particles.

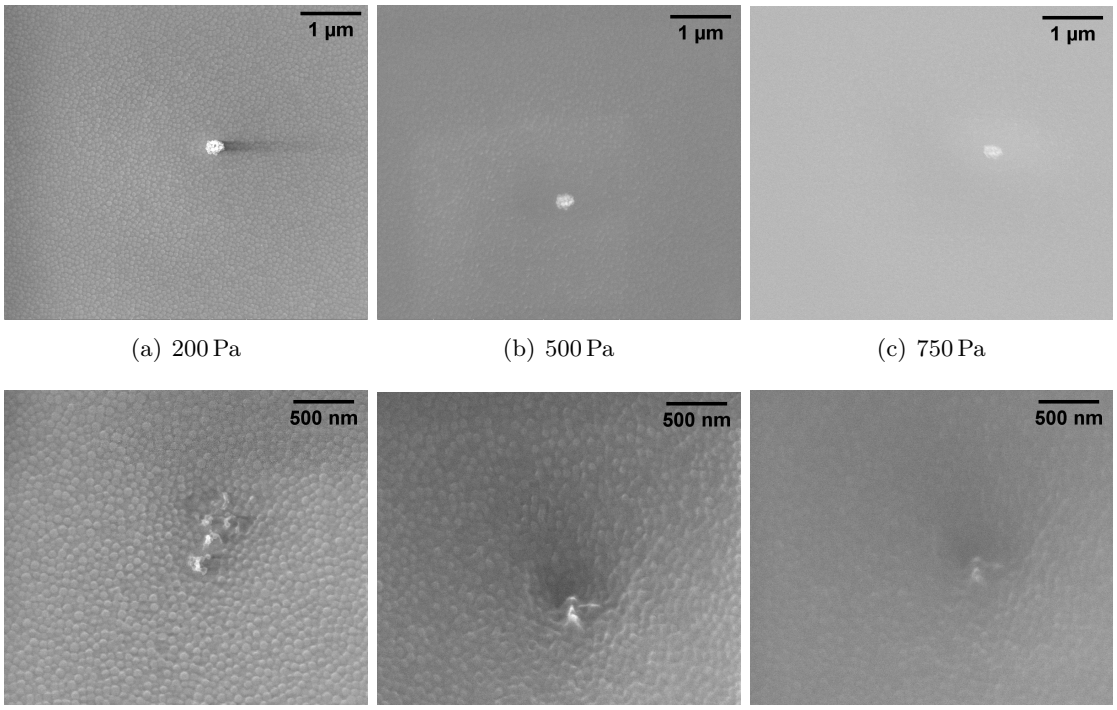

(a) 200 Pa (b) 500 Pa (c) 750 Pa

(d) 200 Pa (e) 450 Pa (f) 600 Pa

Figure A.3.6: Exemplary ESEM images at different water pressures in the sample chamber attributed to different humidities of the sample showing the swelling of the core-shell particles. In the first row, an aggregate of particles is visible. In the second row, the sample's destruction due to the high energy of the electron beam can be seen.

Core-Shell Structure of the Particles - AFM

The AFM images of PS-37-PNIPAm-75, PS-51-PNIPAm-131 and PS-47-PNIPAm-106 are depicted in Figure A.3.7. The core-shell structure is visible due to the different compressibilities of the cores and the shells. The cores appear brighter than the shells.

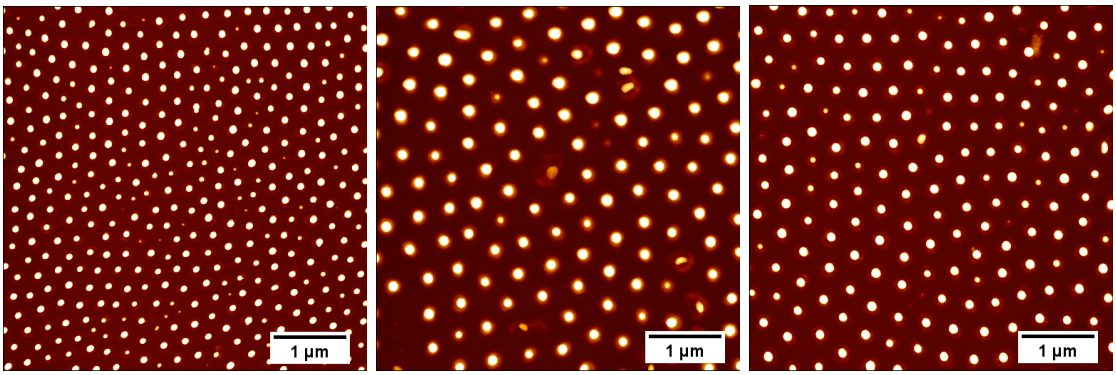

(a) PS-37-PNIPAm-75 (b) PS-51-PNIPAm-131 (c) PS-47-PNIPAm-106

Figure A.3.7: AFM images of the core-shell particles. The cores of the particles appear brighter than the shells.

A.3.2 Linear and Nonlinear Rheological Characterization

A.3.2.1 Normalization Constants

In Table A3, the volume fractions ϕ_{eff} of the bimodal mixture with a mass fraction of $w = 8.62\,\text{wt\%}$ and the corresponding measurement temperature and the normalization constants are depicted.

Table A3: Hydrodynamic radii R_{H}, and normalization constants for the angular frequency and shear rate, as well as the moduli and stress obtained from Equations (6.3) and (6.4) at the measurement temperatures T for the bimodal model system. Additionally, the volume fractions ϕ_{eff} for the bimodal mixture with a mass fraction of $w = 8.62\,\text{wt\%}$ is depicted. The correlation between T and ϕ_{eff} depends on the mass fraction w of the sample, while R_{H} and the normalization factors are universal for a specific temperature.

ϕ_{eff} [-]	T [°C]	R_{H} [nm]	$\frac{Pe_\omega}{\omega_1} = \frac{Pe_0}{\dot{\gamma}}$ [s]	$\frac{\sigma_{\text{red}}}{\sigma} = \frac{G'_{\text{red}}}{G'} = \frac{G''_{\text{red}}}{G''}$ $\left[\text{m s}^2\,\text{kg}^{-1}\right]$
0.73	20	131.2	1.05×10^{-2}	5.58×10^{-1}
0.77	18	132.7	1.15×10^{-2}	5.81×10^{-1}
0.81	16	134.2	1.26×10^{-2}	6.05×10^{-1}
0.83	14	135.6	1.38×10^{-2}	6.29×10^{-1}
0.86	12	137.1	1.52×10^{-2}	6.55×10^{-1}

A.3.2.2 Sealing the Samples with Silicon Oil

The samples were sealed with silicon oil as otherwise evaporation intervened the rheological measurements. In Figure A.3.8, G' and G'' obtained from oscillatory shear measurements in the linear regime at a fixed $\gamma_0 = 1\,\%$ and a fixed $\omega_1 = 6.28\,\mathrm{rad\,s^{-1}}$ are depicted in dependence on the measurement time.

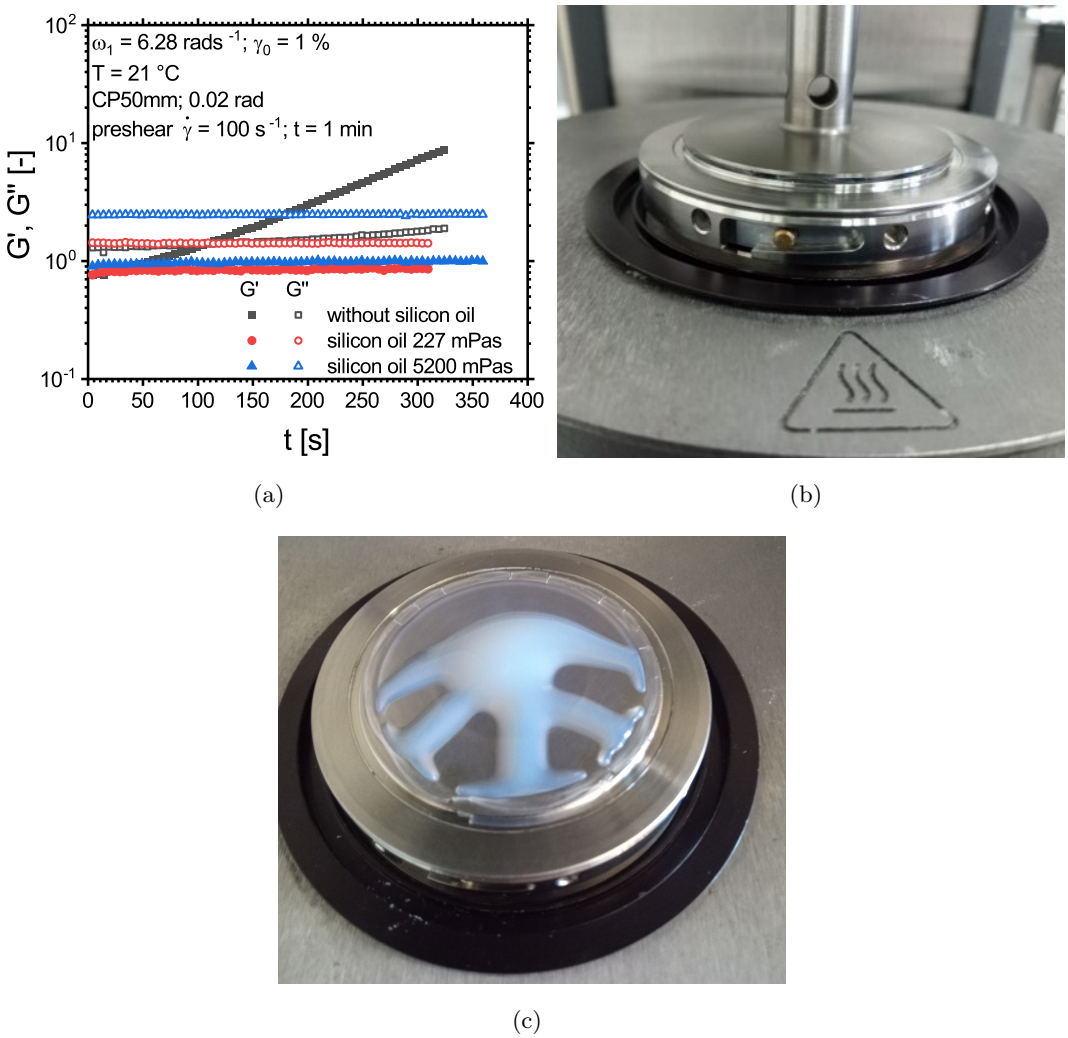

Figure A.3.8: **(a)** Time dependence of the response of the core-shell suspension to a linear oscillatory shear motion at a fixed $\gamma_0 = 1\,\%$ and ω_1 $6.28\,\mathrm{rad\,s^{-1}}$ in the linear regime of the sample. Without sealing G' and G'' are increasing immediately after starting the measurement indicating an evaporation of the dispersion medium. Sealing with a silicon oil with a viscosity of 227 mPa s leads to stable G' and G'' values, which are comparable to the ones obtained without silicon oil. Sealing with a silicon oil with about 5200 mPa s leads to a pronounced increase in G'' of. Therefore, the silicon oil with 227 mPa s was chosen for the sealing of the gap. **(b)** and **(c)** images of the sample after the measurements without sealing showing the building of a polymer film between the plates.

Without sealing, G' and G'' are increasing immediately after the start of the measurement corresponding to the evaporation of the dispersion medium water resulting in higher effective volume fraction of the particles in the suspension and therefore higher G' and G'' values. After 300 s a polymer film between the plates is already build if the sample is not sealed, which can be seen in Figures A.3.8(b) and (c). Sealing the gap with a silicon oil

with a viscosity of 227 mPa s leads to stable G' and G'' values within the measurement time of 300 s, which are comparable to the values obtained without sealing. Sealing with a silicon oil with a viscosity of about 5200 mPa s leads to stable values of G' and G'', but the silicon oil influences the measured moduli. Therefore, the silicon oil with 227 mPa s was chosen for the sealing of the gap during rheological measurements.

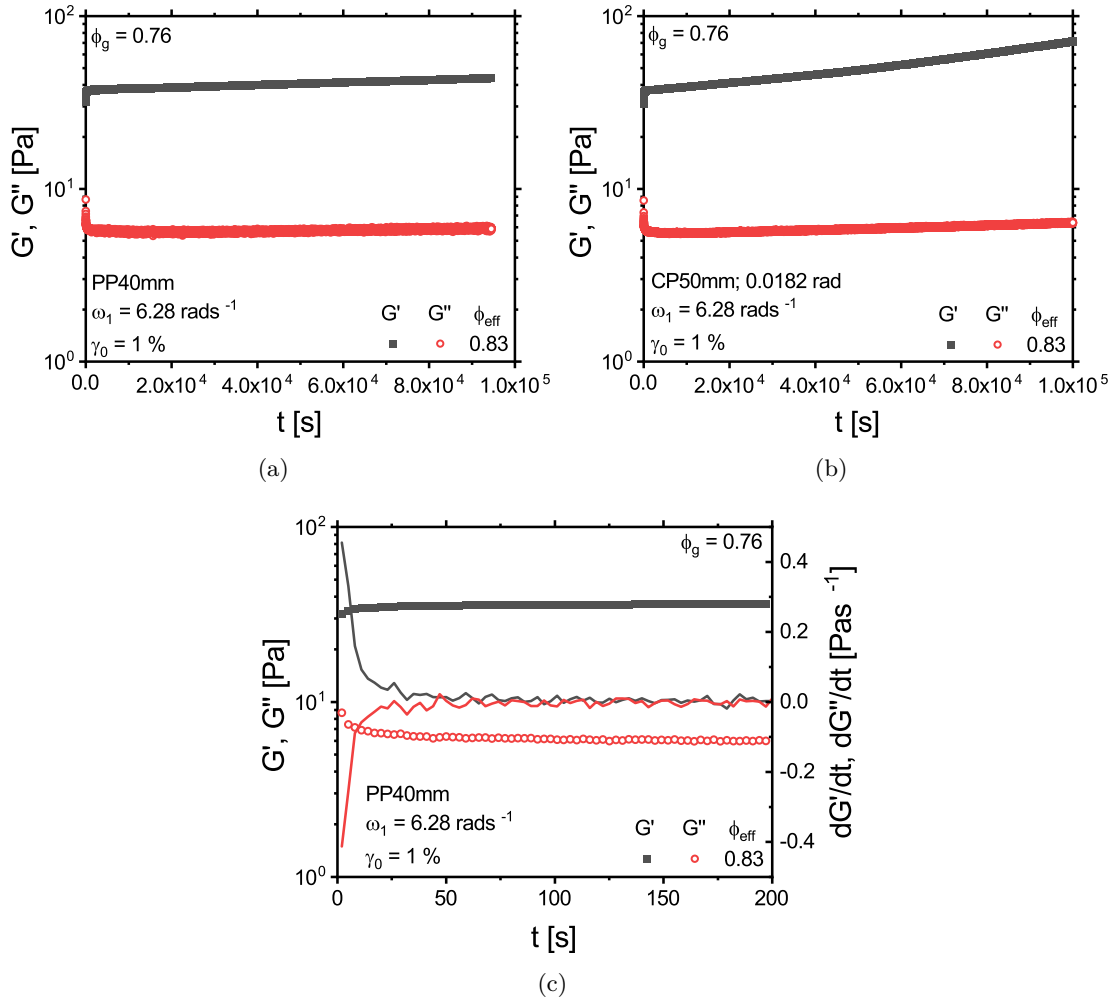

Figure A.3.9: Time dependence of the response of the core-shell suspension to a linear oscillatory shear motion at a fixed γ_0 and ω_1 in the linear regime of the sample measured with a **(a)** plate-plate geometry with a diameter of 40 mm and **(b)** a cone-plate geometry with a diameter of 50 mm and a cone angle of 0.0182. The measurements with the plate-plate geometry show sample stability for longer measurement times. **(c)** shows the same time sweep as **(a)** for the first 200 s measurement time including the nummerical derivatives of G' and G'' to show that after $t < 90$ s after preshearing the microstructure of the colloidal suspension is completely rebuild.

Time sweeps at a fixed ω_1 and a fixed γ_0 in the linear regime were made with a plate-plate geometry with a diameter of 40 mm (see Figure A.3.9(a)) and a cone-plate geometry with a diameter of 50 mm and a cone angle of 0.0182 (see Figure A.3.9(b)). It can be seen, that G' and G'' slightly increase with time related to the evaporation of the surrounding water. The moduli are more stable over time in the measurement with the plate-plate geometry compared to the measurement with the cone-plate geometry. Therefore, the

plate-plate geometry was chosen for the long time measurements conducted within this work. Furthermore, it can be seen that no particle crystallization occurs within 26 h.
In Figure A.3.9(c) the results of the time sweep conducted with the plate-plate geometry are shown for the first 200 s. Additionally, the time derivative of G' and G'' are depicted. After $t < 90$ s no change in G' or G'' with time, despite the slight increase due to slow evaporation of the dispersion medium, are present. From this, we can conclude, that the microstructure of the colloidal suspension rebuilds within $t < 90$ s. Therefore, a waiting time of $t_w = 90$ s after preshearing was chosen for the linear and nonlinear oscillatory shear measurements conducted within this work.

A.3.2.3 Reproducibility and Sample Stability

The reproducibility of the measurements is tested by conducting the same frequency sweeps at different rheometer loadings showing that different rheometer loadings result in deviations from each other around 8 % in G' and G''. The stability of the waterbased sample is tested by repeating this frequency sweep 1.5 month later. The obtained values for G' and G'' have a deviation from the ones measured 1.5 month earlier of about 19 % due to the evaporation of the dispersion medium water. Therefore, the mass fraction of the suspension was tested before conducting rheological measurements. The effective volume fraction for the investigation temperatures was derived from this mass fraction.

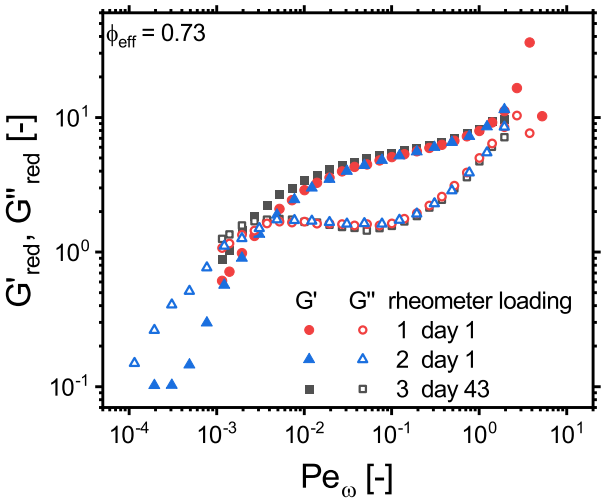

Figure A.3.10: G' and G'' in dependence on the angular frequency ω_1 for the same sample measured with the same parameter to test the reproducibility of the measurements and the sample stability. The deviations between the rheometer loadings are around 8 %. The deviations of G' and G'' after 43 days to the values obtained at day one are below 20 %.

A.3.2.4 Linear Rheological Characterization

In Figure A.3.11, the absolute G' and G'' dependencies on ω_1 and of G'_{red} and G''_{red} on Pe_ω are depicted for the measurements shown in Section 6.2.

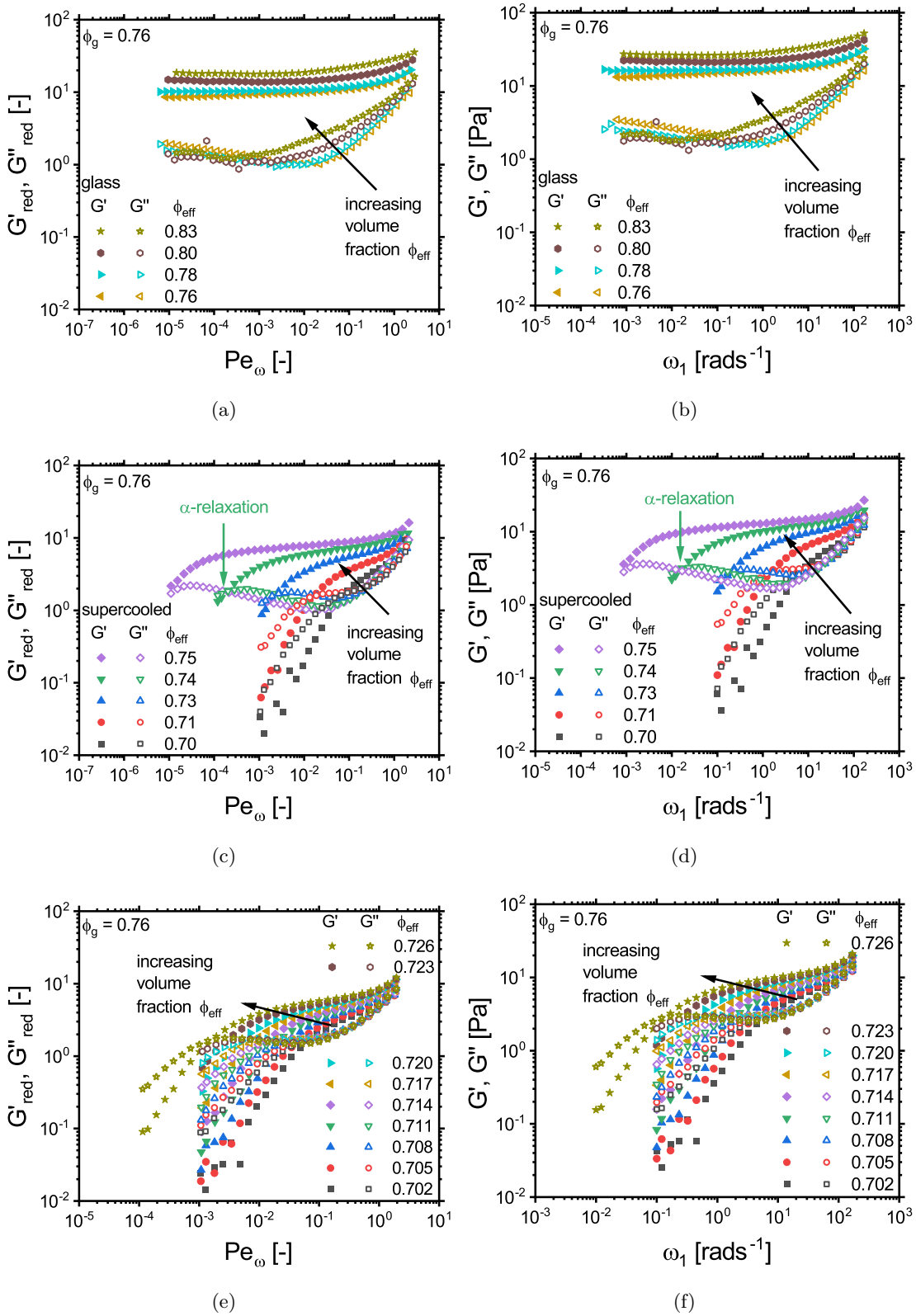

Figure A.3.11: G'_{red} (filled symbols) and G''_{red} (open symbols) in dependence on Pe_ω for **(a)** in the glassy regime ($\phi_{\mathrm{eff}} > \phi_{\mathrm{g}}$), **(c)** and **(e)** in the supercooled regime ($\phi_{\mathrm{eff}} < \phi_{\mathrm{g}}$). In **(b)**, **(d)** and **(f)** the corresponding G' and G'' dependencies on ω_1 are depicted. The crossover points of G'_{red} and G''_{red} are related to the α-relaxation times of the colloids, which increase for increasing volume fraction. The glassy samples exhibit a solid-like behavior ($G'_{\mathrm{red}} > G''_{\mathrm{red}}$) over the whole investigated frequency region, whereas the samples in the supercooled regime show a region with solid-like behavior followed by a crossover of G'_{red} and G''_{red} and a terminal regime for decreasing Pe_ω.

Additionally, frequency sweeps with smaller ϕ_{eff}-steps in the region between $\phi_{\text{eff}} = 0.702$ to 0.726 are depicted. They were conducted to increase the point density of the volume fraction dependence of the relaxation times shown in Section 6.2.1.
In the measurements at the lowest investigated ϕ_{eff} of 0.702 using the PP40 mm geometry, for $\omega_1 \leq 2.3 \times 10^{-1}\,\text{rad}\,\text{s}^{-1}$, the measured oscillation torque of $M = 1.2 \times 10^{-8}\,\text{N}\,\text{m}$ to $3.8 \times 10^{-8}\,\text{N}\,\text{m}$ is already below the lower torque limit in oscillation of $5 \times 10^{-8}\,\text{N}\,\text{m}$ of the manufacturer specifications of the used instrument[137] causing scattering of the G' and G'' values. The scattering of G' and G'' is already visible for $\omega_1 \leq 4.5 \times 10^{-1}\,\text{rad}\,\text{s}^{-1}$, where $M \leq 8.1 \times 10^{-8}\,\text{N}\,\text{m}$ for $\phi_{\text{eff}} = 0.702$ and for $\omega_1 \leq 3.3 \times 10^{-1}\,\text{rad}\,\text{s}^{-1}$, where $M \leq 1.9 \times 10^{-7}\,\text{N}\,\text{m}$ for $\phi_{\text{eff}} = 0.705$, showing that the lower torque limit of the instrument is higher than specified by the manufacturer.

A.3.2.5 Yielding under Steady Shear - Transient Stress

In Figure A.3.12(a), the transient stress of the suspension at the onset of flow is depicted for $\phi_{\text{eff}} = 0.83$ at $\dot{\gamma} = 3.73 \times 10^{-4}\,\text{s}^{-1}$ for different waiting times (t_w) after a preshear of $\dot{\gamma} = 100\,\text{s}^{-1}$ for 2 min. The increase of the steady state stress (σ_st) of $\frac{\Delta\sigma_\text{st}}{\sigma_\text{st}} > 10\,\%$ with increasing t_w for $t_\text{w} \geq 48\,000\,\text{s} \approx 13\,\text{h}$ indicates that evaporation of the dispersion medium, water, intervenes the measurements significantly for $t_\text{w} \geq 48\,000\,\text{s} \approx 13\,\text{h}$ consistent with the findings from oscillatory shear measurements in Figure A.3.9.
In Figure A.3.12(b), the dependence of the relative overshoot stress ($\sigma_\text{peak} - \sigma_\text{st}$) on t_w is depicted for the same ϕ_{eff} and $\dot{\gamma}$. The time to rebuild the disordered microstructure exceeds the waiting time used in the transient measurements in Section 6.3.2 $t_1 > 14\,000\,\text{s} > t_\text{w} = 6000\,\text{s}$ for low shear rates $\dot{\gamma} \leq 3.73 \times 10^{-4}\,\text{s}^{-1}$.

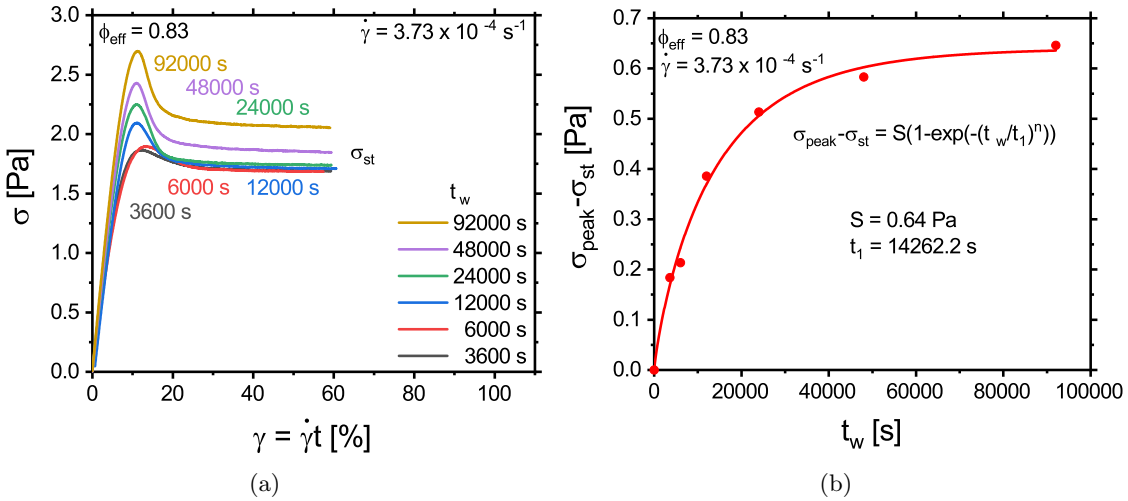

(a) (b)

Figure A.3.12: Influence of t_w on the transient stress at the onset of steady shear flow for $\phi_{\text{eff}} = 0.83$ at **(a)** $\dot{\gamma} = 3.73 \times 10^{-4}\,\text{s}^{-1}$ for $t_\text{w} = 10\,\text{s}$ to $92\,000\,\text{s}$. **(b)** The relative overshoot of the stress $\sigma_\text{peak} - \sigma_\text{st}$ in dependence on t_w showing a saturation. The lines depict the fit of the saturation process with a stretched exponential.

List of Figures

List of Tables

Nomenclature

Abbreviations

AFM	atomic force microscopy
DCS	differential centrifugal sedimentation
DLS	dynamic light scattering
ESEM	environmental scanning electron microscopy
FT	Fourier transform
FT-rheology	Fourier transform rheology
ISHSM	isotropically sheared hard sphere model
LAOS	large amplitude oscillatory shear
MAOS	medium amplitude oscillatory shear
MCT	mode coupling theory
PEP	poly(ethylene-*co*-propylene)
PEO	polyethylene oxide
PMMA	poly(methyl methacrylate)
PNIPAm	poly(*N*-isopropylacrylamide)
PPO	polypropylene oxide
PS	polystyrene
SAOS	small amplitude oscillatory shear
SEM	scanning electron microscopy
TEM	transmission electron microscopy

Physical Quantities

A	area
Ð	dispersity
D	diameter
d	distance
Δx	displacement
D_0	diffusion coefficient under high dilution
D_s	collective short time diffusion coefficient
ϵ	separation parameter
F	force
γ	strain
γ_0	strain amplitude
$\dot{\gamma}$	shear rate
γ_y	yield strain
G	shear modulus
G^*	complex shear modulus
$G'_\mathrm{red,P}$	reduced plateau modulus
G'_P	plateau modulus
G'	storage modulus
G''	loss modulus
G'_red	reduced storage modulus
G''_red	reduced loss modulus
h	distance between the plates
η	viscosity
η_0	zero shear viscosity
η_∞	high shear viscosity
$\eta_{\omega,\infty}$	high frequency viscosity
η_s	solvent viscosity
η_red	reduced viscosity
$\eta_\mathrm{0,rel}$	relative zero shear viscosity
I	intensity
$I_{3/1}$	relative intensity of the third harmonic
κ	electrical conductivity
k_B	Boltzmann constant
n	stretching exponent
Pe	Péclet number
Pe_0	Péclet number in steady shear
Pe_ω	Péclet number in oscillatory shear
ϕ	volume fraction
ϕ_eff	effective volume fraction
ϕ_g	glass transition volume fraction
ϕ_max	maximum volume fraction
ϕ_rcp	volume fraction at random close packing
q	wave vector
Q_0	intrinsic anharmonicity parameter
ρ_n	number density

R	radius
R_{H}	hydrodynamic radius
$R_{\mathrm{H,I}}$	intensity-weighted average hydrodynamic radius
R_{N}	number-weighted average radius
R_{W}	weight-weighted average radius
σ	stress
σ_{red}	reduced stress
σ_{st}	steady state stress
σ_{peak}	overshoot stress
σ_{P}	plateau of the overshoot stress
σ_{y}	yield stress
σ_{dyn}	dynamic yield stress
$\sigma_{\mathrm{dyn,red}}$	reduced dynamic yield stress
σ_{stat}	static yield stress
σ_{rel}	relative standard deviation
t	time
t_1	relaxation time
t_{w}	waiting time
T	temperature
T_{LCST}	lower critical solution temperature
τ	relaxation time
ω_1	angular frequency
ω_{cross}	crossover angular frequency
v	velocity
V	volume
V_{particle}	volume of the particle
$V_{\mathrm{suspension}}$	volume of the suspension
V_{DLVO}	DLVO potential
w	mass fraction

Publications and Conference Contributions

Publications

Fischer, L.; Maier, M.; Dingenouts, N.; Hirschberg, V.; Wittemann, A.; Fuchs, M.; Wilhelm, M. Nonlinear Rheological Behavior of Glass-Forming Colloidal Suspensions under Oscillatory Shear: Experiment and Relation to Mode Coupling Theory Predictions. Submitted to *J. Rheol.*

Conference Contributions

AERC 2022 L. Fischer, A. Wittemann, M. Maier, M. Fuchs, M. Wilhelm, *Rheological Investigations of Thermoresponsive Core-Shel Nanoparticles in Suspension above the Colloidal Glass Transition*, Annual European Rheology Conference (2022), Seville, Spain. – **Poster**

ECIS 2022 L. Fischer, A. Wittemann, M. Maier, M. Fuchs, M. Wilhelm, *Rheological Investigations of Thermoresponsive Core-Shel Nanoparticles in Suspension above the Colloidal Glass Transition*, European Colloid and Interface Society Conference (2022), Chania, Greece. – **Poster**

EYRS 2023 L. Fischer, M. Sutharsan, M. Fuchs, M. Wilhelm, *Medium Amplitude Oscillatory Shear Investigations of a Bimodal Mixture of Thermoresponsive Core-Shell Nanoparticles in Suspension around the Glass Transition*, European Young Rheologists Symposium (2023), online. – **Oral**

ICR 2023 L. Fischer, M. Sutharsan, M. Fuchs, M. Wilhelm, *Nonlinear Rheological Investigations of a Bimodal Mixture of PS-PNIPAm Core-Shell Particles around the Glass Transition*, International Congress on Rheology (2023), Athens, Greece. – **Oral**

Acknowledgements

This thesis could not have been completed without the support of my supervisors, colleagues, friends and family. Therefore, I would like to take the opportunity to express my gratitude to everyone who supported me all the way here:

First and foremost I would like to thank my supervisor *Prof. Dr. Manfred Wilhelm* for giving me the opportunity to pursue my PhD in his group and for his support. Thank you for the freedom to develop my own ideas and giving me the feeling for numbers and units! A special thank you also goes to *Prof. Dr. Patrick Theato* for co-examining this work.
I am grateful to have had the pleasure of working with my collaboration partners from the university of Konstanz *Prof. Dr. Matthias Fuchs*, *Manuel Maier* and *Leonhard Lang* without whom this research would not have been possible. Furthermore, I would like to thank the *German Research Foundation (DFG)* for funding of our project.
I am grateful for the opportunity to spend some months at FORTH in Heraklion, Crete with *Prof. Dr. George Petekidis*. Thank you for your trust, for enhancing my knowledge about colloidal glasses and your encouraging words. And special thanks to *Karlsruhe House of Young Scientists* for funding this research visit to FORTH.
Thank you, *Prof. Dr. Valerian Hirschberg*, for your advice, a lot of fruitful discussions and for always being willing to help. Thanks to *Dr. Nico Dingenouts* for teaching me a lot about colloidal suspensions and DLS and thank you for the lots of scientific discussions. Thanks to *Dr. Masood Khabazian* for helping me set up the ultrafiltration and *Prof. Dr. Alexander Wittemann* for providing an ultrafiltration reservoir and cell as a starting point for building my own system.
Thank you *Matthias Karg* and *Marco Hildebrandt* for conducting the temperature dependent DLS measurements.
My deepest gratitude goes to the whole *AKW* for the pleasent working athmosphere and your helpfulness. Thanks to all the proof-readers with a special thanks to *Tamara Meyer* for supporting me throughout the writing process. Heartfelt thanks goes to *Dr. Maxi Golla* for your solution-oriented thinking and a different perspective on any kind of challenges that came across my way.
I am very grateful for the support of my family and friends, especially of my *mother and sister* and of *Hendrik*. I appreciate your support. Thank you for taking as much weight off my shoulders as you could. Thank you for your unconditional love and trust in me!